EINDHOVEN UNIVERSITY OF TECHNOLOGY

Sorption thermal energy storage for smart grids

Citation for published version (APA):
Scapino, L. (2019). *Sorption thermal energy storage for smart grids: a system-scale analysis*. [Phd Thesis 1 (Research TU/e / Graduation TU/e), Mechanical Engineering]. Technische Universiteit Eindhoven.

Document status and date:
Published: 25/10/2019

Document Version:
Publisher's PDF, also known as Version of Record (includes final page, issue and volume numbers)

Please check the document version of this publication:

• A submitted manuscript is the version of the article upon submission and before peer-review. There can be important differences between the submitted version and the official published version of record. People interested in the research are advised to contact the author for the final version of the publication, or visit the DOI to the publisher's website.
• The final author version and the galley proof are versions of the publication after peer review.
• The final published version features the final layout of the paper including the volume, issue and page numbers.

Link to publication

General rights
Copyright and moral rights for the publications made accessible in the public portal are retained by the authors and/or other copyright owners and it is a condition of accessing publications that users recognise and abide by the legal requirements associated with these rights.

• Users may download and print one copy of any publication from the public portal for the purpose of private study or research.
• You may not further distribute the material or use it for any profit-making activity or commercial gain
• You may freely distribute the URL identifying the publication in the public portal.

If the publication is distributed under the terms of Article 25fa of the Dutch Copyright Act, indicated by the "Taverne" license above, please follow below link for the End User Agreement:

www.tue.nl/taverne

Take down policy
If you believe that this document breaches copyright please contact us at:

openaccess@tue.nl

providing details and we will investigate your claim.

Download date: 16. Nov. 2023

Sorption thermal energy storage for smart grids

A system-scale analysis

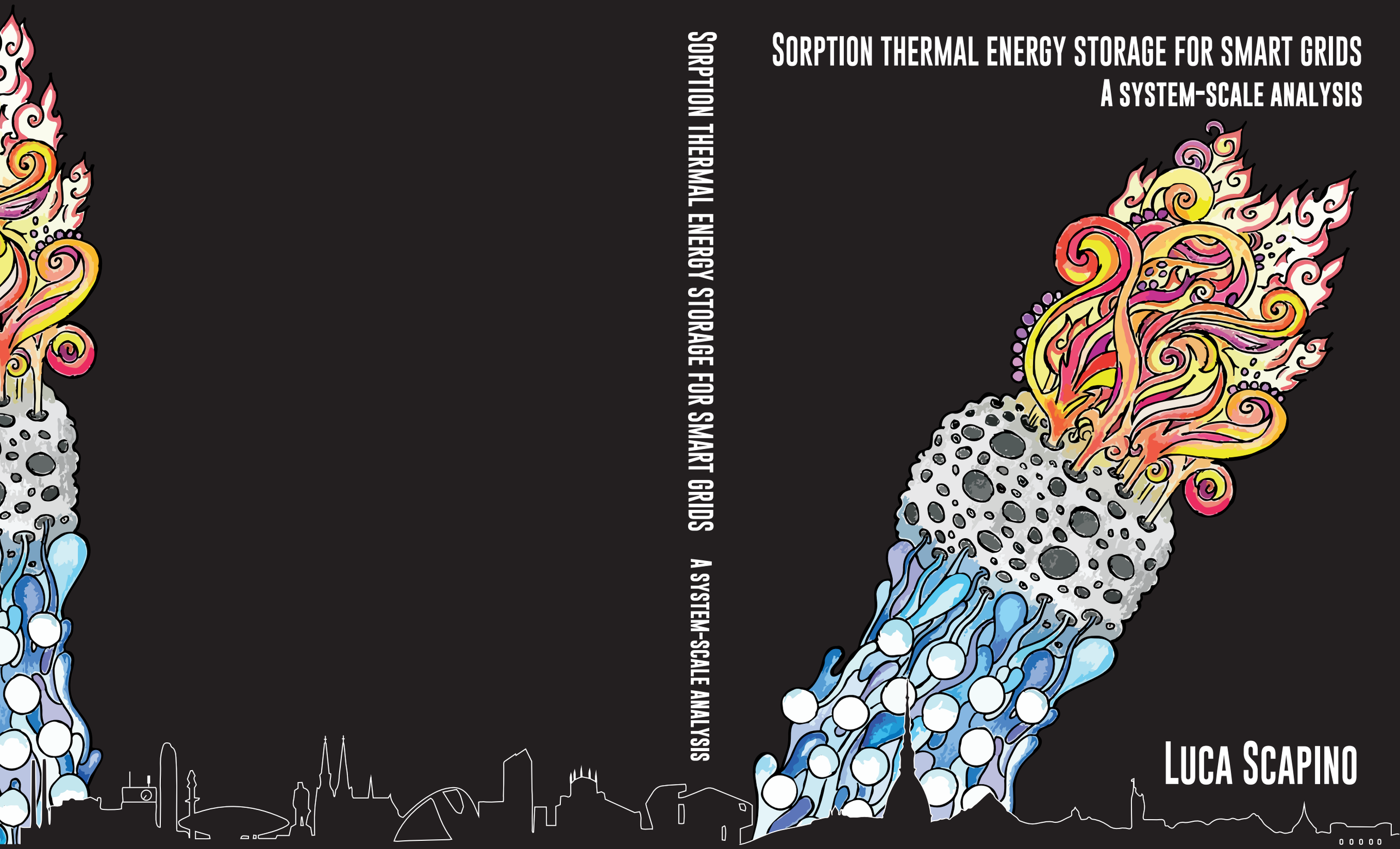

Luca Scapino

Sorption thermal energy storage for smart grids A system-scale analysis

Sorption thermal energy storage for smart grids

A system-scale analysis

PROEFSCHRIFT

ter verkrijging van de graad van doctor aan de
Technische Universiteit Eindhoven, op gezag van de
rector magnificus prof.dr.ir. F.P.T. Baaijens, voor een
commissie aangewezen door het College voor
Promoties, in het openbaar te verdedigen
op vrijdag 25 oktober 2019 om 13:30 uur

door

Luca Scapino

geboren te Turijn, Italië

Dit proefschrift van het proefontwerp is goedgekeurd door de promotoren en de samenstelling van de promotiecommissie is als volgt:

voorzitter:	prof.dr. D.H. van Campen
1e promotor:	prof.dr. H.A. Zondag
2e promotor:	dr.ir. C.C.M. Rindt
leden:	prof.dr. F. Kuznik (Université de Lyon - INSA)
	prof.dr.ir. J.L.M. Hensen
	prof.dr.ir. D.M.J. Smeulders
adviseur(s):	dr. A. Sciacovelli (University of Birmingham)
	dr. J. Diriken (EnergyVille)

Het onderzoek of ontwerp dat in dit proefschrift wordt beschreven is uitgevoerd in overeenstemming met de TU/e Gedragscode Wetenschapsbeoefening.

Dedicated to my parents, Vanda and Dario.
For Simone, Riccardo and Viola: our future.

The most beautiful thing we can experience is the mysterious.
It is the source of all true art and all science.
He to whom this emotion is a stranger,
who can no longer pause to wonder and stand rapt in awe,
is as good as dead: his eyes are closed.

Albert Einstein

©Copyright 2019, Luca Scapino

Copyright of the individual chapters containing published articles belongs to the publisher of the journal listed at the beginning of the respective chapters. All rights reserved. No part of this publication may be reproduced, distributed, or transmitted in any form or by any means, including photocopying, recording, or other electronic or mechanical methods, without the prior permission of the copyright owner.

Cover design: Luca Marchese and Matteo Brino

Printed by Ipskamp Printing B.V.

A catalogue record is available from the Eindhoven University of Technology Library.
ISBN: 978-90-386-4865-1

TABLE OF CONTENTS

CHAPTER 1: INTRODUCTION.....1

1.1 THE ENERGY TRANSITION: TOWARDS SMART GRIDS.....2
1.2 SORPTION THERMAL ENERGY STORAGE.....4
1.3 OBJECTIVES AND THESIS OUTLINE.....5

CHAPTER 2: SORPTION THERMAL ENERGY STORAGE: A REVIEW ON MATERIALS AND REACTOR PROTOTYPES 9

2.1 MATERIALS FOR SORPTION HEAT STORAGE.....10
2.2 SORPTION THERMAL ENERGY STORAGE SYSTEMS.....20
2.3 DISCUSSION AND CONCLUSIONS.....31

CHAPTER 3: A SIMPLE COMPARISON OF IDEAL SYSTEMS: SEASONAL STORAGE FOR SPACE HEATING 35

3.1 INTRODUCTION.....36
3.2 REFERENCE SCENARIO, SYSTEMS AND MATERIALS.....36
3.3 OPEN SOLID SORPTION SYSTEMS 41
3.4 CLOSED SOLID SORPTION SYSTEMS.....50
3.5 LIQUID SORPTION SYSTEMS.....52
3.6 SORPTION SYSTEMS COMPARISON.....55
3.7 CONCLUSIONS 62

CHAPTER 4: STES MODELS FOR SYSTEM-SCALE SIMULATIONS: A PHYSICS-BASED AND A DATA-DRIVEN APPROACH.....65

4.1 INTRODUCTION.....66
4.2 SORPTION SYSTEM DESCRIPTION 67
4.3 HIGH-FIDELITY PHYSICS-BASED MODEL.....69
4.4 TESTS.....74
4.5 SPECTRAL MODEL 77
4.6 DATA-DRIVEN MODEL.....89
4.7 CONCLUSIONS 111

CHAPTER 5: ENERGY SYSTEM OPTIMIZATION I: THE POTENTIAL OF A CENTRALIZED STES OPERATING IN DIFFERENT ENERGY MARKETS.....115

5.1 INTRODUCTION.....116
5.2 REFERENCE ENERGY SYSTEM 118
5.3 REFERENCE ENERGY SYSTEM COMPONENTS.....122

5.4 OPTIMIZATION FRAMEWORK 132
5.5 RESULTS 137
5.6 DISCUSSION AND CONCLUSIONS.....151

CHAPTER 6: ENERGY SYSTEM OPTIMIZATION II: THE POTENTIAL OF A DECENTRALIZED STES OPERATING IN A DOMESTIC ENVIRONMENT.....155

6.1 INTRODUCTION 156
6.2 REFERENCE ENERGY SYSTEM 157
6.3 OPTIMIZATION FRAMEWORK 173
6.4 RESULTS 178
6.5 DISCUSSION AND CONCLUSIONS.....195

CHAPTER 7: CONCLUSIONS.....203

APPENDICES 209

APPENDIX A: ACTIVE MATERIALS DATA AND EQUILIBRIUM CURVES.....211
APPENDIX B: ADDITIONAL PARAMETERS FOR THE SYSTEMS DESIGN.....213
APPENDIX C: ESTIMATION OF THE IDEAL LIQUID SORPTION SYSTEM.....214
APPENDIX D: HIGH-FIDELITY PHYSICS-BASED MODEL PARAMETERS.....219
APPENDIX E: ADDITIONAL SIMULATION RESULTS FOR THE SPECTRAL MODEL.....220
APPENDIX F: THE "BIG-M" METHOD FOR CONDITIONAL STATEMENTS.....221

BIBLIOGRAPHY.....223

NOMENCLATURE 237

SUMMARY 245

LIST OF PUBLICATIONS 249

ACKNOWLEDGEMENTS 251

CURRICULUM VITAE 255

CHAPTER 1

INTRODUCTION

This chapter introduces the framework of the present research (1.1) and the main working principle of the thermal energy storage technology addressed in this work (1.2). In section 1.3, the outline of this thesis is presented.

1.1 The energy transition: towards smart grids

The awareness of humankind's role into climate change [1] and the increasing energy intensity in developing and underdeveloped countries [2] are amongst the main drivers for a transition towards energy conservation and a more sustainable use of energy. At European level, long-term strategies aim to reduce, by 2050, the greenhouse gases emissions by at least 80 % compared to 1990 levels, while maintaining or improving the EU energy security, and economic growth [3,4].

The energy grid consists of a system in which multiple carriers (e.g. electricity and heat) are produced, transported, consumed, and stored. The level of complexity of this system is constantly increasing due to technological advancements such as energy production systems with new requirements, transportation and storage methods that are more efficient, new policies, and new types of consumers and other stakeholders. The increasing penetration of renewable energy sources, cogeneration, and intermittent power sources in general, is drastically changing the requirements on the energy grid, and it poses new challenges for the energy system. Some of the new energy production units are characterized by relatively low and decentralized installed capacities, and they can produce multiple energy carriers. Moreover, their energy production pattern can be intermittent and unpredictable, determined by the owner's needs or by the energy source availability. Therefore, the energy network is constantly evolving [5,6] to cope with new challenges such as new types of stakeholders and an increasing penetration of intermittent distributed production sources. To this extent, the smart grid concept adds an additional carrier beside the energy carriers: information. Through remote sensing, data collection and forecasting, monitoring, control, and analysis techniques, smart grids tackle the abovementioned challenges by optimizing the system operation, improving its reliability [7].

The European Commission, in 2011, defined a smart grid as "*an electricity network that can cost efficiently integrate the behavior and actions of all users connected to it – generators, consumers and those that do both – in order to ensure economically efficient, sustainable power system with low losses and high levels of quality and security of supply and safety*" [8]. The abovementioned definition is mainly focused on the electricity grid. However, it can be extended to a multi-carrier energy grid given the increasing interdependency between different carriers due to, for example, cogeneration (e.g. electricity and thermal energy), energy storage of specific carriers (e.g. cogeneration and storage of only one energy carrier), energy conversion (e.g. electricity-to-heat or vice versa).

According to the European task force for the implementation of smart grids into the European internal market (SGTF) [9], the expected services and functionalities of a smart grid will:

- Allow consumers to play an active role in the system optimal operation.
- Provide greater information and usage options to energy producers and customers.
- Facilitate the connection of different production technologies.

- Accommodate renewable energy production peaks.
- Significantly reduce the environmental impact of the energy system.
- Increase the system reliability.
- Allow demand response programs and services.
- Foster market integration towards an European integrated market.

Storage of multiple energy carriers, demand side management, exchange and relocation through conversion of energy carriers are amongst the main practices that the future energy system will have to incorporate to gain the needed flexibility [10] and cope with possible geographical and temporal mismatches between energy production and consumption. Energy storage is useful to handle fluctuations in energy demand to spread the production of energy needed during demand peaks over a different time period and to make efficient use of fluctuating production sources such as renewables, increase energy grid safety, and improve the overall system efficiency [11]. Thermal energy storage is an attractive storage category because in principle it can be more economical than other technologies, it has a wide range of storage possibilities with storage periods ranging from minutes to months, and finally because thermal energy dominates the final energy use in sectors such as the domestic built environment (Figure 1.1). In this dissertation, special focus is on sorption thermal energy storage (STES), a thermal energy storage technology which has the potential to store large amounts of energy with low thermal losses and for long time periods. Due to these advantages, STES integration in the future smart grids has the potential to increase the system flexibility and the penetration of renewable energy sources.

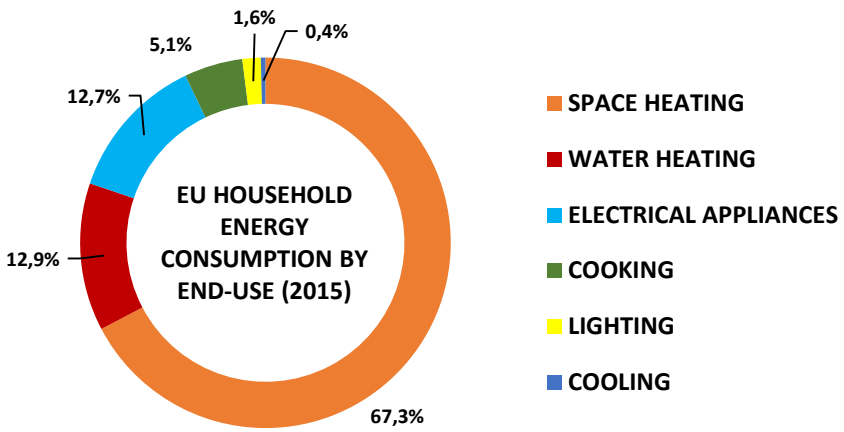

Figure 1.1: Average EU household energy consumption by end-use in 2015 [12].

1.2 Sorption thermal energy storage

Thermal energy storage can be divided into three main categories according to how energy is stored: sensible heat (e.g. water tanks, underground storage) [13–15], latent heat (e.g. ice, phase change materials) [16–18], and sorption heat storage [19–21].

The main advantages of sorption heat storage are higher energy density and negligible heat losses compared to a conventional thermal storage based on sensible heat. A conventional water storage needs to be approximately five to ten times larger than a sorption heat storage system for storing the same amount of energy. Sorption heat storage implies the use of physical or chemical bonds to store energy. The principle of sorption (Figure 1.2) occurs during a reaction in the form $A_{(solid)} + B_{(gas)} \leftrightarrow AB_{(solid)} + heat$. In order for the reaction to take place, at least two components are needed: a sorbent (A), which is typically a liquid or solid, and a sorbate (B), which is typically a vapor (e.g. water vapor). During the charging process (desorption), the endothermic reaction occurs, and the sorbent and sorbate are separated. The two components can then be stored separately, ideally without energy losses. During the discharging process (sorption), sorbent and sorbate react, producing an exothermic reaction that releases heat. This work mainly focuses on sorption reactions involving water as sorbate. Thus, within this work, the desorption reaction is also referred as dehydration, and the sorption reaction as hydration.

Due to its advantages, potential applications of sorption heat storage are those where conventional sensible heat storage technologies would require a large amount of storage medium or would produce an unacceptable amount of thermal losses. For example, one of the most interesting applications in the built environment for this type of technology consists of storing solar energy in summer to satisfy the space heating and domestic hot water (DHW) demand of households during winter. From the system integration perspective, solar energy can be harvested with solar thermal collectors and used for the endothermic reaction that separates the sorbate and the sorbent. During winter, the reverse exothermic reaction can be induced, and the heat can be used for the household thermal energy needs. If compactness is a main requirement, using STES for shorter storage periods could become an option. However, the shorter the storage time is, the more sensible heat storage becomes competitive. Other possible introductory markets for STES are applications in which an industrial waste heat source can be used for the desorption reaction, or in which thermal energy has to be transported from the production location to the consumption location [22].

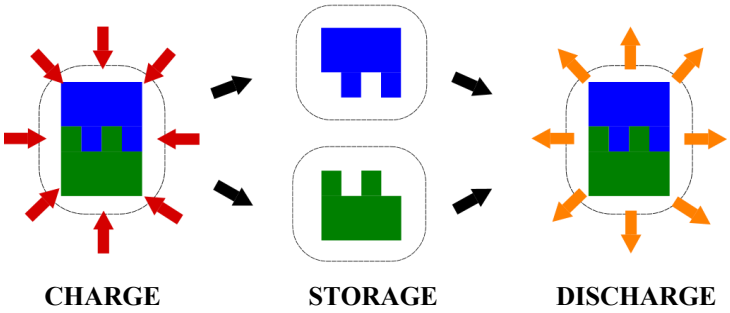

Figure 1.2: Sorption heat storage concept. Partially adapted from Scapino et al. [19].

1.3 Objectives and thesis outline

Sorption heat storage has still several challenges to be addressed before reaching a maturity level suitable for commercialization. Especially for applications requiring low-grade heat (e.g. 40 °C – 90 °C), most of the scientific research is still focused on material-scale to find suitable sorbent/sorbate candidates that have the required stability, cyclability and performance requirements to be suitable for commercial applications. At reactor-scale, the main technological challenges concern the reactor design, heat and mass transfer issues, possible corrosion, high efficiency and energy density at the operating conditions. The reactor is connected with the auxiliary components of the sorption thermal energy storage (STES) necessary for its operation, and the full STES design needs to be optimized. The type of auxiliary components depends on the system layout, heat sources, and the type of application. Finally, the STES interaction with the energy system, being a small decentralized STES in a building or a large centralized STES, is also a matter of research. It is important to study the competitivity of this technology for different applications and markets in order to direct the scientific research towards the most critical challenges, both at material- and reactor-scale.
After a comprehensive review on the STES advancements at material- and reactor-scale, this work focuses on the system-scale. In particular, it investigates several challenges concerning the simulation of a sorption reactor for system-scale simulations, and the possible role of STES in the energy system through techno-economic analyses and energy system optimization. In this work, the following main objectives, in the form of research questions, are addressed:

1. What is the current state of the art and what are the main bottlenecks in the development of materials and system prototypes for sorption thermal energy storage, and in particular for domestic applications?

2. What is the economic competitivity of different sorption thermal energy storage materials and system layouts for a conventional application such as space heating in the built environment?

3. What is the most compact and efficient model for sorption thermal energy storage to be integrated in an energy system model, which can be used to perform dynamic system simulations?

4. What are the impact and the benefits of integrating a sorption thermal energy storage in an energy system? And how can a sorption heat storage be modeled in a techno-economic optimization framework?

In Chapter 2, the first research question is addressed. A review on the recent advancements on sorption thermal storage at material- and prototype-scales is presented. The focus is on applications requiring low-grade heat, mostly in the built environment. At material-scale, emphasis is put on solid/gas reactions with water as sorbate. In particular, salt hydrates, adsorbents, and recent advancements on composite materials are reviewed. At prototype-scale, the article provides an updated review on system prototypes based on the reviewed materials. Main design issues such as heat and mass transfer in the reactors are addressed.

In Chapter 3, the second research question is answered. A performance comparison in terms of energy density and storage capacity costs of different ideal sorption heat storage systems used for seasonal heat storage is carried out. The reference scenario for the analysis consisted of satisfying the yearly space heating demand of a passive house. Three salt hydrates ($MgCl_2$, Na_2S, and $SrBr_2$), one adsorbent (zeolite 13X) and one ideal composite based on $CaCl_2$, are used as active materials for the investigated solid sorption systems, and sodium hydroxide (NaOH) is considered as active material for a liquid sorption system.

Chapter 4 deals with the third research question. In particular, two types of numerical models are presented to dynamically simulate a sorption reactor: a compact physics-based model and a data-driven model. The first model is directly based on the physics governing the phenomena in the sorption reactor. The second model is a black-box model based on neural networks that, with available simulation data from a high-fidelity physics-based model, is trained to reproduce the dynamic sorption reactor behavior within prescribed operating conditions. The performance of the two models is then compared and discussed.

Chapter 5 addresses the last research question. A techno-economic optimization model of a reference energy system operating in different energy markets is developed and analyzed. The system consists of a geothermal doublet providing thermal energy to a low-temperature district heating network and to an organic Rankine cycle. The latter can produce electrical energy when the thermal energy is not used by the district heating network. A formulation

within the optimization framework of a centralized STES, with different modular units operating in parallel, is developed. Different scenarios are studied for price schemes in the energy markets of Belgium and UK. In particular, the impact of different energy market mechanisms on the overall yearly system profits is investigated.

In Chapter 6, the last research question is investigated as well. However, a different energy system is investigated, and a different STES formulation in the optimization framework is developed. In particular, the integration of a decentralized STES in a single-family house is studied. The energy system can produce thermal energy with a conventional gas boiler or with solar thermal collectors, Differently from Chapter 5, the STES consisting of several modular units is assumed not to be operating in a parallel configuration. Therefore, only one STES unit at a time can be charged and discharged. During the charging mode, a variable charging power is present, depending on the available solar energy in a specific moment of the year. Then, the impact of the STES integration on the yearly system costs and solar fraction is investigated. Finally, a sensitivity analysis on relevant system parameters, such as the electricity-gas price ratio or the STES capacity cost, is carried out.

Chapter 7 addresses the main conclusions of this work, and the main results are summarized.

CHAPTER 2

SORPTION THERMAL ENERGY STORAGE

A REVIEW ON MATERIALS AND REACTOR PROTOTYPES

Based on:
Scapino L. Zondag H. A., Van Bael J., Diriken J., Rindt C. C. M.
Sorption heat storage for long-term low-temperature applications:
A review on the advancements at material and prototype scale
Appl Energy 2017;190:920–48
doi:10.1016/j.apenergy.2016.12.148

The aim of this chapter is to provide an overview on the last advancements on sorption heat storage technologies for long-term low-temperature applications based on solid/gas reactions with water as sorbate. The focus of this chapter is on the state of the research at material- and prototype-scale for applications requiring heat within a temperature range of 30 °C - 150 °C such as space heating, domestic hot water production, and some industrial processes. The current work is divided into three main sections. In section 2.1, the focus is on sorption materials and current advancements on their research. In section 2.2, a review on the state-of-the-art research on solid sorption storage systems is carried out, and their performances are discussed and compared. Finally, in section 2.3, the main conclusions from the materials and prototypes review are presented.

2.1 Materials for sorption heat storage

2.1.1 Terminological framework

The terminological framework of sorption heat storage has been defined by Yu et al. [21], based on the work of many authors, and this terminology will be adopted in the present work. Sorption includes different phenomena, and it is a prerequisite for a chemical process mediated by a surface. Sorption reactions can be divided into two categories according to the sorption mechanism: absorption and adsorption.

Absorption is defined as *"the process of one material (absorbate) being retained by another (absorbent)"* [23]. It occurs at the sorbent molecular level, and it alters the composition and morphological structure of a solid sorbent. Therefore, during the process, a material expansion typically occurs and significantly higher activation energy than for adsorption is present. This energy is mainly related to covalent bonding of atoms and molecules. Absorbents can be liquids or solids, and the main difference is that their concentration during the reaction process varies stepwise for solids or continuously for liquids. Absorbates can be liquids or gases, which have a different amount of binding energy released as heat of reaction. If the absorbate is in liquid state, part of the binding energy is needed to break the bonds within the liquid, therefore, only part of it will be released as heat of reaction. For absorbents in vapor state, all the binding energy is released as heat of reaction.

Adsorption is defined as "*a phenomenon occurring at the interface between two phases, in which cohesive forces act between the molecules of all substances irrespective of their state of aggregation*" [24]. Therefore, adsorption occurs at the surface of the adsorbent forming an extremely thin layer of atoms or molecules on the adsorbent surface, while leaving its structure unaltered. No expansion occurs and no or negligible activation energy is involved.

A further division amongst sorption phenomena can be made based on the cohesive forces involved in the process: physisorption and chemisorption. In physisorption, the sorption energy is typically related to the weak intermolecular forces (Van der Waals forces) and hydrogen bonding [23] and no activation energy is required. In chemisorption, stronger covalent bonding is involved, and in some cases, it can be irreversible. Often, both processes can simultaneously happen, and a clear distinction cannot be made.

Yu et al. [21] divided sorption heat storage into four main categories: liquid absorption, solid adsorption, chemical reaction and composite materials. This division emphasizes the predominant type of reaction that occurs during the sorption processes. A similar subdivision is presented in Figure 2.1, in which the "Composites" sub-category is shared between the "Chemical Reaction" and the "Solid Adsorption" categories since both phenomena are present.

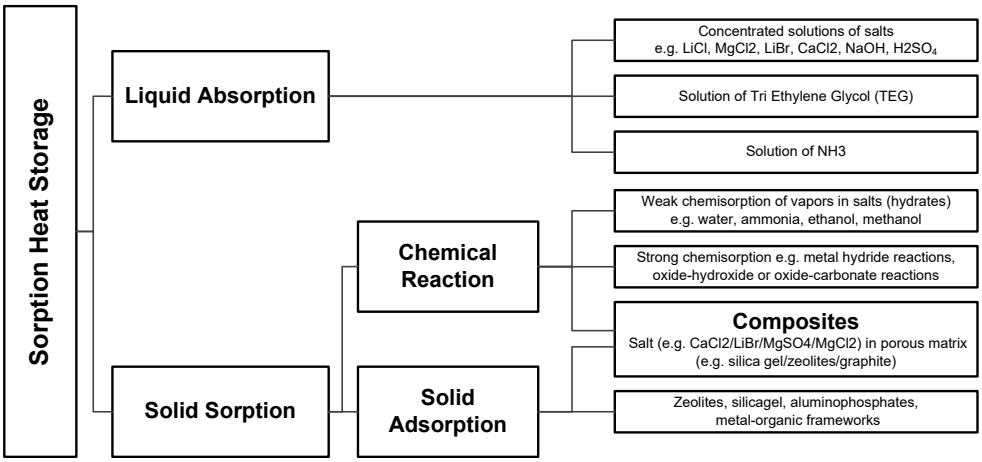

Figure 2.1: Classification of sorption heat storage. Partially adapted from [21] **.**

2.1.2 Materials selection criteria

In order to use a sorption material for thermal energy storage purposes, certain criteria should be met concerning the material energy density, physical characteristics and safety. In Table 2.1, the selection criteria for a sorption material for long-term low-temperature heat storage purposes are shown. In principle, a high uptake of sorbates leads to a high energy density. However, many requirements concerning the kinetics are also present such as regeneration temperature and time. Water is the preferred sorbate because it is abundant, low cost and non-hazardous.

Table 2.1: Selection criteria for suitable sorption materials [20,27–29]

• High uptake of sorbate	• Small molar volume of the products to minimize storage volume
• High energy density at system operating temperatures	• Small volume variation during reaction
• Regeneration at relatively low temperature	• High thermal conductivity
• Short regeneration time	• Rapid separation of products during storage
• Good mass transport of the sorbate	• Reaction compounds easy to handle
• Good heat transport from/to the sorbent	• Non-toxic

- Reactions completely reversible without secondary reactions
- High yield of reaction at charge and discharge temperatures
- Large reaction enthalpy to maximize storage capacity
- Preferably components non-reactive to O_2
- Sufficiently high discharge temperature at system operating conditions
- Non-flammable/explosive
- Non-corrosive
- Low cost
- Material commercially available

2.1.3 Solid sorption

Solid sorption materials can be divided into three categories (Figure 2.1): chemical reaction, solid adsorption and composites. The chemical reaction category includes materials undergoing solid/gas reactions in which an absorption process is predominant but, in principle, also adsorption may be occurring. The solid adsorption category includes purely adsorbent materials. Finally, composite materials can be a combination of the abovementioned categories including also inert components.

Chemical reaction: salt hydrates

In the following paragraph, the chemical reaction materials category is discussed. The emphasis is on materials that can be suitable for long-term low-temperature heat storage purposes. Therefore, materials with too high desorption temperatures or too many unmet requirements from Table 2.1 are marginally discussed. In particular, the focus of this section is on salt hydrates. Other materials such as hydroxides, carbonates and ammoniates are further discussed in Scapino et al. [19].

Extensive research on salt hydrates is being carried out for thermal storage purposes. The main reasons are a high theoretical energy density of the materials, desorption temperatures achievable with waste heat sources and solar thermal collectors, and discharge temperatures useful for low-temperature heat applications such as space heating and domestic hot water production. Currently, research at material level is still ongoing due to technical drawbacks of salt hydrates, which are further discussed in the following paragraphs. The general reversible reaction of a salt hydrate can be written as in equation 2.1.

$$Salt \cdot \nu H_2O_{(solid)} + Heat \leftrightarrow Salt_{(solid)} + \nu H_2O_{(gas)} \qquad 2.1$$

The reversible reaction can take place in different steps at different desorption temperatures, and intermediate hydrates of the salt can appear in the system. This is because the binding energy of the water molecules increases with the decrease of the water molecules into the salt molecular structure. For some practical applications of salt hydrates for sorption heat storage, only part of the reversible reaction is considered. The reason can be that in order to have a certain salt in its anhydrous form, a too high desorption temperature is required. Conversely, by having a completely hydrated form, deliquescence might occur and the sorbate mass transfer into the system will be blocked causing issues such as high pressure drop and ultimately system failure.

The main findings on the utilization of pure salt hydrates as sorption materials for long-term low-temperature heat storage are presented in Table 2.2. For an extensive discussion of each of the materials presented in the table one is referred to Scapino et al. [19]. In Table 2.2, their energy density measured during experiments at different operating conditions and their main advantages and issues are displayed. The reported desorption temperatures are the maximum desorption temperature in the experiments at which the material was subjected, while the water vapor pressure reported was present during hydration phases. It has to be stated that, in some cases, the experimental conditions were not clear in the scientific literature. Therefore, it is advisable to interpret the data with caution. A proper material characterization at system operating conditions is always advisable before experimentation at larger scales in order to avoid misleading results and indications [25]. Due to the intrinsic disadvantages of every material, their utilization in pure form for sorption heat storage is challenging. Despite the high energy densities measured, they can have stability problems at system operating conditions, slow kinetics, problems with corrosiveness and toxicity, or too high costs.

Solid adsorption

In general, since adsorption reactions have weaker bonding forces than absorption reactions, the energy density of these materials is lower compared to e.g. salt hydrates. Moreover, for certain adsorbents such as zeolites, the water uptake is relatively low due to the structural limitations of the matrix itself. On the other hand, heat and mass transport are improved compared to salt hydrates due to a better stability of the materials. Typically, adsorption materials should have a large internal pore volume and surface area for a large adsorption capacity, fast adsorption kinetics, good mechanical strength and they should be easily regenerable [26].

In Table 2.3, a summary of the energy densities and desorption/adsorption temperatures of the most promising adsorption materials is presented. In Scapino et al. [19], research on various zeolites, aluminophosphates (ALPOs), silico-aluminophosphates (SAPOs), and metal organic frameworks (MOFs) is discussed more in detail. It is evident that material energy density values are lower compared to pure salt hydrates. However, the investigated adsorption materials do not present large instability issues at system operating conditions. Moreover, corrosiveness or toxicity issues were not found.

Table 2.2: Summary of main advantages and disadvantages of the investigated pure salt hydrates.

	E_{vol} [GJ/m^3]	T_d [°C]	p_w [mbar]	C_{wt} [€/t] [34,46]	Main issues	Advantages	Ref
$MgSO_4$	1.8-2.2	150	12.5 -13	77	Heat release above 50 °C not possible; low temperature lift.	Most of the energy stored below 90 °C	[27–32]
Na_2S	1.93-2.66	100	19	348	Melting reduced mass transfer; operation under vacuum required; highly corrosive; formation of H_2S.	High energy density	[33,34]
$MgCl_2$	1.89-1.94	150	11.8-31.6	154	Deliquescence and overhydration below 40 °C; thermal decomposition and HCl formation above 110-130 °C.	Relatively large temperature lifts	[28,29,34–39]
$CuSO_4$	1.93	150	2.13-69	134	Low temperature lift; environmental toxicity.		[29,31]
$SrBr_2$	2.02	80	9.7-17.5	2400	High cost.	High stability and energy density	[34,40–42]
K_2CO_3	1.2 - 1.3	65	12	1000	Formation of $KHCO_3$ in open system;	High stability; safe; low dehydration temperature; good cyclability.	[43–45]

Concerning AlPOs, SAPOs and MOFs, maximum discharging temperatures of 40 °C were set during tests; therefore, their ability to produce higher temperature heat is not investigated yet. Zeolites, on the other hand, presented adsorption temperatures suitable for low temperature heating and DHW production.

Table 2.3 Energy density and desorption temperature ranges for the investigated adsorption material category [19]. **E_{vol} = volumetic energy density. T_d: desorption temperature. T_s: sorption temperature.**

Adsorption Material	E_{vol} [GJ/m^3]	T_d [°C]	T_s [°C]
Zeolites	0.4-0.6	Up to 180	Up to 80
AlPOs and SAPOs	0.61*-0.86	95-140	30-40
MOF (MIL-101)	1.6	90-140	30-40

* Assuming a packed density of 840 kg/m3 for SAPO-34 [47]

Composites

Sorption heat storage through chemical reactions, and in particular with salt hydrates, is of main interest. Chemical reactions have high theoretical energy densities, desorption temperatures achievable with solar thermal collectors or with waste heat, and discharge temperatures useful for low temperature heating. However, many issues are still present at material level like overhydration and deliquescence at low temperatures, material decomposition at high temperatures, degradation after a few cycles, poor thermal conductivity and low power output [29,37,48,49]. In order to overcome these disadvantages, composite materials for heat storage purposes are being investigated. They consist of at least two materials in which, in general, one gives structural support (host matrix) and the other is the active material that undergoes the sorption reaction. The host matrix should have a large porosity in order to retain the largest amount of active material possible. However, a compromise between pores occupied by the active material and free pores has to be present in order not to impede the sorbate transport [49]. Other functions of the host matrix are to increase the composite thermal conductivity and stability [50]. The matrix can provide also sorption heat if the pore size is small, but the amount of salt uptake decreases. On the other hand, large pores are able to retain larger amount of salt, but the host matrix will not participate in the sorption process. For example, a matrix of zeolite 13X could provide a consistent amount of sorption heat and participate in the heat storage process, however the adsorbent desorption temperature should be achieved in order to utilize its heat of sorption. The sorption process of salts hydrate/porous matrix composites includes a non-linear combination of the characteristics of an adsorption system and a chemical reaction system [51]. The result is typically a type VI adsorption isotherm in which each sorption step reflects a chemical reaction between the salt and the sorbate [52]. It is expected that the gas-solid reaction of a confined salt is much faster than a bulk one since the rate of sorption is controlled by the intra-particle vapor diffusion [53]. A review of current studies on composite materials is presented in [19] together with the experimental operating conditions and the main findings. In Table 2.4, a summary of the performance and main findings is presented.

The water vapor pressure, when available, refers to hydration reactions. The two values of temperature refer to sorption and desorption, respectively. Energy densities are often the highest or most achievable ones related to the most promising composite material in the study, if more composites were investigated. It is clear that research at material level is still needed to find a suitable composite material that can satisfy the requirements of a long-term low-temperature heat storage system; in which high energy density, material hydrothermal stability at system operating conditions, and other relevant requirements (Table 2.1) need to be satisfied. It is noticeable that the research is still investigating a broad range of materials to be used as matrices and active materials; highlighting the fact that the scientific community is still in a screening phase. Moreover, further requirements have to be satisfied at technical and economic levels. For example, zeolite 13X showed good performance as host matrix beside as pure active material, leading to a 27 % higher energy density of a composite impregnated with $MgSO_4$ (15 wt%) compared to pure zeolite 13X. However, its high cost and desorption temperatures, have to be taken into account because it will largely increase the system costs and decrease the system efficiency. Moreover, due to the small pore size, it cannot incorporate a large amount of salt.

Composite materials, compared to zeolite 13X, if stable at system operating conditions, can lead at least to lower system costs. On the other hand, compared to pure salt hydrates, composites can be stable materials. Considering a composite made by a salt and an inert matrix, the energy density might not be much higher than e.g. pure zeolite 13X, supposing suitable operating conditions. However, if the material costs are lower, the system might be able to become commercially attractive even if a relatively large volume of material is required.

Ultimately, the active material selection depends on the intended application that imposes the system operating conditions. As suggested by Aristov et al. [52], research should continue to be focused on systematic testing of novel adsorbents initially used for different purposes, and tailoring of new adsorbents/composites that can perform at their best at the selected system operating conditions.

Table 2.4: Summary of investigation on composites materials for sorption heat storage [19].

Matrices	Salts	Salt Content wt%	Experimental conditions		E_{vol} [GJ/m^3]	Main findings	Ref.
			T [°C]	p_v [mbar]			
Silica gel, zeolite 13X; vermiculite	$CaCl_2$, $MgSO_4$, $Ca(NO_3)_2$, $LiNO_3$ and LiBr	2 – 65****	30 - 140	-	up to 0.18	Micro-pore network of some matrices partially destroyed due to cyclical salt expansion/shrinking.	[54]
Carbon foam; expanded natural graphite	KCl; $CaCl_2$	63 - 90	25 - 200	20	up to 0.63	Improved heat conductivity and higher water uptake.	[49]
Wakkanai siliceous shale	LiCl; CaCl2	9.6	15 - 150	22.1	0.2	Discharge temperature above 50 °C with 22.1 mbar of water vapor pressure at 25 °C. Cyclability assessed for a desorption temperature of 60 °C. Formation of salt solution limited the sorbate sorption process.	[55]
Graphite, copper, zeolite A, sand	$MgCl_2$	46 - 69	35 - 200	11.8 - 21.8	0.56*	Adding graphite increased conductivity and allowed reactions at 10-15 °C lower for high heating rates. Salt decomposition above 125 °C did not allow zeolite to be used as active material.	[56]
Activated carbon, silica solution, expanded graphite	LiCl	32 - 45	30 - 90	25.4	0.72-1.43	Expanded graphite increased thermal conductivity and decreased water uptake. Hysteresis present during the de/sorption cycles.	[48]
Silica Gel; alumina	$CaCl_2$, $MgCl_2$ and LiBr	30 - 75	-	-	-	Thermal conductivity of composite had a large increase after a threshold value, which coincided with the complete matrix meso-pores filling of salt in silica gel. For alumina, this behavior was not present probably due to the material pores structure.	[57]

Table 2.4: Summary of investigation on composites materials for sorption heat storage [19]. Continued.

Matrices	Salts	Salt Content wt%	Experimental conditions		E_{vol} [GJ/m^3]	Main findings	Ref.
			T [°C]	p_v [mbar]			
Silica gel; vermiculite	$CaCl_2$	-	-	-	-	Thermal conductivity increase up to 90-112 % compared to pure salt.	[50]
Silica SBA-15	$CaCl_2$	43	50 - 100	0 - 50	-	Hydration happened at a 2,5-4 times lower vapor pressure than for the pure salt	[58]
Zeolite 13X; silica gel	$MgSO_4$	15	25 - 150	21.5	0.6	Temperature lift of 30 °C achieved with Zeolite 13X matrix in open system; no material degradation after three cycles	[59]
Silica Gel; Aluminosilicate	$MgCl_2$; $CaCl_2$	30	-	-	0.6	Composites could be used only if good heat and mass transport were achieved within the material. Max discharge temperature of 40 °C for composites.	[60]
Attapulgite	$CaCl_2$	30	40 - 400	-	1.08 (40 °C) 0.41 (60 °C)**	Low energy density of the composite measured at a discharge temperature of 60 °C.	[61]
Attapulgite	$MgSO_4$; $MgCl_2$	33	30 - 130	36	880 [kJ/kg]***	Salt solution formation due to high deliquescence of $MgCl_2$.	[62]
FeKIL2	$CaCl_2$	7	40 - 150	11.8 - 55.3	560 [kJ/kg]***	Stability assessed after 20 cycles: 3.6 % decrease of water uptake	[63]
Expanded natural graphite; Activated carbon foam	KCl; $CaCl_2$	31 - 90	25 - 200	10 - 20	1451 – 1310 [kJ/kg]***	Thermal conductivity tripled for sample impregnated in expanded natural graphite. Water uptake increased to 160% and 195 % after dehydrations at 100 °C and 200 °C, respectively, compared to untreated $CaCl_2$.	[64]

* calculated for the composite MgCl2·6H2O/Zeolite (1:1,17) assuming material densities of 1569 and 900 kg/m3 respectively.

** Calculated by assuming densities of attapulgite and calcium chloride of 854 and 2150 kg/m3 respectively. *** Composite density not available.

**** Estimated from the bulk densities of the materials given by the authors.

2.1.4 Conclusions on materials review

In the first part of this work, the main results of a review of the sorption materials categories is performed. Special focus is on promising materials for long-term low-temperature sorption heat storage applications based on solid/gas reactions.

Promising materials of the chemical reaction category are salt hydrates, which possess high theoretical energy densities. However, they present several issues for their implementation in pure form such as overhydration and deliquescence at low temperatures (e.g. $MgCl_2$), decomposition at high temperatures, slow kinetics leading to a low temperature lift (e.g. $MgSO_4$), corrosiveness and toxicity (e.g. Na_2S), low mass transport due to the material macrostructure and, if used in closed systems, low heat transport because of a typically low thermal conductivity.

Adsorption materials have the main advantage of a more hydrothermally stable behavior. However, since the main sorption phenomenon is adsorption, lower energy content is intrinsic in that materials category. Moreover, they have typically higher costs per mass compared to salt hydrates, which further decreases their attractiveness if coupled with the fact that they have lower energy densities. Costs reduction could be achieved by optimizing manufacturing processes and by economy of scale. Zeolite 13X is considered as one of the most promising materials amongst the zeolites. Experiments achieved temperature lifts of 35 - 45 °C in lab-scale reactors in an open system configuration and micro-scale experiments at system operating conditions. However, the main drawback is a too high desorption temperature, which is difficult to achieve by heat sources such as solar thermal collectors at a reasonable efficiency.

Silico-/Aluminophosphates and metal organic frameworks presented also a promising performance in terms of water uptake relative to the amount of sorbent. Moreover, they require lower desorption temperatures compared to zeolites. APO-Tric and MIL-101 resulted to have the most promising performances amongst these materials categories, with measured energy densities, at adsorption temperatures of 30 - 40 °C, of 0.86 and 1.6 GJ/m^3, at water vapor pressures of 12 and 55 mbar, respectively. However, DHW production would not be possible at the previously mentioned heat release temperatures. Research on this kind of materials for thermal storage is still at material-scale stages, and a proper experimentation at prototype-scale is required. From the economic perspective, the utilization of the abovementioned materials for seasonal heat storage would drastically increase the system costs.

Composite materials are being researched with the aim of reducing instabilities at material levels of salt hydrates. The host matrices can be made of a porous material that could be also used as active adsorption material if a sufficiently high desorption temperature is achieved. However, small pore sizes necessary for the matrix to be involved in the sorption process lead to low salt filling in the matrix. However, also inactive materials such as expanded graphite, sand, silica gel and vermiculite have been tested for solely structural support.

Several studies have been reported but research on promising working pairs is still ongoing. General issues are a reduced mass transport within the matrix pores and salt deliquescence or overhydration with possible leaking of the active material. Finally, the experimental conditions in the investigated studies are heterogeneous and some of them are far from typical conditions of low-temperature heat storage.

2.2 Sorption heat storage systems

In designing a low-temperature long-term sorption heat storage, materials investigation is only one of the challenging fields to be tackled. The main criteria for the suitability of a material for sorption heat storage purposes (Table 2.1) have to be satisfied also at system-scale. The focus of this section is on the current state of the art of sorption systems for long-term low-temperature heat storage purposes using solid/gas reactions with water as sorbate. The main system layouts, reactor arrangements, system parameters, and performance of the existing prototypes are presented and discussed in the next paragraphs.

2.2.1 System design

Sorption systems can be divided into solid open and closed systems, and liquid systems. A conceptual scheme of the system concepts is shown in Table 2.5, together with their main advantages and drawbacks [65]. A solid open system exchanges mass and energy with the environment, and it operates typically at ambient pressure. The sorbate is transported together with other species, e.g. water vapor into the airflow. The main disadvantages of these systems are that a fan is needed to drive the moist flow through the reactor, a humidifier can be required to reach the desired sorbate vapor pressure, and the temperature step over the reactor is limited by the thermal mass of the flow, which requires a heat recovery unit to obtain temperatures useful for space heating and DHW production. Moreover, due to the fact that mass is also exchanged with the environment, hazardous materials and components cannot be employed. The main advantage is that the system is generally simple, not pressurized, it has a good and controllable heat transfer, and requires less components compared to a closed one. During desorption, valve V1 (Table 2.5 left) directs the flow through the heat exchanger HX1 to be heated from a high-T source, and valve V2 bypasses HX2. During sorption, valve V1 bypasses HX1 and valve V2 directs the heated flow after sorption into the heat exchanger HX2 to transfer heat to the appliances and then to the heat recovery unit HR.
Solid closed systems exchange only energy with the environment, and they are normally evacuated in order to have a satisfactory sorbate transport between the reactor and the sorbate reservoir. During desorption HX3 (Table 2.5 middle), is used to separate sorbent and sorbate with a high-T heat source. Sorbate is then condensed in the sorbate tank in which HX4 is used to remove the condensation heat. During sorption, a low-T source evaporates the sorbate through HX4, which is transported by pressure difference back into the sorbate tank. The

heat of reaction is removed through HX3. The main system advantage is that a fan is usually not needed since the sorbate is driven by the vapor pressure difference between the system components, a faster transport mechanism compared to diffusion in open systems [66]. On the other hand, main disadvantages are that, often, the system needs to be periodically evacuated due to the formation of incondensable gases that block the sorbate flow to the condenser. Moreover, the presence of the sorbate storage, condenser and evaporator decrease the overall system energy density. Finally, liquid sorption systems, which are also closed systems, have a working principle similar to the closed solid sorption systems. During the desorption mode, heat is provided in the absorber/desorber unit though HX5 (Table 2.5 right), and the sorbate is evaporated from the weak solution, which then becomes a strong solution, and is stored separately. During sorption, HX6 provides the required evaporation heat to transport the sorbate vapor into the absorber/desorber unit, in which the strong solution is flowing. This generates a weak solution and reaction heat, which is extracted through HX5. The main advantages and drawbacks of this type of systems are similar to the solid closed systems, with the additional advantage that the materials involved, being in liquid form, can easily be transported and stored.
Abedin et al. [67] performed an energy and exergy analysis on open and closed systems. The main findings were that the investigated open system had higher overall efficiencies compared to the closed ones. However, system basic parameters like sorbate flows, discharge temperatures and pressures had major influence on the analysis. Therefore, a universal conclusion on the better performance of an open or closed sorption system could not be drawn.

2.2.2 Reactors design and related issues

Reactor layout

Reactors for sorption heat storage systems can be divided into two main categories from the active material location perspective: integrated and separate. Integrated reactors contain the total amount of the system active material. Therefore, the material does not have to be moved once placed inside it. The main disadvantage is that a large reactor able to handle the de/sorption conditions has to be built.
Separate reactors require the material to be injected and extracted from it; therefore, a material transport system has to be present resulting in a more complex design. However, the material storage can be made of cheaper materials since it does not have to withstand the reaction operating conditions, and a smaller reactor has to be designed compared to the integrated one, which results also in a smaller thermal mass [68].
Modular reactors can be considered a sub-category of the integrated reactors, since the active material is not transported, while they have the additional advantage that it is not necessary to flush the entire amount of material by the sorbate flow during system operation, causing a large pressure drop.

Table 2.5: Basic schematic diagrams of solid open (left) and closed (middle) systems, and liquid systems (right) with their main advantages and drawbacks [65].

	Open System	Closed System	Liquid system
	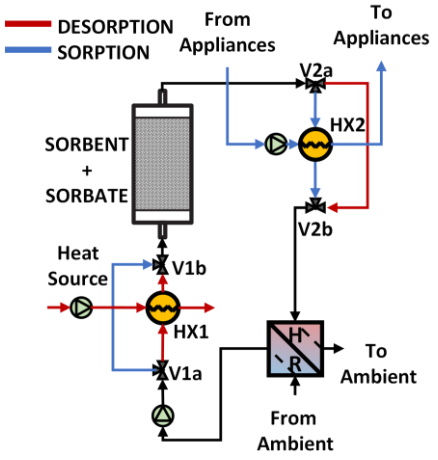	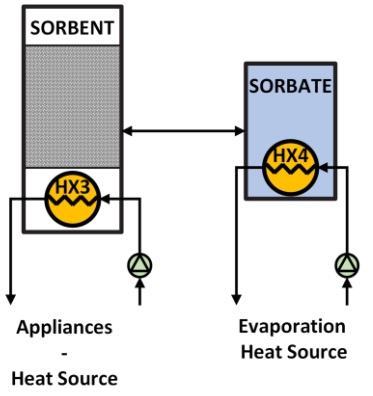	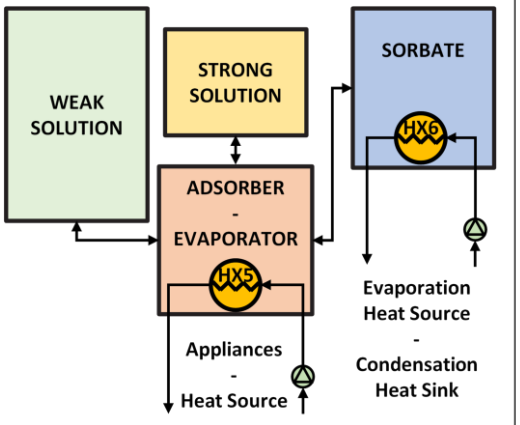
Advantages	• Atmospheric pressure • Simple system • Less components than for a closed system • Heat transfer increased by forced circulation	• Higher discharging temperature than for an open system at similar vapor pressure • No mass exchange with environment • Can be used as an adsorption heat pump for cooling and heating	• No mass exchange with environment • Can be used as an adsorption heat pump for cooling and heating • Material easily stored and transported
Drawbacks	• Fan and humidifier often needed to drive the sorbate flow and provide partial humidification • Sorbate safety requirements • High sorbate flow leads to significant pressure drop • Mass transfer limiting step • Auxiliary energy required for fan operation	• Complex system • Condenser/evaporator required • Heat transfer limiting step • Sorbate needs to be stored • Periodical evacuation required • Sorbate evaporation energy to be fully provided • Large heat transfer area required in the reactor	• Condenser/evaporator required • Absorber/desorber required • Sorbate needs to be stored • Periodical evacuation to avoid non-condensable gases • Sorbate evaporation energy to be fully provided

The material is stored into several smaller reactors with smaller thermal mass that have a volume optimized for the system purpose. Modular reactors have the advantage that an extension/reduction of the system-scale needs low technical effort and can be done using standard procedures, achieving competitive prices compared to other solutions.
A disadvantage of modular reactors is that each module might need additional volume for its own components leading to higher system costs.
De Jong et al. [66] suggested a possible operational strategy for modular reactors. Instead of on-demand delivery, which would require a reactor design for high peak powers, it is an option to discharge, e.g. daily, one module to heat up a conventional sensible storage system, and then provide the thermal power required with a mature and well-known technology. Some of the operational considerations were the following: the water storage has to store the sorption heat of at least an entire module; conventional storage has to afford the daily demand fluctuations; when the conventional storage needs to be charged, an entire module is discharged.
Another alternative considered was an open system with separate reactor and a periodical refilling of dried material and removal of hydrated material, which will be dried elsewhere e.g. where waste heat is available [22]. However, transportation costs have to be taken into account. In 2006, a preliminary investigation [69] for waste heat transportation modes in the industrial area of Nyköping (Sweden) showed that transportation of dried zeolites by train was the most cost effective solution.
Concerning the reactor charging strategy, Mette et al. [70] proposed a method to reduce the charging temperature of an open system by pre-drying the air at the inlet of the sorption reactor. In the system investigated based on zeolite 13X (CWS-NT), normally a dehydration temperature of 180 °C was applied. The authors proposed an additional adsorption unit based on the same sorption material to reduce the water content of the supply air during the desorption phase, before the air-to-air heat exchanger. With a reduced water content in the supply air, a desorption temperature of 130 °C was able to remove more water from the sorption reactor compared to the supply air at 180 °C without pre-drying. The additional adsorption unit was also regenerated at 130 °C. For the pre-drying process, additional sorption material and energy are required. The authors assumed that solar energy during summer was used for the desorption process. Therefore, the solar thermal collectors have to be sized to provide both desorption energy for the main sorption reactor and the additional adsorption unit.

Reactor design

The most common reactor configurations are packed bed for solid reactors and separate reactors for liquid reactors. However, different reactor designs were investigated for sorption heat storage systems in order to tackle main system issues such as control of the system heat capacity, heat losses reduction, and heat and mass transfer improvement [21]. Zondag et al. [71] investigated three reactor layouts: agitated reactor, fluidized bed reactor and gravity-

assisted bulk flow reactor. The authors' conclusion was that an agitated reactor, and in particular a screw reactor, was the best option because active material stirring greatly improved the system performances in their preliminary experiments. However, a main drawback of this option was that mechanical stirring could irreversibly damage the active material and might reduce reliability and increase maintenance costs for the system. The use of layouts with extended surfaces increase heat transfer areas and guarantee a better heat transport from and to the active material, which has a generally low thermal conductivity. Finned tubes [66], plate heat exchangers [40], plate-fin heat exchangers and coated spiro-tubes [72] were possible design options. Extended surfaces are suitable if the volume change between de/sorption cycles is not significant. Large cross-flow areas with a minimum bed length [68] or porous matrices could be used to achieve a low pressure drop for the air flow. For example, Mette et al. [68] developed a reactor that could be operated both in fixed bed and quasi-continuous mass flow configurations. For the reactor concept, three considerations were decisive: large cross flow section area for the airflow and minimal material width in flow direction for pressure loss minimization; material transport to be realized in a reliable and technical inexpensive way with low material losses; a compact construction with short distance between heat source and heat removal in order to minimize heat losses. In the quasi-continuous flow configuration, the material moved from the top to the bottom driven by gravity. Air was fed from one lateral side and exited from the opposite side, in a crossflow configuration. The main advantages of this design were a constant power output and a stationary reaction zone. The main challenge was to maintain a uniform material flow through the reactor. Moreover, well-defined hard spherical particles might be necessary for this reactor concept. On the other hand, the fixed bed reactor had the advantage of a stationary material. However, reaction front, temperature, and grade of conversion were moving. After the sorption reaction was completed, the material inside the reactor had to be replaced. No constant thermal power could be provided and power reduction at start-up and end of conversion took place.

Reactor heat and mass transfer

In closed systems, heat transfer is often the limiting step while in open systems the mass transfer is the main issue. This is often the combination of unfavorable material and system characteristics. Material coagulation can happen due to contact with liquid water, local deliquescence and swelling. Material pulverization can occur due to the periodical material expansion/shrinking [66]. Beside the already mentioned instabilities, the choice of the materials particle size within the system is often a compromise to have a sufficient amount of active material with good kinetics, and sufficient effective bed porosity and permeability that allow good sorbate transport and acceptable pressure drop. To this regard, N'Tsoukpoe et al. [65] reviewed different studies to investigate how heat and mass transfer were influenced by the particle size distribution of the sorbents in open and closed system configurations. They found that adsorption kinetics were influenced by particle size until the

"grain size insensitive regime" was achieved, below certain particle dimensions. In other words, the particle size has to be small enough to achieve this regime, but large enough to avoid a large pressure drop. The ratio between the heat transfer surface area and the amount of adsorbent was detected as an important parameter for system optimization in a packed bed reactor. As an example, a ratio in the range of 1-5 m^2/kg, characterized the grain size insensitive regime for silica gel, activated carbon and SAPO-34 in closed system experiments. Typically, the reviewed studies evidenced the use of pellets in the range of 0.2-0.6 mm for closed systems. The authors stated that, in principle, it is not necessary to select a precise grain size as long as the insensitive regime is reached. On the other hand, for every specific application there is an optimal combination of parameters that are also dependent on the particle size (e.g. effective thermal conductivity, permeability, etc.) that have to be optimized.

For open systems, powders and pellets were considered. However, by using powders, low power output and a high pressure drop were found in the reported studies. This indicated that higher pressure drop and the use of larger particles could have been necessary. The authors stated that the contact between the heat exchanger and the active material could be another issue if salt hydrates are used because their cyclical expansion and shrinking during system cycles varies the contact area. A permeability of $1\text{-}5\cdot10^{-12}$ m^2, effective thermal conductivity of 1 W/(m·K), and heat transfer coefficients between heat exchangers and adsorbent of 200 $W/(m^2\cdot K)$ were suggested for closed evacuated systems. To conclude, the authors suggested to include the method based on the determination of the grain size insensitive regime in the design optimization of packed bed reactors, and that results based solely on TGA/DSC analyses can be misleading due to the small amount of material involved. Influence of grain size on heat and mass transfer was discussed also by Michel et al. [42]. The authors tried to enhance the mass transfer by adding a gas diffuser in form of a foam up to the mid-height of a fixed bed reactor. This solution increased the system permeability by 1.7 times and provided slightly higher specific power without affecting the energy density. Another option to decrease the pressure drop within the reactor was used in the MonoSorp project [73]. The authors used honeycomb structures (monoliths) made out of a zeolite that could be placed in different configurations so that a modular, simple, and flexible system could be designed.

Components corrosion

Side reactions can produce corrosive or toxic byproducts together with the depletion of the active material. For example, a system based on Na_2S can produce H_2S if the sorbent is in contact with liquid water but also, at lower pace, with water vapor. Then, H_2S can dissolve into liquid water and cause metal corrosion and H_2 formation. With an undesirable gas production, the system condenser can be blocked, reducing the sorption reaction rate. This is why periodical system evacuation is needed. To prevent this, corrosion resistant coatings, H_2S and H_2 getters or the addition of hydroxides can be supportive [66]. To this regard, Solé et al. [74] tested four common metals: copper, aluminum, stainless steel 316 and carbon steel

against five salt hydrates: $CaCl_2$, Na_2S, $MgSO_4$ and $MgCl_2$. Immersion tests were performed at the operating conditions that simulate an open system: immersion temperature of 60 °C and humidity at 99 %. The metal samples were removed after one, four, and twelve weeks. The results are visible in Table 2.6.

Table 2.6: Corrosion tests results from Solé et al. [74]

Salts	Copper	Stainless Steel	Carbon Steel	Aluminum
$CaCl_2$	Recommended with caution	Recommended for long-term service	Recommended with caution	Recommended with caution
Na_2S	Destroyed	Recommended for long-term service	Recommended with caution	Destroyed
$MgCl_2$	Recommended with caution	Recommended for long-term service	Not recommended (>1 year)	Recommended with caution
$MgSO_4$	Not recommended (>1 year)	Recommended for long-term service	Not recommended (>1 month)	Recommended with caution

2.2.3 Existing prototypes performance

In the following section, the main results of a review of existing sorption systems for low-temperature sorption heat storage are presented [19]. The focus is on open and closed systems with water vapor as sorbate and solid adsorbents, salt hydrates or composites as active materials.

In Table 2.7, energy densities, maximum desorption and sorption temperatures of the reviewed studies are shown. It has to be pointed out that all the values used are those reported by the references. Moreover, the energy density is reported based on the volume of the active material, or on the system volume, if this information was present in the references. The energy density based on the system volume, can be based on the reactor volume, or including also the system components. For more information, the reader is invited to consult the references for each prototype. Investigations on both open and closed systems were carried out without a clear preference for one of the two systems. On the material level, especially for open systems, the choice of adsorbents or composites rather than pure salts is evident. This is because large open systems with pure salt hydrates will face the stability problems mentioned in Table 2.2. Therefore, more stable materials with a lower energy density are often preferred for systems development, waiting for new inputs from the materials research. It can be also observed that, often, performance parameters such as the energy density are not uniformly referred to e.g. the system volume or the material volume. This makes the systems comparison difficult.

In Figure 2.2, the energy density of some prototypes is related to their maximum desorption temperature. The graph can give an indication on the system performance but cannot demonstrate the better suitability of one system compared to another, and the presented data have to be interpreted with caution.

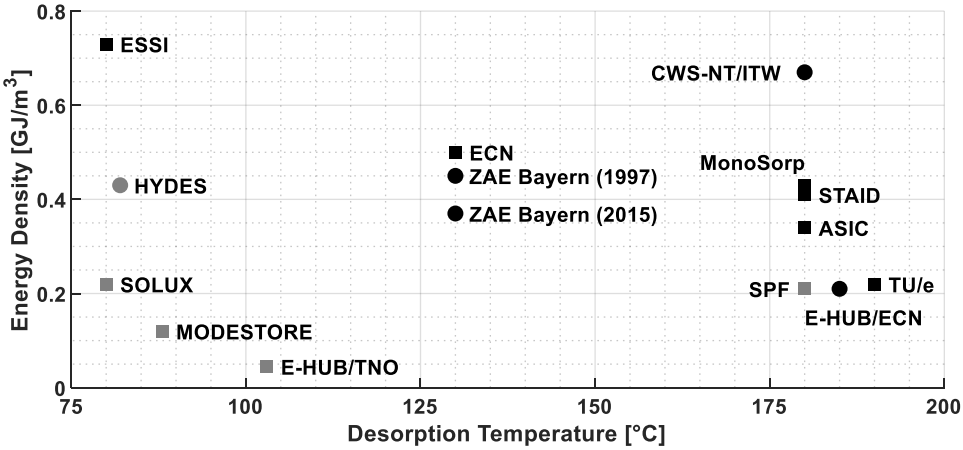

Figure 2.2: Prototypes max desorption temperature vs energy density. Square marker: Energy density based on system/reactor volume. Circle marker: Energy density based on material volume. Black marker: open system. Grey marker: closed system.

The main reason is that energy density is only one of the important system performance indicators. Deliverable and stable thermal power, system thermal losses, material stability within the system, system size and scalability, sorption temperature and water vapor pressure during sorption are other useful indicators that describe the system performance and suitability for a specific application. For example, the HYDES project indicated that silica gel was not suitable as active material since a limited temperature step was achievable at the operating conditions of that system. ZAE Bayern projects are in a relatively advanced stage of development (TRL 5 [75]) compared to the analyzed prototypes. They consist of two large systems with an energy density of 0.37 - 0.45 GJ/m^3 already implemented in real case scenarios. Moreover, at their operating conditions, they reach the highest adsorption temperatures among the investigated systems (Figure 2.3). In order to achieve adsorption temperatures suitable for space heating and domestic hot water production, relatively high desorption temperatures are needed. Most of the systems able to deliver temperatures above 40 °C are based on zeolites, and they need desorption temperatures of 180 °C or higher. The system from ZAE Bayern of 2015 achieved an adsorption temperature of 160 °C. However, during discharge, the system was flushed with humid air at 60 °C from a drying plant, and due to the high water vapor pressure (~ 200 mbar), a very high adsorption temperature was achieved. Therefore, the application was not for space heating and DHW production, but it demonstrated how sorption heat storage could be integrated in an industrial process operating at specific temperature ranges and with the possibility to generate the required water vapor pressure. Finally, it is noticeable that all the systems with a sorption temperature suitable for DHW production, higher than 60 °C, are based on zeolite 13X. Systems based on these materials would be particularly expensive due to the relatively high specific cost of the active material. An exception was the lab prototype from ECN based on $MgCl_2$, which reached a

maximum temperature of 64 °C (temperature step of 14 °C), but as already mentioned, the material instability was a main issue.

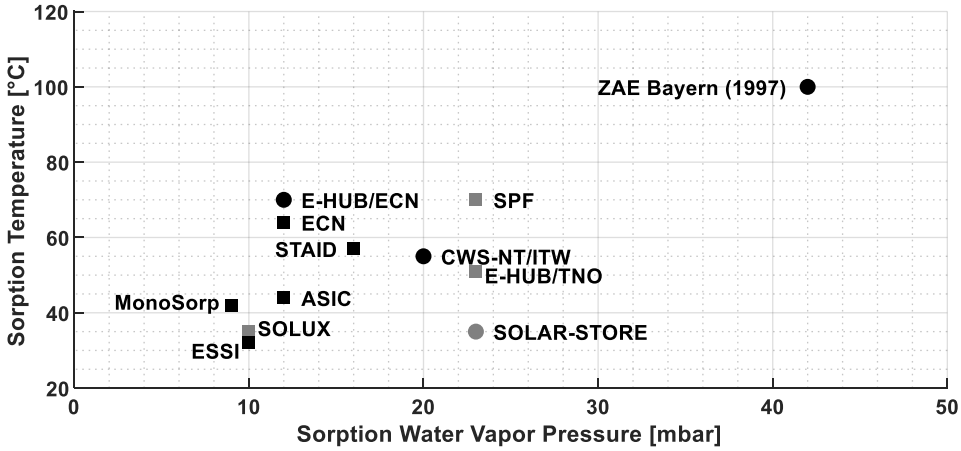

Figure 2.3: Prototypes sorption water vapor pressure vs max sorption temperature. Black marker: open system. Grey marker: closed system.

Table 2.7: Summary of the sorption heat storage systems based on solid/gas reactions with water vapor as sorbate investigated for long-term low-temperature heat storage.

Project Name / Institution	Active Material	Additive Material	Type	E_{vol} [GJ/m^3]	P_d [kW]	P_s [kW]	T_d [°C]	T_s [°C]	$T_{s,max}$ [°C]	p_v [mbar]	C [k€]	Ref.
ZAE Bayern	Zeolite 13X	-	O	0.45^{MH} 0.36^{MC}	135^{H}	130^{H} 50^{C}	130^{H} 80^{C}	25-30	110	42	60^{S}	[73,76,77]
HYDES	Silica Gel	-	C	0.43^{M}	1.7	2.87	82	-	32	-	-	[73,76,78,79]
SWEAT/ECN	Na_2S	Cellulose	C	2.81^{MH} 1.84^{MC}	1.2	0.5-0.7	86-77	25 - 15	-	12 - 17	-	[72,80]
MCES	Na_2S	Graphite	C	-	-	0.15-0.24	95-80	-	-	-	-	[73,81]
SOLAR-STORE	$SrBr_2$	ENG	C	-	-	$\sim 48^{V,C}$ $27\text{-}36^{V,H}$	70^{H} 80^{C}	-	35	23	-	[41]
MonoSorp	Zeolite 4A	-	O	0.58^{M} 0.43^{S}	2-2.5	1.0-1.5	180	20	42	9	$2.5 – 3.5^{M,V}$	[73]
SPF	Zeolite 13X	-	C	0.65^{M} 0.21^{S}	-	0.8-1.8	180	-	70	23	$2 – 3^{M,V}$	[73]
MODESTORE	Silica Gel	-	C	0.18^{M} 0.12^{S}	1-1.5	0.5-1.0	88	-	-	19 - 35	$4.3^{M,V}$	[73,79,82]
SOLAR-STORE (Solux)	$SrBr_2$	ENG	C	0.22^{SH} 0.14^{SC}	2.5-4	-	80-70	-	35^{H} 18^{C}	10^{H} 20^{C}	-	[40]
CWS-NT/ITW	LiCl	Zeolite 13X	O	0.67^{MA}	-	0.4	180	35	55	20	-	[68,83]
Fraunhofer	Zeolites/ $CaCl_2$	Attapulgite Poolkohl	C	-	-	$0.02\text{-}0.05^{W}$	90-200	30	-	42	-	[84]
TNO	Zeolites/ Composite	-	O	-	-	0.60^{W}	-	-	29	-	-	[85]
ECN	$MgCl_2$	-	O	0.50^{S}	-	0.15	130	-	64	12	-	[86,87]
E-HUB/TNO	Zeolite 5A	-	C	0.17^{M} 0.04^{S}	12	0.80	103	20	51	23	-	[87,88]

Table 2.7: Summary of the sorption heat storage systems based on solid/gas reactions with water vapor as sorbate investigated for long-term low-temperature heat storage. Continued.

Project Name / Institution	Active Material	Additive Material	Type	E_{vol} [GJ/m³]	P_d [kW]	P_s [kW]	T_d [°C]	T_s [°C]	$T_{s,max}$ [°C]	p_v [mbar]	C [k€]	Ref.
E-HUB/ECN	Zeolite 13X	-	O	~0.21^{M*}	2	0.40	185	25-60	70	12	-	[87,89]
ASIC	Zeolite 4A/ X	-	O	0.55-0.34^{S}	-	1.50	>230-180	25	84-44	25 - 12	-	[90,91]
ESSI	$SrBr_2$	-	O	0.73^{S}	1.6-0.4	0.80-0.40	~80	25	32	10		[92]
ZAE Bayern	Zeolite 13X	-	O	~0.37^{M*}	255	125	130	60	160	199	89.5^{S} - 324^{S}	[22]
STAID	Zeolite 13X	-	O	~0.41^{M}	-	2.25	180-120	20	57	16	-	[93]
TU/e	Zeolite 13X	-	O	0.22^{S}	5	3.60	190	10-~65	~85	10	-	[94,95]

• **Type**: O=Open system; C=Closed system • **Superscripts**: A = Assumed by the authors; M = Material-based; S = System-based; H = Heating mode; C = Cooling mode; W = per kilogram; V = per m³; *Assuming a material density of 630 kg/m³ [96]

2.3 Discussion and conclusions

2.3.1 Discussion

Sorption heat storage for long-term low-temperature applications has still challenges to face at both micro- and macro-scale levels. Research is still ongoing in order to find unhazardous and low cost sorbent materials with an acceptable stability at system operating conditions and a sufficiently high energy density to make a system commercially feasible. Currently, composite materials are investigated because they have the potential to overcome the disadvantages of pure salt hydrates by enhancing their stability. This is done by mixing or impregnating salt hydrates with highly porous host matrices or powders. However, problems in heat and mass transport still can arise due to the reduction of empty pores, possible deliquescence and leakage of the salt from the composite, and degradation. To this regard, further research is needed to overcome these problems and to understand extensively the kinetics of a composite material, which does not follow a typical behavior of a salt hydrate nor of an adsorbent. Various prototype reactors and systems were developed by the scientific community to study the performances of sorption materials at macro-scale. Open and closed solid sorption systems have been analyzed and compared. Among the reviewed prototypes, mostly systems based on zeolites were able to achieve temperatures suitable for space heating or DHW production. For these systems, relatively high desorption temperatures were required, unachievable, for example, by conventional solar thermal collectors.

To make future research comparable, the development of uniform key performance indicators for compact heat storage to be used by the entire scientific community would be a consistent step towards understanding the optimal choices and performances from the material and system points of view. For example, a consistent way to define energy density is advisable. Due to the presence of different system layouts and various levels of development, it can be useful to define multiple energy densities related to different investigation scales. At material-scale, beside the crystal energy density, often used for salt hydrates, experimental energy density should be always measured through TGA/DSC experiments on material samples in which the macro structure and operating conditions are taken into account (sorbate pressure, temperature cycles, etc.). This first indicator can give information about the material suitability and stability at chosen operating conditions. In this case, the energy density refers to the material weight, or if measurable, to the volume occupied by the sample. At reactor-scale, the effective energy density is influenced by additional phenomena related to heat loss, uniformity of reaction and power distribution over time. Therefore, a second indicator can be useful to define the energy density taking into account the reactor domain. This energy density value is often based on the volume of the active material in the reactor but should be based on the overall reactor volume including walls and insulation. At this stage of development, auxiliary systems are simulated by the lab equipment, and do not have to be taken into account. At system-scale, the volume of auxiliary components (e.g. heat

exchangers, fans, humidifiers, etc.) should be included in the energy density calculation together with their eventual energy consumption. The domain boundaries are the system inlets and outlets i.e. from and to other applications and infrastructures. In calculating energy density indicators, temperatures and sorbent vapor pressure at charging and discharging conditions should be always mentioned. By comparing the energy densities at different scales, it is also possible to identify the system components that decrease the system performance most.

It has to be pointed out that a decrease in the energy density by increasing the research scale is inevitable because more system components are taken into account while the energy potentially stored in the active material remains the same.

Future research on sorption heat storage systems at different scales could make use of similar indicators to compare experimental studies in a more homogeneous way.

Finally, only in few studies considerations about the economic feasibility of the systems were made. This is mainly because the research is still at material- and lab-scales; therefore, wide economic investigations would probably lead to misleading results. However, where possible, basic key performance indicators related to e.g. materials cost, system complexity and system ancillary energy consumption can be drawn with the aim to have a first rough estimation of the system profitability. When working prototypes almost at commercial-scale are developed, additional economic considerations related to system operation, such as lifetime and operation and maintenance costs, could be included with the aim to define and evaluate a business case. By considering economic aspects at the earliest stages of the research, the scientific community can focus its efforts on research paths considering technical and economic feasibilities.

2.3.2 Conclusions

To conclude, further research on long-term low-temperature sorption heat storage should take into account the following considerations:

- Research at material level is still needed to find a suitable active material with sufficient energy density, hydrothermal stability and cyclability at system operating conditions. Composite materials are promising but further research on host/active material working pairs is still necessary.
- Modular reactor layouts, especially in open systems, have to be preferred to limit the pressure drop that in turn increases the auxiliary systems consumption. Separate reactors with efficient material transport systems can further increase the system performance by decreasing the overall reactor thermal mass.
- To make future research on sorption heat storage comparable, common key performance indicators should be adopted by the research community. For example, energy density at different research stages should be calculated defining a common

reference temperature. Moreover, together with the energy density, the appropriate volume should be specified, which depends on the research scale (material, reactor, system).

- Economic considerations should be taken into account at the earliest stages of the research. Materials cost can already provide indications on the profitability of a future system in an intended application. When increasing the scale, all the components and auxiliary systems should be taken into account for the cost estimation.

In order to address this last consideration, Chapter 3 of this dissertation compares different ideal sorption thermal energy storage systems, and it estimates their energy density and storage capacity costs for a common reference scenario.

CHAPTER 3

A SIMPLE COMPARISON OF IDEAL STES SYSTEMS

SEASONAL STORAGE FOR SPACE HEATING

Based on:
Scapino L. Zondag H. A., Van Bael J., Diriken J., Rindt C. C. M.
Energy density and storage capacity cost comparison of conceptual solid and liquid sorption seasonal heat storage systems for low-temperature space heating
Renew Sustain Energy Rev, 2017;76:1314-31
doi:10.1016/j.rser.2017.03.101

In this chapter, a performance comparison in terms of energy density and storage capacity costs of different sorption system concepts used for seasonal heat storage is performed. For this purpose, a common reference scenario and different active materials are considered. This analysis focuses mainly on open solid sorption systems, which are compared with closed and liquid sorption systems. In section 3.2, the investigated reference scenario, sorption systems configurations, and active materials are introduced. In sections 3.3, 3.4, and 3.5 the performance estimation of open, closed, and liquid sorption systems is performed, respectively. Finally, in section 3.6 the sorption systems are compared and in section 3.7 the main conclusions are drawn.

3.1 Introduction

The objective of this chapter is to provide a performance estimation of ideal sorption thermal energy storage (STES) systems in terms of energy densities and storage capacity costs in a common reference scenario, assuming different active materials. The aim is to provide initial considerations about their techno-economic feasibility and competitiveness in the market. Special focus is on open systems based on solid/gas reactions with water as sorbate, which are then compared with closed systems and liquid absorption systems. First, an ideal reference scenario is considered, with the aim to compare the systems at the same operating conditions. Then, for selected materials, the energy density is calculated according to the equilibrium curves (for salt hydrates) or adsorption isotherms/iso-concentration (for adsorbents). Afterwards, assumptions and estimations are made about the size of the systems and the auxiliary components needed, and cost estimations for the active materials and reactor materials are made. Finally, a comparison with closed systems and liquid sorption systems is made in terms of energy densities and active material costs by considering the acceptable storage capacity costs of three user categories: industry, building and the so-called energy enthusiast. This analysis mainly focuses on the storage capacity costs in terms of active materials and reactor materials costs, without considering the auxiliary components, and systems dynamics. Additional important aspects to be considered in real systems are thermodynamic efficiencies during the systems operation, cost-sizing factors and relations among overall system costs and the main systems parameters, which are not included in the present work. For a proper investigation on some of the abovementioned aspects, especially techno-economic indicators, a higher maturity level of this technology is required.

3.2 Reference scenario, systems and materials

3.2.1 Reference scenario

A common application considered for the integration of a STES is a family passive-house, which has a space heating and domestic hot water demand, and solar thermal collectors on its roof able to provide the required desorption temperature. The aim of the STES systems considered in this analysis is to store thermal energy during summer and release it in winter to satisfy the space heating demand. This is the main concept of seasonal heat storage. Modern houses can make use of low temperature space heating systems such as floor heating, which can operate with supply temperatures below 40 °C [97]. This relatively low space heating temperature can be provided during the discharge phase of a sorption system operating within the boundary conditions listed in Table 3.1. On the contrary, if traditional heating systems would be present (e.g. heating temperatures of 70 °C) the use of STES systems would become much more challenging. During the system discharge (sorption phase), evaporation heat from a low temperature source has to be provided in order to have

a sufficient water vapor pressure at the system inlet. A borehole system, aquifer, surface water system, ambient air, or solar thermal collectors can cover this function. In order to test the systems at the same operating conditions, a reference scenario is defined. This implies that for all the systems analyzed, the same maximum temperature used to desorb the active materials (T_d) and the same energy demand required from the consumer (E_{SH}) are assumed. Ferchaud et al. [29,30] and Zondag et al. [86] assumed a maximum temperature of 150 °C from the solar thermal collectors in similar analyses. The minimum system discharging temperature mainly depends on the applications. Low temperature space heating can make use of a temperature of approximately 40 °C. However, for DHW production, temperatures of 60 °C are normally required for prevention against legionella. In this scenario, only energy for space heating is considered, and a yearly demand (E_{SH}) of 10 GJ is assumed [66]. The system has to store the entire amount of energy required (seasonal storage). Therefore, the thermal storage will perform only one sorption/desorption cycle per year. It is also assumed that the building is located in Amsterdam, the Netherlands, with 212 heating days per year (October - April), and that the low temperature heating system consumes a constant power during those days. The ambient temperature (T_{amb}) entering the system, i.e. after an eventual humidification system, is set at 10 °C. The main data of the reference scenario is presented in Table 3.1. Additional parameters assumed for this analysis, where not mentioned in the text, can be found in Appendix B.

Table 3.1: Reference scenario: passive house in Amsterdam (the Netherlands) with low temperature space heating and solar thermal collectors.

Parameter	Value
T_d [°C]	150
T_{SH} [°C]	35/28
E_{SH} [GJ/year]	10
Heating days	212
T_{amb} [°C]	10
$p_{v,sat}(T_{amb})$ [mbar]	12.4

3.2.2 Sorption thermal energy storage systems

This analysis focuses on three main types of sorption systems: open and closed solid sorption systems, and a liquid sorption system (Table 2.5). The main working principle of these systems are explained in Chapter 2 (2.2.1). Given the low maturity level of STES, several assumptions are made throughout the analysis. For example, heat losses are not included in this analysis, since they are mostly dependent on the components design. Moreover, the heat absorbed by the reactor thermal mass is neglected. Table 3.2 summarizes the main general elements included and excluded in this analysis. Assumptions specific to a single system

configuration, are presented elsewhere in the chapter (i.e. section 3.3 for open systems, section 3.4 for closed systems, and section 3.5 for liquid systems).

Table 3.2: Important general elements included and excluded in this analysis.

Included	Excluded
- Active materials volume and cost - Reactors material volume and cost	- Heat losses through the reactor walls - Auxiliary components - Thermodynamic efficiencies - Heat absorbed by reactor thermal mass

3.2.3 Active materials

The materials investigated in this assessment for solid sorption systems are three pure salt hydrates ($MgCl_2$, Na_2S and $SrBr_2$), one pure adsorbent (zeolite 13X), and one ideal composite. For the liquid sorption system, NaOH has been selected based on literature (see section 3.5.1). The boundary conditions of the reference scenario establish the achievable level of de/hydration for every material. Equilibrium curves in Appendix A were estimated with NBS tables [98] to have a first estimation of the materials theoretical energy density. Additional assumptions at material level are shown in Table B.1 in Appendix B. For every reaction step, the reaction enthalpy and entropy are calculated with the enthalpies and entropies of formation at standard conditions [98]. Then, equilibrium temperatures can be calculated according to equation 3.1:

$$\Delta G = \Delta H^0 - T\Delta S^0 + R_g T lnZ \qquad 3.1$$

with

$$Z = \frac{\prod_i p_{product,i}}{\prod_i p_{reactant,i}} \qquad 3.2$$

Here, Z is the ratio of the partial vapor pressures of products and reactants in the gas phase. The equilibrium curves can be calculated over a selected range of water vapor pressures, and in turn, a range of Z values. For every material, the equilibrium curves of relevant reaction steps are calculated (Appendix A) together with the energy densities referred to the material in the most hydrated form. As an example, the values for $MgCl_2$ are reported in Table 3.3. Data for the other materials are present in Appendix A. From Table 3.3, a theoretical energy density of 2.49 GJ/m^3 can be seen for the material. However, in order to allow a proper mass transfer within the material, and to account for the material porosity, an effective bed porosity ε_b of 0.5 is assumed. The effective bed porosity halves the theoretical energy density that can be extracted from the material, supposed in a sorption reactor.

Table 3.3: $MgCl_2$ properties. Reaction enthalpy data from [98]**. Investigated reaction steps: $MgCl_2 \cdot H_2O \leftrightarrow MgCl_2 \cdot 2H_2O$, $MgCl_2 \cdot 2H_2O \leftrightarrow MgCl_2 \cdot 4H_2O$, $MgCl_2 \cdot 4H_2O \leftrightarrow MgCl_2 \cdot 6H_2O$**

$MgCl_2$			
$\rho_{MgCl_2 \cdot 6H2O}$ [kg/m^3]		1569	
$M_{mol,MgCl_2 \cdot 6H2O}$ [g/mol]		203.31	
Moles of water in solid phase	1↔2	2↔4	4↔6
mol_w	1	2	2
ΔH_{reac} [kJ/mol_w]	71.27	67.82	58.2
$mol_w/kg_{MgCl2 \cdot 6H2O}$	4.92	9.84	9.84
T_{eq} [°C]	117.1	96.88	60.79
E_{vol} [GJ/m$^3_{MgCl2 \cdot 6H2O}$]	0.55	1.05	0.90
$E_{vol,tot}$ [GJ/m$^3_{MgCl2 \cdot 6H2O}$]		2.49	
$E_{vol,bed}$ [GJ/m$^3_{MgCl2 \cdot 6H2O}$]		1.25	
$C_{wt,sm}$ [€/t] [34]		154	

In order to estimate the energy density of zeolite 13X, adsorption iso-concentration lines (Figure A.1) are calculated with the Langmuir-Freundlich isotherm (equations 3.3 - 3.5).

$$q_{eq} = \frac{q_{max} b_{LF} p_v^{n_{LF}}}{1 + b_{LF} p_v^{n_{LF}}} \tag{3.3}$$

$$b_{LF} = b_{0,LF} e^{\left(\frac{\Delta E_{LF}}{R_g T}\right)} \tag{3.4}$$

$$n_{LF} = n_{1,LF} + \frac{n_{2,LF}}{T} \tag{3.5}$$

Here, q_{eq} represents the moles of water per kilogram of material adsorbed at equilibrium conditions, q_{max} the maximum number of moles adsorbed per kilogram of material, p_v the water vapor pressure, R_g the ideal gas constant, and T the temperature. The parameters used for the Langmuir-Freundlich isotherm are given in Table 3.4.

Table 3.4 Langmuir-Freundlich isotherm parameters for zeolite 13X [99]

Parameter	Value
$n_{1,LF}$ [-]	-0.3615
$n_{2,LF}$ [K]	274.23
q_{max} [mol/kg]	18
$b_{0,LF}$ [1/Pa^n]	$308 \cdot 10^{-6}$
ΔE_{LF} [J/mol]	18016

Assuming a desorption temperature of 150 °C, the maximum theoretical energy density achievable is 0.72 GJ/m^3. A bed porosity (ε_b) of 0.5 decreases the available energy density to 0.36 GJ/m^3. In order to estimate the maximum temperature lift (ΔT_{lift}) achievable from the reaction steps, two different methods are applied. For closed systems, the equilibrium temperature is considered as the sorption temperature achievable within the reactor. If multiple reaction steps are present, the lowest equilibrium temperature is considered. For open systems, the lowest temperature increase between the previous approach and the "c_p approximation" approach, showed in equation 3.6, is used. The latter assumes that all the water in the air reacts with the material, and that the energy released during the reaction is used to heat up the air mass flow. The temperature lift then becomes:

$$\Delta T_{lift} = \frac{\rho_v \Delta H_{reac}}{M_{mol,w} \rho_a c_{p,a}} \qquad 3.6$$

with

$$\rho_v = \frac{p_v M_{mol,w}}{R_g T} \qquad 3.7$$

Here ρ_v is the water vapor density, ΔH_{reac} the average reaction enthalpy per mole of water, $c_{p,a}$ the air specific heat capacity, ρ_a the air density, p_v the water vapor pressure, $M_{mol,w}$ the molar mass of water, R_g the ideal gas constant, and T the temperature. This assumption has been made based on two counterbalancing concepts. The first is that, in system based on multi-step reactions (e.g. $MgCl_2$), the reactor outlet temperature is typically higher than the lowest reaction equilibrium temperature because there are also other reaction steps contributing in the sorption process. The second is that the thermal losses in the components, that will decrease the reactor outlet temperature, have not been considered. Therefore, for a rough system approximation, the assumption used for the reactor outlet temperature represents a compromise between these two opposing effects. For the closed system based on zeolite, it is assumed that the sorption temperature bed is kept at a temperature above the space heating required temperature, allowing 11 moles of water per kilogram of material to be released from the system discharge (Figure A.1). Finally, the performance of an ideal composite material is estimated, together with the related costs. For this analysis, the following assumptions are made:

- The composite is assumed to be made out of an inert hosting matrix and $CaCl_2$.
- The salt in its hexahydrate form occupies 50 % of the material volume, and the other half of the volume is occupied by the hosting matrix.
- The overall composite porosity is assumed to be 50 %, as for the other materials investigated.

- The hosting matrix cost ($C_{wt,mx}$) is assumed to be 600 €/t and its density (ρ_{mx}) 180 kg/m^3 [100].

Calcium chloride has been already investigated for STES purposes [101] in its pure form [28], in composites [38,39,54,58,61,63,64,102,103], and in salts mixtures [104]. It is assumed that pure calcium chloride is unstable at the ambient temperature and water vapor pressure of the reference scenario, and deliquescence would occur [105]. It is assumed that the hosting matrix is able to retain efficiently the salt into its pores, therefore avoiding leakages of the active material. The density value of the hosting matrix is for expanded vermiculite, which has an intermediate density among the possible hosting matrices. In addition, the cost is assumed as an average value among various materials that can be used as hosting matrix. However, these values are highly dependent on the chosen material and its processing. The reactions relevant for STES purposes at the reference scenario conditions are displayed in Table 3.5.

Table 3.5: Ideal $CaCl_2$ composite properties. Reaction enthalpy data from [98]**. Investigated reaction steps: $CaCl_2 \leftrightarrow CaCl_2 \cdot H_2O$, $CaCl_2 \cdot H_2O \leftrightarrow CaCl_2 \cdot 2H_2O$, $CaCl_2 \cdot 2H_2O \leftrightarrow CaCl_2 \cdot 4H_2O$**

$CaCl_2$ Composite			
$\rho_{CaCl2 \cdot 6H2O}$ [kg/m^3]		1710	
$M_{mol,CaCl2 \cdot 6H2O}$ [g/mol]		219.08	
Moles of water in solid phase	0↔1	1↔2	2↔4
mol$_w$	1	1	2
ΔH_{reac} [kJ/mol$_w$] [98]	73.93	51.63	61.14
mol$_w$/kg$_{CaCl2 \cdot 6H2O}$	4.56	4.56	9.13
T_{eq} [°C]	106.10	61.86	44.48
E_{vol} [GJ/m$^3_{CaCl2 \cdot 6H2O}$]	0.58	0.40	0.95
ρ_{mx} [kg/m^3]		180	
Volume of composite occupied by the salt [vol%]		50	
ρ_{cmp} [kg/m^3]		1136.5	
$E_{vol,cmp}$ [GJ/m$^3_{cmp(CaCl2 \cdot 6H2O)}$]		0.97	
$E_{vol,bed}$ [GJ/m$^3_{cmp(CaCl2 \cdot 6H2O)}$]		0.49	
$C_{wt,sm}$ [€/t] [34]		116	
$C_{wt,mx}$ [€/t]		600	
$C_{wt,cmp}$ [€/t]		153	

3.3 Open solid sorption systems

In an open system, the mass transfer of the sorbate through the sorbent is the main issue because the pressure drop within the porous material can highly reduce the system efficiency.

Therefore, the use of a reactor in which the air flows through the entire material amount at every system charge/discharge is not recommended. On the contrary, a modular or segmented configuration reduces the system pressure drop and the thermal mass of the material to be heated at every charge/discharge cycle. For a rough estimation of a module size, the following assumptions are made:

- Each segment can store the required space heating energy for one day.
- The energy released from the system is transferred to the space heating system with an air-water heat exchanger that is able to deal with the daily fluctuations of the heat demand.
- Every module releases a constant energy flow through the day at a constant power. This energy is transferred to a low temperature heating system such as floor heating, which is not subjected to high peak energy demands, common for older high-temperature heating components.

The total amount of material can be divided into 212 batches, equal to the total amount of heating days per year (according to 3.2.1) that can be single modules or reactor segments. Considering the number of batches, and in order to minimize the amount of reactor material and maximize the reactor compactness, a segmented reactor has been chosen as layout for the open solid sorption system.

3.3.1 Reactor geometry and size estimation

In order to compare the active materials in a common reactor layout, it is assumed that a cubic reactor is divided into cuboids, and that every cuboid (segment) contains the energy required for one day of operation (Figure 3.1). The result is a cubic reactor with 212 segments having the major length equal to one side of the cubic reactor.

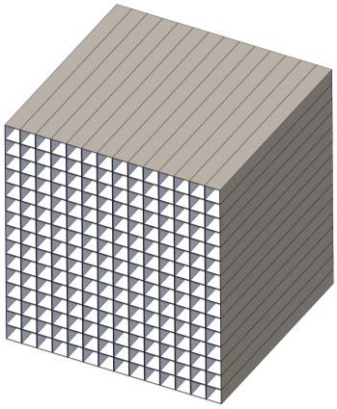

Figure 3.1: Open system segmented reactor layout consisting of a set of cuboids equal to the amount of heating day in the reference scenario.

This might not be the most suitable reactor layout for every STES system, but in order to have a first rough comparison of the resulting pressure loss and the costs involved, this common arrangement is assumed. Further assumptions at reactor level are:

- Each cuboid is contained in a 1 mm stainless steel 316 shell. The choice of stainless steel in this analysis is assumed due to its corrosion resistance to the investigated salt hydrates [74]. The stainless steel density and cost are assumed to be 7740 kg/m^3 and 2.5 €/kg [106], respectively.
- The space heating heat exchanger can exploit the air energy from the reactor up to a temperature of 29 °C. An air-to-air heat recovery unit with a heat recovery efficiency (ε_{HR}) of 90 % [107] is present between the inlet of the reactor and the outlet of the space heating heat exchanger.

The heat transfer medium in an open system is the gas flow (air) that contains the sorbate (water vapor). To estimate the required amount of active material needed, the daily amount of heated air (equation 3.8) has to be estimated depending on the maximum achievable temperature from the STES system and the minimum air temperature achievable in the air-water heat exchanger.

$$\dot{m}_a = \frac{P_{HX,SH}}{c_{p,a}\left(T_{in,a,HX} - T_{out,a,HX}\right)} \qquad 3.8$$

Then, it is assumed that a space heating system working at 35/28 °C (Table 3.1) receives the warm water from a water tank able to store the required daily amount of heat. According to the assumptions, a heat exchanger delivering a constant power ($P_{HX,SH}$) of 546 W to the water tank during the system discharge is estimated. The constant power value is the result of the total yearly energy needed for space heating (10 GJ) divided over the heating days in the year. In Table 2.5 left, a schematic drawing of the assumed layout for an open solid sorption system is shown.

In order to recuperate the air released below 29 °C from the STES, a heat recovery unit is present. Therefore, the ambient air is preheated and a higher outlet temperature from the reactor can be achieved. The preheated air temperature at the reactor inlet can be calculated as in equation 3.9.

$$T_{a,preheated,in} = T_{amb} + \varepsilon_{HR}\left(T_{out,HX} - T_{amb}\right) \qquad 3.9$$

Here, ε_{HR} is the efficiency of the heat recovery unit, $T_{out,HX}$ the air temperature after the heat exchanger in the water tank, assumed to be 29 °C, and T_{amb} the ambient temperature at 10 °C. At those conditions, the preheated temperature is 27.1 °C. The inlet air water vapor pressure is assumed to be 12.4 mbar which is the saturated water vapor pressure at 10 °C.

The STES delivers the design constant power of 546 W above 29 °C to the air-water heat exchanger, then, it delivers low-temperature power used to preheat the ambient air. The packed bed reactor power (P_b) can be computed by considering the temperature difference between its inlet and outlet air, as in equation 3.9.

$$P_b = \dot{m}_a c_{p,a}(T_{reactor,out} - T_{a,preheated,in}) \quad 3.10$$

In an open system, a source of energy consumption is the electrical power needed to drive the air mass flow, which can be estimated with the pressure drop through the reactor (equation 3.11).

$$P_{fan} = \dot{V}_a \Delta p \quad 3.11$$

Here, $\dot{V}_a$ the air volumetric flow and Δp the pressure drop within the reactor bed, estimated with the Ergun equation (equation 3.12).

$$\frac{\Delta p}{L} = \frac{150\mu_a(1-\varepsilon_b)^2}{\varepsilon_b^3 {d_p}^2}|u_a| + \frac{1.75\rho_a(1-\varepsilon_b)}{\varepsilon_b^3 d_p}|u_a|^2 \quad 3.12$$

Here, μ_a is the air viscosity, d_p is the particles diameter, assumed to be 1 mm, ρ_a the air density, and u_a the superficial air velocity in the reactor segment assuming it without active material. The main results are visible in Table 3.6. The annual volume of materials required is in the range of 7.7 - 11.1 m^3 for salt hydrates, 29.8 m^3 for zeolite 13X, and 23 m^3 for the composite material. In order to store the same amount of energy with a temperature difference of ΔT= 50 °C, a water storage of approximately 48 m^3 would be required. The economic indicator considered in this analysis is the storage capacity cost (SCC), shown in equation 3.13, expressed in €/kWh_{cap}. In this analysis, this cost takes into account only the active material and the reactor material costs, and it is defined as:

$$SCC = \frac{C_{reactor} + C_{sm}}{E_{STES,max}} \quad 3.13$$

In real systems, storage capacity costs should include all the investment costs needed to realize the thermal energy storage system. The salt hydrates appear to be the most interesting options in terms of energy densities.

- Sodium sulphide results to be the best option in terms of compactness, by having more than seven times the energy density than a conventional water storage. However, due to hazardousness of the material, it is not possible to use it in an open system configuration.

- Magnesium chloride results to be the best option in terms of active material costs by having it below 1 €/kWh$_{cap}$. However, from previous studies [29,37,108], it is known that the desorption temperature of the reference scenario (150 °C) will lead to material decomposition over the cycles. In order to reduce as much as possible, the decomposition rate of $MgCl_2$, the desorption temperature could be decreased by exploiting only the first two reaction steps (6↔4 and 4↔2), resulting in a higher storage cost and a lower energy density. The relative fan energy costs for discharging the system during the winter season can account for 20 % of the overall reactor and active material costs (Figure 3.2). The relative fan costs appear to be more relevant with economic active materials (i.e. $MgCl_2$, Na_2S and the ideal composite), since they affect more the overall system cost.
- Strontium bromide appears a promising alternative, resulting in a system approximately four times more compact than a water storage. However, due to the high material cost, the total cost of the STES system is more than ten times higher compared to the one based on magnesium chloride.
- The zeolite storage requires a remarkably larger amount of material due to its lower energy density compared to pure salt hydrates. Considering also the high specific cost of the material, this leads to the most expensive options amongst the investigated systems.
- The composite material results in a more compact system compared to the system based on zeolite 13X, with an energy density of 0.43 GJ/m^3. From the economic point of view, the composite option is cheaper than zeolite 13X and $SrBr_2$, having a cost of 1.36 €/kWh$_{cap}$. This could be the most feasible option assuming a sufficient material stability given by the hosting matrix of the composite. Concerning the relative fan energy costs, they account approximately for 23 %

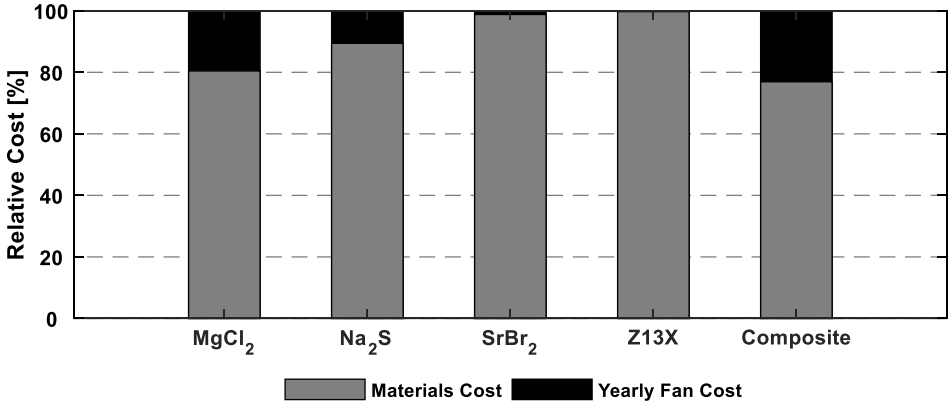

Figure 3.2: Contribution of materials (sorption material + reactor material) cost and yearly fan consumption cost.

Table 3.6: Solid sorption open systems estimation of design parameters for the seven active materials investigated.

	$MgCl_2$	Na_2S	$SrBr_2$	Zeolite 13X	Composite
$\dot{m}_a$ [kg/s]	0.0201	0.0195	0.0253	0.0206	0,0351
$T_{a,max}$ [°C]	56.09	56.86	50.45	55.35	44.48
P_b [W]	584	583	594	585	613
E_b[GJ/year]	10.70	10.68	10.89	10.72	11.23
V_b [m^3]	8.56	7.66	11.11	29.78	23.03
M_b [t]	6.72	6.05	13.25	15.49	10.88
$V_w(\Delta T = 50K)/V_{sm}$	5.6	6.2	4.3	1.6	2.1
L [m]	2.05	1.97	2.23	3.10	2.85
$A_{cross,seg}$ [m^2]	0.0197	0.0183	0.0235	0.0453	0.0382
Δp [bar]	0.17	0.18	0.20	0.07	0.20
P_{fan} [W]	284	289	434	120	583
C_{fan} [€/year]*	250	254	382	105	513
$C_{wt,sm}$ [€/t]	154	348	2400	2500	153**
$SCC_{sm+reactor}$ [€/kWh$_{cap}$]	0.79	1.16	11.90	14.57	1.18
$C_{sm+reactor+1\ year\ fan}$ [€/kWh·year]	0.88	1.25	12.04	14.61	1.36
$E_{vol,reactor}$ [GJ/m^3]	1.17	1.31	0.90	0.34	0.43

* Considering an average electricity price of 0.173 €/kWh for a Dutch household in 2014 [109]

** Related to composite volume

3.3.2 Sensitivity analyses

In order to show the influence of the assumptions made, a sensitivity analysis on selected parameters is carried out. In the open system layout, the varied parameters are the heat recovery efficiency, the particle size diameter of the active material, and the reactor outlet temperature.

Heat recovery efficiency

The heat recovery unit is an essential part of the open system layout, since it significantly improves the overall system performance. The assumed heat recovery efficiency is 90 %. However, real operational values can be far from the nominal one [107]. Thus, the heat recovery efficiency has been varied from 60 % to 90 % and the impact on the energy density and costs are estimated.

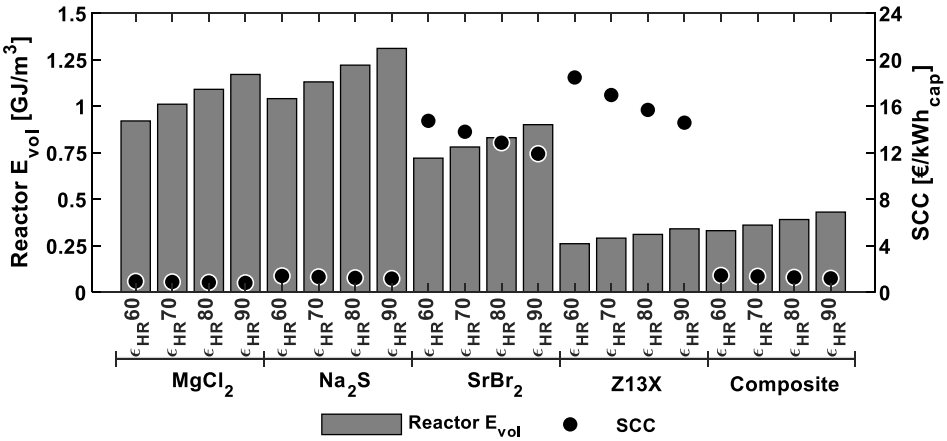

Figure 3.3: Reactor Energy density and storage capacity cost variation by varying the heat recovery efficiency (ε_{HR}) from 60 % to 90 %.

As it is possible to see in Figure 3.3, the heat recovery efficiency has a remarkable effect on the energy density. A higher heat recovery efficiency results in higher achievable outlet reactor temperatures, and higher energy densities. Energy density variations of approximately 20 % are present for pure salt hydrates, based on a heat recovery efficiency of 90 %. Variations of 23 % and 26 % are found for the systems based on zeolite 13X (Z13X) and the ideal composite, respectively. Concerning the storage capacity costs, heat recovery efficiency affects more the cost of the systems based on the more expensive materials. A lower energy density implies larger quantities of material to be employed, therefore a higher materials cost is unavoidable. The importance of the heat recovery efficiency depends on the temperature difference between the two inlet flows (Equation 3.10), i.e. the larger the temperature difference between the two entering flows, the higher the importance of the HR efficiency. In this analysis, a temperature of 29 °C from the space heating heat exchanger and air at 10 ° C from the ambient are assumed to enter the HR unit (section 3.2.1), which implies a temperature difference of 19 °C.

Particle size diameter

The average particle size in the packed bed influences the pressure loss, as it can be seen from equation 3.12. This, in turn, has an influence on the system feasibility and its operational cost. In order to assess properly the impact of varying the particle size diameter on the system, the yearly operational costs due to the fan power are added to the storage capacity costs. Thus, if the system requires a too high amount of fan power to overcome the pressure loss, this will be taken into account in the cost assessment. The particle size has been varied between 0.1 mm and 5 mm, to have a particle size range going from fine powders to relatively large pellets. As it is possible to see from Figure 3.4, by considering one year of system operation cost and the storage cost, particle size diameters of 0.1 mm considerably affect all

the systems, leading to a cost increase from 15 % (zeolite 13X) to 490 % (composite) compared to the systems based on 1 mm particles. Larger particle sizes have a moderate effect on the cost.

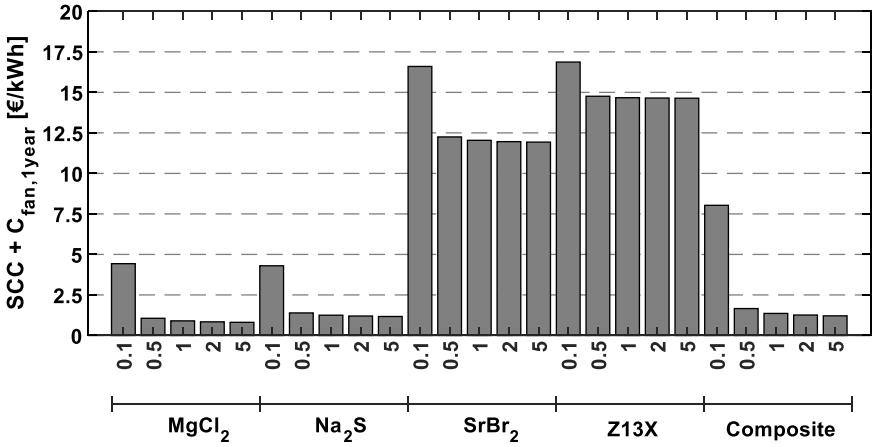

Figure 3.4: Storage capacity cost and one year of fan operational cost by varying the particle size diameter from 0.1 to 5 mm.

Sorption temperature

A strong assumption is that the reactor outlet temperature for open systems corresponds to the lowest value between the lowest equilibrium reaction temperature and the temperature calculated with the "c_p approximation" (equation 3.6).

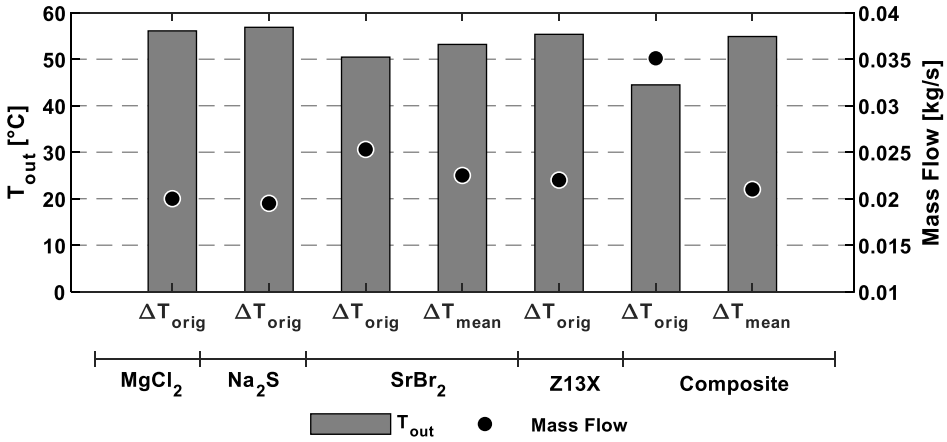

Figure 3.5: Reactor outlet temperatures and mass flows assuming the lowest equilibrium temperature (ΔT_{orig}) or the "cp approximation" approach (ΔT_{mean}) for $SrBr_2$ and the ideal composite material. Data for $MgCl_2$, Na_2S and zeolite 13X already based on the "cp approximation" approach are added for comparison.

Assuming that the thermal losses are minimized in a real system, it is interesting to estimate the systems performances if the reactor would be able to deliver the temperature based on the "cp approximation" approach. The systems in which the outlet temperature was already set as equal to the temperature found with the "c_p approximation" approach ($MgCl_2$, Na_2S, and zeolite 13X), are also reported for comparison (Figure 3.5). The increase of temperature is 5 % ($SrBr_2$) and 23 % (composite), compared to the original outlet temperature. Consequently, the air flows through the reactor have a decrease of -11 % ($SrBr_2$) and -40 % (composite) compared to the original air flows. This is because the power that has to be provided from the reactor to the space heating system remains the same.

In Figure 3.6, the storage costs by varying the outlet temperature are displayed and divided between storage capacity costs and yearly fan operational costs. Overall, a general cost decrease is present due to lower operational costs caused by the reduction of the air flow, and the higher energy densities affecting the storage capacity cost. Finally, the systems energy density (Figure 3.7) increases of 0.9 % ($SrBr_2$) and 4.6 % (composite) because of lower amount of material required since a lower amount of sorbate (water vapor) flows through the reactor and depletes the sorption material.

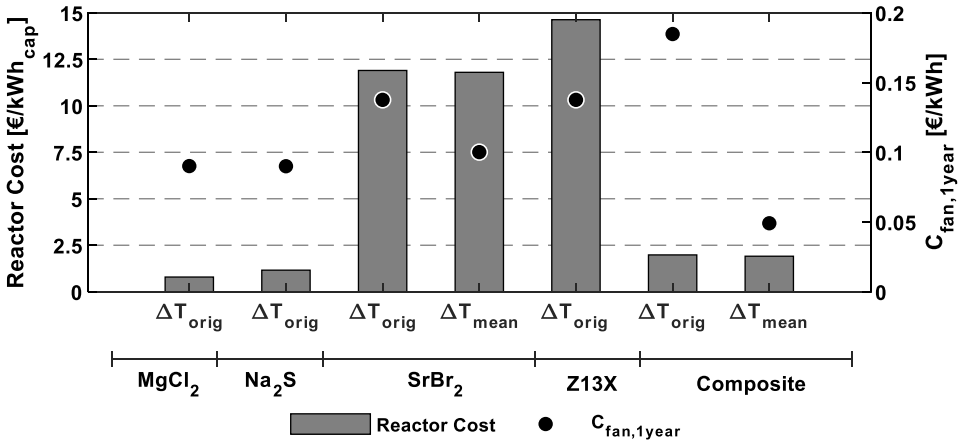

Figure 3.6: Storage costs and operational costs varying the reactor outlet temperature assuming the lowest equilibrium temperature (ΔT_{orig}) or the "cp approximation" approach (ΔT_{mean}) for $SrBr_2$ and the ideal composite material. Data for $MgCl_2$, Na_2S and zeolite 13X already based on the "cp approximation" approach are added for comparison.

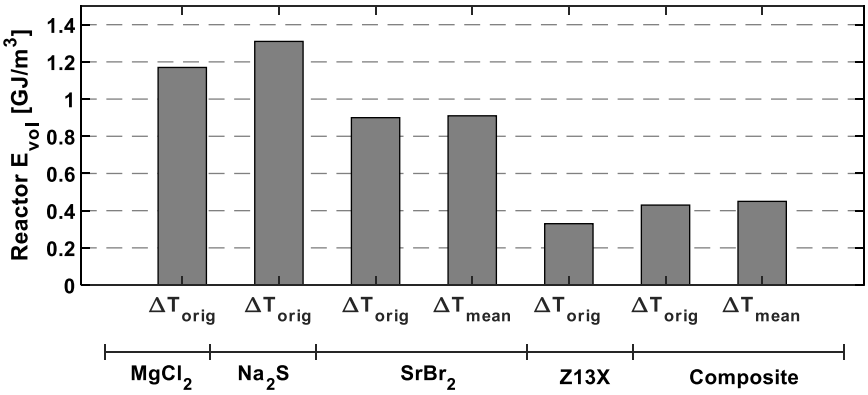

Figure 3.7: Energy density varying the reactor outlet temperature assuming the lowest equilibrium temperature (ΔT_{orig}) in blue and an averaged outlet temperature (ΔT_{mean}) in red for $SrBr_2$ and the ideal composite material. Data for $MgCl_2$, Na_2S and zeolite 13X already based on the "cp approximation" approach are added for comparison.

3.4 Closed solid sorption systems

In the following section, the performance of different closed solid sorption systems based on the previously introduced active materials (3.2.3) are estimated. A closed system requires additional components compared to an open system. During the system discharge, an evaporator is needed to evaporate the sorption water that subsequently reacts with the active material. During the system charge, a condenser is required to condense the sorbate vapor removed from the active material. Differently from an absorption heat pump, the two phenomena do not happen simultaneously; therefore, if properly designed, the condenser and evaporator can be the same component. In this analysis, the heat removed during condensation will be lost and it will not be considered as additional value. Finally, closed systems can require frequent evacuation due to the formation of incondensable gases. This requires additional energy to run the evacuation pumps. This aspect is not considered in this analysis.

The closed system requires a storage volume for the sorbate, which is not released into the environment as for an open system. As a rough system size estimation, the following assumptions are made:

- The volume of the evaporator/condenser heat exchanger is not significant compared to the active material volume and the required sorbate volume. Therefore, it will not be taken into account.
- The sorbent and the sorbate are contained into cylindrical shells with a diameter of 0.3 m and 1.5 m, respectively.

- The active material is divided into modules in which the daily energy demand is stored (Figure 3.8).
- At the sides of each cylindrical there is a cap with a height of 0.05 m.
- The material for the reactor is stainless steel 316, and the container thicknesses are 3 mm and 2 mm for the modules and the sorbate container, respectively.
- The heat transfer area between the water for the space heating system and the active material in every module is not taken into account.
- The energy is efficiently removed from the reactor bed by the heat exchanger. Therefore, all the energy released is transferred to the space heating system.

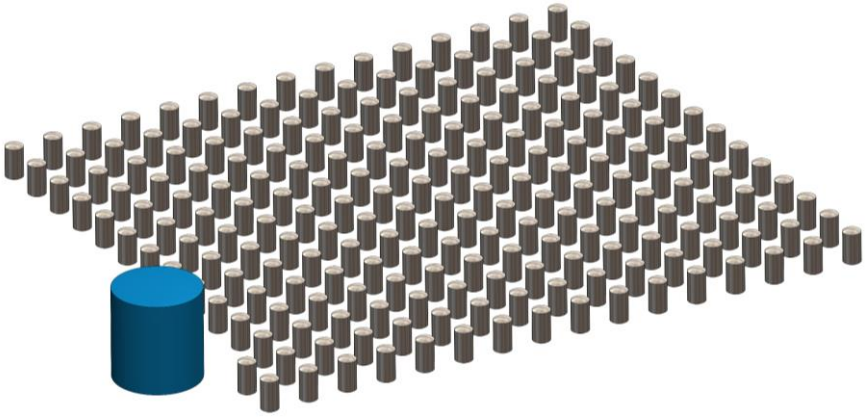

Figure 3.8: Closed system layout assumed for every sorption material. Every active material tank contains the required amount of energy for one day of operation and the water tank contains the sorbate necessary for one year of operation.

The heat transfer area between the water for the space heating system and the active material in every module is not considered because it is strongly dependent on the heat exchanger shape, the heat transfer coefficient between the sorption bed and the fluid inside the heat exchanger, and the temperature of the sorption bed. In particular, the latter is dependent on the amount of water vapor flowing through the bed, which in turn depends on the pressure difference between the evaporator and the sorption bed, which is not constant. Therefore, a numerical model valid for only one single material and reactor shape would be required, and it is out of the scope for a rough size estimation of the system. In reality, the volume of the heat exchanger in each module has also to be considered. With the abovementioned assumptions, the results of the system estimation are visible in Table 3.7. The sorbate volume to be stored depends on the moles of water involved in the sorption reactions for every material. The overall sorbent and sorbate volumes range from 9.9 m^3 (Na_2S) to 13.3 m^3 ($SrBr_2$) for the pure salt hydrates, 28.5 m^3 for zeolite 13X, and 23.4 m^3 for the composite. Pure salt hydrates ($MgCl_2$ and Na_2S) represent the least expensive solutions, followed by the ideal composite. The pure adsorbent is again the most expensive option among the

investigated ones. The storage capacity costs, considering the active material and the reactor material costs, have a range of 2.97 €/kWh$_{cap}$ ($MgCl_2$) to 13.67 €/kWh$_{cap}$ ($SrBr_2$) for salt hydrates, 6.69 €/kWh$_{cap}$ for the ideal composite and 19.48 €/kWh$_{cap}$ for the zeolite 13X system. It has to be recalled that in this analysis the heat exchanger volume inside the active material tanks is not taken into account, and it would contribute to increase the overall system cost and volume occupied, thereby decreasing the energy density.

Table 3.7: Design parameters of a closed sorption system varying the active material.

	$MgCl_2$	Na_2S	$SrBr_2$	Zeolite 13X	Composite
V_b [m^3]	8.00	7.17	10.20	25.64	20.51
V_w [m^3]	2.78	2.73	3.09	2.86	2.91
V_{b+w} [m^3]	10.78	9.90	13.29	28.5	23.42
$V_w(\Delta T = 50K)/V_{sm+w}$	4.4	4.8	3.6	1.7	2.0
	Active Material Tanks Estimation				
$M_{tank,sm}$ [kg]	42.5	37.8	73.0	101.3	77.1
$L_{tank,sm}$ [m]	0.53	0.48	0.68	1.71	1.37
$M_{tanks,sm}$ [t]	9.0	8.0	15.5	21.5	16.3
	Sorbate Water Tank Estimation				
$L_{tank,w}$ [m]	1.58	1.55	1.75	1.62	1.64
$M_{tank,w}$ [t]	2.96	2.90	3.29	3.04	3.09
	Energy density and storage capacity costs estimation				
$SCC_{sm+reactor}$ [€/kWh$_{cap}$]	2.97	2.99	13.67	19.48	6.69
$E_{vol,reactor}$ [GJ/m^3]	0.90	0.98	0.73	0.34	0.41

3.5 Liquid sorption systems

In order to have a general overview of the liquid sorption systems performance and their suitability for the assumed reference scenario, four absorption couples from the literature are analyzed (3.5.1). Then, an ideal liquid sorption system is defined in section 3.5.2.

3.5.1 Liquid sorption systems from literature

In order to estimate an ideal liquid sorption system to compare with the previously estimated solid sorption systems, different absorption couples from Liu et al. [110,111] are considered. General literature references and state of the art reviews on liquid absorption technologies can be found in [112–114] . The data from the study of Liu et al. [111] have been used to define the sorption cycle of a typical system based on the most suitable absorption couple for

the reference scenario in 3.5.2. Possible absorption temperatures in the range of 20 – 45 °C have been investigated by the authors assuming an evaporator temperature of 10 °C and a sorbate storage temperature of 10 °C. However, not all the absorption couples were able to release heat above 35 °C, the space heating system requirement in the reference scenario.

Table 3.8: Different absorption couples, with or without partial crystallization in the storage tank [111].

	LiBr-H_2O	NaOH-H_2O	LiCl-H_2O	KOH-H_2O
T_s [°C]	35	45	35	35
$T_{d,R_{cryst}=0}$* [°C]	72	50	66	63
$T_{d,R_{cryst}=4}$* [°C]	78	57	93	84
$e_{R_{cryst}=0}$ [kJ/kg$_{sm}$]	500	250	750	250
$e_{R_{cryst}=4}$ [kJ/kg$_{sm}$]	1250	500	1650	1000
ρ_{sm} [kg/m^3]	3460	2130	2070	2120
$E_{vol,sm,R_{cryst}=0}$ [GJ/m$^3_{sm}$]	1.73	0.53	1.55	0.53
$E_{vol,sm,R_{cryst}=4}$ [GJ/m$^3_{sm}$]	4.33	1.07	3.42	2.12
$V_{sm,R_{cryst}=0}$ [m^3]	5.8	18.9	6.4	18.9
$V_{sm,R_{cryst}=4}$ [m^3]	2.3	9.4	2.9	4.7
$C_{wt,sm}$ [115] [€/t]	5500	400	2700	1200
$C_{sm,R_{cryst}=0}$ [k€]	110	16	36	48
$C_{sm,R_{cryst}=4}$ [k€]	44	8	16	12
$SCC_{sm,R_{cryst}=0}$ [€/kWh$_{cap}$]	39.6	5.8	12.9	17.3
$SCC_{sm,R_{cryst}=4}$ [€/kWh$_{cap}$]	15.8	2.9	5.9	4.3

*assuming a condenser vapor pressure of 4.2 kPa

In Table 3.8, the energy density of different absorbents, at the stated absorber temperature are reported in case of no crystallization allowed in the storage tank, or a ratio of crystallization equal to 4. The energy density is given considering one cubic meter of pure absorbent material. The ratio of crystallization (R_{cryst}) is defined as the mass ratio of crystal in the storage tank present at the end of the storage period and the mass ratio of solution at the same state. A ratio of crystallization equal to 4 implies that there is 20% of liquid solution in the storage tank at the beginning of the absorption cycle, which has to be high enough to allow the solution recirculation in the absorber at the beginning of the discharge process. As it can be seen in Table 3.8, the active material volume required by a single stage liquid absorption system operating in the reference scenario varies from 5.8 to 18.9 m^3 or from 2.3 to 9.4 m^3 with R_{cryst}= 0 or R_{cryst}= 4, respectively. The maximum absorption temperature at which the storage process has a significant energy density is 35 °C for three of the four absorption couples investigated (LiBr-H_2O, LiCl-H_2O, KOH-H_2O), which is realistically not

enough to achieve 35 °C on the space heating side, considering the system thermal losses and the heat exchanger effectiveness. By increasing the absorber temperature in those absorption couples a too small absorbent concentration difference, e.g. lower than 5 % for the LiBr-H_2O couple, would result in the system. Only the system based on NaOH-H_2O has been investigated at higher absorption temperatures, and it resulted in a relatively low energy density. The resulting active material cost of the only feasible single stage liquid sorption system based on NaOH are 5.8 and 2.9 €/kWh_{cap} with or without partial recrystallization, respectively (Table 3.8). Finally, it is remarkable that the required desorption temperature from the liquid sorption systems is lower compared to solid sorption systems. In particular, according to the authors, the system based on NaOH-H_2O that they considered, required 50°C (p_v = 4.2 kPa) to be charged, assuming R_{cryst}= 0.

3.5.2 Ideal liquid sorption system estimation

From the data of the previous paragraph, it appears that a NaOH-H_2O system can deliver the energy above the minimum temperature required in the reference scenario. Therefore, a first rough estimation of this system operating in the reference scenario is carried out in Appendix C with the aim to compare it with the solid sorption systems performance. A minimum useful temperature of 35 °C is set even though, at realistic operating conditions, a higher temperature has to be provided in order to have 35 °C at the space heating system side. The assumptions of this analysis are displayed in Table 3.9, and the main results are displayed in Table 3.10. A similar procedure to the one employed by Liu et al. [111] is adopted.

Table 3.9: Assumptions for the liquid sorption system estimation

Evaporator temperature [°C]	10
Minimum storage temperature $T_{storage}$ [°C]	10
Useful heat temperature [°C]	>35

It is interesting to notice the remarkable energy density reduction if the required tanks volume and the reactor material is taken into account. In Figure 3.9, the energy density based on the pure absorption material of the absorption couples taken from the literature (3.5.1) and the liquid sorption system based on NaOH estimated in this section are shown. It is possible to see that for the system based on NaOH taken from the literature, a lower pure absorbent energy density $E_{vol,sm,R_{cryst}=0}$ (0.53 GJ/m^3) is present due to the considered minimum heat release temperature of 45 °C, while for the system estimated in this section (2.18 GJ/m^3) the minimum heat release temperature was set at 35 °C, according to the reference scenario in Table 3.9. For the ideal NaOH system estimated in this section, the energy density based on the required tanks volume and the costs including also the reactor material is also displayed (red marker) and calculated in Appendix C. It is possible to see the strong decrease (-91 %) in the energy density due to the required volume of water involved in the process, which

determines the strong solution, weak solution and pure sorbate tanks volume. A significant decrease in energy density is expected also for the absorption couples from the literature, if the required tanks volume is taken into account. Equations C.2 – C.7, in Appendix C, illustrate how to derive the ideal system energy density considering the tanks volume from the pure absorbent energy density. For the comparison with the ideal solid sorption systems estimated in this analysis (section 3.6), only the ideal NaOH-H_2O system, considering also the tanks volume and cost, is considered.

Table 3.10: Main parameters of the liquid sorption system based on NaOH-H_2O

$E_{vol,sm}$ [GJ/m^3]	2.18
$E_{vol,system}$ [GJ/m^3]	0.20
$SCC_{sm+tanks}$ [€/kWh$_{cap}$]	1.44

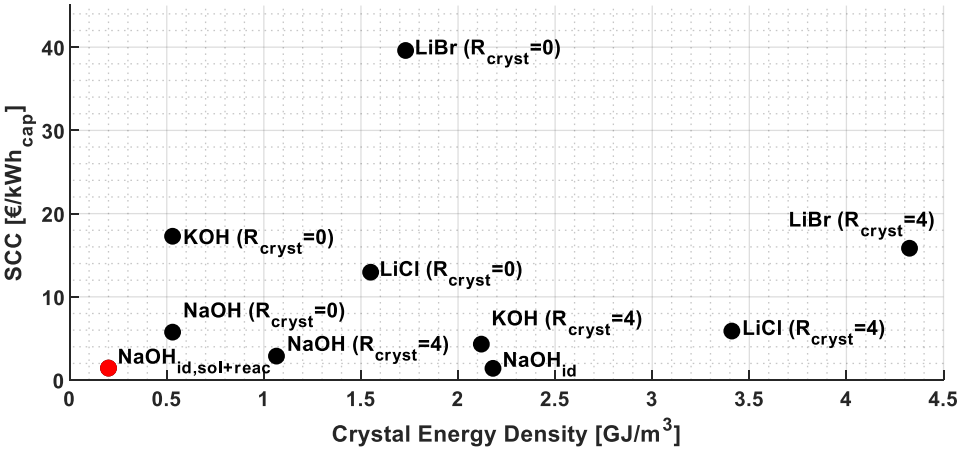

Figure 3.9: Energy density and costs of liquid sorption materials from the literature and the estimated NaOH liquid sorption system based on the pure absorbent energy density (black markers). The red marker indicates the solution + reactor material volume energy density of the ideal liquid sorption system based on NaOH.

3.6 Sorption systems comparison

In this section, a comparison between open and closed solid sorption systems is made in terms of reactor energy density and storage capacity cost (3.6.1). Then, a sensitivity analysis on the ideal composite material parameters (3.6.2) is carried out with the aim to understand their influence on the energy density and storage capacity cost of the reactor. Finally, the previously estimated open and closed solid sorption systems are compared in terms of energy density and storage capacity cost with the liquid sorption system (3.6.3).

3.6.1 Open and closed solid sorption systems

From a first estimation of the sizes of both open and closed systems based on three salts hydrates, zeolite 13X, and an ideal composite, it is possible to draw preliminary conclusions on the systems performances and storage capacity costs defined as the ratio of the system costs and the installed storage capacities. The system costs considered are the active materials and the main reactor material costs. From Figure 3.10, it is possible to notice that the energy densities of open systems are higher. This is because the closed systems require the sorbate to be stored, therefore increasing the overall system volume. Additionally, for pure salt hydrates, the assumed open system layout is more compact whereas the closed system is divided into a number of tanks equal to the yearly heating days. The large number of tanks implies also a large use of reactor material; thereby increasing the system capacity costs. In particular, this is remarkable in the zeolite system, which requires a relatively large amount of reactor material, because of the relatively low material energy density, resulting in the highest storage capacity cost. For zeolite 13X, the energy density of the closed system layout is slightly higher because the volume required to store the active material and the sorbate is lower compared to the volume to store the active material in the open system layout. This is because in the open system, part of the energy stored is lost to the environment in the heat recovery unit (Table 2.5); while, for the closed system, it is assumed that the energy is entirely transferred to the space heating system. Thus, in an open system, more material is needed compared to a closed system, and if the material energy density is low enough, it can be that the required additional volume of the material in the open system is larger than the volume required in the closed system to store both the active material and the sorbate (water).

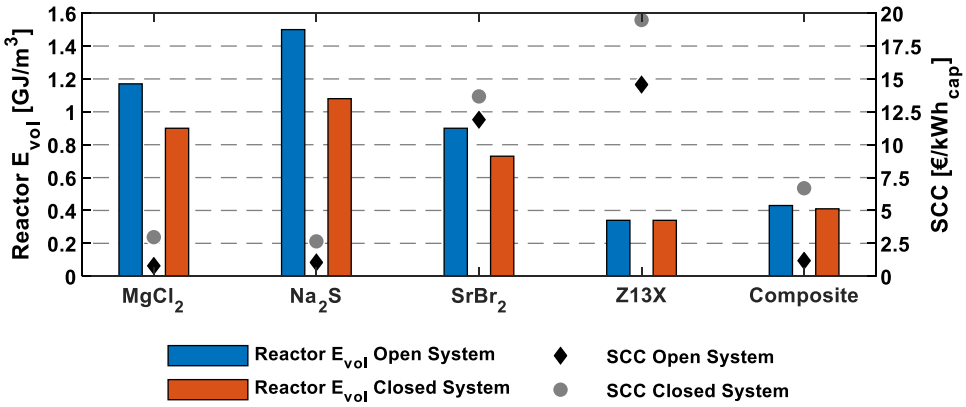

Figure 3.10: Open and closed systems comparison in terms of systems energy density and storage capacity cost.

Systems based on the composite material have energy densities above the systems based on pure adsorbents (0.43 – 0.41 GJ/m^3), with a slightly higher value for open systems. Moreover, their storage capacity costs are remarkably lower being approximately 6 – 12 times lower for closed and open systems, respectively.
Concerning the storage capacity costs, open systems resulted in lower costs compared to closed systems. This is because the reactor layout assumed for the closed systems requires more material compared to an open system. In Figure 3.11, the reactor material cost percentage related to the overall materials costs for open and closed sorption systems is shown, and it is remarkably higher for closed systems, in particular for the most compact and inexpensive systems. This means that, for the systems in which the reactor material cost heavily affects the overall system cost, the choice of a suitable and inexpensive material is essential.

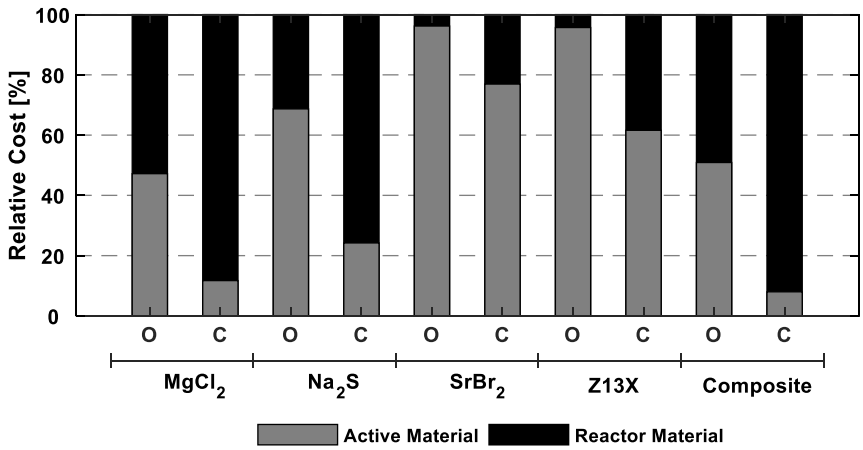

Figure 3.11: Reactor and active materials costs ratio for open (O) and closed (C) solid sorption systems.

3.6.2 Sensitivity analysis on composite materials parameters

Two of the main parameters of the composite material that affect the investigated system performance are the amount of active material present in the composite and the hosting matrix price. By varying the amount of active material, the overall energy density is directly affected (Figure 3.12). The amount of active material in the composite is varied between 20 vol% and 80 vol% for both open and closed systems layouts. Assuming a hosting matrix density of 180 kg/m^3, volume fractions of 20 - 80 vol% would correspond to weight fractions of approximately 70 - 97 wt%, respectively. For comparison, values of 90 wt% of $CaCl_2$ are achieved for composites with ENG matrices [64,116]. A substantial and proportional increase in the energy density is present by increasing the amount of active material in the ideal composite. For open systems, the energy density variation is in the range from -60 % (20 vol%) to +63 % (80 vol%) compared to the 50 vol% case. For closed system, the range is

within -56 % - +49 % for the same volume percentage of active material in the composite. It can be noticed that, by increasing the amount of active material, the energy density increase is sharper in open systems. This is due to the chosen layouts and assumptions in open and closed systems estimation, which in turn result in different amounts of reactor material required for open and closed system layouts. Concerning the storage capacity costs, closed systems have larger amounts of reactor material (Figure 3.11) and their costs decrease more rapidly by increasing the amount of active material in the composite. Its nonlinear tendency is due to the mutual effects between the decrease of composite material required by increasing the amount of active material in the composite, and the consequent lower amount of reactor material required. Closed systems have a cost range within +131 % (20 vol%) and – 32 % (80 vol%) and open systems between +20 % and – 2.5 % for the same active material percentages, referred to the costs at 50 vol% of active material under the present assumptions. Concerning the hosting matrix price, its value has been varied between ±75 % of the initial value (600 €/t) to investigate its influence on the storage capacity costs of the systems. The results can be seen in Figure 3.13. As expected, a linear behavior in the storage capacity variation (ΔSCC) costs is present for both open and closed systems. For open systems, a range of ±13.5 % of the matrix price, compared to the original matrix price, is estimated. For closed systems this range is within ±2.1 %. A smaller influence of the matrix price in closed systems is due to the fact that they are more influenced by the reactor material costs (Figure 3.11).

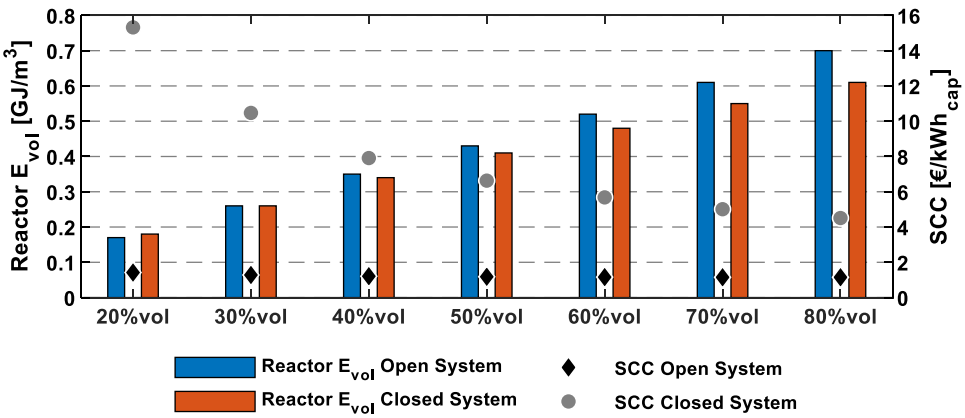

Figure 3.12: Open and closed systems comparison for different amounts of active material in the composite material.

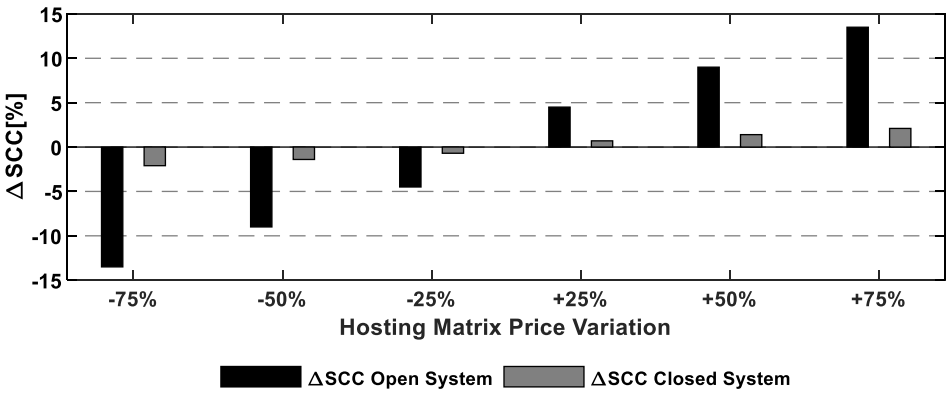

Figure 3.13: Open and closed systems comparison varying the composite hosting matrix price. Closed systems are less sensible to hosting matrix price variation due to the higher influence of the reactor material cost.

3.6.3 Solid and liquid sorption systems

In Figure 3.14, a comparison amongst the solid sorption systems and the liquid sorption system is shown. The cost of the active materials is represented by the markers and the cost increase due to the reactor material is represented by the vertical red lines. Auxiliary system components and the system operation costs would increase further the system costs and decrease the overall energy density. For solid sorption open systems, only the sorbent volume is considered since the sorbate is not stored. For the liquid sorption system estimated in this analysis, the energy density is referred to the volume occupied by the solution during the process (V_{HCT} + V_{LCT} + V_{ST}). Open and closed systems performance have already been discussed in 3.6.1, and they have comparable energy densities amongst the pure salt hydrates: 0.90 – 1.31 and 0.73 – 1.16 GJ/m^3 for open and closed systems, respectively. Lower energy densities are instead present for the open systems (0.33 – 0.43 GJ/m^3) and the closed systems (0.35 – 0.43 GJ/m^3) based on zeolite 13X and on the ideal composite, respectively. The liquid sorption system based on NaOH has an energy density of 0.20 GJ/m^3. Rathgeber et al. [117,118], within the framework of IEA SHC Task 42 / ECES Annex 29, made an economic evaluation of thermal energy storages, and set the economic boundaries for different user categories: industries, buildings and enthusiasts. Industries can accept payback periods of 5 years and interest rates on the capital costs of 10 %; buildings can accept payback periods of 15 – 20 years and interest rates of 5 % and enthusiasts can accept interest rates of 1 % and payback periods of 25 years. With the interest rates on the capital costs and the acceptable payback periods of the user classes, the acceptable annuity factors can be estimated. Another indicator considered in the economic evaluation is provided by the reference energy costs (REC) which represent the cost of energy supplied by the market. The assumption of the authors was that the costs of the energy supplied by a thermal energy storage should not

exceed the costs of the same thermal energy supplied by the market. It is noteworthy to mention that they depend on many external factors such as the economic and political conditions of each country (e.g. energy taxation and subsidization policies, political agendas, country energy dependency), and they are related also to the portfolio of technologies used to provide thermal energy in a specific country (i.e. gas boilers, district heating networks, cogeneration units, etc.). Therefore, the reference energy costs can vary geographically and over the time due to the abovementioned reasons. Gas prices or the cost of heat in district heating networks could be used as an indication for the reference energy costs. For example, in the second half of 2018, the average gas prices in European countries for households and non-households consumers were 0.067 €/kWh and 0.032 €/kWh, respectively [119]. Concerning the cost of heat in district heating networks, Werner [120] estimated an average heat price of 0.065 €/kWh in European countries, in 2013. The estimation was based on the annual revenues and heat sales of district heating systems in the investigated European countries, excluding VAT. Ultimately, in this analysis, the REC values from Rathgeber et al. [118] are assumed. The authors considered a range of reference energy costs (REC) and annuity factors (AF) for every user category, and they estimated the acceptable storage capacity costs (SCC_{acc}) of different existing thermal energy storages with equation 3.14. The results are visible in Table 3.11, and it can be seen that for the building and industry categories, the costs range are similar to the abovementioned gas prices.

$$SCC_{acc} = \frac{REC\ N_{cycles}}{AF} \qquad 3.14$$

The acceptable storage capacity costs are defined in function of the substituted reference energy costs, the annuity factors, and the number of yearly cycles that the thermal storage undergoes. Since in this analysis only seasonal thermal energy storages are considered, only one annual cycle is performed. In Figure 3.14, the range of acceptable storage capacity costs by the three different users defined by the authors are displayed assuming one charging/discharging cycle of the systems every year.

Table 3.11: Acceptable storage capacity costs for one system cycle per year [118]**.**

User Class	REC [€/kWh]	AF [1/y]	SCC_{acc} [€/kWh$_{cap}$]
Industry	0.02 – 0.04	0.25 – 0.30	0.07 - 0.16
Building	0.06 – 0.10	0.07 – 0.10	0.60 - 1.43
Enthusiast	0.12 – 0.16	0.04 – 0.06	2 - 4

Based on the results of Figure 3.14, it is possible to notice that the active material costs of the investigated systems are not competitive for an industrial user. For building users, some of the systems based on pure salt hydrates ($MgCl_2$ and Na_2S) are within the acceptable storage capacity costs by considering only their active material cost. However, as already mentioned,

their hydrothermal stability issues (e.g. $MgCl_2$) make these systems hardly feasible. Moreover, open systems based on Na_2S, face environmental issues due to the toxicity of the salt hydrate and its byproducts such as hydrogen sulfide. Therefore, only closed systems based on Na_2S are advisable. However, the production of non-condensable gases during the system operation decreases the system efficiency; therefore, they have to be periodically removed to keep the system pressure at optimal levels.

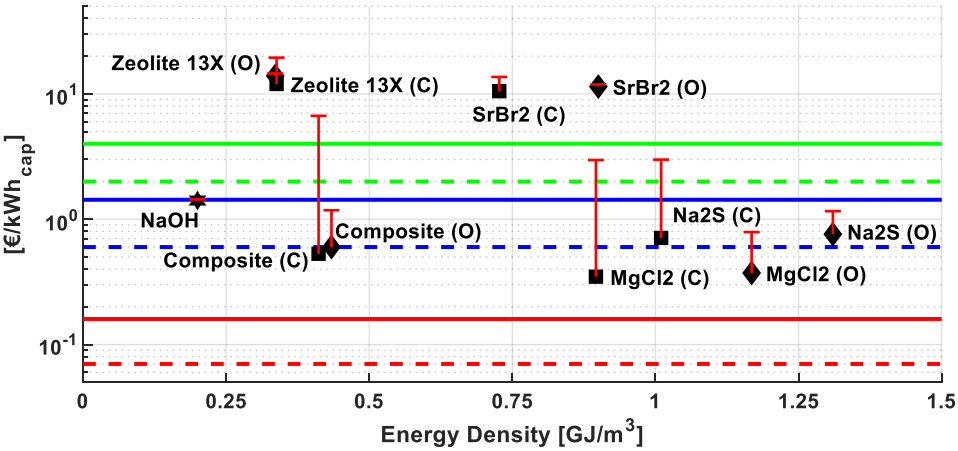

Figure 3.14: Materials energy density vs active material costs (markers) and active materials + reactor material costs (red vertical lines). Marker types: Rhomboids = open systems (O), Squares = closed systems (C), Hexagram = ideal liquid sorption system. Minimum (dashed line) and maximum (solid line) acceptable storage capacity costs of a thermal storage operating one cycle per year [118] **for industry (red), building (blue) and enthusiast (green) users.**

The systems based on the ideal composite material, assuming a sufficient material stability, would represent a promising option since they have relatively low storage capacity costs (0.60 – 0.53 €/kWh_{cap} for the closed and open system, respectively) affordable for the buildings category. However, they would result also in approximately two and a half times larger systems compared to the open system based on pure $MgCl_2$. The liquid sorption system estimated in 3.5.2, having an energy density of 0.20 GJ/m^3 released at a temperature above 35 °C has active material costs within the acceptable storage capacity costs of the building users (1.44 €/kWh_{cap}). Finally, the solid systems based on strontium bromide and zeolite 13X resulted above the storage capacity costs affordable from all the user categories (10.0 – 14.6 €/kWh_{cap}). In case of applications requiring more charge/discharge cycles per year, their costs can decrease, and they might become affordable for the investigated user categories. Considering also the reactor material costs estimated in this analysis, by looking at the vertical red lines in Figure 3.14, it is possible to notice that solid sorption systems, especially closed systems, have a large cost increase since the reactor material cost is relatively high (Figure 3.11). The liquid sorption system estimated in 3.5.2 has a moderate increase due to the relatively small amount of material estimated to store the sorbent and the sorbate in the

different staged of the process. In particular, the closed systems based on $MgCl_2$, Na_2S and the composite material shift from the building user class to the enthusiast user class range of storage capacity costs. The open systems based on the same materials remain below the maximum storage capacity costs acceptable from the building user. To conclude, it has to be remarked that, for the sake of comparison, only active material and reactor material costs are estimated and considered in Figure 3.14. For liquid sorption systems taken from the literature only active material costs are considered, and the energy density is given for one cubic meter of solution after the desorption phase. Other system materials, components and operational costs are not considered in this analysis and they would increase additionally the storage capacity costs of the thermal storages investigated. Existing thermal storage systems evaluated with the abovementioned approach can be found in Rathgeber et al. [117].

3.7 Conclusions

In this chapter, ideal STES systems are estimated and compared in terms of energy densities and storage capacity costs. A common reference scenario for the analysis has been assumed, and it consists of a seasonal heat storage for space heating of a passive house located in Amsterdam, the Netherlands. Five conceptual solid open systems and five closed systems based on different salt hydrates, zeolite 13X, and an ideal composite material have been estimated. Moreover, a conceptual liquid sorption system based on NaOH is compared with the solid sorption systems in the same reference scenario. The results showed that the closed systems are in general more expensive and less compact than the open systems for the assumed reactor layouts, and the liquid system would result in a larger and more expensive system compared to the solid systems based on the ideal composite material and certain salt hydrates. On the contrary, the liquid system would be more affordable compared to systems based on zeolite 13X and the most expensive salt hydrates. Finally, the open system based on the composite material, could represent a valid compromise between energy density and storage capacity costs, assuming a sufficient material stability. From the economic perspective, the active material costs assumed for the investigated systems are too high for industry users. For implementation in domestic buildings, systems based only on certain pure salt hydrates, on the ideal composite material, and on the liquid sorption system become affordable. When reactor material costs are also considered, the overall system cost, especially for closed solid sorption systems, increases remarkably. This analysis highlights that the costs for the investigated sorption seasonal heat storage systems, even when considering only the active material and the reactor material costs, are still relatively high for the user classes considered in this analysis. Especially considering that the cost of auxiliary system components (e.g. the heat exchangers in solid sorption closed systems and the absorber in the liquid sorption system) and the operational costs are not taken into account. The acceptable storage capacity costs used in this analysis are largely affected by the energy prices, which are dependent on multiple factors determining the market conditions. For

example, an increase in reference energy costs (REC) due to, for example, the increase of gas prices, would increase the acceptable storage capacity costs. Conversely, if the storage could perform multiple charge/discharge cycles per year, the acceptable storage capacity costs would increase remarkably. Thus, in the upcoming future, sorption seasonal heat storage systems like the ones investigated in this analysis can become more competitive in the energy sector according to the future energy market conditions.

To this extent, Chapter 5 of this dissertation investigates the profitability of a STES system at the presence of different energy markets, and it shows how certain balancing market mechanisms can make the STES integration profitable for a particular reference scenario. Similarly, Chapter 6 of this dissertation investigates the potential of a STES in a domestic environment and, among other parameters, it investigates the influence of the electricity and gas prices on the profitability of the system.

CHAPTER 4

STES MODELS FOR SYSTEM-SCALE SIMULATIONS

A PHYSICS-BASED AND A DATA-DRIVEN APPROACH

Based on:
Scapino L., Zondag H. A., Diriken J., Rindt C. C. M. Sciacovelli A.
Modeling of a sorption heat storage reactor using nonlinear autoregressive neural networks Eurotherm Semin. #112 - Adv. Therm. Energy Storage, Lleida: 2019.

Scapino L., Zondag H. A., Diriken J., Rindt C. C. M. Van Bael J., Sciacovelli A.
Modeling the performance of a sorption thermal energy storage reactor using artificial neural networks
Appl Energy 2019;253:113525
doi:10.1016/j.apenergy.2019.113525

This chapter investigates the performance of two numerical models, a spectral physics-based model and a data-driven model, to predict the dynamic behavior of a sorption thermal energy storage reactor. Several dynamic tests are performed, in which the two models are compared with a high-fidelity model. In section 4.2, the STES system is introduced and described. In sections 4.3 and 4.4, the high-fidelity model and the dynamic tests that are performed for both models are introduced, respectively. In section 4.5, the spectral physics-based model is presented. Section 4.6 includes the data-driven model and its further improvement. Finally, section 4.7 presents the chapter conclusions, in which the developed models are compared in terms of accuracy.

4.1 Introduction

The aim of this chapter is to investigate two different approaches for modelling the packed bed of a STES for dynamic systems simulations.

In the scientific literature, especially if focused on material- or reactor-scale, sorption reactors for STES are modeled using mesh-based approaches such as the finite element method (FEM) or the finite volume method (FVM) (e.g. [121–124]). These models are based on the laws of physics governing the involved phenomena. In practice, the models are based on a set of partial differential equations (PDEs), describing the heat and mass transfer in the reactor, coupled with other equations describing specific aspects such as the kinetics. Typically, the temporal and spatial resolution required for solving the PDEs is relatively high. The main advantage of these models is that they can produce a detailed description of the simulated variables along the spatial and temporal domains. However, the computational cost is also typically high.

In the dynamic simulation of an energy system, the system components are co-simulated in a common modeling environment and, if an extensive temporal horizon has to be modeled, the temporal resolution of the simulation can be a bottleneck in terms of computational cost. Each system component should be modeled in terms of inputs and outputs that are relevant for the dynamic simulation. Therefore, a relatively simple model for each system component, which can still give accurate prediction of the component outputs given the inputs, is desirable.

In light of this, two models of a sorption reactor are investigated with the future aim of integrating them in a dynamic simulation of an energy system. The two models investigated should be less computationally expensive than e.g. models based on FEM, but still able to efficiently predict the relevant inputs/outputs of the sorption reactor.

The first model investigated (section 4.5) is a physics-based model that uses a spectral method for the spatial discretization. The reason for this choice was that, in general, spectral methods exhibit exponential convergence for smooth profiles, necessitating less degrees of freedom compared to conventional mesh-based approaches to reach a given accuracy. Moreover, this model results in a matrix-vector system that admits easy integration in a broader simulation environment in which other models are present and can be co-simulated.

The second model investigated (4.6) is a data-driven model that uses artificial neural networks (ANNs) to simulate the sorption reactor outputs given its inputs. The main advantage of this type of model is that, once that the model is trained, the computational cost during a dynamic simulation is very low. However, the training process can be computationally expensive, and the availability of good quality and representative data is a crucial requirement. The performance of both models is individually compared with a FEM model, which is used as a high-fidelity model. The same model is also used to produce the necessary datasets for the training and validation of the data-driven model.

4.2 Sorption system description

The STES considered in this chapter consists of an open sorption system, and the sorption reactor unit consists of a packed bed in which the sorbent is stored as a porous solid, and the sorbate flows through the packed bed in gas form. The main concept is illustrated in Figure 4.1. When the reactor is charged (Figure 4.1 top), a hot airflow induces the endothermic reaction that separates the sorbent from the sorbate. During the reactor discharge (Figure 4.1 bottom), the sorbate in the airflow reacts with the solid sorbent and the heat from the exothermic reaction is extracted through the airflow.

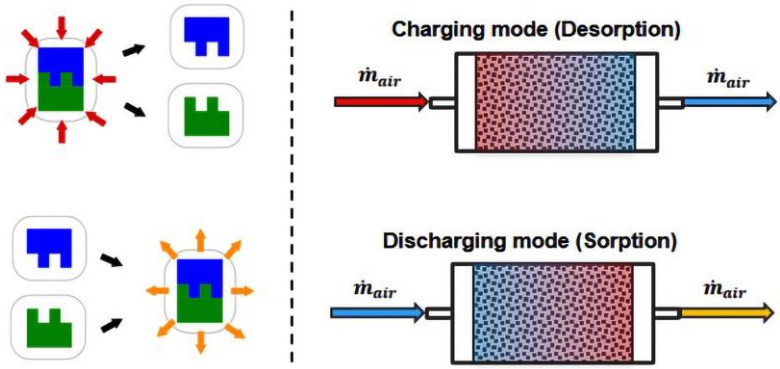

Figure 4.1: Packed bed of an open sorption thermal energy storage. Top: Charging mode (desorption). Bottom: Discharging mode (sorption).

The main system components (Figure 4.2 left) are the sorption reactor, a fan (F1) to drive the sorbate flow, a heat recovery unit to recuperate the heat still present in the exhaust airflow after the thermal load, and a heat exchanger (HX2) to provide the heat to the demand side. From a system modeling perspective, the sorption reactor parameters necessary for the interaction with the other system components, assuming a fixed airflow rate, are the inlet temperature and sorbate concentration, the outlet temperature, and the reactor state of charge. With this information, it is possible to quantify the amount of energy that the reactor stores/delivers in a dynamic system simulation.

Concerning the sorption material in the system, in chapter 2 different candidates have been investigated. Potassium carbonate was among the most promising sorption materials in terms of stability, cyclability and safety. Therefore, in this work it is assumed that the sorption material in the STES is anhydrous potassium carbonate (K_2CO_3), which reacts with water vapor to produce potassium carbonate sesquihydrate (equation 4.1).

$$K_2CO_{3\,(solid)} + 1.5H_2O_{\,(gas)} \leftrightarrow K_2CO_3 \cdot 1.5H_2O_{\,(solid)} \qquad 4.1$$

The sorption reactor operating mode (dehydration or hydration) is determined by the reaction equilibrium pressure (p_{eq}) and the sorbent vapor pressure in the reactor (p_v). The equilibrium pressure can be estimated according to the van't Hoff equation (equation 4.2) while the sorbent vapor pressure is calculated assuming that the sorbate behaves as an ideal gas (equation 4.3).

$$\ln\left(\frac{p_{eq}}{p_0}\right) = -\frac{\Delta H_{reac}}{R_g T} + \frac{\Delta S_{reac}}{R_g} \qquad 4.2$$

$$p_v = cR_g T \qquad 4.3$$

In equations 4.2 and 4.3, ΔH_{reac} and ΔS_{reac} are the reaction enthalpy and entropy expressed per mole of sorbent, p_0 is the reference pressure of 1 bar, R_g is the ideal gas constant, T is the temperature and c is the sorbent molar concentration. In Figure 4.2 right, the reaction equilibrium pressure and the water vapor pressure with a constant water vapor concentration ($c = 0.4\, mol/m^3$) are shown for different temperature values. When $p_v/p_{eq} > 1$, the hydration reaction occurs while if the ratio decreases below 1, the dehydration happens.

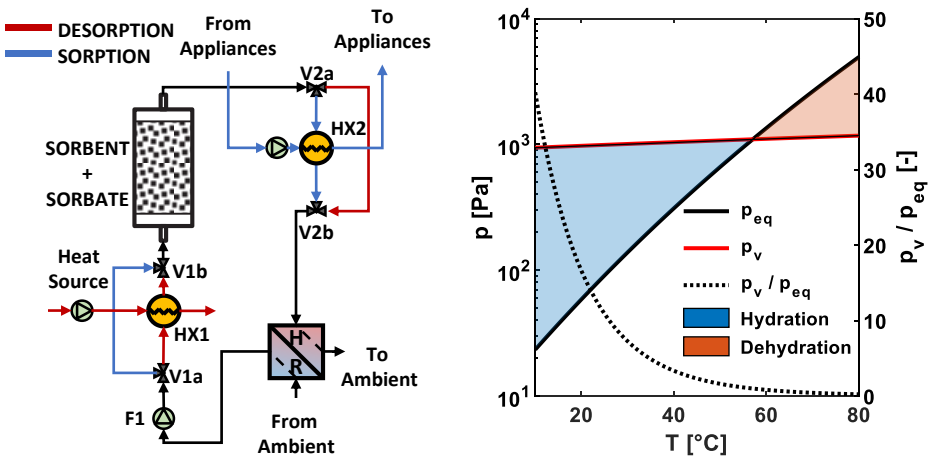

Figure 4.2. Left: Open system design concept [125]**. During desorption, valves V1a and V1b direct the flow through the heat exchanger HX1 to be heated from a high-T source, and valves V2a and V2b bypass HX2. During sorption, valves V1a and V1b bypass HX1 and valves V2a and V2b direct the heated flow after sorption into the heat exchanger HX2 to transfer heat to the appliances and then to the heat recovery unit HR. Partially adapted from Scapino et al.** [126]**. Right: Equilibrium pressure (black solid line) for the sorption reaction $K_2CO_3 + 1.5H_2O \leftrightarrow K_2CO_3 \cdot 1.5H_2O$, sorbent vapor pressure (red solid line), and their ratio (dotted line) by increasing the temperature and keeping a constant sorbent vapor concentration of 0.4 mol/m³. Blue area: hydration zone. Red area: dehydration zone.**

4.3 High-fidelity physics-based model

A physics-based quasi 2D-model developed in COMSOL Multiphysics [127] is used to produce the required dataset for the data-driven model and to compare both the physics-based and data-driven compact models with realistic hydration and dehydration simulations.
The reactor main body is assumed to be a stainless-steel cylinder with multiple insulation layers (Figure 4.3), with an axial length L of 0.5 m and an inner diameter d_i of 0.35 m. The inner insulation is made out of Teflon, and the outer insulation of glass wool. The reactor is filled with the porous sorption material with porosity ε_b, through which an airflow is flowing along the axial direction with a velocity u_a.

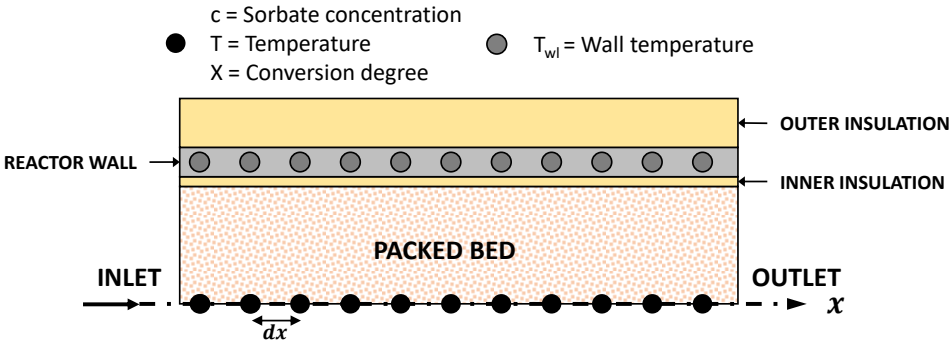

Figure 4.3: Quasi 2D model of the sorption reactor: conceptual representation.

The quasi 2D-model consists of a set of partial differential equations describing the sorbent mass balance (equation 4.4), the packed bed energy balance (equation 4.5) assuming the solid and the gas phases to be in thermal equilibrium, and the wall energy balance (equation 4.6), which has been developed and described in detail by Gaeini et al. [121] for an existing prototype reactor in which zeolite 13X was used as sorption material. In order to describe the reaction advancement and the reaction rate, a kinetic model (equation 4.7) based on a linear driving force, already used for modeling gas/solid sorption reactions at reactor scale has been implemented [124].

$$\varepsilon_b \frac{\partial c}{\partial t} + u_a \frac{\partial c}{\partial x} - D_x \frac{\partial^2 c}{\partial x^2} + \frac{(1-\varepsilon_b)\nu\rho_{sm}}{M_{mol,sm}} \frac{dX}{dt} = 0 \qquad 4.4$$

$$\overline{\rho c_p} \frac{\partial T}{\partial t} + \rho_a c_{p,a} u_a \frac{\partial T}{\partial x} - \lambda_{eff} \frac{\partial^2 T}{\partial x^2} - \frac{(1-\varepsilon_b)\nu\rho_{sm}\Delta H_{reac}}{M_{mol,sm}} \frac{dX}{dt} + \frac{4(T-T_{wl})}{\pi d_i^2 R_i} = 0 \qquad 4.5$$

$$\rho_{wl} c_{p,wl} \frac{\partial T_{wl}}{\partial t} - \lambda_{wl} \frac{\partial^2 T_{wl}}{\partial x^2} = \frac{(T - T_{wl})}{R_{th,i} A_{wl}} - \frac{(T_{wl} - T_{amb})}{R_{th,o} A_{wl}} \quad 4.6$$

$$\begin{cases} \frac{dX}{dt} = k_{LDF}(1 - X)\left(1 - \frac{p_{eq}(T)}{p_v(c,T)}\right) & \frac{p_v}{p_{eq}} \geq 1 \\ \frac{dX}{dt} = k_{LDF} X \left(1 - \frac{p_{eq}(T)}{p_v(c,T)}\right) & \frac{p_v}{p_{eq}} < 1 \end{cases} \quad 4.7$$

In equation 4.4, D_x is the axial mass dispersion coefficient, ν is the sorption reaction stoichiometric coefficient, ρ_{sm} and $M_{mol,sm}$ are the sorption material density and molar mass. In equation 4.5, $\overline{\rho c_p}$ is the bed mean heat capacity, λ_{eff} is the effective axial thermal conductivity, d_i is the packed bed diameter, $R_{th,i}$ is the thermal resistance between the packed bed and the stainless-steel wall, and T_{wl} is the stainless steel wall temperature. In equation 4.6, $R_{th,o}$ is the thermal resistance between the reactor stainless-steel wall and the outer environment, ρ_{wl}, $c_{p,wl}$, and λ_{wl} are the wall density, specific heat capacity, and thermal conductivity. Finally, in equation 4.7, the local material conversion degree X, ranging from 0 to 1, is defined as the amount of material present in hydrated form over the total amount of material present in a domain element. The kinetic constant term k_{LDF} is selected within a range identified by Gaeini [128]. The main model parameters are displayed in Appendix D in Table D.1.

The overall STES state of charge at time t (SOC_t) is defined based on the material conversion degree, defined as in equation 4.8, and discretized in the spatial domain along the packed bed axial direction as in equation 4.9.

$$SOC_t = 1 - \frac{1}{L} \int X_t dx \quad 4.8$$

$$SOC_t = 1 - \frac{1}{N_{mesh}} \sum_{n=1}^{N_{mesh}} X_{t,n} \quad 4.9$$

Here, N_{mesh} is the overall amount of equidistant mesh elements in the spatial domain and $X_{t,n}$ is the material conversion degree of mesh element n at time t. With the abovementioned definition, a state of charge equal to 0 means that all the material is in hydrated form (reactor completely discharged) and a state of charge equal to 1 means that the material is fully in dehydrated form (reactor completely charged). The thermal resistance values $R_{th,i}$ and $R_{th,o}$ are determined by the geometrical parameters of the reactor. In particular, $R_{th,i}$ is composed by two terms: the convective component inside the packed bed reactor, for which the Nusselt number has been calculated according to Ahn et al. [129], and the conductive component for

the inner insulation. The thermal resistance outside the reactor wall is determined by the thermal resistance of the outer insulation; the additional resistance due to the natural convection outside the reactor wall is neglected. In this model, the sorption material properties have been assumed constant and equal to the properties of the material in hydrated state. The effective axial thermal conductivity (λ_{eff}) is calculated with the Zehner and Schlunder model [130], the bed mean heat capacity ($\overline{\rho c_p}$) is calculated with equation 4.10, and the axial mass dispersion coefficient (D_x) is calculated from the Gunn's correlation [131].

$$\overline{\rho c_p} = \rho_a c_{p,a} \varepsilon_b + \rho_{sm} c_{p,sm} (1 - \varepsilon_b) \qquad 4.10$$

In equation 4.10, the first and second terms of the right-hand side represent the volumetric heat capacity of the air and of the packed bed, respectively. It is assumed that the sorption material particles have no internal porosity. The initial and boundary conditions are described in Table 4.1. The initial sorbate concentration c_0 is assumed to be the concentration at the equilibrium sorbate vapor pressure at the initial reactor temperature T_0.

Table 4.1: Initial (IC) and boundary (BC) conditions of the COMSOL model for hydration (H) and dehydration (D) modes.

			c	T	T_{wl}	X
H	BC	In	$c = c_{in,s}$	$T = T_{in,s}$	$T_{wl} = T_{in,s}$	
		Out	$\left.\frac{\partial c}{\partial x}\right\|_{x=out} = 0$	$\left.\frac{\partial T}{\partial x}\right\|_{x=out} = 0$	$\left.\frac{\partial T_w}{\partial x}\right\|_{x=out} = 0$	
	IC		$c = c_{0,s}$	$T = T_{0,s}$	$T_{wl} = T_{0,s}$	$X = X_{0,s}$
D	BC	In	$c = c_{in,d}$	$T = T_{in,d}$	$T_{wl} = T_{in,d}$	
		Out	$\left.\frac{\partial c}{\partial x}\right\|_{x=out} = 0$	$\left.\frac{\partial T}{\partial x}\right\|_{x=out} = 0$	$\left.\frac{\partial T_{wl}}{\partial x}\right\|_{x=out} = 0$	
	IC		$c = c_{0,d}$	$T = T_{0,d}$	$T_{wl} = T_{0,d}$	$X = X_{0,d}$

The results of a hydration and a dehydration simulation are shown in Figure 4.4 and Figure 4.5, and the input values used in both operating modes are shown in Table 4.2. For both simulations, a constant ambient temperature T_{amb} of 10 °C has been assumed.

Table 4.2: Input conditions and initial material conversion degree used for the hydration and dehydration examples.

HYDRATION		DEHYDRATION	
$c_{in,s}$	0.4 mol/m^3	$c_{in,d}$	0.4 mol/m^3
$T_{in,s}$	10 °C	$T_{in,d}$	100 °C
$X_{0,s}$	0	$X_{0,d}$	1

The reactor heat flows can be expressed as in Table 4.3. Here, P_{reac} is the heat produced from the exothermic reaction, P_{conv} is the heat transported by convection out of the reactor, P_{sens} is the heat flow involved in the variation of the reactor bed temperature (sensible heat), and P_{loss} is the heat transferred from the packed bed to the reactor wall. Therefore, the sensible heat stored in the reactor wall, i.e. part of the energy transferred from the packed bed through the Teflon insulation, is accounted in this last term.

Table 4.3: Sorption reactor power flows calculation.

Power flow	Equation
P_{conv}	$\dot{m}_a c_{p,a}(T_{out} - T_{in})$
P_{reac}	$\int_0^L (1-\varepsilon_b)\frac{\nu}{M_{mol,sm}}\rho_{sm}A_{cross,b}\frac{dX}{dt}\Delta H_{reac}dx$
P_{sens}	$\int_0^L \overline{\rho c_p}A_{cross,b}\frac{\partial T}{\partial t}dx$
P_{loss}	$\int_0^L \frac{T - T_{wl}}{R_{th,i}}dx$

The simulation error, defined here as the violation of the power balance in the packed bed, can be defined according to equation 4.11.

$$P_{conv} + P_{sens} + P_{loss} - P_{reac} = Error \qquad 4.11$$

In Figure 4.4, a hydration simulation is shown. The dehydrated material is being hydrated with an incoming flow of sorbent at a fixed temperature ($T_{in,s}$) and water vapor concentration ($c_{in,s}$). The exothermic reaction produces heat that is transferred to the air flow, which is then removed from the reactor by convection. During hydration, the SOC, defined as in equation 4.9, decreases from 1 to 0. Once that the SOC approaches 0, the reaction rate decreases rapidly, and the outlet temperature decreases too until it reaches the inlet temperature level. It can be seen (Figure 4.4 right) that, at the beginning of the simulation, most of the energy

released during the exothermic reaction is used to increase the reactor temperature (P_{sens}). Hence, the convective power out of the reactor is almost zero. Once that the temperature front reaches the outlet, the convective power rises. It can be noticed that the energy used to increase the whole reactor temperature is constantly released back into the airflow while the reaction front is moving towards the outlet. Finally, the thermal losses increase until the whole reactor is at high temperature, then they slowly decline with the reaction front advancement. Towards the end, the thermal losses have a slightly negative value because part of the heat stored in the reactor wall is transferred back to the packed bed, which is now at a lower temperature than the wall temperature. An error in the heat flows balance is present at the beginning of the simulation and it has a peak of -15 W when the simulation starts. This error can be due to the sharp gradient in P_{sens}, which is calculated through an integral over the spatial domain of the time derivative of the packed bed temperature (fourth term in Table 4.3).

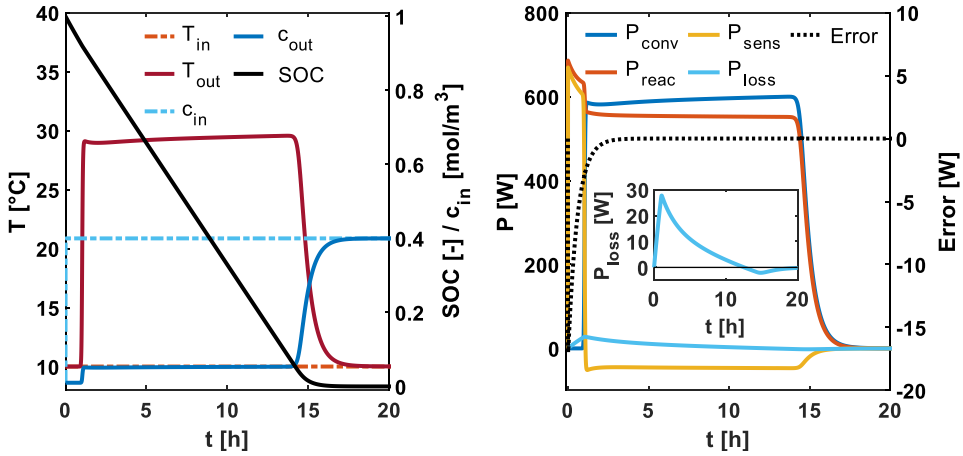

Figure 4.4: Hydration simulation. Left: Inlet (dashed light blue) and outlet (dashed dark blue) water vapor concentration, SOC (black), and inlet (dashed orange) and outlet temperature (red). Right: Power components. Dark blue: P_{conv}. Red: P_{reac}. Yellow: P_{sens}. Light blue: P_{loss}. Dashed black: Error.

In Figure 4.5, the dehydration simulation is displayed. An airflow at a constant temperature of 100 °C containing 0.4 mol/m^3 of water vapor enters the reactor and removes the sorbate molecules from the sorbent. The outlet temperature has an initial increase and it remains relatively constant during the dehydration reaction. The temperature of this plateau corresponds to the equilibrium temperature of the reaction for a water vapor concentration of approximately 0.9 mol/m^3, which is the concentration present after the reaction front, where the reaction still has to take place. In this phase, the reaction front is moving from the inlet towards the outlet, and the thermal energy above the local packed bed temperature is used for the endothermic reaction. Then, at the end of the dehydration, when the SOC approaches 1, the reaction front reaches the outlet and all the mass of the reactor is heated up to a

temperature close to the inlet temperature. The power balances, in Figure 4.5 right, have a similar behavior compared to the ones during the hydration simulation. Initially, the thermal power provided by P_{conv} is used to increase the packed bed temperature (P_{sens}), and to carry out the endothermic reaction P_{reac} close to the reactor inlet. Then, while the reaction front is advancing, most of the convective power is used for the endothermic reaction, except for a small and constant fraction (P_{sens}). Here P_{sens} accounts for the temperature increase from approximately 70 °C to 100 °C of the packed bed fraction in which the reaction front is just passed. The thermal losses are increasing up to an initial peak corresponding to the time in which the packed bed outlet temperature reaches the first plateau, at approximately 70 °C. Then, the reaction front is advancing and the packed bed temperature is increasing, from the inlet to the outlet, to approximately 100 °C. In this period, the thermal losses decrease also because part of the heat is transferred longitudinally towards the colder part of the reactor, where the reaction is not completed, yet. Then, after reaching a minimum value, the thermal losses are increasing again due to the counterbalancing effect of having most of the packed bet at a temperature of approximately 100 °C. At the end of the reaction, the thermal losses have again an exponentially decreasing trend because the reactor wall temperature is increasing up to a steady value, thereby reducing the temperature difference between the packed bed and the reactor wall, which is the driving force of the thermal losses.

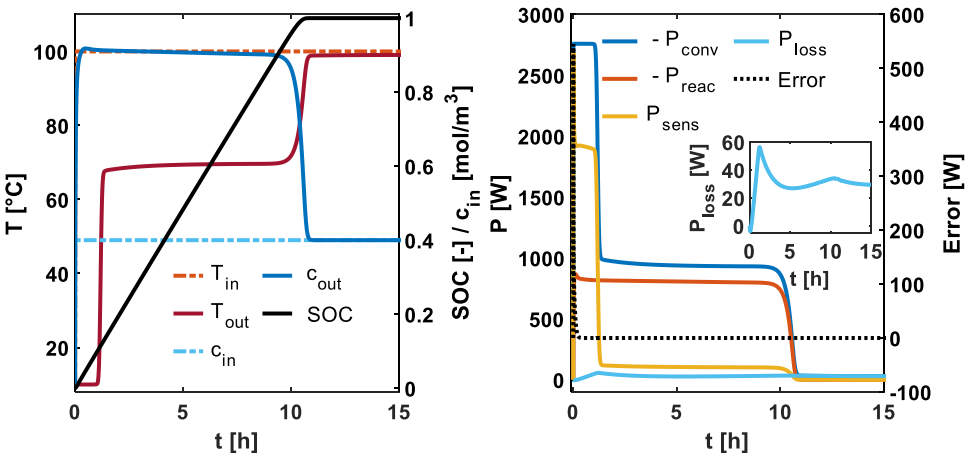

Figure 4.5: Dehydration simulation. Left: Inlet (dashed light blue) and outlet (dashed dark blue) water vapor concentration, SOC (black), and inlet (dashed orange) and outlet temperature (red). Right: Power components. Dark blue: P_{conv}. Red: P_{reac}. Yellow: P_{sens}. Light blue: P_{loss}. Dashed black: Error.

4.4 Tests

In this work, different dynamic tests (Table 4.4) have been performed with the aim to evaluate the numerical models under events that the sorption reactor could experience. For hydration, four tests are carried out. In tests H1 and H2, the inlet temperature or concentration is varied

in a single step during the hydration process. In test H3, a continuous variation of both inlet temperature and concentration is applied. The reason is that, in a real system, the two inputs might vary according to the ambient conditions if, for example, humid air is directly fed from the environment into the reactor. Finally, a scenario with real operating conditions (test H4) for a hydration is investigated assuming the system as depicted in Figure 4.2 left, and the input data are taken from a typical meteorological year for the area of Uccle (BE). In this test, described more in detail in section 4.4.1, it is assumed that air at ambient conditions flows through the heat recovery unit and then into the sorption reactor.
During dehydration, the sorption heat storage can interact with different heat sources (i.e. waste heat, solar thermal collectors, a district heating network connection, etc.) that have the main requirement to deliver the heat at a temperature above the equilibrium temperature of the reversible reaction. Assuming that for a dehydration process ambient air is used, a variation in water vapor concentration in the air due to the daily atmospheric variations is a realistic assumption. The same single step variations are performed as for hydration (tests D1 and D2). A dynamic variation of both variables is not performed because in a real application, a continuous variation of temperature and concentration is unlikely to happen. The reason is that, since a high temperature is required, the heat source is often at a relatively constant temperature or it can be controlled with, for example, mass flow controllers in case of technologies like solar thermal collectors. Moreover, the influence of the concentration is relatively small (i.e. the relative humidity of the airflow is small).

Table 4.4: Summary of the tests performed. H = Hydration. D = Dehydration. c_{in} = Inlet concentration [mol/m^3]. T_{in} = Temperature [°C].

	Test	Input changed	Input variation (from-to)
H	**H1**	c_{in}	0.32 – 0.47
	H2	T_{in}	15 – 23
	H3	c_{in}, T_{in}	Variable
	H4	c_{in}, T_{in}	Variable (Realistic)
D	**D1**	c_{in}	0.55 – 0.33
	D2	T_{in}	90 –130

4.4.1 Development of test H4

A reference scenario for a hydration experiment is assumed, in which the sorption heat storage system is connected to a thermal load. Thus, realistic dynamic input values ($T_{in,s}$ and $c_{in,s}$) can be estimated. The sorption reactor (Figure 4.6) is assumed to be connected to an air/water heat exchanger (HX2) and a heat recovery unit, as in [95,125]. In the hydration mode, the hot air at the outlet of the reactor ($T_{3,a}$) heats up the water in the air/water heat exchanger HX2 from $T_{1,w}$ to $T_{2,w}$. Then, the air at the outlet of the heat exchanger ($T_{4,a}$) is used to preheat the moist incoming ambient air ($T_{1,a}$) in a heat recovery unit having a heat

recovery efficiency (ε_{HR}) of 0.9 [107]. Finally, the preheated moist air enters the sorption reactor at a temperature $T_{2,a}$. No additional humidification system is assumed. Therefore, the reactor inlet water vapor concentration is equal to the ambient concentration ($c_{2,a} = c_{1,a}$).

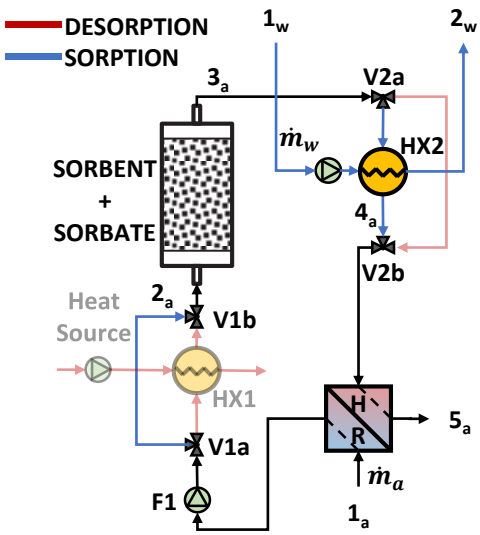

Figure 4.6: Sorption heat storage system configuration assumed during the hydration (sorption) phase.

The ambient air temperature and water vapor concentration $T_{1,a}$ and $c_{1,a}$ are taken from a period in June of a typical meteorological year weather file for Uccle (BE) [132]. It is assumed that the thermal load has a constant inlet water temperature and mass flow. The selected relevant model parameters are shown in Table 4.5.

Table 4.5: Model parameters for test H4.

Parameter	Value	Units	Description
$\dot{m}_a/\dot{m}_w$	3	-	Air to water mass flow ratio
$T_{1,w}$	10	°C	Water inlet temperature
$\varepsilon_{HX,a/w}$	0.8	-	Air/water heat exchanger effectiveness
ε_{HR}	0.9	-	Air/air heat recovery efficiency

With the abovementioned data, the aim is to estimate realistic values of the inlet reactor temperature and concentration (i.e. $T_{2,a}$ and $c_{2,a}$) after the heat recovery unit. To establish the level of preheating, preliminary values for $T_{3,a}$ are required, which are then used to estimate the values of $T_{2,a}$. $T_{3,a}$ values are estimated by assuming that the outlet reactor temperature cannot exceed the equilibrium temperature of the reaction (T_{eq}), and that all the reaction energy is transferred to the air mass flow (equation 4.12).

$$\Delta T_{lift} = \frac{c_{1,a}\Delta H_{reac}}{\rho_a c_{p,a}} \quad 4.12$$

The ideal temperature at the outlet of the reactor can then be calculated as in equation 4.13. In this equation, the inlet reactor temperature of the previous time step is used.

$$T_{3,a} = \min\left(T_{eq}, T_{2,a} + \Delta T_{lift}\right) \quad 4.13$$

The air and water temperatures at the outlet of the air-water heat exchanger HX2 ($T_{4,a}$ and $T_{2,w}$) are calculated with the heat exchanger effectiveness $\varepsilon_{HX,a/w}$. The resulting reactor inlet temperature and water vapor concentration (T_{in}= $T_{2,a}$ and c_{in}= $c_{2,a}$) are shown in Figure 4.7. The fluctuations in the water vapor concentration and temperature are the result of the natural variation of temperature and relative humidity present in the weather file over the 20 hours considered in this scenario.

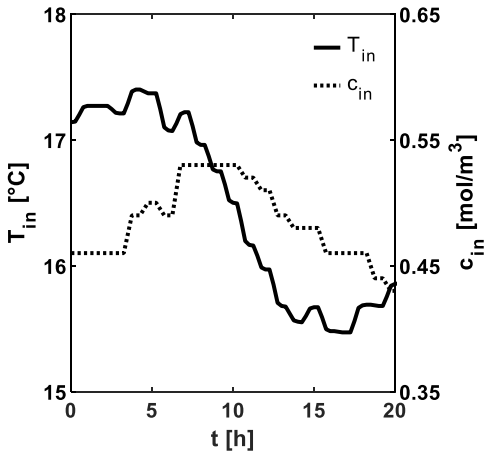

Figure 4.7: Reactor inlet temperature (T_{in}=$T_{2,a}$) and water vapor concentration (c_{in}=$c_{2,a}$) used for test H4.

The reactor inlet temperature and water vapor concentration values are determined with this procedure are then used as inputs for the compact physics-based model and for the data driven model.

4.5 Spectral model

In this section, the spectral sorption reactor model for dynamic simulations is investigated. In particular, a model based on a spectral method for the spatial discretization has been

developed. Spectral methods for a system of equations such as 4.4 - 4.7 can have spectral convergence for sufficiently smooth profiles. This allows for an accurate approximation of the equations solution with less degrees of freedom compared to a mesh-based discretization [133]. The model is developed in MATLAB® [134] and executed in Simulink®, as a representative software for dynamic systems simulations.

4.5.1 General model description

The main equations solved in the compact model are the same as in the high-fidelity model (i.e. equations 4.4 - 4.7). They can be written in their general form as in equation 4.14.

$$\begin{cases} \dfrac{\partial S}{\partial t} = A_S \dfrac{\partial S}{\partial x} + B_S \dfrac{\partial^2 S}{\partial x^2} + F \\ S(x,0) = S_0(x) \\ S(0,t) = S_{in}(t) \\ \left.\dfrac{\partial S}{\partial x}\right|_{x=L} = 0 \end{cases} \qquad 4.14$$

Where S represents one of the variables (c, T, T_{wl}, X), A_S and B_S are constant coefficients depending on the partial differential equation, F is a generic source term, which can contain a nonlinear dependency on the state variables, and $x \in [0, L]$ is the space variable of the physical domain.

Spatial discretization

The set of unsteady nonlinear advection-diffusion-reaction equations are spatially discretized using a spectral method based on the Chebyshev expansion [133] (equation 4.15), in which $\phi_k(\eta)$ is the kth order Chebyshev polynomial (equation 4.16).

$$S(\xi, t) = \sum_{k=0}^{N_M} \tilde{S}_k(t)\phi_k(\xi) \qquad 4.15$$

$$\phi_k(\xi) = \cos\big(k\, arccos(\xi)\big) \qquad 4.16$$

In equation 4.15, N_M is the expansion order of the spectral discretization scheme and $\xi \in [-1,1]$ is the computational domain in which the spectral method is defined. The transformation of the spatial physical domain into the computational domain through a linear mapping is expressed in equation 4.17.

$$\xi = \frac{2x - L}{L} \tag{4.17}$$

The expansion coefficients $\tilde{S}_k$ are evaluated via the discrete Chebyshev transform expressed in equation 4.18.

$$\tilde{S}_k = \frac{2}{N_M c_{GL,k}} \sum_{j=0}^{N_M} \left(\frac{S(\xi_j)\phi_k(\xi_j)}{c_{GL,j}} \right) \tag{4.18}$$

Here, ξ_j are the Gauss-Lobatto quadrature nodes $\xi_j = \cos(\pi j / N_M)$, and the coefficients $c_{GL,k}$ are equal to 1 if $1 \leq k \leq (N_M - 1)$ or 2 in the other cases [133]. The transformation from the spatial physical domain to the computational domain results in equation 4.19, in which the constant coefficients are grouped in the terms A'_S and B'_S.

$$\begin{cases} \dfrac{\partial S}{\partial t} = \dfrac{2A_S}{L}\dfrac{\partial S}{\partial \eta} + \dfrac{4B_S}{L^2}\dfrac{\partial^2 S}{\partial \eta^2} + F = A'_S \dfrac{\partial S}{\partial \eta} + B'_S \dfrac{\partial^2 S}{\partial \eta^2} + F \\ S(\eta, 0) = S_0(\eta) \\ S(-1, t) = S_{in}(t) \\ \left.\dfrac{\partial S}{\partial \eta}\right|_{\eta=1} = 0 \end{cases} \tag{4.19}$$

The substitution of the expansion coefficients formulation (equation 4.15) into equation 4.19 results in equation 4.20, expressed in matrix-vector form [133].

$$\frac{\partial \tilde{\boldsymbol{S}}}{\partial t} = A'_S \mathcal{D}_1 \tilde{\boldsymbol{S}} + B'_S \mathcal{D}_2 \tilde{\boldsymbol{S}} + \tilde{\boldsymbol{F}} \tag{4.20}$$

Here $\tilde{\boldsymbol{S}} = \left(\tilde{S}_0, \dots, \tilde{S}_{N_M}\right)^T$ is the Chebyshev spectrum of the general variable S, and $\mathcal{D}_1$ and $\mathcal{D}_2$ represent the discretization of the first and second spatial derivatives of equation 4.19, respectively. $\mathcal{D}_1$ and $\mathcal{D}_2$ effectively relate the spectrum $\tilde{\boldsymbol{S}}$ to its first and second spatial derivative through linear algebraic relations. In particular the coefficients of matrices $\mathcal{D}_1$ and $\mathcal{D}_2$ are a consequence of a recursive relation between the Chebyshev polynomials and their derivatives. The coefficients of matrix $\mathcal{D}_1$ have elements equal to zero except for the elements in which the sum of the row and column indexes is odd (equation 4.21). The coefficients $C_{\mathcal{D}_{ij}}$ are equal to 2 if $i = 1$, or 1 otherwise [133].

$$\mathcal{D}_{1,ij} = \frac{2}{C_{\mathcal{D}_{ij}}}(j - 1) \quad \forall \{(i + j)\ odd\ \cap\ j > (i + 1)\} \tag{4.21}$$

Concerning matrix $\mathcal{D}_2$, their nonzero elements are found in elements for which the sum of their column and row indexes is even (according to equation 4.22), except for elements in the first column, which are all zeroes [133].

$$\mathcal{D}_{2,ij} = \frac{(j-1)}{C_{\mathcal{D}_{ij}}}((j-1)^2 - (i-1)^2) \quad \forall \{(i+j)\ even\ \cap \{j > (i+1)\}\} \tag{4.22}$$

By grouping the constant coefficient matrices in matrix $\mathcal{M}$, the semi-discretized ordinary differential set of equations can be written as in equation 4.23.

$$\frac{d\tilde{\boldsymbol{S}}}{dt} = \mathcal{M}\tilde{\boldsymbol{S}} + \tilde{\boldsymbol{F}} \tag{4.23}$$

Temporal discretization

Equation 4.23 has been discretized in time using a semi-implicit Euler scheme (equation 4.24 resulting in equation 4.25), which determines the state $\tilde{\boldsymbol{S}}_{n+1}$ at time level $t_{n+1} = (n+1)\Delta t$ from the state at the previous time level $t_n = n\Delta t$. In equations 4.24, I is the identity matrix.

$$\begin{cases} \mathcal{P}\tilde{\boldsymbol{S}}_{n+1} = \tilde{\boldsymbol{G}}_n \\ \mathcal{P} = (I - \Delta t\mathcal{M}) \\ \tilde{\boldsymbol{G}}_n = \tilde{\boldsymbol{S}}_n + \Delta t\tilde{\boldsymbol{F}}_n \end{cases} \tag{4.24}$$

$$\frac{(\tilde{\boldsymbol{S}}_{n+1} - \tilde{\boldsymbol{S}}_n)}{\Delta t} = \mathcal{M}\tilde{\boldsymbol{S}}_{n+1} + \tilde{\boldsymbol{F}}_n \tag{4.25}$$

Boundary conditions

The model spatial boundary conditions are imposed according to Table 4.1. In particular, at the domain inlet a Dirichlet boundary condition is imposed while at the domain outlet a Neumann boundary condition is prescribed. In the spectral model, the boundary conditions have been implemented with the tau method, according to Canuto et al. [135]. In this approach, the modes $k = N_M - 1$ and $k = N_M$ of the system in equation 4.24 are replaced by equations 4.26.

$$\begin{cases} S(-1,t) = \sum_{k=0}^{N_M} (-1)^k \tilde{S}_k(t) = S_{in}(t) \\ \left.\frac{\partial S}{\partial \eta}\right|_{\eta=1} = \sum_{k=0}^{N_M} k^2 \tilde{S}_k(t) = 0 \end{cases} \tag{4.26}$$

4.5.2 Full system discretization

In this section, the full system of equations is discretized according to the numerical model described in section 4.5.1. Equations 4.4 - 4.6 can be rewritten in the form of equations 4.27 - 4.29.

$$\frac{\partial c}{\partial t} = A_c \frac{\partial c}{\partial x} + B_c \frac{\partial^2 c}{\partial x^2} + C_c \frac{dX}{dt} \qquad 4.27$$

$$\frac{\partial T}{\partial t} = A_T \frac{\partial T}{\partial x} + B_T \frac{\partial^2 T}{\partial x^2} + C_T \frac{dX}{dt} + D_T T + E_T T_{wl} \qquad 4.28$$

$$\frac{\partial T_{wl}}{\partial t} = B_{T_{wl}} \frac{\partial^2 T_{wl}}{\partial x^2} + D_{T_{wl}} T + E_{Twl} T_{wl} + H_{T_{wl}} \qquad 4.29$$

The constant coefficients of each equation term are displayed in Table 4.6. For example, the coefficient C_c is the table element in the third row and first column, and B_T is the element in the second row and second column.

Table 4.6: Coefficients of the spectral model according to equations 4.27 -4.29.

	Variable		
	c	T	T_w
A	$-\frac{u_a}{\varepsilon_b}$	$-\frac{u_a \rho_a c_{p,a}}{\overline{\rho c_p}}$	
B	$\frac{D_x}{\varepsilon_b}$	$\frac{\lambda_{eff}}{\overline{\rho c_p}}$	$\frac{\lambda_{wl}}{\rho_{wl} c_{p,wl}}$
C	$-\frac{(1-\varepsilon_b)\nu\, \rho_{sm} k_{LDF}}{\varepsilon_b M_{mol,sm}}$	$\frac{(1-\varepsilon_b)\nu \rho_{sm} \Delta H_{reac} k_{LDF}}{\overline{\rho c_p} M_{mol,sm}}$	
D		$\frac{-4}{\pi d_i^2 R_{th,i} \overline{\rho c_p}}$	$\frac{1}{R_{th,i} A_{wl} \rho_{wl} c_{p,wl}}$
E		$\frac{4}{\pi d_i^2 R_{th,i} \overline{\rho c_p}}$	$-\frac{R_{th,i} + R_{th,o}}{\rho_{wl} c_{p,wl} A_{wl} R_{th,o} R_{th,i}}$
H			$\frac{T_{amb}}{R_{th,o} A_{wl} \rho_{wl} c_{p,wl}}$

Concerning equation 4.7, it can be rewritten in a form that is independent of the system operating mode (sorption or desorption) according to equation 4.30.

$$\frac{\partial X}{\partial t} = k_{LDF}(X_{eq} - X) \qquad 4.30$$

Here the term $(X_{eq} - X)$ represents the general driving force that determines the reaction kinetics and the magnitude of the source terms in equations 4.4 - 4.5. The variable X_{eq} is defined according to the operating mode following equations 4.31 and 4.32 for hydration and dehydration, respectively. It can be noticed that equation 4.7 can be easily derived by substitution of equation 4.31 and 4.32 into 4.30.

$$X_{eq,s} = 1 + \frac{p_{eq}}{p_v}(X - 1) \qquad 4.31$$

$$X_{eq,d} = X\left(2 - \frac{p_{eq}}{p_v}\right) \qquad 4.32$$

Based on the coefficients in Table 4.6 and on equations 4.27 - 4.30, the matrices $\mathcal{M}$ ($\mathcal{M}_c$, $\mathcal{M}_T$, $\mathcal{M}_{T_{wl}}$, $\mathcal{M}_X$) and vectors $\widetilde{\boldsymbol{F}}_{\boldsymbol{n}}$ ($\widetilde{\boldsymbol{F}}_{c,n}$, $\widetilde{\boldsymbol{F}}_{T,n}$, $\widetilde{\boldsymbol{F}}_{T_w,n}$, $\widetilde{\boldsymbol{F}}_{X,n}$) can be expressed as indicated in Table 4.7.

Table 4.7: Matrices $\mathcal{M}$ and vectors $\widetilde{F}_n$ values, according to equations 4.24, for the discretized system of equations 4.27 - 4.30.

Variable	$\mathcal{M}$	$\widetilde{\boldsymbol{F}}_{\boldsymbol{n}}$
c	$A_c\mathcal{D}_1 + B_c\mathcal{D}_2$	$C_c(\widetilde{\boldsymbol{X}}_{eq,n} - \widetilde{\boldsymbol{X}}_{n+1})$
T	$A_T\mathcal{D}_1 + B_T\mathcal{D}_2 + D_T\mathrm{I}$	$C_T(\widetilde{\boldsymbol{X}}_{eq,n} - \widetilde{\boldsymbol{X}}_{n+1})$
T_{wl}	$B_{T_{wl}}\mathcal{D}_2 + E_{T_{wl}}\mathrm{I}$	$H_{T_{wl}}$
X	$-k_{LDF}\,\mathrm{I}$	$k_{LDF}\,\widetilde{\boldsymbol{X}}_{eq,n}$

Table 4.8: Matrices $\mathcal{P}$ and vectors G_n according to equation 4.23, for the discretized system of equations 4.27 - 4.30.

Variable	$\mathcal{P}$	$\widetilde{\boldsymbol{G}}_n$
c	$\mathrm{I} - \Delta t\mathcal{M}_c$	$\tilde{\boldsymbol{c}}_n + \Delta t C_c(\widetilde{\boldsymbol{X}}_{eq,n} - \widetilde{\boldsymbol{X}}_{n+1})$
$\begin{bmatrix} T \\ T_{wl} \end{bmatrix}$	$\begin{bmatrix} \mathrm{I} - \Delta t\,\mathcal{M}_T & \Delta t E_T\mathrm{I} \\ -\Delta t D_{T_{wl}}\mathrm{I} & \mathrm{I} - \Delta t\,\mathcal{M}_{T_{wl}} \end{bmatrix}$	$\begin{bmatrix} \widetilde{\boldsymbol{T}}_n + \Delta t C_T(\widetilde{\boldsymbol{X}}_{eq,n} - \widetilde{\boldsymbol{X}}_{n+1}) \\ \widetilde{\boldsymbol{T}}_{wl,n} + \Delta t H_{T_{wl}} \end{bmatrix}$
X	$\mathrm{I} - \Delta t\mathcal{M}_X$	$\widetilde{\boldsymbol{X}}_n + \Delta t k_{LDF}\widetilde{\boldsymbol{X}}_{eq,n}$

Finally, the fully discretized system can be expressed with the matrices $\mathcal{P}$ ($\mathcal{P}_c$, $\mathcal{P}_T$, $\mathcal{P}_{T_{wl}}$, $\mathcal{P}_X$) and the vectors $\widetilde{\boldsymbol{G}}_n$ ($\widetilde{\boldsymbol{G}}_{c,n}$, $\widetilde{\boldsymbol{G}}_{T,n}$, $\widetilde{\boldsymbol{G}}_{T_{wl},n}$, $\widetilde{\boldsymbol{G}}_{X,n}$) as in Table 4.8. In the solution process, the system written in the form of equations 4.24 is solved as a global coupled system.

Stability criterion

In order to ensure the convergence of the numerical model, an adaptive time stepping algorithm has been implemented based on the physics of the system and empirical observations of its dynamical behavior. The stability criterion leans on the assumption that instabilities originate from the evolution equation (4.4) for concentration c. This is suggested by the observed behavior of the numerical model, which showed that c was the first variable to become unstable or take negative values, especially during hydration, if a too large timestep is imposed. It can easily be noticed from equation 4.4 that, if a too large timestep is used, the nonlinear source term could take a too large negative value, which in turn can lead to a negative value of c, which is not realistic. Thus, the adaptive time stepping criterion is based on the discretization (equation 4.24) for the variable c only. The nonlinear vector equation has the form $\mathcal{P}\tilde{\boldsymbol{c}}_{n+1} = \tilde{\boldsymbol{G}}_n(\tilde{\boldsymbol{c}}_n)$. The equation can be written as in equation 4.33.

$$\tilde{\boldsymbol{c}}_{n+1} = \tilde{K}_n(\tilde{\boldsymbol{c}}_n) = \mathcal{P}^{-1}\tilde{\boldsymbol{G}}_n(\tilde{\boldsymbol{c}}_n) \qquad 4.33$$

In order for the nonlinear dynamical system to not exhibit chaotic dynamics and prevent numerical instabilities, the eigenvalues of the Jacobian matrix $\tilde{J}_K$, $\Lambda_K = eig(\tilde{J}_K) = eig\left(\frac{d\tilde{K}_n}{dc_n}\right)$, should have a magnitude $|\Lambda_K| \leq 1$. The Jacobian $\tilde{J}_K = d\tilde{K}_n/d\tilde{\boldsymbol{c}}_n$ can be approximated by $\tilde{J}_K = \mathcal{P}^{-1}d(\tilde{\boldsymbol{G}}_n\,(\tilde{\boldsymbol{c}}_n\,))/d\tilde{\boldsymbol{c}}_n$ due to the fact that the norm of $\mathcal{P}$ can be roughly equal to one for sufficiently small timesteps. Hence, the error amplification is mainly caused by the derivative of $\tilde{\boldsymbol{G}}_n$ to $\tilde{\boldsymbol{c}}_n$ $d(\tilde{\boldsymbol{G}}_n\,(\tilde{\boldsymbol{c}}_n\,))/(d\tilde{\boldsymbol{c}}_n\,)$. Therefore, to good approximation, the eigenvalues for the adaptive time stepping criterion are defined as in equation 4.34.

$$|\Lambda_G| = \left|eig\left(\frac{d\left(\boldsymbol{G}_n(\boldsymbol{c}_n)\right)}{d\boldsymbol{c}_n}\right)\right| = \left|1 - \Delta t_n C_c \frac{d\boldsymbol{X}_{eq,n}}{d\boldsymbol{c}_n}\right| \leq 1 \qquad 4.34$$

In equation 4.34, the partial derivative $d\boldsymbol{X}_{eq,n}/d\boldsymbol{c}_n$ is evaluated in the physical domain at the Gauss - Lobatto nodes, based on equations 4.30 - 4.32, and Δt_n is the timestep between the state at time t_n and the state at time t_{n+1}. Therefore, the final stability criterion can be expressed according to equation 4.35, in which the maximum value of the partial derivative evaluated at the quadrature nodes is considered for the timestep limitation.

$$\Delta t_n = \frac{2}{C_c \max\left(\frac{d\boldsymbol{X}_{eq,n}}{d\boldsymbol{c}_n}\right)} \qquad 4.35$$

Moreover, by calculating the partial derivative $(d\boldsymbol{X}_{eq,n})/d\boldsymbol{c}_n$ for both hydration and dehydration operating modes, the timestep proportionality with respect to the three variables

c, T, and X is shown in equations 4.36 and 4.37, for a node subject to hydration (Δt_s) or dehydration (Δt_d), respectively. For both operating modes, the direct proportionality with c^2 clearly shows that, when a low water vapor concentration is present, the timestep reduces, preventing the concentration to take negative values.

$$\Delta t_s \propto \frac{c^2 T}{(1-X)p_{eq}(T)} \tag{4.36}$$

$$\Delta t_d \propto \frac{c^2 T}{X p_{eq}(T)} \tag{4.37}$$

Finally, also an upper limit is imposed to the timestep, which is equal to the model sampling time (20 s), i.e. the timesteps at which the model solution is stored. An upper bound on the timestep value is necessary because, according to equations 4.36 and 4.37, the timestep size could have an infinite value at the end of both hydration ($X = 1$) and dehydration ($X = 0$).

4.5.3 Spectral model performance

In this section, the spectral model performance is evaluated with the tests presented in section 4.4, in which the high-fidelity model outputs are compared with the compact model solved with 64 modes (i.e. N_M = 64). The choice of using 64 modes is the result of a compromise, based on preliminary simulations, between accuracy and computational cost. Tests H1, H2, D1, and D2 are described in detail in this section. Results for tests H3 and H4 are shown in Appendix E. As a performance indicator, in order to compare the two models, the mean squared error is used (equation 4.38). Here, Q is the total number of data points in the two simulations, and y_{COMSOL} and $y_{SPECTRAL}$ are the outputs from the COMSOL model and the spectral model, respectively.

$$MSE = \frac{1}{Q}\sum_{q=1}^{Q}\left(y_{COMSOL_q} - y_{SPECTRAL_q}\right)^2 \tag{4.38}$$

Test H1 – Step-wise concentration increment

In this first test, the response to a step function in the inlet water vapor concentration is calculated. During a hydration simulation (Figure 4.8), the input water vapor concentration was kept equal to 0.32 mol/m^3 during the first 8 hours and then is increased in a single step to 0.47 up to the end of the experiment. The inlet temperature has been kept constant at 10°C. Consequently, the reaction rate increases due to a higher water vapor pressure entering in the reactor. The expected behavior of the sorption reactor is that it is discharged at a higher rate due to the reaction rate increase. Therefore, when the concentration increases, the slope of the state of charge becomes steeper (Figure 4.8 right). For the same reason, the outlet

temperature increases (Figure 4.8 left). Once that the reaction front approaches the reactor outlet and the SOC approaches to zero, the outlet temperature profile starts to decrease rapidly until it reaches the inlet temperature value, meaning that no more energy is generated inside the packed bed and the discharge phase is complete. From Figure 4.8, it can be seen that the models are in good agreement. In particular, for the SOC, an MSE of $9.2 \cdot 10^{-7}$ is calculated while for the outlet temperature, an MSE of $4.5 \cdot 10^{-3}$ °C^2 is present.

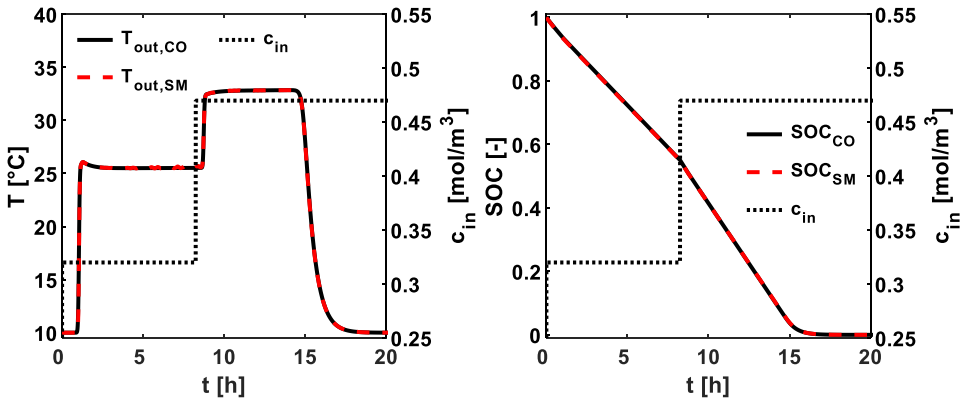

Figure 4.8: Test H1 for the spectral model. CO = COMSOL model. SM = Spectral model. Left: Reactor outlet temperatures. Right: SOC. Black solid line: COMSOL model. Red dashed line: spectral model. Black dotted line: inlet water vapor concentration. Inlet temperature T_{in}: 10 °C. MSE_{SOC} = $9.2 \cdot 10^{-7}$. MSE_{Tout} = $4.5 \cdot 10^{-3}$ °C^2.

The number of modes N_M considered in the system discretization directly affects the quality of the solution. In Figure 4.9, test H1 is carried out with the spectral model considering different number of modes (48, 64 and 128). The presence of local oscillations in the outlet temperature during the two temperature plateaus can be seen especially for the model with 48 modes. This is due to the Gibbs phenomenon [135], which is reduced by including a higher number of modes in the system discretization at the cost of computational time. The reduction of oscillations in the outlet temperature also has an impact on the SOC estimation leading to a better accuracy (Figure 4.9 right). In particular, the MSE_{SOC} decreases from $5.1 \cdot 10^{-6}$ to $1.1 \cdot 10^{-6}$ and the MSE_{Tout} from $6.4 \cdot 10^{-2}$ °C^2 to $3.5 \cdot 10^{-3}$ °C^2 using 48 and 128 modes, respectively. As a compromise between accuracy and computational cost, 64 modes are used in the spectral model for the rest of this analysis.

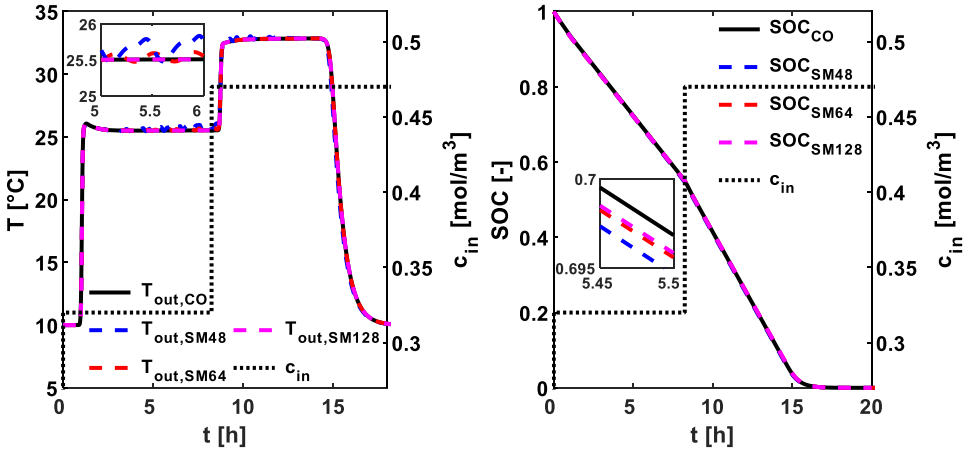

Figure 4.9: Test H1 performed with 48 (dashed blue line), 64 (dashed red line) and 128 (dashed magenta line) modes. CO = COMSOL model. SM = Spectral model. Left: T_{out}. Right: SOC.

Test H2 – Step-wise temperature increment

In test H2, the inlet temperature T_{in} has been increased in a single step as for the inlet concentration c_{in}, in test H1. The concentration has been kept constant to 0.4 mol/m^3 throughout the whole experiment. The temperature has been increased in a single step from 15 °C to 23 °C after the first 7 hours of the test.

The results are shown in Figure 4.10. In Figure 4.10 left, the outlet temperature has a first increase from the ambient temperature of 10 °C to approximately 33 °C. Then, the outlet temperature increases up to approximately 39 °C due to the inlet temperature increase. An increase in the inlet temperature leads to an increase in equilibrium water vapor pressure, which in turn leads to smaller source terms in equations 4.4 and 4.5. This can be easily verified by looking at the behavior of the term dX/dt and the role of the ratio $(p_{eq}\,(T))/(p_v\,(c,T))$ in equation 4.7 and Figure 4.2 right. Therefore, a decrease in the discharging rate with an increasing inlet temperature is expected. For the abovementioned reasons, the outlet temperature increases but the temperature lift within the reactor is smaller. Before the inlet temperature increase, a temperature lift of 18 °C was achieved while, after the temperature increase, a temperature lift of 15 °C is present. Concerning the MSE, for the SOC and the outlet temperature an MSE of $9.5 \cdot 10^{-7}$ and $9.1 \cdot 10^{-3}$ °C^2 are calculated, respectively.

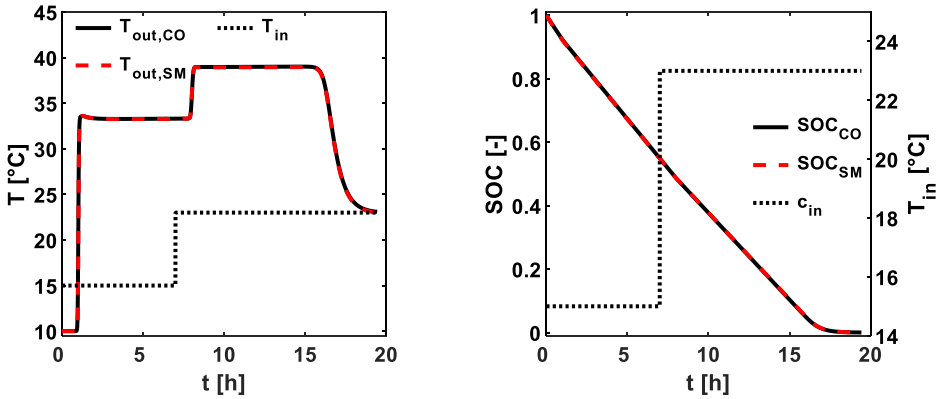

Figure 4.10: Test H2 for the spectral model. CO = COMSOL model. SM = Spectral model. Left: Reactor outlet temperatures. Right: SOC. Black solid line: COMSOL model. Red dashed line: spectral model. Black dotted line: inlet temperature. Inlet water vapor concentration c_{in}: 0.4 mol/m^3. MSE_{SOC} = 9.5·10^{-7}. MSE_{Tout}= 9.1·10^{-3} °C^2.

Test D1 – Step-wise concentration increment

During a dehydration experiment, the concentration has been decreased in a single step from 0.55 to 0.25 mol/m^3 after 3.75 hours, approximately halfway the dehydration process. The temperature has been kept constant at 110 °C. Figure 4.11 shows that the outlet temperature plateau after the first temperature increase slightly decreases once that the inlet water vapor concentration is decreased after 3.75 hours. This is because the equilibrium temperature of the reaction decreases due to a lower water vapor concentration after the reaction front, where the reaction still has to take place, as already described for Figure 4.5 left.

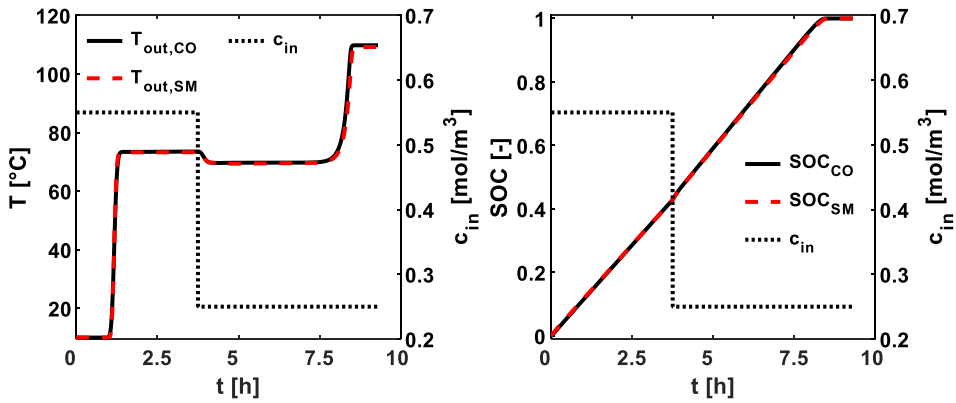

Figure 4.11: Test D1 for the spectral model. CO = COMSOL model. SM = Spectral model. Left: Reactor outlet temperature from the COMSOL model (black solid line) and the spectral model (red dashed line), and inlet temperature (black dotted line). Inlet temperature T_{in}: 110 °C. MSE_{SOC} = 8.9·10^{-6}. MSE_{Tout}= 1.12 °C^2.

From Figure 4.11, it can be noticed that the results of the spectral model are in good agreement with the COMSOL model. The MSE for the SOC and outlet temperature are $8.9 \cdot 10^{-6}$ and 1.12 °C^2, respectively.

Test D2 – Step-wise temperature increment

The test consisted of increasing the inlet temperature from 90 °C to 130 °C after 4.75 hours and keeping the water vapor concentration constant at 0.35 mol/m^3. The MSE for the SOC and outlet temperature are $4.7 \cdot 10^{-6}$ and 1.05 °C^2, respectively. A delay can be noticed between the input temperature change and the outputs change (SOC and T_{out}). The reason is that the inlet temperature change has first to propagate through the reactor bed up to the reaction front in order to have an effect on the sorption reaction and, consequently, on the outputs.

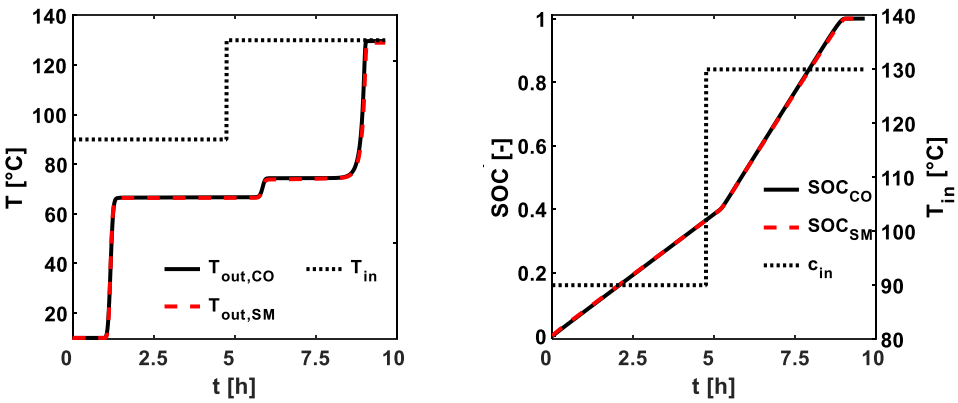

Figure 4.12: Test D2 for the spectral model. CO = COMSOL model. SM = Spectral model. Left: Reactor outlet temperature from the COMSOL model (black solid line) and the spectral model (red dashed line), and inlet temperature (black dotted line). Inlet water vapor concentration c_{in}: 0.35 mol/m^3. MSE_{SOC} = 4.75·10^{-6}. MSE_{Tout}= 1.05 °C^2.

Computational cost of the spectral model

Figure 4.13 left shows the average timestep size (Δt_{mean}) evolution over the six tests. On the horizontal axis, the normalized simulation time (t_{NORM}) with respect to each test simulation time is shown. Due to memory limitations, the timestep size selected by the adaptive timestep technique has been averaged (Δt_{mean}) every 20 seconds, in Figure 4.13 left, and the state variables solution is stored every 20 seconds. In general, dehydration tests have larger timesteps compared to hydration tests. At the beginning of the hydration tests, the timestep is in the order of $2 \cdot 10^{-3}$ s while for the dehydration tests it is approximately 10^{-2} s. This is mainly due to the low values of vapor concentration during the hydration simulation, which restricts the timestep size to lower values (see equations 4.36 - 4.37) according to the stability criterion (4.35).

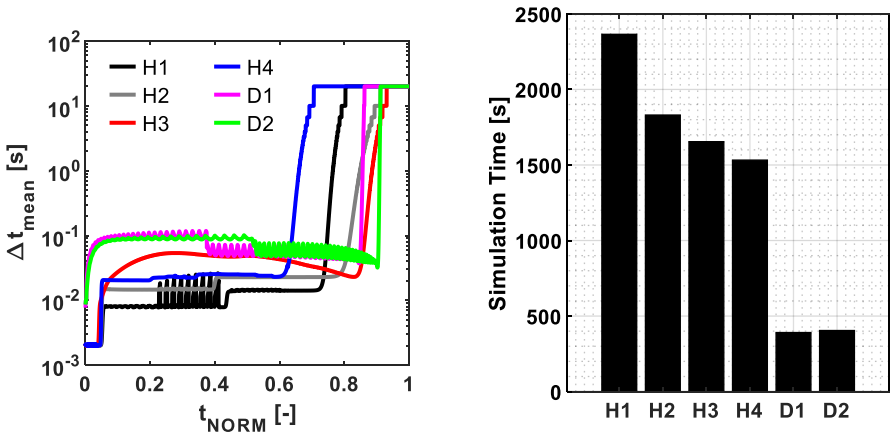

Figure 4.13: Left: Timestep size evolution during the six tests. Right: Simulation time of the spectral model for the six tests. Black bars: simulation time. Grey squares: average simulation time per timestep.

Finally, in Figure 4.13 right, the simulation time of the six tests solved with the spectral model is shown. The model has been solved on a computer with an Intel® Core™ i7-7820HQ CPU and 32 GB of RAM. It can be seen that hydration simulations required between 1500 s (H4) and approximately 2500 s (H1) while dehydration simulations were faster, requiring less than 500 s for each test.

4.6 Data-driven model

The aim of this section is to investigate the capabilities of a data-driven model based on neural networks for modeling the sorption system described in section 4.2. The model takes as inputs the inlet temperature (T_{in}), the inlet sorbate concentration (c_{in}), the reactor state of charge (SOC) at the previous timestep, and it returns as outputs the reactor state of charge at the current timestep and the reactor outlet temperature (T_{out}).

4.6.1 Introduction on neural networks

Neural networks are machine learning models used mainly to classify or predict data. The model architecture, instead of being based on physical laws (i.e. transport phenomena equations), is created starting from data and learning rules [136]. That is, a neural network architecture is trained with data through a training algorithm to predict a subsequent set of data. The basic fundamental concept in neural networks is the single neuron model [137] (Figure 4.14, right). The input vector $\boldsymbol{p}_{NN}$ consisting of J elements from the previous layer or, if it is the first layer, from the input data layer, are weighted with the weights $\boldsymbol{w}_{NN}$ and, together with a neuron bias b_{NN}, they are summed and fed as an argument to an activation function f_{NN}. The output of the activation function is the neuron output a_{NN} (equation 4.39).

$$a_{NN} = f_{NN}\left(\sum_{j=1}^{J}\left(w_{NN,j}p_{NN,j}\right) + b_{NN}\right) \qquad 4.39$$

The activation function f_{NN} is usually selected based on the knowledge about the problem and the data. It is important to notice that, in this work, multiple neurons in a network layer have the same activation function i.e. all the neurons in a network layer have the same activation function but different layers can have different activation functions within a network architecture. When multiple layers of neurons are employed in a network architecture (Figure 4.14 left), the layer whose outputs are the output of the network is the output layer, while the layers between the input and output layers are the hidden layers. In a multi-layer architecture, the number of inputs in the first layer (input layer) J and the number of outputs in the last layer (output layer) are dictated by the problem specifications. In a classification problem with a predetermined number of output categories, the number of neurons in the output layer is equal to the number of output categories. In a regression problem, in which the value of a variable quantity should be predicted, only one output neuron is present.

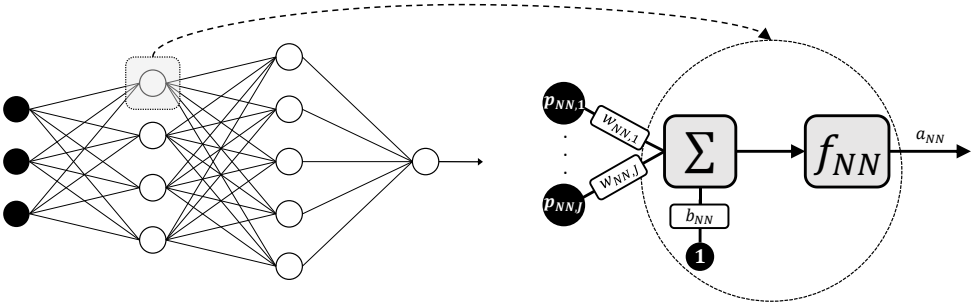

Figure 4.14: Left: Conceptual scheme of deep neural network with three inputs in the input layer, two hidden layers, and one output in the output layer. Right: conceptual scheme of a multi-input neuron model for a single layer.

In general, increasing the number of neurons per layer improves the capability of the network to approximate more complex phenomena, and adding hidden layers improves the capability of the network to take better into account nonlinear relations among the inputs. The optimal choice for the number of hidden layers and number of neurons in each layer is problem-dependent and a systematic approach is still a matter of research (e.g. [138,139]). A common approach is to train multiple neural networks and decide which architecture suits the problem best, based on a performance indicator. Concerning the number of hidden layers, it is unusual to exceed two or three hidden layers. Concerning the number of neurons per layer, a systematic trial and test procedure is often used. Multiple network architectures exist [137,140] in which, for example, the input layer is connected also partially to some or all of

the hidden layers (cascade-forward networks), or the outputs of the network are used as inputs for the next outputs estimation (autoregressive neural networks).

4.6.2 Neural networks applied to energy storage

In past studies, neural networks were used successfully to tackle research problems involving energy storage, energy efficiency related applications, and heat transfer [141] also with porous media involved [142]. The accuracy of these models, when an experimental dataset was used for training, was comparable or even higher compared to physics-based models. In particular, a higher accuracy was found in works related to energy efficiency improvement in buildings from Buratti et al. [143]. The authors used a neural network with one hidden layer consisting of 79 neurons, which was able to predict the indoor temperature given the outdoor climate conditions and the characteristics of the building envelope. The model based on the neural network outperformed a physics-based model based in terms of mean squared error. Among heat transfer studies, Ermis et al. [144] used a feed forward neural network to analyze the heat transfer process of a finned tube in which Ethyl-alcohol was flowing at low temperature at the inner side and water was solidifying on the outer surface of the tube. The neural network inputs were the heat transfer area, the Reynolds number, the inlet temperature of the inner fluid, and the time. The output was the amount of stored thermal energy in the water. They found a better agreement with experimental data for their neural network model than for a physics-based numerical model in terms of absolute mean error, standard deviations in the relative error, and absolute fraction of variance. Lecoueche et al. [145] ,who used 50 identical neural networks connected in series to simulate a single tube heat exchanger with constant tube outer surface temperature, found a difference between a physical model solving the energy balance of the inner fluid and the heat diffusion equation along the tube wall, and the neural network model lower than 1 % in terms of fluid outlet temperature. The authors trained the neural network model with a training dataset produced with the physical model and tested its accuracy with a validation dataset.

Data-driven models were also used to predict intrinsic energy storage characteristics such as performance degradation over the storage lifetime. Richardson et al. [146] employed gaussian process regression to forecast Lithium-ion batteries state of health instead of conventional modelling approaches with more computationally expensive electrochemical or equivalent circuit models. The authors predicted the capacity values of batteries until the battery end of life (EoL), and also the EoL itself. The dataset consisted of strongly correlated data of batteries cycled at equivalent thermal conditions and current profiles. The root mean squared error on the capacity prediction of the best performing model was in the order of 0.025, and EoL prediction root mean squared error was 4.57 days.

Other storage characteristics requiring a previous state of the system, such as the temperature evolution within a sensible heat storage, were also successfully modeled. Géczy-Víg et al. [147] developed a neural network model to estimate, with a five minutes resolution, the

temperature at different locations in a water storage tank within a solar thermal system. Among the main neural network inputs at the current timestep (e.g. mass flow rates of load and solar collector, solar irradiation, etc.) the temperature at the same locations in the previous timestep was used. The model had an average deviation of 0.24 °C over the entire validation dataset. The same approach was used for a latent heat storage system by Ghani et al. [148], who used a neural network to predict the outlet fluid temperature of the storage given, among other parameters, the outlet temperature at the previous state. By using a test dataset (i.e. a dataset not used for training the neural network) the authors found an error based on the energy balance of 5.1 % and 7.1 % for charge and discharge phases, respectively. Finally, within the field of sorption cooling, a recent study from Jani et al. [149] addressed the use of neural networks for predicting the performance of solid desiccant cooling systems. Concerning sorption heat storage, various physics-based reactor models have been developed in the past regarding this technology (e.g. [121,124,150–152]). However, most of the research is still focused on challenges at material- and reactor-scale. For system-scale investigations, data-driven models can be useful to decrease the modeling computational cost, while still providing an acceptable accuracy. However, there seems to be a lack of investigations about data-driven models regarding this technology. Therefore, this work aims to tackle for the first time the topic of sorption heat storage from a data-driven perspective.

4.6.3 NARX-FFNN model

Architecture selection

For the determination of the sorption reactor state of charge, the neural network architecture was selected considering that the state of charge at the previous timestep (SOC_{t-1}), together with the inputs at the previous timestep ($c_{in,t-1}, T_{in,t-1}$), define the state of charge at the current timestep (SOC_t), according to equation 4.40.

$$SOC_t = SOC_{t-1} + \Delta SOC_{t-1\rightarrow t}(c_{in,t-1}, T_{in,t-1}) \qquad 4.40$$

Therefore, the selected neural network architecture should have autoregressive capabilities to include the previous output value as an input for the current output estimation, together with additional inputs representing the inlet temperature and water vapor concentration. The abovementioned desired features are present in a NARX (nonlinear autoregressive network with exogenous inputs) architecture, which has been selected to estimate the SOC of the sorption reactor. The activation function in the hidden layers is chosen to be the saturating linear transfer function, which performed best in preliminary investigations compared to other investigated activation functions such as the more commonly used hyperbolic tangent sigmoid transfer function. For the output layer, a linear transfer function is used.

For the architecture of the neural network that is used to estimate the sorption reactor outlet temperature, it has been assumed that the response time of the system outputs due to input variations is short compared to the simulation timesteps (900 s). Therefore, the output in the previous timesteps is not considered, and autoregressive capabilities are not required for this neural network architecture. The inputs in the previous timestep ($c_{in,t-1}, T_{in,t-1}, SOC_{t-1}$) are used to estimate the reactor outlet temperature for the current timestep ($T_{out,t}$). With the abovementioned considerations, a FFNN (feedforward neural network) has been selected as architecture. The activation function in the hidden layers is the hyperbolic tangent sigmoid transfer function, which is one of the possible functions that can be used in the hidden layers satisfying the requirements of being nonlinear, bounded, and monotonic. For the output layer, a linear transfer function is used. The sorption reactor model based on the two neural networks is conceptually shown in Figure 4.15, and this architecture is used for both hydration and dehydration modes. The output of the NARX is used as input for the FFNN for the reactor outlet temperature estimation. From the implementation perspective, the two networks do not have to be interconnected if the inputs (c_{in}, T_{in}) are already known and prescribed a priori over the time domain. On the other hand, in case of a control problem in which real time decisions must be made, the two networks must be interconnected so that at every new timestep the current state of charge can serve as input for the FFNN. For each operating mode (hydration and dehydration) the most suitable NARX and FFNN in terms of hidden layers and neurons number will be chosen, as will be explained later in this chapter.

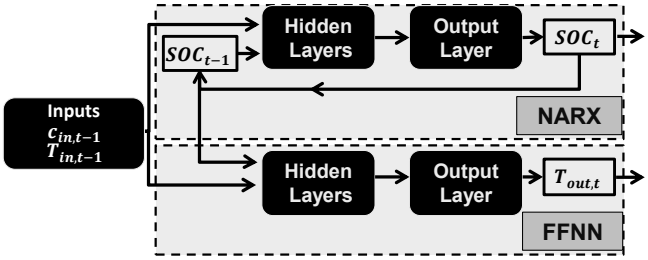

Figure 4.15: Conceptual sorption reactor model based on neural networks

Performance indicator

The performance indicator is the quantity that, during the training procedure, should be minimized by adjusting the network parameters. It is based on the difference between the neural network outputs and the COMSOL model outputs (targets). In this work, the mean squared error (MSE) is used, as for the spectral model (section 4.3), and it is defined for a single output as in equation 4.41.

$$MSE = \frac{1}{Q}\sum_{q=1}^{Q}\left(y_{COMSOL,q} - y_{NN,q}\right)^2 \qquad 4.41$$

Where Q is the overall number of elements in the dataset, $y_{COMSOL,q}$ is the target of the qth data point and $y_{NN,q}$ is the output of the neural network of the qth data point.

Training procedure

The training algorithm used in this work is the Levenberg-Marquardt algorithm [153,154], a modified version of the backpropagation algorithm [155]. Moreover, Bayesian regularization has been used to improve the generalization capabilities of the neural networks and avoid overfitting [137,156,157]. The model development has been carried out in MATLAB® [134] with the Neural Network Toolbox [158].

Several neural networks were created and trained in a systematic procedure on a cluster node with 16 Intel® Xeon® CPU E5-2670. The number of neurons was varied according to the values in the set {2,3,5,7,10,15,20,25}. The values in the abovementioned set have been chosen empirically, and they have a higher resolution especially when the number of neurons is low (i.e. {2,3,5,7}), in which the training time would be shorter as well. The number of hidden layers was varied from 1 to 4. All the combinations of the abovementioned number of neurons and hidden layers were investigated for each neural network type (NARX and FFNN) and for each operating mode (hydration and dehydration).

The initial weights assigned to each neural network are based on the random number generator of the software, and they can influence the final performance of the trained neural network. To minimize the influence of the initially random weights, the same neural network is trained ten times with different random number generator seeds, and the one with the best performance indicator (MSE) is selected.

The input data for the neural networks training and validation have been produced with the high-fidelity model described in section 4.3. Several hydration and dehydration simulations have been performed to obtain a dataset of inputs and outputs within a range of expected operating conditions for hydration and dehydration modes (Table 4.9). The minimum and maximum values have been selected within a range of realistic boundary conditions for both hydration and dehydration modes. In particular, for dehydration, temperatures 70 °C – 150 °C are selected to simulate either a low/medium temperature waste heat source or a highly efficient solar thermal collector system. For hydration, an inflow temperature within the range 10 – 45 ° C is selected, assuming that either ambient air is used directly, or that a heat recovery unit is present to preheat the inlet air.

The boundaries for the water vapor concentration have also been selected within realistic operating conditions. For hydration, slightly higher values have been selected compared to the dehydration case assuming the possibility to have a humidification unit before the reactor inlet.

Table 4.9: Datasets of hydration (H) and dehydration (D) modes. c_{in} is expressed in [mol/m^3] and T_{in} in °C.

			Min	Step	Max	n° simulations
H	**Training dataset**	T_{in}	10	5	45	64
		c_{in}	0.30	0.05	0.65	
	Validation dataset	T_{in}	12.5	5	42.5	49
		c_{in}	0.325	0.05	0.625	
D	**Training dataset**	T_{in}	70	10	150	72
		c_{in}	0.20	0.05	0.55	
	Validation dataset	T_{in}	75	10	14	56
		c_{in}	0.225	0.05	0.525	

Two data sets have been produced for each operating mode. The training dataset was used during the training procedure of the neural networks while the validation dataset was used as an additional set of data. The validation dataset consists of intermediate operating conditions within the operating condition boundaries set by the extremes of the training dataset. For the neural network selection, the MSE is calculated from the validation dataset, which is a completely new set of data that has not been used for the neural network training. This procedure avoids the overfitting problem, i.e. having a neural network that performs well with the training data, but it poorly represents data not used for training.

Neural networks selection

The neural networks were trained with the training datasets. The training algorithm makes use internally of the MSE calculated with the training dataset. However, as already mentioned in the previous paragraph, the selection is made based on the validation dataset. In Figure 4.16, the results in terms of MSE for the neural network selection are displayed for both SOC and T_{out} in both hydration and dehydration mode. According to Figure 4.16 top and middle-top (for hydration and dehydration respectively), the best performing neural networks for the SOC estimation consist of a network with 1 hidden layers with 10 neurons in each layer for the hydration mode, and with 1 hidden layers with 20 neurons in each layer for the dehydration mode, respectively. For the outlet temperature estimation (Figure 4.16 middle-bottom and bottom), a neural network consisting of 3 hidden layers and 25 neurons for hydration mode and 4 hidden layers and 7 neurons for dehydration mode performed best.

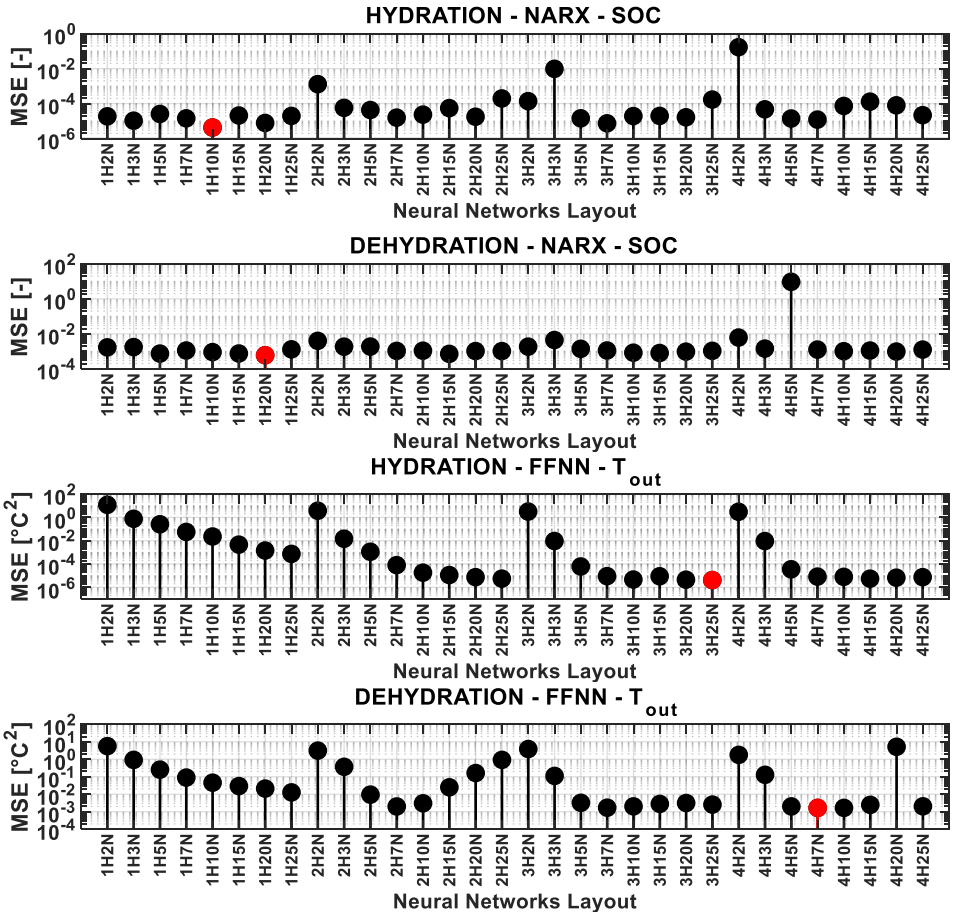

Figure 4.16: MSE values for the investigated neural network architectures. From top to bottom: SOC in hydration mode, SOC in dehydration mode, T_{out} in hydration mode, and T_{out} in dehydration mode.

Neural networks model performance

In the following section, the model performance in the tests performed (Table 4.4) is assessed through the MSE value for the SOC (MSE_{SOC}) and T_{out} (MSE_{Tout}). In order to track also the SOC error propagation in the T_{out} estimation, an additional MSE ($MSE_{Tout,SOC-CO}$) is calculated by predicting the outlet temperature of the sorption reactor using as input the SOC values from the COMSOL model instead of the SOC values from the neural networks model. This last error estimation gives an indication about the individual prediction accuracy of the neural network for the outlet temperature estimation. By comparing MSE_{Tout} and $MSE_{Tout,SOC-CO}$, the impact of the SOC prediction accuracy on T_{out} can be assessed.

Test H1 – Step-wise concentration increment

The COMSOL and the neural networks models are in good agreement. The MSE for the SOC is $8.5 \cdot 10^{-5}$, while the MSE for the outlet temperature is 1.6 °C^2.

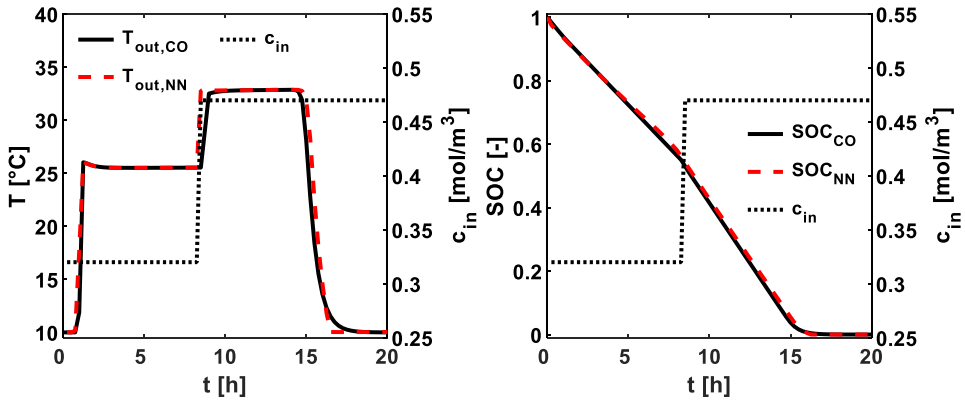

Figure 4.17: Test H1 with water vapor concentration change during hydration experiment. CO = COMSOL model. NN = Neural networks model. MSE_{SOC}= 8.5·10^{-5}. MSE_{Tout}=1.6 °C^2. $MSE_{Tout,SOC-CO}$= 0.6 °C^2.

The error in the outlet temperature estimation from the FFNN is partially a result of the error propagation of the SOC estimation from the NARX. By using the COMSOL SOC values, it is found that the resulting $MSE_{Tout,SOC-CO}$ is lower (0.6 °C^2).

Finally, it has to be remembered that the neural networks have been selected based on their performance for the hydrations in the validation dataset, and not based on this specific test condition. Therefore, there might be a more suitable neural network that reproduces better this test. In this case, it has been found that a neural network with 3 hidden layers and 3 neurons (3H3N) leads to a slightly better estimation of the outlet temperature of the reactor, especially towards the end of the test (Figure 4.18).

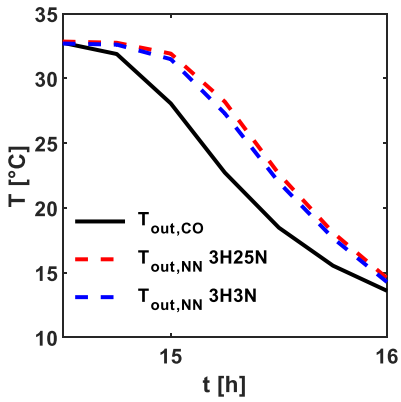

Figure 4.18: Detail from test H2 in which the neural network 3H3N would perform better than 3H25N, selected according to the systematic selection procedure. CO = COMSOL model. NN = Neural networks model.

However, it is impractical to select the most representative network architecture for a specific experiment. The selected neural networks for the model should indeed cover a wide range of operating conditions with sufficient accuracy. By considering that the outlet temperature error caused by the SOC error propagation, assuming a full hydration experiment, is caused by only few timesteps in which SOC values are smaller than 0.05, from a practical perspective this discrepancy is considered acceptable. The same considerations apply also for the other tests.

Test H2 – Step-wise temperature increment

The comparison between the COMSOL model (Figure 4.19) and the neural networks model resulted in an MSE for the SOC of $5.1 \cdot 10^{-5}$, and an MSE for the outlet temperature of 1.9 °C^2. A relatively large discrepancy between the target temperature and the temperature estimated from the neural networks model is present at the moment in which the inlet temperature is changed. The reason of this discrepancy resides in the intrinsic limitation of the feed forward neural network architecture used for the outlet temperature estimation. The FFNN architecture is not considering the past values of the output (i.e. the past state of the reactor); therefore, the thermal inertia of the packed bed is not considered (i.e. a change in the input values immediately results in a change of the output values). Moreover, also the SOC profile shows a discrepancy due to the similar reason. In fact, the neural network architecture used considers the previous neural network SOC output as feedback input, but it is not considering the past values of the inlet temperature and concentration inputs.

The importance of this feature depends on the magnitude of the timesteps, the magnitude of the inlet temperature variation rate, and the acceptable errors sizes. Also, for hydration experiments, the output discrepancy depends on the point of the hydration at which the input temperature changes. The later the input temperature varies during the experiment (i.e. smaller SOC values and reaction front further from the reactor inlet) the larger will be the output discrepancy (i.e. effect of reactor thermal inertia). In Figure 4.20 left, test H2 is repeated by varying the moment in time where the step-wise inlet temperature change is applied. In Figure 4.20 right, it is shown that the outputs discrepancy is larger for step-wise changes applied later in the hydration process. Furthermore, also in this experiment, the SOC error propagation into the outlet temperature estimation has a contribution of roughly one third of MSE_{Tout}.

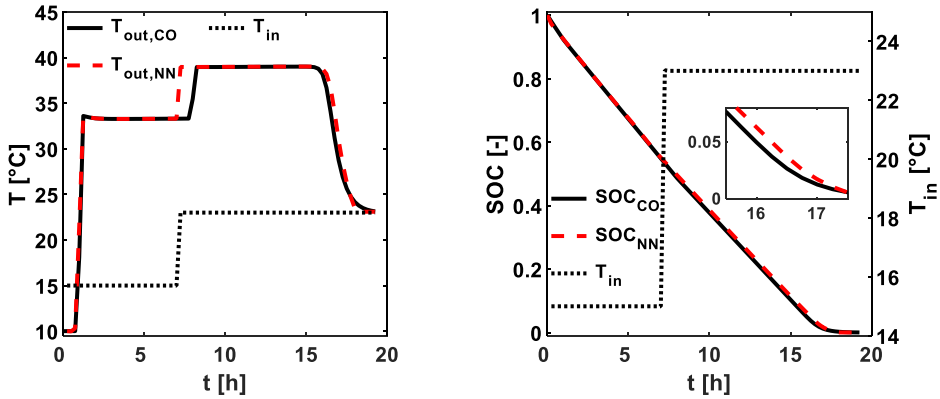

Figure 4.19: Test H2 with temperature change during hydration experiment. CO = COMSOL model. NN = Neural networks model. MSE_{SOC}= 5.1·10^{-5}. MSE_{Tout}= 1.9 °C^2. $MSE_{Tout,SOC-CO}$= 1.4 °C^2.

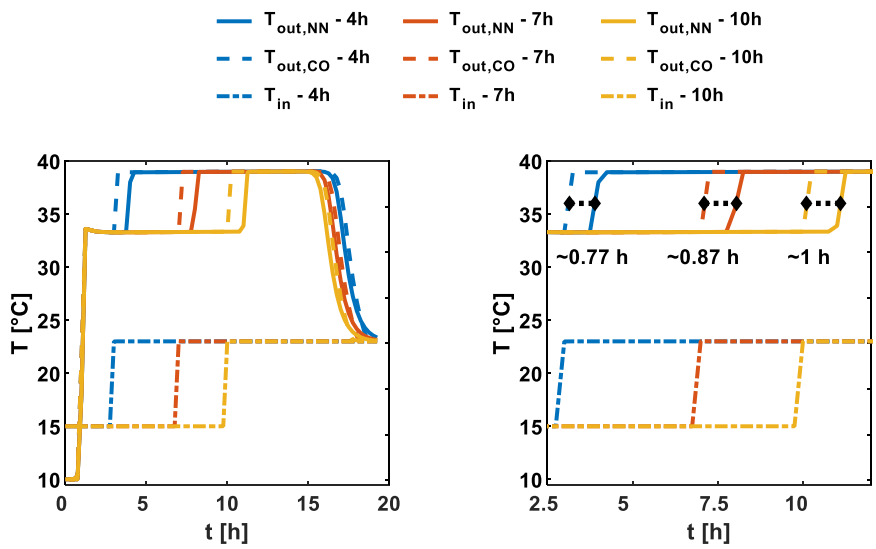

Figure 4.20: Left: example of outputs discrepancy due to the thermal inertia effect. Test H2 repeated with step-wise inlet temperature changes after 4, 7, and 10 hours from the beginning of the hydration. Right: zoomed version of the left figure between 2.5 h. and 12 h. CO = COMSOL model. NN = Neural networks model.

Test H3 – Fully variable temperature and concentration

The inlet concentration and temperatures have been varied continuously and randomly, within the boundary conditions of the training set (Table 4.9), see also Figure 4.21.

The state of charge profile is in a good agreement with the target value, with an MSE_{SOC} of 1.7·10^{-4}. The outlet temperature profile shows discrepancies in the presence of large

variations in the inlet temperature, especially in the second half of the hydration process. The reason is identical to the previous experiment. An abrupt inlet temperature variation especially when the reaction front is far from the reactor inlet (i.e. larger absolute heat capacity of the already reacted portion of the packed bed) is a source of error because the thermal inertia of the reactor is not considered in the FFNN. The MSE for the outlet temperature profile is 3.3 °C^2. The impact of the SOC error on the outlet temperature is not dominant since MSE_{Tout} and $MSE_{Tout,SOC-CO}$ are similar. The main source of error in this test happens approximately at t = 15 h, when both inputs (T_{in} and c_{in}) have simultaneously a large variation.

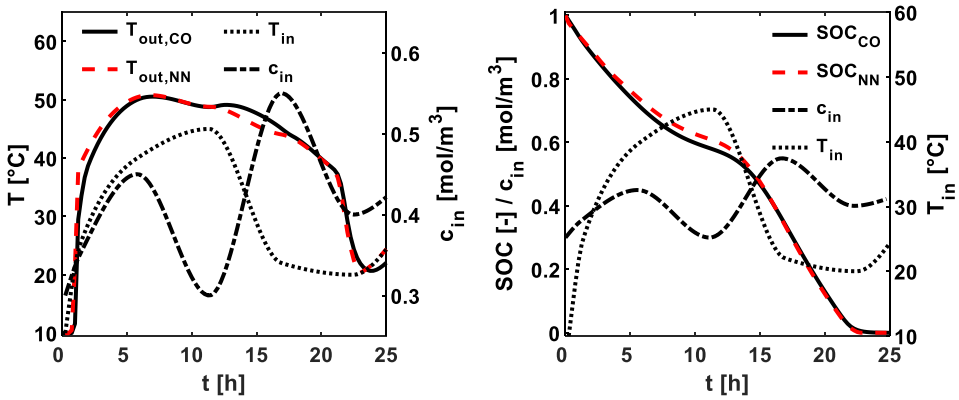

Figure 4.21: Test H3 with temperature and concentration changes during hydration experiment. CO = COMSOL model. NN = Neural networks model. MSE_{SOC}= 1.7·10^{-4}. MSE_{Tout}= 3.3 °C^2. $MSE_{Tout,SOC-CO}$= 2.6°C^2.

Test H4 – Realistic operating conditions

From Figure 4.22 and the MSE values for both the SOC and the outlet temperature, it can be noticed how the temperature profile predicted by the neural networks model matches much better with the target temperature profile compared to the previous dynamic tests. The main reason is that the variation in both the magnitude and the frequency of the inlet temperature input is reduced. This results in a low MSE for the outlet temperature (2.1·10^{-1} °C^2). In this test, the water vapor concentration depends directly on the outer conditions. On the other hand, the inlet temperature variation depends also on the heat recovery unit efficiency and on the air temperature after the thermal load ($T_{4,a}$). In real systems, the heat recovery efficiency can vary substantially during the system operation and be far from the nominal one [107].

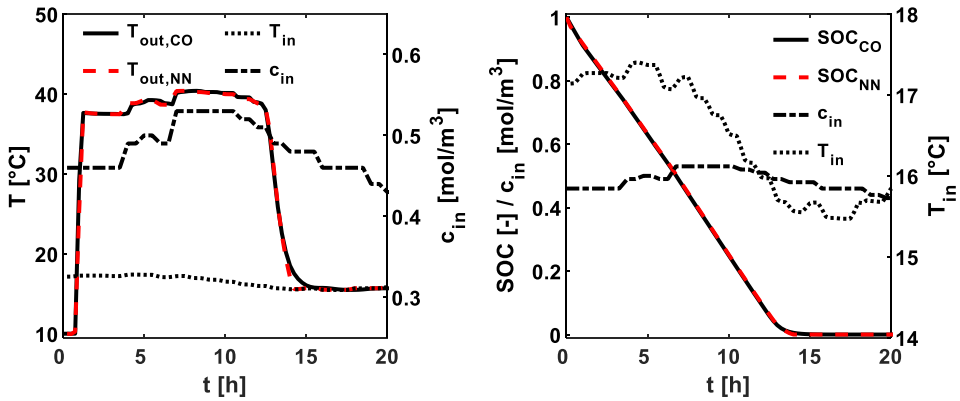

Figure 4.22: Test H4 with temperature and concentration changes during hydration experiment. CO = COMSOL model. NN = Neural networks model. MSE_{SOC} = 3.6·10^{-6}. MSE_{Tout} = 2.1·10^{-1} °C. $MSE_{Tout,SOC-CO}$= 0.6·10^{-1} °C^2.

Test D1 – Step-wise concentration increment

The results in Figure 4.23 show that, as for the same tests in hydration mode, there is a good agreement in terms of outlet temperature and state of charge profiles compared to the COMSOL model. A discrepancy is visible almost at the beginning of the dehydration process, in which a large temperature gradient is present, and it is attributable to the SOC error propagation from the NARX network to the feed forwards network calculating T_{out}.

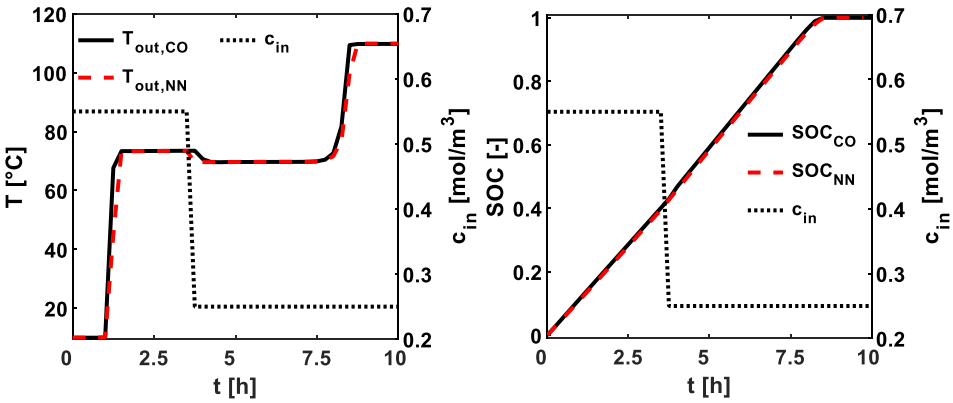

Figure 4.23: Test D1 with concentration change during dehydration experiment. CO = COMSOL model. NN = Neural networks model. MSE_{SOC}= 3.4·10^{-5}. MSE_{Tout}= 14.4 °C^2. $MSE_{Tout,SOC-CO}$= 0.36 °C^2

A relatively small discrepancy in the outlet temperature is visible at the moment in which the concentration is changed. This is due to the slight decrease in the equilibrium temperature of

the dehydration process, due to a lower inlet concentration, which propagates from the reaction front location at the moment of the concentration change, towards the outlet of the reactor. The discrepancy, as already mentioned, is caused by the fact that the model is not considering the thermal inertia of the system. An MSE of $3.4 \cdot 10^{-5}$ and 14.4 °C^2 for, respectively, the state of charge and the outlet temperature have been estimated during the test. By using as inputs the COMSOL values for the SOC, the MSE would strongly decrease to 0.36 °C^2, meaning that the SOC error impact is significant.

Test D2 – Step-wise temperature increment

As for the hydration test, the change in inlet temperature during the dehydration process causes a discrepancy due to the absence of thermal inertia in the neural network model which causes an instantaneous response in the outlet temperature (Figure 4.24 left), and state of charge (Figure 4.24 right). The magnitude of the discrepancy depends on the stage of the dehydration process at which the inlet temperature change is applied, together with the inlet temperature change magnitude. An MSE of $1.2 \cdot 10^{-3}$ and 49.6 °C^2 have been measured for the SOC and outlet temperature outputs, respectively. As for the previous test, the SOC error impact on the outlet temperature estimation is relatively large ($MSE_{Tout,SOC-CO}$ = 6.2 °C^2).

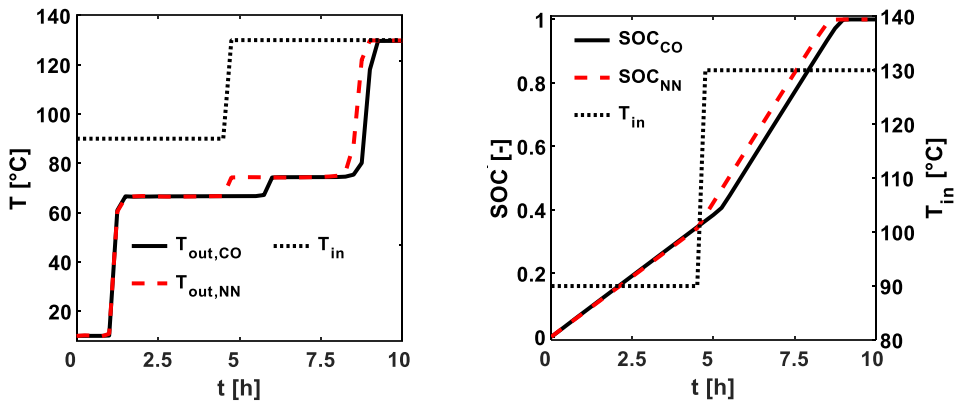

Figure 4.24: Test D2 with temperature change during dehydration experiment. CO = COMSOL model. NN = Neural networks model. MSE_{SOC}= $1.2 \cdot 10^{-3}$. MSE_{Tout}= 49.6 °C^2. $MSE_{Tout,SOC-CO}$= 6.2 °C^2.

Computational cost of the neural networks model

Figure 4.25 shows the advantage from a computational cost perspective of using a data driven model such as the one developed in this work. The six tests performed with the data driven model required between 0.12 s and 0.16 s, which is much faster than the 500 - 2400 sec shown in Figure 4.13 for the compact physics-based model. However, as already mentioned, for this type of models the training process must be carried out with either experimentally

obtained data or data from numerical models. The training time of all the trained neural networks, following the systematic training procedure, took approximately two weeks.

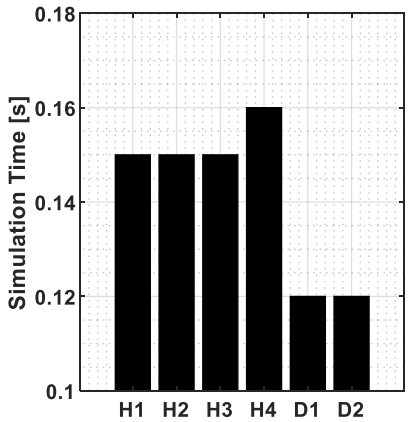

Figure 4.25: Simulation time of neural networks model for the six tests.

4.6.4 Model improvement

The previous model (Model 0), shown in Figure 4.15, consists of a nonlinear autoregressive neural network with exogenous inputs (NARX) for the state of charge estimation and a FFNN for the outlet temperature estimation. The NARX network takes into consideration the previous output (SOC_{t-1}) for the estimation of the following one (SOC_t). The previous results showed that the model had good capabilities in predicting the sorption reactor outputs for several tests. However, the main source of error was the incapability of the model to account for the thermal inertia of the reactor in the prediction of the output temperature. In this section, an additional analysis with more complex architectures is shown, based on Scapino et al. [159]. Special focus is on the capability of the compact model to predict the outputs for dynamic inputs that are changing with variable rates.

New architectures investigated

To account for the thermal inertia, the use of the NARX architecture for both the SOC and outlet temperature estimation is investigated. The idea is to use a NARX architecture that considers the system outputs of the previous 10 timesteps (with a timestep of 900 s), to predict the next outputs. This architecture is henceforth denoted as $NARX_{10}$. The neural network models investigated in this section are shown in Figure 4.26 and Table 4.10. Model 1 consists of a $NARX_{10}$ architecture for the SOC and a FFNN for the T_{out} estimation while models 2 and 3 have a $NARX_{10}$ architecture for the prediction of both outputs. The difference between model 2 and model 3 is the choice of the activation function f (equation 4.39) used in the hidden layers of the neural network used for the T_{out} prediction. Model 2 uses a hyperbolic

tangent sigmoid (HTS) transfer function ($NARX_{10,HTS}$), while model 3 uses a Leaky Rectified Linear Unit (LReLU) function ($NARX_{10,LReLU}$). The HTS has been extensively used in the past as activation function in the hidden layers while more recently the LReLU is also increasingly used due to certain numerical advantages over the HTS. More details about activation functions and the advantages and drawbacks of each one can be found in [137,160–162].

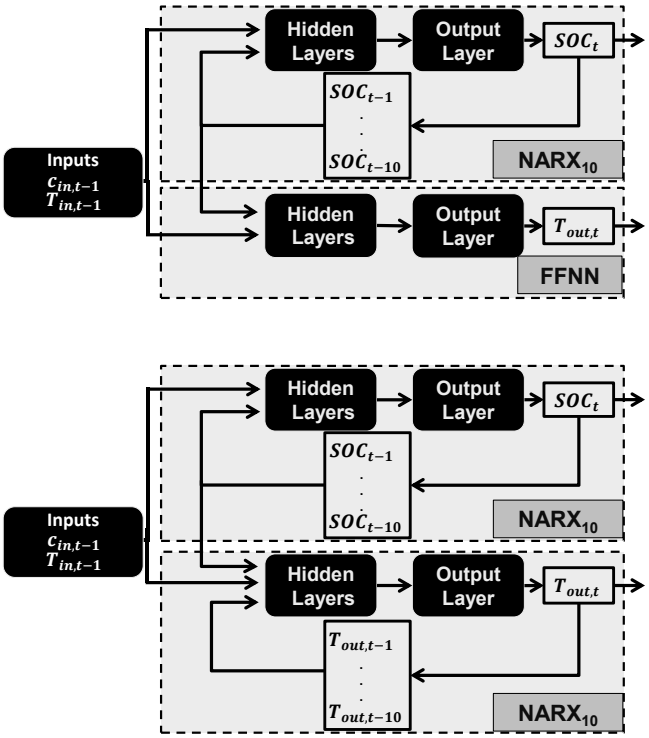

Figure 4.26: Neural networks models proposed in this work. Top: Model 1. NARX10 architecture for the SOC estimation and FFNN architecture for the outlet temperature estimation. Bottom: Common architecture of Model 2 and Model 3. A NARX10 architecture is used for both SOC and outlet temperature estimation.

Table 4.10: Selected neural networks and models investigated in this work.

Model	Output	Architecture	Model	Output	Architecture
0	SOC	$NARX_1$	2	SOC	$NARX_{10}$
	T_{out}	FFNN		T_{out}	$NARX_{10,HTS}$
1	SOC	$NARX_{10}$	3	SOC	$NARX_{10}$
	T_{out}	FFNN		T_{out}	$NARX_{10,LReLU}$

Training dataset expansion

The training and validation datasets consist of the datasets already used in the development of the first neural networks model (Table 4.9) expanded with additional dynamic simulations. In particular, two additional datasets have been added to the training dataset. The first dataset (Stepwise) consists of 48 simulations per operating mode, in which c_{in} or T_{in} are varied stepwise during the simulation (similarly to tests H1, H2, D1, and D2). The second dataset (Full) consists of 5 simulations per operating mode, in which both inputs are varied continuously during the whole simulation time (similarly to test H3). A summary of the datasets is shown in Table 4.11.

Table 4.11: Datasets for hydration (H) and dehydration (D) modes for the improved neural networks model.

	Dataset	Type		n° simulations
H	Training	Static		64
		Dynamic	Stepwise	48
			Full	5
	Validation	Static		49
D	Training	Static		72
		Dynamic	Stepwise	48
			Full	5
	Validation	Static		56

The datasets in Table 4.11 as well as the improved model tests in the following sections are produced with a COMSOL model based on the one presented in section 4.3. However, additional equations have been used to model the sorption material properties (Appendix D, Table D.1) based on the material hydration state (hyd for hydrated and $dehyd$ for dehydrated). In particular, the salt specific heat capacity ($c_{p,sm}$), thermal conductivity (λ_{sm}), and density (ρ_{sm}) are depending on the reaction degree of conversion X, following equations 4.42 - 4.44.

$$c_{p,sm} = c_{p,sm,hyd}X + c_{p,sm,dehyd}(1 - X) \quad 4.42$$

$$\lambda_{sm} = \lambda_{sm,hyd}X + \lambda_{sm,dehyd}(1 - X) \quad 4.43$$

$$\rho_{sm} = \rho_{sm,hyd}X + \rho_{sm,dehyd}(1 - X) \quad 4.44$$

$$\varepsilon_b = \varepsilon_{b,hyd} X + \varepsilon_{b,dehyd}(1 - X) \quad 4.45$$

The dependence of those properties on the degree of conversion X, has a direct consequence on other properties, namely the bed porosity (ε_b) calculated with equation 4.45, the effective axial thermal conductivity (λ_{eff}), the bed mean heat capacity ($\overline{\rho c_p}$), the axial mass dispersion coefficient (D_x), and the convective term of the thermal resistance inside the reactor wall.

Neural networks selection

Each network has a certain number of hidden layers (HL) and neurons per hidden layer (NpL). This information is displayed using the notation $NARX_{10,HL/NpL}$. For the state of charge, a $NARX_{1,2/5}$ and a $NARX_{10,4/20}$ are selected for hydration while a $NARX_{1,3/15}$ and a $NARX_{10,4/20}$ are selected for dehydration. For the outlet temperature, a $FFNN_{4/15}$, a $NARX_{10,HTS,2/10}$, and a $NARX_{10,LReLU,1/15}$ are selected for hydration. For dehydration, a $FFNN_{2/7}$, a $NARX_{10,HTS,3/3}$, and a $NARX_{10,LReLU,1/7}$ are selected. These networks are then combined into the models (Table 4.10) that contain a neural network for the state of charge and one for the outlet temperature prediction. In Figure 4.27, the MSE values of the selected neural networks are shown. It is noted that for the SOC prediction, which has a relatively simple profile increasing or decreasing in a range between 0 and 1, the $NARX_{10}$ outperformed the $NARX_1$, while for the T_{out} prediction, both $NARX_{10}$ (LReLU and HTS) performed worse than the FFNN. In general, if more past system outputs are considered, the training process of the NARX network is more computationally expensive due to the higher number of training parameters. Therefore, this can be a reason why lower MSE could not be achieved during the training process of the $NARX_{10}$ for the outlet temperature estimation. Finally, it can be noticed that the $NARX_{10}$ with the hyperbolic tangent sigmoid function used as activation function for the hidden layers is performing better than the LReLU function.

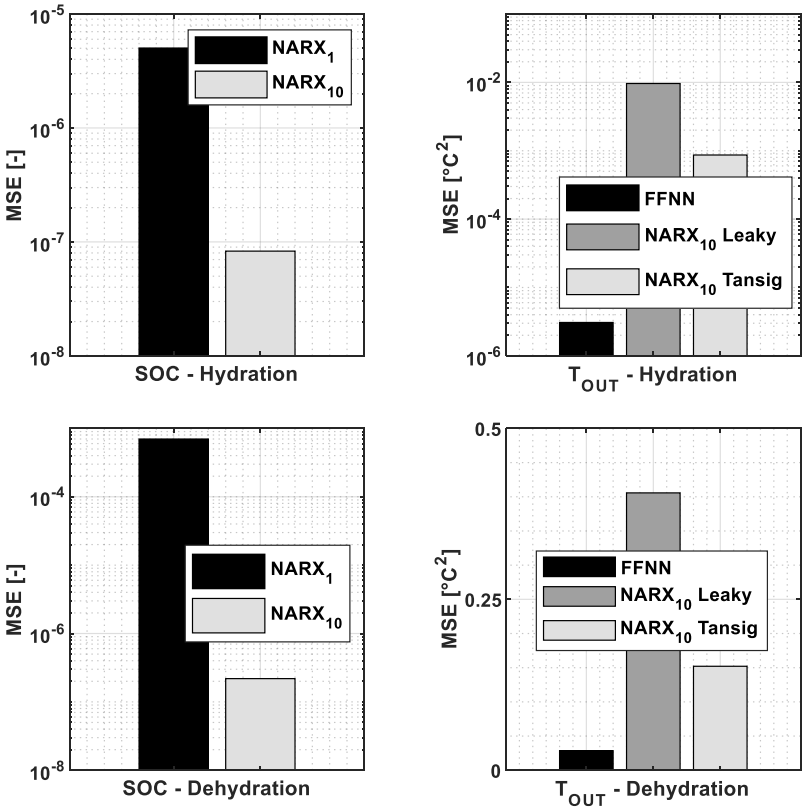

Figure 4.27: MSE values of the selected neural networks (Table 4.10). Top left: SOC for hydration mode. Top right: T_{out} for hydration mode. Bottom left: SOC for dehydration mode. Bottom right: T_{out} for dehydration mode.

Improved model tests

For the improved model, several dynamic tests have been performed based on the tests in Table 4.4. The tests were specifically focused on assessing the thermal inertia effect of the system. For this purpose, for tests H1, H2, D1, and D2, the model inputs are varied from the initial to the final value with four different variation rates (a-d), as shown in Table 4.12. A slower variation rate corresponds to a higher variation time and vice versa. Moreover, as for the previous physics-based and data-driven models, tests H3 and H4 are performed.

Table 4.12: Variation time for tests H1, H2, D1, and D2 for the improved neural networks model tests.

Test label	Variation time [h]
a	0.25
b	2
c	4
d	6

Improved model performance

State of charge

The models presented in Table 4.10 are used to perform the tests presented in Table 4.4. In particular, for tests H1, H2, D1, and D2, multiple variation rates (a/b/c/d) are applied (Table 4.12).

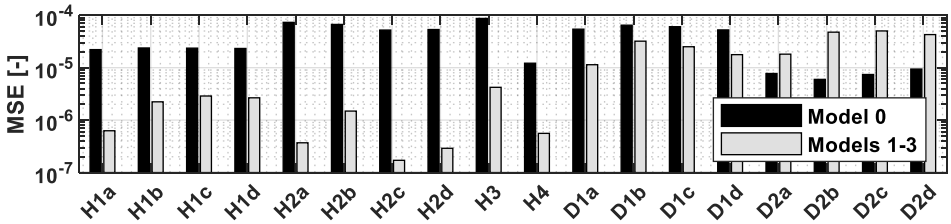

Figure 4.28: MSE of the SOC output for the $NARX_1$ (Model 0) and $NARX_{10}$ (Models 1 to 3) architectures.

In Figure 4.28, the MSE for all the tests of the two neural networks used to predict the SOC are shown. Model 0 uses a $NARX_1$ architecture and models 1, 2, and 3 use the same new $NARX_{10}$ architecture (Table 4.10). For the hydration tests H, the MSE is reduced at least by an order of magnitude for all the tests, if the $NARX_{10}$ is used. For the dehydration mode D, the MSE decreases for tests in which the inlet sorbate concentration is varied (D1-tests) but not for the tests in which the inlet temperature is varied (D2-tests). For the latter, an increase in the MSE is noticed. Thus, the error in the SOC prediction was larger by using the $NARX_{10}$ architecture compared to the $NARX_1$ architecture.

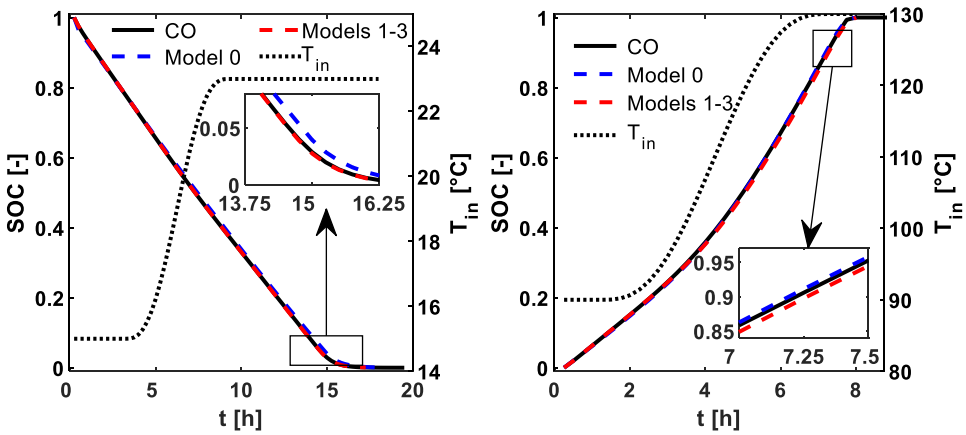

Figure 4.29: SOC prediction for tests H2d (left) and D2d (right). Black solid line: COMSOL model. Blue dashed line: Model 0. Red dashed line: Models 1,2, and 3.

In Figure 4.29, two test results are shown. On the left, the SOC prediction of test H2d is displayed. During hydration, the SOC decreases from 1 to 0 and the inlet temperature is increased from 15 °C to 23 °C in a 6 hours interval (Figure 4.29 left). While the SOC prediction with the $NARX_1$ (Model 0) has a discrepancy generated during the inlet temperature change, the SOC prediction with the $NARX_{10}$ (Models 1-3) follows correctly the target values. On the other hand, in test D2d (Figure 4.29 right), the SOC prediction using the $NARX_{10}$ has a larger discrepancy by underestimating the SOC value starting from the inlet temperature variation. The SOC estimation error is then reflected in the outlet temperature prediction especially towards the end of the hydration and dehydration, shown in the next section.

Outlet temperature

In Figure 4.30, the MSE for the T_{out} prediction is shown for the four models. Model 1 outperforms Model 0 in every test with the highest difference in test D1a (-3.91 °C^2) and the lowest difference in test H1c (-0.019 °C^2). Therefore, the use of a $NARX_{10}$ architecture for the SOC prediction has a positive impact on the T_{out} prediction even if a FFNN architecture is used for the latter (Model 1). Models 2 and 3, in which the $NARX_{10}$ is used also for predicting the T_{out}, are always performing worse than Model 1, that is using the FFNN for T_{out}.

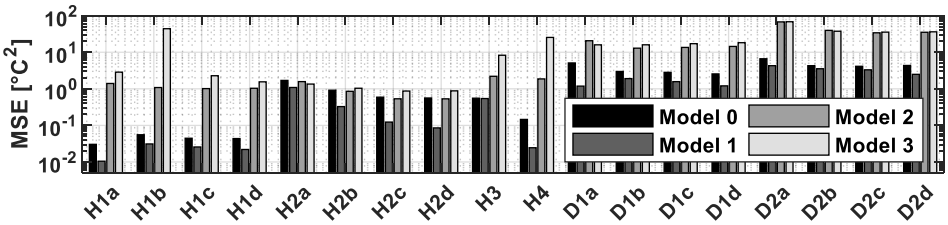

Figure 4.30: MSE of the T_{out} output for the four models investigated.

In Figure 4.31, the T_{out} prediction with the four models investigated in this work is displayed for a hydration (left) and a dehydration (right) test, characterized by a change in T_{in} with a variation time of 6 hours, according to Table 4.12. On the left, the test H2d is shown. The legend shows that Model 1 is the most accurate with an MSE of 0.08 °C^2. Models 0,2, and 3 have MSE values of roughly one order of magnitude higher (0.56 °C^2, 0.88 °C^2 and 0.53 °C^2, respectively). The discrepancies are mostly present at the end of the hydration, for the SOC approaching 0 (i.e. around the 15th hour). Model 2 is the one performing best during the inlet temperature change period of the experiment (see zoomed graph) because it is the one following most closely the targets.

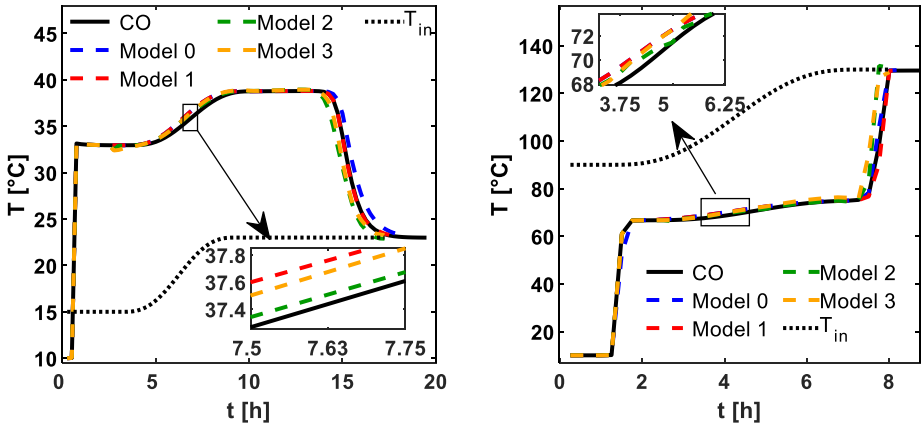

Figure 4.31: T_{out} prediction with the four models investigated in this work. CO = COMSOL model. Left: Test H2d. MSE_{Tout} values: Model 0 = 0.56 °C², Model 1 = 0.08 °C², Model 2 = 0.88 °C², Model 3 = 0.53 °C². Right: Test D2d. MSE_{Tout} values: Model 0 = 4.35 °C², Model 1 = 2.49 °C², Model 2 = 36.19 °C², Model 3 = 35.18 °C².

However, the larger error at the end of the hydration due to the premature temperature decrease (dashed green line) compared to the COMSOL values (solid black line) is greatly increasing its MSE_{Tout}. In the dehydration tests, all models show larger MSE values than for the hydration tests because the involved temperature variations, and in turn the discrepancies between the COMSOL model and the data-driven model, are larger. Hence, the impact on the MSE is higher as well. In Figure 4.31 right, the dehydration test D2d is displayed. As for test H2d, the best performing model is Model 1. Models 2 and 3 are again performing worse due to the misrepresentation of the outlet temperature towards the end of the dehydration. However, Model 2 is the one following better the targets during the inlet temperature change period in the middle of the experiment (roughly between hour 10 and hour 25). Finally, comparing tests H2a – H2d (Figure 4.32) for the best performing model (Model 1), it is clear that the model performs better for smoother input changes. In both hydration and dehydration, the MSE_{Tout} decreases by increasing the input variation period (i.e. from tests 1 towards tests 4). The reason is that the smoother the input variation is, the smaller the thermal inertia effect is during the experiment.

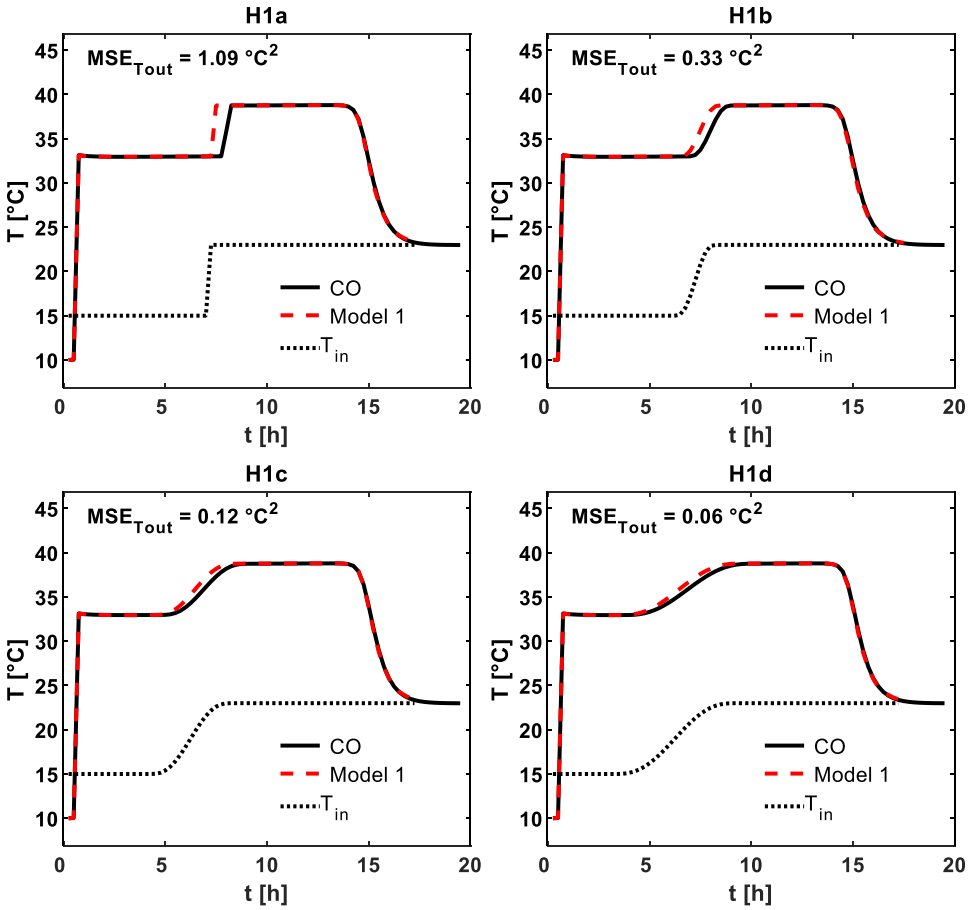

Figure 4.32: T_{out} for tests H2a (top left), H2b (top right), H2c (bottom left), and H2d (bottom right) for model 1. CO = COMSOL model.

4.7 Conclusions

In this chapter, two main numerical models are investigated for the simulation of a sorption heat storage reactor. The main objective was to investigate the suitability of the two modeling approaches for dynamic energy systems simulations. The main model requirements were a relatively low computational cost during the simulations, and the possibility to integrate the models into broader system models in a common simulation environment. The two models were then compared with a high-fidelity model developed in COMSOL Multiphysics®.

The first model (spectral model) is based on the physics governing the sorption reactor i.e. on the PDEs describing the relevant mass and energy balances of the packed bed, and on additional equations describing the kinetics, and the heat and mass transfer phenomena happening inside the reactor. A spectral method has been used for the spatial domain

discretization, and a semi-implicit Euler method has been used to discretize the temporal domain.

The second model (neural networks model) consists of a data-driven model based on two neural networks that estimate the outlet temperature and the sorption reactor state of charge given as inputs the inlet temperature and water vapor concentration, and the STES SOC at the previous timestep.

The models were compared with several hydration and dehydration tests (Table 4.4), in which their MSE values for the SOC and outlet temperature has been calculated.

The results (Figure 4.33) show that the spectral model is able to accurately predict the model outputs with MSE values for both the SOC and outlet temperature that are always lower compared to the neural networks model (Neural Networks).

Concerning the SOC, the smallest MSE for the spectral model occurred for the hydration test H1 ($9.24 \cdot 10^{-7}$) and the highest for the dehydration test D1 ($8.89 \cdot 10^{-6}$). The same trend occurs for the outlet temperature with an MSE for tests H1 and D1 of $4.5 \cdot 10^{-3}$ °C^2 and 1.12 °C^2, respectively.

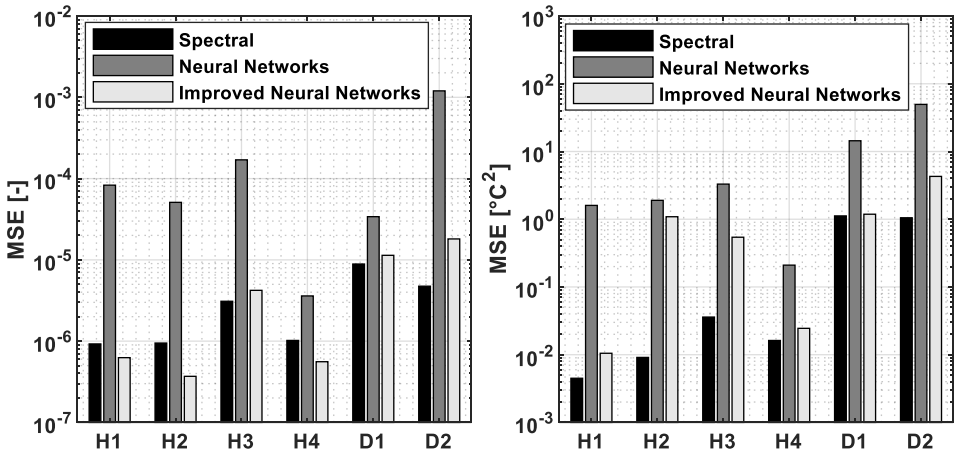

Figure 4.33: MSE values of the SOC (left) and T_{out} (right) outputs for the six tests performed on the spectral model (black), neural networks model (dark grey), and improved neural networks model (light grey).

The neural networks model had the minimum and maximum MSE values for the SOC in tests H4 ($3.6 \cdot 10^{-6}$) and D2 ($1.2 \cdot 10^{-3}$), respectively. Also, regarding the outlet temperature, the minimum and maximum MSE values occurred in tests H4 ($2.1 \cdot 10^{-1}$ °C^2) and D2 (49.6 °C^2), respectively. It has been found that the behavior of the developed model, and the source of errors in terms of discrepancies from the COMSOL model, derive from the underlying physical parameters of the sorption heat storage such as the thermal inertia of the system. The latter is not effectively tracked with the selected neural network architecture for the outlet temperature estimation.

Afterwards, the $NARX_{10}$ architecture was investigated to tackle the abovementioned issue, and several tests for both hydration and dehydration modes were performed. In this last analysis, a COMSOL physics-based model with variable sorption material properties based on the material hydration state was used to produce the training and test datasets. The use of a $NARX_{10}$ improved the SOC estimation for all the tests except the dehydration tests in which the inlet temperature is changed. There, the $NARX_{10}$ was slightly underestimating the reactor SOC when the inlet temperature started to vary. Concerning the outlet temperature estimation, the best performing model (Model 1) had a $NARX_{10}$ for the SOC estimation and a FFNN for the T_{out} estimation. For T_{out}, the $NARX_{10}$ architecture performed worse than the FFNN architecture. This behavior already emerged after the training process, in which the FFNN achieved a lower MSE with the validation dataset compared to the $NARX_{10}$ architectures.

Therefore, the improved neural networks model consisted of a $NARX_{10}$ architecture for the SOC estimation and a FFNN architecture for the outlet temperature estimation. The reasons why a $NARX_{10}$ architecture performed worse than a FFNN architecture for the outlet temperature estimation can be multiple. First, the $NARX_{10}$ is a more complex architecture and harder to train compared to the FFNN. Thus, the imposed maximum number of training epochs (1000) might not have been sufficient. However, due to the relatively long training process (~4 weeks in total), it can be difficult to further extend the number of epochs while still having a reasonable training time. Furthermore, the amount of past system states considered in the $NARX_{10}$ has been selected assuming that the past 2.5 hours (10 system states with a resolution of 900 s) of the system were sufficient to predict the next system state. In Figure 4.33 left, the MSE values for the SOC of the improved neural networks model are sensibly lower than the previous neural networks model. For tests H1, H2, and H4, the improved model outperforms also the spectral model. Concerning the outlet temperature estimation (Figure 4.33 right), the improved model has a lower MSE in all the tests compared to the initial neural networks model, but the spectral model always has the highest accuracy by having roughly at least one order of magnitude lower MSE values.

By considering that the six tests, with the simulation times shown in Figure 4.13, simulated the reactor behavior for durations between 10 h (tests D1 and D2) and 25 h (test H3 in Appendix E), and that the model purpose should be for dynamic simulations with an extensive temporal horizon, for example one year of simulation, it is concluded that the computational cost of the spectral model is relatively high. In this model, the materials and reactor properties have been kept constant. The computational cost of the spectral model would have increased even further if the material and reactor properties would have been varied according to, for example, the material conversion degree (X) as for the improved neural networks model. In order to include also variable properties, the model coefficients in Table 4.6, and in turns the matrices and vectors in Table 4.7 and Table 4.8, should be computed at every timestep instead of only at the beginning of the simulation.

In general, the use of a more complex data-driven model for the SOC estimation, such as the one used in Model 1, could be useful to limit the error propagation of the SOC in the temperature estimation in cases where this leads to a significant discrepancy. If the discrepancy arises only at the very end of the reactor hydration or dehydration (e.g. $SOC >$ 0.95), such as for test H2d in Figure 4.31 left, the use of a more complex model might not be necessary. However, as shown in Figure 4.24 (test D2), during dehydration a steep temperature gradient might lead to a significant discrepancy. Therefore, if heat sources with temperature variations such as solar thermal collectors are used, the SOC error accumulation might lead to a significant discrepancy in both the SOC and the outlet temperature estimation, and a more accurate SOC estimation can be useful.

To conclude, the spectral model showed the highest accuracy compared to the neural networks model, especially in the outlet temperature estimation. However, the computational cost during the simulation was much higher than the neural networks models. Conversely, the computational cost of the neural networks models was much lower, but also required significant training time. Moreover, their accuracy was lower than the spectral model due to the incapability of effectively tracking the system thermal inertia effect.

Finally, further research with different networks architectures suitable for time series prediction such as the recurrent neural networks [163] or a NARX accounting for a different amount of past system states could lead to better results. Moreover, further systematic investigations on different number of neurons in each hidden layer and different hidden layers can be a starting point for future research. Ultimately, the type of sorption system, its size, and the outputs time resolution will determine the relevance of the thermal inertia effect and whether it is necessary to integrate it within this type of data-driven models.

CHAPTER 5

ENERGY SYSTEM OPTIMIZATION I

THE POTENTIAL OF A CENTRALIZED STES OPERATING IN DIFFERENT ENERGY MARKETS

Based on:
Scapino L., De Servi C., Zondag H.A., Diriken J., Rindt C.C.M., Sciacovelli A.
Techno-economic optimization of an energy system with sorption thermal energy storage in different energy markets
Submitted 2019.

This chapter investigates, within an optimization framework, the economic impact of a STES in a reference energy system operating in different energy markets. In particular, the aim of the optimization is to maximize the yearly energy system profits for every investigated scenario. This chapter is divided into five main sections, beside the introduction (5.1). Section 5.2 introduces the reference energy system (5.2.1), the energy markets (5.2.2), and the different scenarios investigated in this work (5.2.3). Section 5.3 focuses on the modelling methodology and describes the different system components, with special focus on the STES. Section 5.4 presents the optimization framework by introducing the optimization variables (5.4.1), the objective function and the problem optimization constraints (5.4.2). Section 5.5 presents the results of the analysis. First, the major highlights and results overview for all the scenarios are shown (5.5.1). Then, each scenario is individually addressed and discussed (5.5.2 - 5.5.5). Finally, in section 5.6, the main conclusions of this work are presented.

5.1 Introduction

Understanding the potential of different producers, storage technologies, and consumers in future energy systems through techno-economic analyses is a crucial step for the accelerated adoption of the most promising technologies, and their optimal integration into the energy systems. In order to do so, optimization techniques applied to energy systems are widely used in literature. In particular, mixed integer linear programming (MILP) [164] has been widely used for investigations of multi-energy systems at different spatial and temporal scales. Studies at country-level [5,165] investigated the system capability to deal with the coexistence of intermittent production sources and cogeneration plants [166]. Micro-grids as stand-alone systems [167], interacting with the main grid [168], and their ability to provide market services such as reliability and flexibility [169] have also been studied within a MILP framework. Concerning electrical storage, different battery technologies have been investigated for community energy storage and market service provision [170] or for profit maximization of renewable energy systems [171]. Regarding thermal energy storage and conversion, the use of a thermal battery to convert electricity into heat and cold energy and serve as flexibility provider has been studied [172]. Finally, also the integration of seasonal heat storage at district level has been investigated for increasing the amount of renewable heat supply [173].

Despite its wide applicability, MILP has also intrinsic weaknesses. Often, the system components have to be simplified to be described by linear relations or to be representative for a whole class of technologies (e.g. thermal energy storage). Therefore, often a compromise between model representativeness and computational complexity is made and, as a consequence, specific technological aspects are marginally addressed. Especially for investigations with an extensive spatial and temporal domain, techno-economic optimizations with oversimplified system components might lead to conclusions that are distant from reality. Typically, a daily, weekly or yearly optimization temporal horizon is used with a resolution of one or more hours. Several solutions are being investigated to reduce the computational cost of the optimization problems by considering e.g. representative periods [174–179].

Within the MILP optimization framework, the future potential of advanced thermal energy storage technologies such as latent [16,17] or sorption [19–21,80,180] heat storage in different systems and market scenarios has not yet been extensively investigated. Among the main reasons, fundamental scientific challenges at technological level are still to be overcome. However, techno-economic analyses, involving sufficient technological knowledge, are crucial to have consistent and physics-based insights that, in turn, can lead to the optimal integration of new technologies in future energy systems. These analyses provide essential insights required for the creation of favorable market conditions by policy makers and market stakeholders. This is especially true for technologies that are still under research, with a low TRL, or that have a niche market. In particular, a proper definition within a MILP

framework of a sorption heat storage, including specific technological characteristics and constraints, is missing.

In light of this, the aim of this chapter is to investigate, within a MILP framework, the economic impact of an open solid sorption thermal energy storage (STES) in a reference energy system operating in different energy markets. The reference energy system consists of a main heating grid (HG) that extracts the thermal energy from a geothermal doublet, inspired by an existing installation in Belgium, and provides it to two consumers: a low temperature district heating network (DHN) and an organic Rankine cycle (ORC). The impact of a STES on the energy system yearly profit is assessed for different storage sizes in the presence of different market mechanisms. The electricity markets considered in this work are the Belgian day ahead market (2013 data), and the UK market (2017 data). The Belgian market has been selected because the location of the existing geothermal doublet is in Belgium. The additional investigation on the UK market has been done due to the presence of various balancing services that would make the integration of energy storage profitable.

Two main contributions are present within this chapter. The first contribution is a STES definition within the MILP framework taking also into account the specific technological aspects of this storage type. The second contribution is an assessment of the economic benefits of adding an innovative thermal storage technology within different economic frameworks. Sorption heat storage is a technology still under research. Therefore, it is essential to understand its future competitivity in the energy network and to focus the scientific research on the most critical issues and main challenges for the integration of this technology in the market. In particular, this chapter investigates the benefits for an energy producer to operate simultaneously in different energy markets, i.e. the retail market and balancing services, in order to maximize the energy producer yearly profits.

Beside the chapter outline mentioned in the front page of this chapter, a conceptual representation of the chapter structure is shown in Figure 5.1.

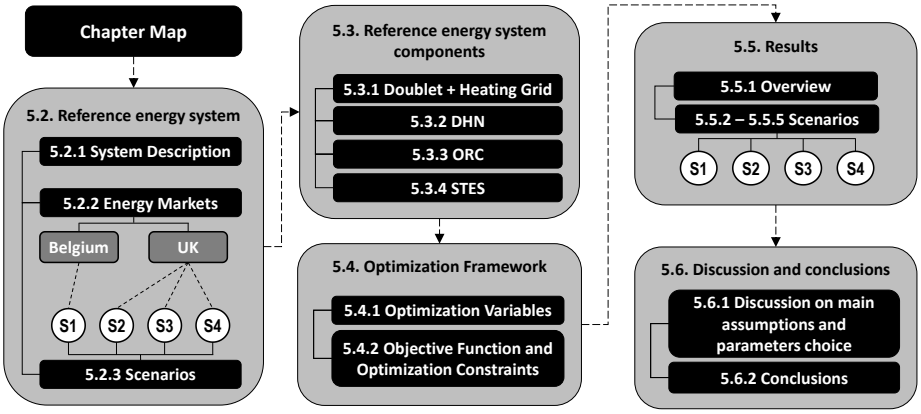

Figure 5.1: Conceptual map of the chapter structure.

5.2 Reference energy system

The main components of the reference energy system are described in section 5.2.1. Then, the energy market mechanisms that are being investigated are defined (5.2.2) and the different scenarios in which the reference energy system is operating are shown (5.2.3).

5.2.1 General description

In this section, a general overview of the reference energy system is presented. The details and assumptions about every system component are given in section 5.3. The reference energy system and the interaction between the different components is displayed in Figure 5.2. The system consists of a deep geothermal doublet delivering thermal energy to a main medium-temperature heating grid (HG). Two main consumers are connected. The first consumer is a low-temperature district heating network (DHN), supplying a neighborhood with thermal energy for space heating and domestic hot water, which has priority as heat consumer. The second consumer is an organic Rankine cycle (ORC), which can produce electricity from the remaining fraction of mass flow in the geothermal plant that is not used for providing the demand of the DHN. Within this energy system, a STES consisting of several modular units is integrated. The STES size (the number of modular units) is varied in order to find the optimal STES size for every scenario that maximizes the yearly system profit.

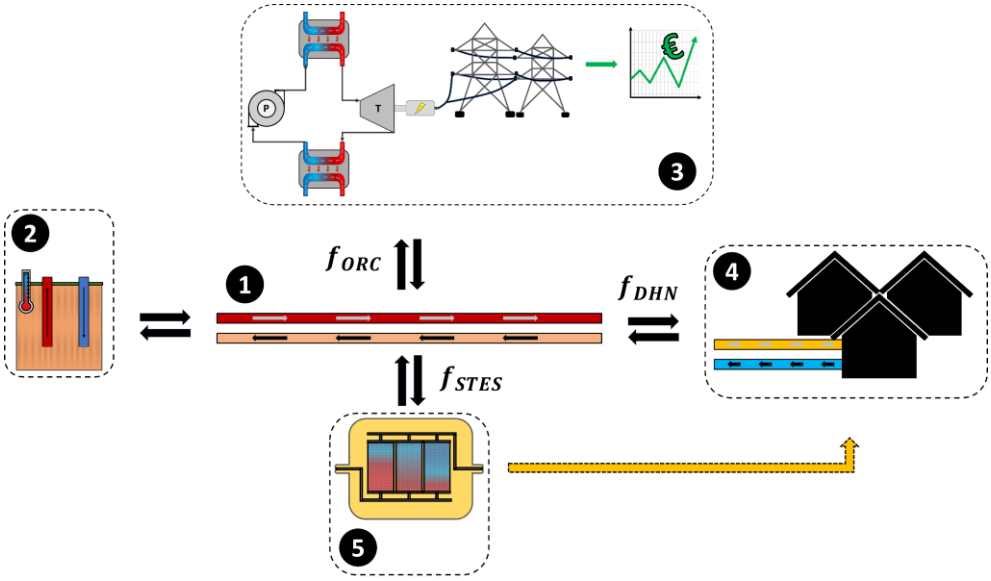

Figure 5.2: Top: Reference Scenario. 1: Main heating grid (HG). 2: Geothermal doublet. 3: Organic Rankine cycle. 4: Low temperature district heating network (DHN). 5: Sorption thermal energy storage (STES).

A key point of this work is to investigate the impact of different energy markets, in which the reference energy system is operating. Different market mechanisms can provide additional revenues and make the use of the STES more or less profitable. The aim of the optimization is to assess the optimal STES size and its role as flexibility provider while maximizing the overall system profit during a year of operation and respecting the main system constraints such as guaranteeing the energy provision to the DHN. At every moment in time, part of the energy from the main heating grid can be used to satisfy the thermal energy demand from the DHN ($\boldsymbol{f_{DHN}}$), for the electricity production with the ORC ($\boldsymbol{f_{ORC}}$), or for charging (desorption) the STES ($\boldsymbol{f_{STES}}$). The STES could partially satisfy the DHN demand when the ORC is making high revenues in selling electrical power to the energy markets. Therefore, the mass flow fraction used by the ORC to produce electrical power at a specific moment can be increased. The optimization problem consists of selecting the water mass flow fractions from the heating grid to the three energy consumers ($\boldsymbol{f_{DHN}}$, $\boldsymbol{f_{ORC}}$, $\boldsymbol{f_{STES}}$,) at every time step.

5.2.2 Energy markets

Energy markets and balancing services are numerous and differ among countries and among each other in terms of availability in time, remuneration schemes, and technical requirements of the electricity producers to operate in a specific market. Among the typical technical requirements for an electricity producer there is the minimum installed capacity, a minimum delivery time during which the committed capacity has to be constantly delivered, and the generator response time. The latter, for a balancing service, is a crucial parameter. Balancing services for the grid frequency control require response times typically within one second while services for fast reserve of active power typically require response times in the order of few minutes.

In this work, several energy market mechanisms in Belgium and UK have been considered. The reason why the Belgian market has been selected is that the deep geothermal doublet is inspired by an existing installation in Mol (BE). Moreover, the aggregated thermal energy demand profile of the DHN represents an existing urban district located in Genk (BE). For the investigated Belgian market, the data from 2013 have been used due to their availability. The reason why the UK region has been selected is that in UK there are various balancing market mechanisms that remunerate the energy producers with additional or higher revenue streams for the provision of flexibility. For the UK markets investigated in this work, the most recent available data (2017) have been used. Three main market mechanisms are investigated. The day ahead market (DAM), a market that is always active, in which the electricity price is set according to the forecasted energy demand and production; the capacity market (CM), a UK compensation mechanism based on the yearly committed capacity of a generation unit that has to be available during stressful events (e.g. unforeseen availability of a producer); and the short term operating reserve (STOR), a UK balancing service that is

used to fill the gap between the forecasted demand required by the grid and the actual demand. In this work, when multiple market mechanisms are active in the same scenario, the ORC can sell the energy to all of them.

Day ahead market (DAM)

The day ahead market is a traditional market mechanism in which consumers and producers establish the electricity price one day ahead of the delivery. Within this market, the ORC can sell electricity with the principle of tariff arbitrage. Therefore, the ORC tries to sell as much electricity as possible when the price (p_{DAM}) is high.

Capacity market (CM)

The Capacity Market (CM) [181] is a mechanism that provides a predictable yearly revenue stream for a generation unit. The generation unit is compensated for committing its capacity to the national grid for a predefined amount of years. In exchange for the yearly compensation, the unit is committed to generate during stressful grid events (CM-event), otherwise penalties are faced. A stressful event might arise due to e.g. an unforeseen availability of a generator, and the national grid might not have sufficient production resources to fulfill the forecasted demand, already including other balancing services. There has not been a CM-event since 2016 in the UK grid [182]. Within this work, the clearing price (p_{CM}) of the 2016 CM market auction is used [183], 22.5 €/(kW·year), and shown in Table 5.1. Moreover, a CM-event is imposed into the optimization model on January 5th. In this work, the revenues from the CM market depend on how much power the ORC delivers to an energy market during the CM-event. For example, if during the CM-event, the ORC produces an electric power of 1 MW and sells the energy to a market (DAM or STOR), an additional yearly revenue stream of 22500 € is produced.

Short term operating reserve (STOR)

The Short Term Operating Reserve (STOR) [184] is a balancing service used in UK at certain times of the day in order to provide extra capacity in case that the forecasted electricity demand is higher than the actual demand or in case of unforeseen unavailability of generators. The service is typically active during two time windows of the day to address the morning and evening peaks. The time interval of each window can vary depending on whether it is a business or weekend day. Moreover, the availability windows vary over the year according to six periods, hereafter referred as “STOR seasons”. Currently, this market is open to generators with a capacity of 3 MW or larger. However, aggregated contracts can be possible, and lower capacity units can operate together to meet the minimum capacity requirement. The compensation system of the STOR balancing service consists of two parts. The generator is compensated, with an availability price ($p_{STOR_{AP}}$), for committing a certain capacity to the service, even if it is not used. Moreover, in case the generator is called to generate, it will be compensated, with a utilization price ($p_{STOR_{UP}}$), for the generated electricity. In this work, the average availability and utilization prices for 2017 are used [185] and shown in Table 5.1.

It has to be remarked that the availability price ($p_{STOR_{AP}}$) compensates the producer for the committed power in every time window (i.e. €/(MW·h)) while the utilization price ($p_{STOR_{UP}}$) compensates the producer for the energy effectively sold in a time window (i.e. €/(MWh)).

Table 5.1: STOR and CM market parameters

Parameter	Value	Unit
p_{CM}	22.5	€/(kW·year)
$p_{STOR_{AP}}$	4.76	€/(MW·h)
$p_{STOR_{UP}}$	168.64	€/(MWh)

The optimization model in this work is a deterministic model. Therefore, a utilization profile of the generation unit has to be known a priori. In order to do so, a probability to generate is calculated for every time window based on the amount of days present in the STOR season and the amount of days in which the service has been effectively used by the electricity grid in that STOR season [185]. With that, a probability-based generation profile for the STOR service is produced. In this work, it is assumed that the generator (ORC) is always able to provide the committed capacity to the STOR market. However, in a real case scenario, there might be energy delivery failures from an energy producer due to various reasons (i.e. technical issues).

5.2.3 Scenarios

The reference energy system presented in section 5.2.1 is investigated with different scenarios (Figure 5.3). For every scenario, the amount of sorption reactor segments is varied and the impact on the overall system profit is assessed. The first two scenarios, S1 and S2, assume that the reference energy system can operate only in the day ahead market (DAM) and sell energy with a strategy based on tariff arbitrage. The STES integration could be beneficial for the ORC to produce more electricity when prices on the DAM are higher. This would allow the main heating grid to allocate more mass flow for the ORC electricity production and satisfy the DHN demand by discharging the STES. Scenarios S3 and S4 include additional balancing services in which the ORC can operate, in the UK market. Scenario S3 assumes that the generation unit can also operate in the capacity market. In this scenario, the ORC could maximize its committed capacity during grid stressful events thanks to the STES presence. Finally, S4 adds also the STOR market among the possible balancing services in which the ORC can operate. Being a market available only during certain time windows of the day, the STES integration could allow the ORC to maximize its energy production during those time periods.

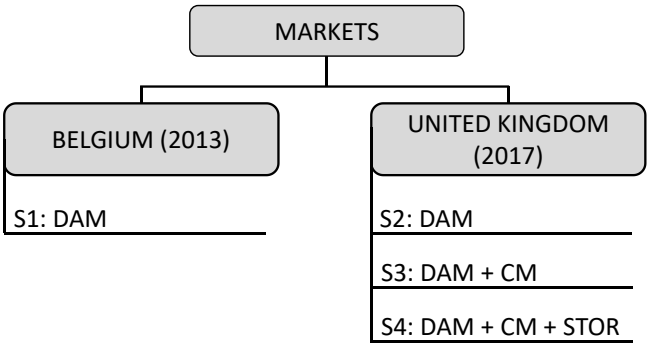

Figure 5.3: Market mechanisms present in each scenario. DAM = day ahead market. CM = capacity market. STOR = short term operating reserve.

5.3 Reference energy system components

In this section, the main system components are described individually. In section 5.3.1, the relevant information is presented on the deep geothermal doublet and on the main heating grid, operating at medium-temperature. In sections 5.3.2 and 5.3.3, the low temperature district heating network and ORC are described, respectively. Finally, in section 5.3.4, the STES main concepts and operational behavior are described in detail. In Table 5.2, the main parameters of the energy systems components are shown.

5.3.1 Geothermal doublet and heating grid

The deep geothermal doublet and main heating grid relevant parameters are based on an existing installation in Mol, Belgium [186]. It is assumed that the doublet will deliver a fixed thermal power at a constant temperature of 125 °C throughout the whole year. Due to this assumption, in the modeling framework, the doublet will not be directly simulated. The thermal energy is then transferred to a heating grid through a heat exchanger in which the heating grid supply ($T_{HG,sp}$) and return temperatures ($T_{HG,rt}$) are 114 °C and 70 °C, respectively, and a fixed mass flow ($\dot{m}_{HG}$) of 161 kg/s is used (Table 5.2).

5.3.2 Low temperature district heating network (DHN)

A 4th generation district heating network [187] has been assumed in the reference scenario. It is defined as a thermal energy system able to satisfy the thermal energy needs of low energy buildings with low temperature heat sources. In terms of operating temperatures, a supply temperature ($T_{DHN,sp}$) of 55 °C and a return temperature ($T_{DHN,rt}$) of 30 °C have been assumed (Table 5.2). The DHN thermal energy demand, P_{DHN}, has been inspired from a urban district in Genk (BE), consisting of approximately seven thousand buildings (Figure 5.4). A tool based on the work of Remmen et al. [188] and De Jaeger et al. [189], which

includes building models taking into account the building type (detached, semi-detached, terraced), geometry and the year of construction, together with a stochastic occupancy model [190], has been used to estimate the aggregated demand of the abovementioned urban district. For this work, the aggregated profile has been scaled down so that the DHN thermal energy demand can be satisfied in every period of the year with the assumed mass flow rate of the main heating grid ($\dot{m}_{HG}$), leading to a maximum deliverable power of approximately 29.65 MW and corresponding to the maximum heating demand of approximately 1200 dwellings . Based on the stochastic occupancy model, the heating temperature set point can vary within the interval between 15 °C and 20 °C. The DHW demand supply temperature at the building level is assumed at 55 °C and the mains temperature at 10 °C. The heating demand has been determined using the data from a typical meteorological year from a weather station of Uccle (BE), representative for the Belgian climate. It has to be remarked that the typical meteorological year does not represent a specific year, but it is the result of using historical data to produce typical conditions for 12 representative months [191]. Therefore, in this work, the heating demand is based on the typical meteorological year data, while the price signals are specific for one year (2013 for Belgium and 2017 for UK).

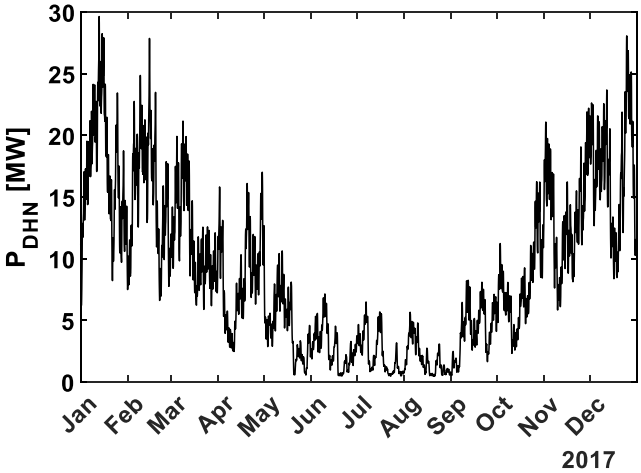

Figure 5.4: Aggregated thermal energy demand of the district heating network.

5.3.3 Organic Rankine cycle

An ORC model, in which a cooling tower is used to remove the heat from the condenser water, has been used to estimate the net electric power P_{ORC} produced given three main input parameters: the available mass flow fraction from the heating grid f_{ORC}, which determines the amount of ORC fluid that can be evaporated; the temperature $T_{amb,t}$ and humidity $RH_{amb,t}$ of the ambient air, which determine the performance of the cooling tower and, consequently, also the power required from the auxiliary systems such as the cooling tower

fan and condenser water pump. The model has as main inputs several assumptions and technological constraints inspired by a project under development in Mol (BE) [186]. The modeled ORC consists of a subcritical Rankine cycle with propane as organic fluid and a nominal power of 2.5 MW. The ORC fluid properties and thermodynamic states were estimated with CoolProp [192] while the design guidelines and components sizing have been done according to Sinnot [193]. It is assumed that the ORC can operate with a minimum evaporator mass flow ($f_{ORC,min}$) of 20 % of the nominal one, and that the return temperature of the evaporator is fixed at $T_{HG,rt}$. Regional weather data from 2007 to 2016 have been used to define the operating boundaries of the ORC in terms of relative humidity and temperature of ambient air. Then, the off-design net power produced at every possible weather condition and evaporator mass flow has been mapped. In Figure 5.5 left, the net power delivered at three different evaporator mass flows is shown. In Figure 5.5 right, the net power delivered at four different temperature and humidity levels is displayed. At low ambient temperature and humidity, the cooling tower is able to minimize the condenser water temperature, resulting in higher enthalpy difference in the ORC turbine, and therefore in higher produced power. Vice versa, at higher temperature and humidity, the ORC condensation temperature is increased, and the ORC fluid enthalpy difference exploited in the ORC turbine is lower resulting in a lower net power produced. For certain conditions, the auxiliary power required is greater than the power produced by the turbine, resulting in a negative net power delivered from the system.

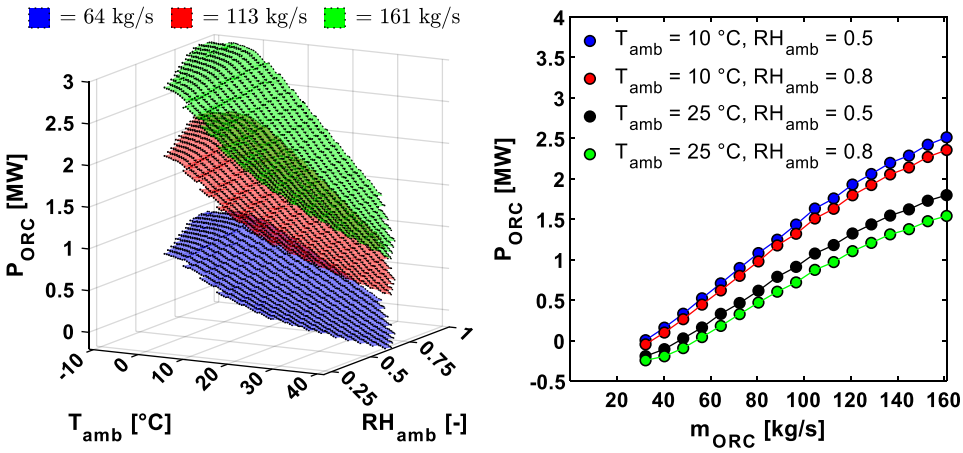

Figure 5.5: ORC net power in function of ambient temperature and humidity, and evaporator mass flow. Left: Net power production for three different evaporator mass flows. Right: Net power production for four fixed ambient temperature and humidity levels.

5.3.4 Sorption thermal energy storage

In this chapter, a salt hydrate/H_2O open solid sorption system is considered, in which the porous material (sorbent) is stored in cylindrical packed beds and the sorbate is transported by an air flow. In particular, the salt hydrate properties of potassium carbonate, which has been identified as possible candidate for STES [43,44], are used in this work. Potassium carbonate has a reversible reaction from anhydrous to sesquihydrate, displayed in equation 5.1. The estimated reaction crystal energy density is 1.3 – 1.4 GJ/m^3 [43,194].

$$K_2CO_{3\,(solid)} + 1.5H_2O_{\,(gas)} \leftrightarrow K_2CO_3 \cdot 1.5H_2O_{\,(solid)} \qquad 5.1$$

In Figure 5.6, the equilibrium temperature and deliquescence [195] lines for the selected material, together with the water saturation line are shown.

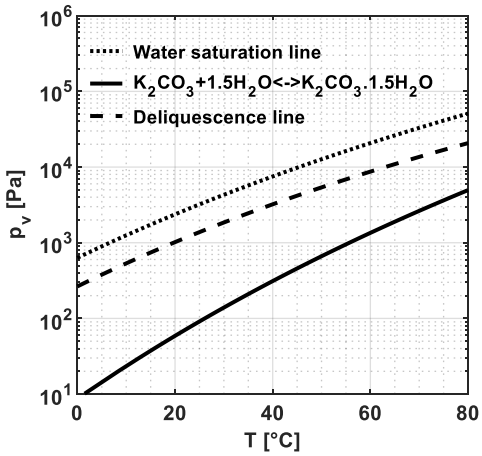

Figure 5.6: Equilibrium curve for $K_2CO_3 + 1.5H_2O \leftrightarrow K_2CO_3 \cdot 1.5H_2O$ (solid line), deliquescence line [195] **(dashed line), and water vapor saturation line (dash-dotted line).**

During desorption (Figure 4.1, top), warm air is flushed into the reactor and separates the water molecules from the porous material. As a result, a colder and more humid airflow exits from the system. During sorption (Figure 4.1, bottom), water vapor in the cold and humid airflow flushing the reactor produces an exothermic reaction with the porous material, and warm and drier air exits from the system. The STES is connected to both the heating grid HG and the low temperature district heating network DHN as shown in Figure 5.7. An air/water heat exchanger (HX1) connects the main heating grid to the storage in order to provide the necessary thermal energy for the desorption phase (i.e. storage charging). A second air/water heat exchanger (HX2) connects the storage to the low temperature heating network, for the sorption phase (storage discharging). In this work, it is assumed that both heat exchangers

can transfer the useful heat up to a minimum temperature difference between the two fluids of $\Delta T_{min,HX} = 1° C$. A heat recovery (HR) with a rated efficiency ε_{HR} of 90 % [107] is assumed in order to preheat the inlet air with the storage exhaust air. During the desorption phase (red line), the valves V1 and V2 direct the preheated airflow of state 2 towards the heat exchanger from the main heating grid where the air is heated with the water from the main heating grid (3_d), and valve V3 and V4 direct the airflow towards the heat recovery unit bypassing the DHN heat exchanger. During the sorption phase (blue line), the valves V1 and V2 bypass the heat exchanger used for the desorption phase (HX1) and direct the flow from the heat recovery unit towards the inlet of the reactor (3_s). Valve V3 directs the flow towards the heat exchanger for the low temperature DHN (4_s). In both sorption and desorption phases, the heat recovery unit preheats the inlet airflow with the waste heat remained after the thermal load (sorption phase) or the reactor desorption. Finally, only during sorption, the ambient airflow can be mixed with saturated air through valve V6 or mixed with the exhaust dry air through valves V5a and V5b (blue-black dashed lines). This is done in order to prevent the sorption material deliquescence, and to guarantee, where possible, a minimum temperature lift in the sorption reactor. The sorption reactor is divided conceptually into a set of units, or cylindrical segments ($N_{STES,tot}$). The segments are supposed to work in a parallel configuration in which every segment can be active or inactive. Therefore, if multiple segments are active at a certain timestep, they will be exposed to the same operating conditions in terms of airflow, inlet temperature and sorbate concentration.

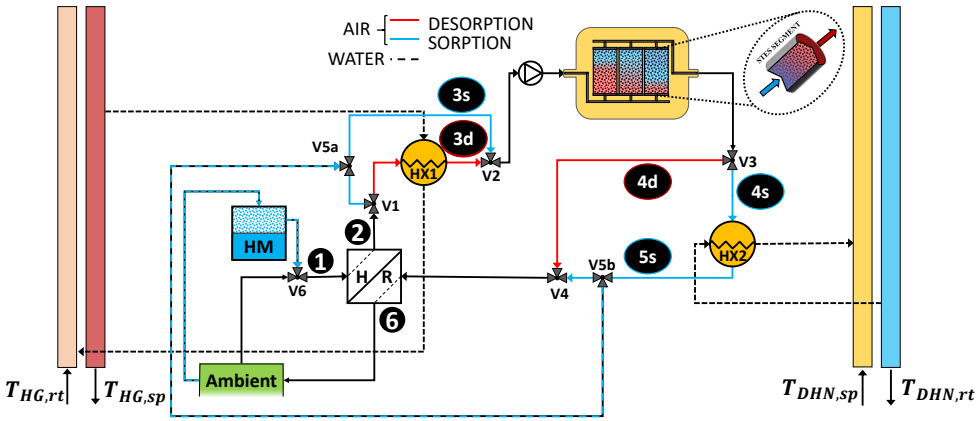

Figure 5.7: Sorption heat storage system integrated into the reference energy system. HM = humidification. HR = heat recovery. $T_{HG,sp}$ = 114 °C. $T_{HG,rt}$ = 70 °C. $T_{DHN,sp}$ = 55 °C. $T_{DHN,rt}$ = 30 °C.

The main objective of the STES model is to quantify the charging ($P_{STES-d,unit,t}$) and discharging ($P_{STES-s,unit,t}$) power required by every STES unit depending on the sorption material characteristics, the reactor main parameters, the ambient conditions and the technological characteristics of other system components such as the heat recovery unit.

The preheated reactor inflow air temperature during sorption (T_{2s}) can be calculated according to equations 5.2-5.3.

$$T_{3s,t} = T_{2,t} = T_{1,t} + \varepsilon_{HR}(T_{5s} - T_{1,t}) \quad 5.2$$

$$T_{5s} = T_{DHN,rt} + \Delta T_{min,HX} \quad 5.3$$

Where $T_{1,t}$, T_{5s} and $T_{DHN,rt}$ are the airflow temperatures at the inlet of the heat recovery unit and after the thermal load, and the DHN return temperature of the water, respectively. The temperature lift achieved from the exothermic reaction ($\Delta T_{lift,STES,t}$) and the reactor outlet temperature ($T_{4s,t}$), are estimated assuming that all the reaction energy is used to heat up the air flow, and that the outlet temperature cannot exceed the reaction equilibrium temperature ($T_{eq-s,t}$), according to equation 5.4-5.6.

$$T_{4s,t} = \min\left(T_{3s,t} + \Delta T_{lift,STES,t}, T_{eq-s,t}\right) \quad 5.4$$

$$\Delta T_{lift,STES,t} = \frac{c_{3s,t}\Delta H_{reac}}{\rho_a c_{p,a}} \quad 5.5$$

$$T_{eq-s,t} = \frac{-\Delta H_{reac}}{-\Delta S_{reac} - R_g ln\left(\frac{1}{p_{v,3s,t}\left(T_{3s,t}, c_{3s,t}\right)}\right)} \quad 5.6$$

Here, ΔH_{reac} and ΔS_{reac} are the enthalpy and entropy of reaction per mole of water, respectively. R_g is the ideal gas constant, $p_{v,3s,t}$ the water vapor pressure in the airflow at time t, and $c_{3s,t}$ the water vapor molar concentration. The inlet water vapor concentration has been calculated for the whole year from the weather data ($T_{amb,t}$ and $RH_{amb,t}$). Moreover, a lower and upper limit are assumed for c_{3s} in order to achieve a minimum temperature lift ($\Delta T_{lift,STES,t}$) and to prevent the sorption material deliquescence, respectively. In order to prevent that the sorbent material faces deliquescence due to too high values of sorbate concentration, an upper limit has been imposed ($c_{max,t} = 0.95c_{del,t}$) for the water vapor concentration. The limit is based on the sorbate concentration that would cause the sorbent material deliquescence ($c_{del,t}$), which is a function of the ambient relative humidity, based on the work of Greenspan et al. [195]. If, at specific times of the year, the ambient air would have a higher water vapor concentration than $c_{del,t}$, then it is mixed with part of the exhaust air at T_{5s}, assumed dry, with a mixing ratio $X_{mix,dry,t}$. The exhaust air is

assumed to be extracted before entering in the heat recovery unit, and it is mixed with the ambient airflow after the heat recovery unit. Counter wise, in order to guarantee a minimum amount of sorbate concentration in the airflow during sorption, it is also assumed that saturated air at a temperature T_{hum} of 10 °C is available. Therefore, providing that the maximum sorbate concentration $c_{max,t}$ is not exceeded, the incoming airflow can be humidified with a mixing ratio$X_{mix,hum,t}$ up to a maximum water vapor concentration of $c_{sat,10°C} = c(T = 10°C, RH = 100\ \%)$. This could be achieved, for example, by recovering part of the low temperature heat from the ORC cooling tower. Therefore, the concentration at every time step t of the year follows equation 5.7.

$$c_{3s,t} = \min\left(\max\left(c_{sat,10°C}, c_{amb,t}\right), c_{max,t}\right) \qquad 5.7$$

If air humidification occurs, then the incoming airflow temperature is calculated according to equation 5.8. Alternatively, if mixing with dry exhaust occurs, the resulting airflow temperature entering in the reactor ($T_{3s,t}$) is adjusted according to equation 5.9.

$$T_{1,t} = T_{hum}X_{mix,hum,t} + \left(1 - X_{mix,hum,t}\right)T_{amb,t} \qquad 5.8$$

$$T_{3s,t} = X_{mix,dry,t}T_{5s} + \left(1 - X_{mix,dry,t}\right)T_{2,t} \qquad 5.9$$

Here, $T_{2,t}$ is the temperature of the ambient air at the outlet of the heat recovery unit and T_{5s} is the exhaust air from the STES, after the thermal load. The thermal power from one STES unit discharge process ($P_{STES-s,unit,t}$) can be calculated according to equation 5.10, with $\dot{m}_a$ and $c_{p,a}$ the air mass flow and specific heat capacity, respectively.

$$P_{STES-s,unit,t} = \dot{m}_a c_{p,a}(T_{4s,t} - T_{3s,t}) \qquad 5.10$$

In equation 5.10, $T_{4s,t}$ and $T_{3s,t}$ are the airflow temperatures at the inlet and outlet of the heat exchanger transferring the heat to the thermal load (HX2). The STES discharging efficiency η_{STES-s}, defined as the amount of thermal power effectively transferred to the DHN, can be defined as in equation 5.11.

$$\eta_{STES-s,t} = \frac{T_{4s,t} - \left(T_{DHN,rt} + \Delta T_{min,HX}\right)}{T_{4s,t} - T_{3s,t}} \qquad 5.11$$

The energy transferred to the DHN water through the heat exchanger HX2 is calculated with equation 5.12.

$$P_{STES-DHN,unit,t} = \eta_{STES,s,t} P_{STES-s,unit,t} \quad 5.12$$

Finally, after the thermal load, the residual thermal energy in the airflow after the heat exchanger HX2 (at T_{5s}), is used in the heat recovery unit to preheat the incoming airflow (equation 5.2). Similarly, during the desorption phase, the inlet hot air temperature in the heat recovery unit corresponds to the outlet temperature of the reactor during desorption, which in turn is equal to the reaction equilibrium temperature ($T_{4d,t} = T_{eq-d,t}$). Thus, the preheated ambient air temperature ($T_{2d,t}$) can be estimated with equation 5.13.

$$T_{2d,t} = T_{1,t} + \varepsilon_{HR}(T_{4d,t} - T_{1,t}) \quad 5.13$$

$$T_{3d} = T_{HG,sp} - \Delta T_{min,HX} \quad 5.14$$

The preheated ambient air ($T_{2d,t}$) is heated up to the temperature T_{3d} (equation 5.14) in the heat exchanger HX1 from the main heating grid (HG) supply water flow at $T_{HG,sp}$. The water vapor concentration present in the air corresponds to the one at ambient conditions ($c_{1,t}$). In the desorption phase, there is no risk of material deliquescence nor a minimum concentration value has to be achieved. Therefore, minimum and maximum concentration limits are not required. The useful desorption energy for charging the STES ($P_{STES-d,unit,t}$) is only the one released above the reaction equilibrium temperature ($T_{eq-d,t}$), assuming that all the heat above $T_{eq-d,t}$ is absorbed in the reactor. Similar to the sorption phase, the desorption energy transferred from the heating grid (HG) to the airflow ($P_{STES-HG,unit,t}$) can be calculated according to equations 5.15-5.18.

$$T_{eq-d,t} = \frac{-\Delta H_{reac}}{-\Delta S_{reac} - R_g ln\left(\frac{1}{p_{v,3d,t}(T_{3d}, c_{1,t})}\right)} \quad 5.15$$

$$P_{STES-d,unit,t} = \dot{m}_a c_{p,a}(T_{3d} - T_{eq-d,t}) \quad 5.16$$

$$\eta_{STES-d,t} = \frac{T_{HG,sp} - T_{eq-d,t}}{T_{HG,sp} - T_{2d,t}} \quad 5.17$$

$$P_{STES-HG,unit,t} = \frac{P_{STES-d,unit,t}}{\eta_{STES-d,t}} = \dot{m}_a c_{p,a}\left(T_{HG,sp} - T_{2,t}\right) \quad 5.18$$

The maximum amount of energy that can be stored in one STES unit ($E_{STES,unit}$) can be calculated with equation 5.19.

$$E_{STES,unit} = \frac{(1-\varepsilon_b)\rho_{sm} V_{STES,unit} \nu \Delta H_{reac}}{M_{mol,sm}} \quad 5.19$$

Where ε_b is the porosity of the sorption material in the cylindrical packed bed, ρ_{sm} is the salt density, ν is the reaction stoichiometric coefficient (equation 5.1), $M_{mol,sm}$ is the salt molar mass, and $V_{STES,unit}$ is the volume of one STES unit. To estimate the electricity consumption required by the fan to drive the airflow through the porous cylindrical STES unit, the Ergun equation is used to estimate the pressure loss ($\Delta p_{STES,unit}$) and subsequently the fan consumption ($P_{fan,unit}$). A radial fan with a constant efficiency (η_{fan}) of 70 % is assumed [196] (equations 5.20 - 5.21).

$$\frac{\Delta p_{STES,unit}}{L_{STES,unit}} = \left(\frac{\alpha_{erg}\rho_a(1-\varepsilon_b)}{d_p \varepsilon_b^3}|u_a|^2 + \frac{\beta_{erg}\mu_a(1-\varepsilon_b)^2}{d_p^2 \varepsilon_b^3}|u_a|\right) \quad 5.20$$

$$P_{fan,unit} = \frac{\dot{m}_a \Delta p_{STES}}{\rho_a \eta_{fan}} \quad 5.21$$

Here, α_{erg} and β_{erg} are determined according to Cheng et al. [197], ρ_a is the air density, μ_a the air viscosity, d_p the particle diameter of the sorption material, u_a the superficial air velocity in the STES unit and $L_{STES,unit}$ the axial length of one STES unit.
From the economic perspective, the annual fixed STES cost ($C_{STES,fix}$) is calculated with equations 5.22 - 5.23, in which an annuity factor (AF) is taken into account.

$$C_{STES,fix} = N_{STES,tot} E_{STES,unit} SCC_{STES} AF \quad 5.22$$

$$AF = \frac{IR}{1-(1+IR)^{-lt_{STES}}} \quad 5.23$$

Here, $N_{STES,tot}$ is the total amount of STES units, SCC_{STES} is the fixed storage capacity cost expressed in €/kWh$_{cap}$, IR is the yearly interest rate and lt_{STES} is the STES operational

lifetime. The fixed reference storage capacity cost of the STES system (SCC_{STES}) used in this analysis was 2.5 €/kWh$_{cap}$ corresponding roughly to 0.4 €/kg$_{sm}$. However, this value would include only the active material costs, and it assumes an inexpensive material (see e.g. [19,34,125]). The cost of a full system will be higher, and it includes also the auxiliary materials and components of the storage such as the reactor costs in which the active material is contained, the fan cost, and the various heat exchangers. Due to the relatively low technology readiness level (TRL) of this storage technology, an exact prediction of these costs in terms of €/kWh$_{cap}$ is not possible. However, this cost can be varied to understand what is the approximate value of the maximum cost that makes the installation of the STES economically viable. Several material and STES parameters are assumed for the optimization model, and they are listed in Table 5.2. The reactor geometrical parameters ($d_{STES,unit}$, $L_{STES,unit}$) have been selected so that the single STES unit volume would be approximately 50 liters, a volume comparable to a prototype developed in Gaeini et al. [198,199]. The selected packed bed axial length ($L_{STES,unit}$) and diameter ($d_{STES,unit}$) result in a STES unit aspect ratio (d_{STES}/L_{STES}) of 0.7. The choice for this aspect ratio was based on the aspect ratio of an existing lab prototype [121]. These geometrical parameters lead to a STES unit coefficient of performance (COP) of approximately 100 during sorption mode, and between 140 and 240 during desorption mode. The STES COP and its influence on the overall performance of the energy system is investigated more in detail in Chapter 6. The sorption material density ρ_{sm} [200] and the packed bed porosity ε_b are assumed by considering the material in hydrated state. The selected airflow velocity in the packed bed is similar to the one used in Gaeini et al. [121,122].

Table 5.2: Main parameters for the heating grid (HG), low temperature district heating network (DHN), sorption thermal energy storage (STES), and the airflow in the STES.

Parameter	Value	Parameter	Value
STES		**HG**	
ρ_{sm} [kg/m^3]	2.4	$T_{HG,sp}$ [°C]	114
ΔH_{reac} [kJ/mol$_w$]	63.6	$T_{HG,rt}$ [°C]	70
ΔS_{reac} [J/(mol$_w$ ·K)]	155	$\dot{m}_{HG}$ [kg/s]	161
$M_{mol,sm}$ [g/mol]	165.2	**DHN**	
d_p [mm]	2.5	$T_{DHN,sp}$ [°C]	55
SCC_{STES} [€/kWh$_{cap}$]	2.5	$T_{DHN,rt}$ [°C]	30
$L_{STES,unit}$ [m]	0.5		
$d_{STES,unit}$ [m]	0.35	**STES Airflow**	
lt_{STES} [years]	20	u_a [m/s]	0.26
IR [%]	3	ρ_a [kg/m^3]	1.2
ε_b [-]	0.5	c_{p_a} [J/(kg·K)]	1004
ε_{HR} [-]	0.9	η_{fan} [-]	0.7

5.4 Optimization framework

In this section, the reference energy system and the market mechanisms described in sections 5.2 and 5.3 are formulated as a MILP optimization problem. Then, the scenarios in section 5.2.3 are investigated and the STES size and the system operational behavior are optimized with the aim of maximizing the yearly system profit. The structure of the optimization problem consists of a linear objective function, containing the optimization variables, to be minimized while respecting a series of linear optimization constraints. The objective function in this work aims at maximizing the overall system profits while the optimization constraints describe the techno-economic behavior of the system components and the market mechanisms. Within this work, the optimization variables are written in **bold** while known parameters and constants are given in plain text. The optimization temporal domain (t_{sim}) consists of one year of operation with a bi-hourly timestep ($\Delta t = 2$ h). A year simulation with an hourly resolution has been found too computationally expensive for the investigated model. With the bi-hourly resolution, a single optimization could take up to 6 hours with a machine consisting of an Intel® Core™ i7-7820HQ and 32 Gb of RAM. With a hourly resolution, the time required for a single simulation would generally increase exponentially [201]. The electricity price signals of the energy markets and the DHN demand, with an hourly resolution, have been averaged accordingly. Moreover, the periodicity of the time domain is imposed at the domain boundaries i.e. $\{t_1, \dots, t_{end}, t_1, \dots, t_{end}, t_1\}$. In this way, the STES state of charge ($\boldsymbol{SOC}_{STES,t}$) depending on its own value at the previous timestep can be represented with a yearly cyclic behavior (i.e. $\boldsymbol{SOC}_{STES,t_{sim}+1} = \boldsymbol{SOC}_{STES,1}$). The optimization model has been solved using MATLAB© as modeling environment, Gurobi [202] as solver, and YALMIP [203] as interface between the solver and the modeling environment.

5.4.1 Optimization variables

The main variables solved in the optimization model and their domain boundaries are displayed in Table 5.3. Continuous variables can have any value within their domain; integer variables can have only integers within their domain; and semi-continuous variables can take a value of zero or any value within a domain that has both lower and upper bounds in the positive numbers domain. The revenue variables can take positive numbers and they can be revenues from the DAM ($\boldsymbol{R}_{DAM,t}$) and STOR ($\boldsymbol{R}_{STOR,t}$) market calculated at every timestep of the temporal domain t_{sim} or they can be the revenues from the capacity market CM ($\boldsymbol{R}_{CM}$) that are independent of the time domain but depend only on the ORC power allocated during the CM-event. The cost variables $\boldsymbol{C}_t$ consider only the operational costs of the STES fan. The fixed STES cost $C_{STES,fix}$ is a parameter known a priori and based on the total number of storage units $N_{STES,tot}$ for a specific simulation. The ORC mass flow fraction $\boldsymbol{f}_{ORC,t}$ is a semi-continuous optimization variable defined at every timestep that can take the value of

zero or a number between the minimum ORC mass flow fraction and 1. The other mass flow fraction variables ($\boldsymbol{f}_{DHN,t}$, $\boldsymbol{f}_{STES,t}$, and $\boldsymbol{f}_{Res,t}$) can take any value from 0 to 1. The residual mass flow fraction ($\boldsymbol{f}_{Res,t}$) is defined in order to relax the optimization problem and track the amount of the main heating grid flow that the optimizer might not allocate to any of the three consumers. Its role is explained in more detail in section 5.4.2. The optimization variables for the electrical power at every moment in time ($\boldsymbol{P}_t$) track four different quantities defined in the set $\{ORC, DAM, STOR, fan\}$, at every moment in time. $\boldsymbol{P}_{ORC,t}$ is the power produced by the ORC, which is then divided into the power allocated to each market ($\boldsymbol{P}_{DAM,t}$ and $\boldsymbol{P}_{STOR,t}$). $P_{fan,t}$ is the power required by the STES fan for the STES charging or discharging process. The thermal power discharged from the STES for the DHN demand is defined as $\boldsymbol{P}_{STES-s,t}$ and it is defined in the negative domain representing the energy extracted from the STES. Conversely, the STES charging power required from the main heating grid ($\boldsymbol{P}_{STES-d,t}$) is defined in the positive domain. The number of STES units active at every moment in time $\boldsymbol{N}_{STES,t}$, either during the STES charge ($\boldsymbol{N}_{STES} > 0$) or the STES discharge ($\boldsymbol{N}_{STES} < 0$), are integer variables defined in the temporal domain. Therefore, a negative value of $\boldsymbol{N}_{STES,t}$ implies that the STES is discharging $\boldsymbol{N}_{STES,t}$ units (sorption), and a positive $\boldsymbol{N}_{STES,t}$ value implies that the STES is charging $\boldsymbol{N}_{STES,t}$ units (desorption). Finally, the STES state of charge ($\boldsymbol{SOC}_{STES,t}$) is defined as a continuous variable ranging from 0 to 1 at every moment in time.

Table 5.3: Main optimization variables types and boundaries. Variable types: C = continuous; I = integer; SC = semi-continuous.

Optimization variable	Type	Boundaries	Units
$\boldsymbol{R}_{CM}$	C	$[0, +inf)$	€
$\boldsymbol{R}_{DAM/STOR,t}$	C	$[0, +inf)$	€
$\boldsymbol{C}_t$	C	$[0, +inf)$	€
$\boldsymbol{f}_{ORC,t}$	SC	$\{0, [f_{ORC,min}, 1]\}$	-
$\boldsymbol{f}_{DHN/STES/Res,t}$	C	$[0,1]$	-
$\boldsymbol{P}_{ORC/DAM/STOR/fan,t}$	C	$[0, +inf)$	MW
$\boldsymbol{P}_{STES-d,t}$	C	$[0, +inf)$	MW
$\boldsymbol{P}_{STES-s,t}$	C	$[-inf, 0)$	MW
$\boldsymbol{N}_{STES,t}$	I	$[-N_{STES,tot}, N_{STES,tot}]$	-
$\boldsymbol{SOC}_{STES,t}$	C	$[0,1]$	-

5.4.2 Objective function and optimization constraints

The objective function $\boldsymbol{z}$ in the optimization problem aims at maximizing the overall profits of the investigated scenario over the simulated timeframe. It can be written as in equation 5.24.

$$min\, \boldsymbol{z} = C_{STES,fix} - \boldsymbol{R}_{CM} + \sum_{t=1}^{t_{sim}} (\boldsymbol{C}_t - \boldsymbol{R}_t) \qquad \forall t \quad 5.24$$

Here, $\boldsymbol{C}_t$ and $\boldsymbol{R}_t$ are the energy systems costs and revenues at time t, respectively.
The energy system costs taken into account in this work consist of the fixed and operational costs of the STES, the latter defined as in equation 5.25. $\boldsymbol{C}_t$ represents the cost of the energy ($\boldsymbol{P}_{fan,t}\Delta t$) used by the fan to drive the airflow.

$$\boldsymbol{C}_t = \boldsymbol{P}_{fan,t} p_{DAM,t} \Delta t \qquad \forall t \quad 5.25$$

The revenues are defined according to equations 5.26 - 5.27, and they are representing the profits generated by selling to the different markets the electricity produced from the ORC. In particular, equation 5.26 represents the revenues from the capacity market, calculated as the power allocated during the CM-event ($\boldsymbol{P}_{CM}$) multiplied by the CM price p_{CM} expressed in €/(MW·h).

$$\boldsymbol{R}_{CM} = \boldsymbol{P}_{CM} p_{CM} \qquad 5.26$$

$$\boldsymbol{R}_t = \sum_{k=\{\mathrm{DAM,STOR}\}} \boldsymbol{P}_{k,t} p_{k,t} \Delta t \qquad \forall t \quad 5.27$$

The net electrical power of the ORC is estimated with the performance maps generated with an off-design ORC model (see section 5.3.3). Being a deterministic model, the ambient conditions are known a priori for the whole simulation temporal domain t_{sim}. Therefore, only the mass flow fraction from the heating grid to the ORC evaporator $\boldsymbol{f}_{ORC,t}$ is an optimization variable. Thus, at every moment in time, the 3D-performance maps (Figure 5.5 left) are projected into a 1D function of the mass flow fraction $\boldsymbol{f}_{ORC,t}$ (Figure 5.5 right). This nonlinear relationship has been approximated with piecewise linear functions, which can be implemented into the MILP modeling framework [204]. In particular, for given ambient conditions, the resulting 1D-performance map of output power versus flowrate (Figure 5.5, right) is divided into 4 linear segments for every time step. The number of linear segments is a compromise between accuracy and computational cost. A higher resolution (i.e. a higher number of segments) would have caused a too computationally expensive model due to the high amount of additional integer variables required. A constraint (equation 5.28) is used to impose that the electrical power produced by the ORC has to be equal to the one delivered to the markets, and equal or greater than the one delivered during the CM-event (equation 5.29).

$\boldsymbol{P}_{CM}$ is a sparse vector in which the only nonzero elements are those at timesteps where the CM-event is imposed.

$$\boldsymbol{P}_{ORC,t} = \sum_{k=\{\mathrm{DAM,STOR}\}} \boldsymbol{P}_{k,t} \qquad \forall t \quad 5.28$$

$$\boldsymbol{P}_{ORC,t} \geq \boldsymbol{P}_{CM,t} \qquad \forall t \quad 5.29$$

The DHN thermal energy balance is imposed with equation 5.30. It implies that the thermal energy supplied by the main heating grid HG through the mass flow fraction $\boldsymbol{f}_{DHN,t}$,and the one from the sorption reactor discharge are equal to the total thermal energy demand from the dwellings. It is remarked that, in equation 5.30, $P_{STES-s,t}$ has negative values according to its definition.

$$\boldsymbol{f}_{DHN,t}\dot{m}_{HG}c_{p,w}\left(T_{HG,sp} - T_{HG,rt}\right) - P_{STES-s,t}\eta_{STES,s} = P_{DHN,t} \qquad \forall t \quad 5.30$$

The mass balance of the main heating grid is defined in equation 5.31. It implies that the sum of the mass flow fractions directed towards the DHN, ORC, STES, and the residual mass flow fraction ($\boldsymbol{f}_{Res,t}$) are equal to one at every moment in time.

$$\boldsymbol{f}_{DHN,t} + \boldsymbol{f}_{ORC,t} + \boldsymbol{f}_{STES,t} + \boldsymbol{f}_{Res,t} = 1 \qquad \forall t \quad 5.31$$

The objective function displayed in equation 5.24 is minimized when all the thermal energy from the main heating grid is allocated at every moment in time. However, there can be moments in time in which this is not possible, and a relatively small amount of energy cannot be allocated. In particular, the energy from the main heating grid cannot be completely allocated when, at the same moment, the STES is fully charged, the DHN demand is not requiring more energy than what the main heating grid is already delivering, and the mass flow fraction directed towards the ORC would be lower than the minimum mass flow allowed for the ORC to work. Without the relaxing variable $\boldsymbol{f}_{Res,t}$, the equality in 5.31 can lead to an unfeasible optimization problem for certain timesteps. Alternatively, equation 5.31 can be seen also as an inequality in which the $\boldsymbol{f}_{Res,t}$ is not present and the sum of the other terms must be lower than or equal to one. In a real system, a value of $\boldsymbol{f}_{Res,t}$ larger than zero would imply that the main heating grid return temperature ($T_{HG,rt}$) increases. Therefore, the magnitude of $\boldsymbol{f}_{Res,t}$ can be interpreted as a measure of which the assumption of having a fixed supply and return temperature of the main heating grid is respected.
The STES constraints define the mass flow fraction from the heating grid that is required during the STES charging (equation 5.32), the STES state of charge (equation 5.33), the

overall discharge (equation 5.34) and charge power (equation 5.35), and the STES fan power (equation 5.36).

$$\boldsymbol{f}_{STES,t} = \frac{P_{STES-d,t}}{\eta_{STES-d}\dot{m}_{HG}c_{p,w}(T_{HG,sp} - T_{HG,rt})} \qquad \forall t \qquad 5.32$$

$$\boldsymbol{SOC}_{STES,t} = \boldsymbol{SOC}_{STES,t-1} + \frac{(\boldsymbol{P}_{STES-d,t} + \boldsymbol{P}_{STES-s,t})\Delta t}{N_{STES,tot}E_{STES,unit}} \qquad \forall t \qquad 5.33$$

$$\boldsymbol{P}_{STES-s,t} = \begin{cases} 0 & \boldsymbol{N}_{STES,t} > 0 \\ \boldsymbol{N}_{STES,t}P_{STES-s,unit} & \boldsymbol{N}_{STES,t} \leq 0 \end{cases} \qquad \forall t \qquad 5.34$$

$$\boldsymbol{P}_{STES-d,t} = \begin{cases} \boldsymbol{N}_{STES,t}P_{STES-d,unit} & \boldsymbol{N}_{STES,t} \geq 0 \\ 0 & \boldsymbol{N}_{STES,t} < 0 \end{cases} \qquad \forall t \qquad 5.35$$

$$\boldsymbol{P}_{fan,t} = |\boldsymbol{N}_{STES,t}|P_{fan,unit} \qquad \forall t \qquad 5.36$$

Where $\boldsymbol{SOC}_{STES,t}$ and $\boldsymbol{SOC}_{STES,t-1}$ are the STES state of charge at the current and previous time, respectively, and Δt is the simulation timestep of 2 hours. In order to formulate the optimization problem minimizing the required amount of constraints, a sign convention for $\boldsymbol{N}_{STES,t}$ is adopted, and a piecewise linear representation of the terms $\boldsymbol{P}_{STES-d,t}$, $\boldsymbol{P}_{STES-s,t}$, and $\boldsymbol{P}_{fan,t}$ is made. The domain of the optimization variable $\boldsymbol{N}_{STES,t}$ has the range $[-N_{STES,tot}\ ,\ N_{STES,tot}]$, in which negative values imply that the reactor units are discharging, and positive values imply that the reactor units are charging. Furthermore, the values of the overall charging and discharging STES powers are equal to zero for the domain side (negative or positive, respectively) in which they have no physical meaning (Figure 5.8).

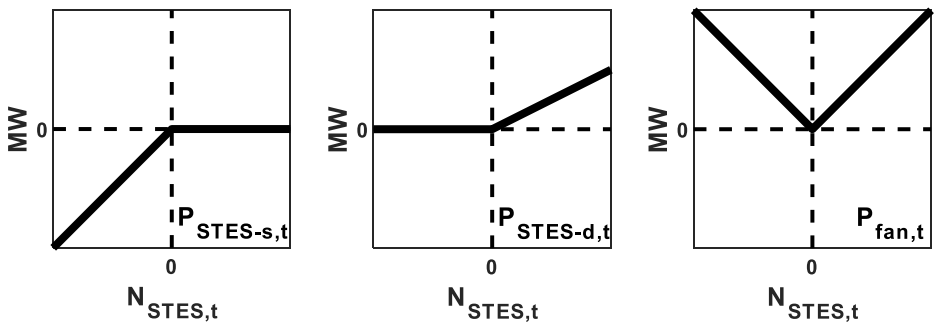

Figure 5.8: Conceptual graph of the reactor discharging ($P_{STES,s,t}$), charging ($P_{STES,d,t}$), and fan ($P_{fan,t}$) powers in function of the amount of active units $N_{STES,t}$ on the left, middle, and right, respectively.

For example, the STES charging power ($\boldsymbol{P}_{STES-d,t}$) has nonzero values in the positive domain and a value of zero in the negative domain (equation 5.35). It remarked that the slopes of the two lines for $\boldsymbol{P}_{STES-s,t}$ and $\boldsymbol{P}_{STES-d,t}$ are different because $P_{STES-s,unit,t}$ and $P_{STES-d,unit,t}$ are calculated differently (equations 5.10 and 5.16, respectively).
The optimization problem consists of minimizing the objective function (equation 5.24) subject to the constraints expressed in equations 5.25 - 5.36. Different optimizations are performed by varying the STES storage size (i.e. by varying $N_{STES,tot}$) in order to identify the optimal STES size, with the optimal operational behavior, that maximizes the objective function.

5.5 Results

In this section, the scenarios presented in 5.2.3 are investigated for the reference energy system presented in 5.2.1 operating in the markets described in section 5.2.2. In 5.5.1, a main overview of the scenarios is given through representative economic indicators. Then, every scenario is individually analyzed from section 5.5.2 to 5.5.5.
In order to evaluate the system performance from an economic perspective, three main indicators are selected: the relative profit increase (RPI), the normalized net present value ($NNPV$) and the levelized cost of storage ($LCOS$). The relative profit increase is defined as in equation 5.37, in which $\boldsymbol{z}$ is the value of the objective function for a specific STES size (defined as in equation 5.24), and $\boldsymbol{z}_{N_{STES,tot}=0}$ is the value of the objective function without the STES integrated into the energy system.

$$RPI = \frac{\left(\boldsymbol{z} - \boldsymbol{z}_{N_{STES,tot}=0}\right)}{\boldsymbol{z}_{N_{STES,tot}=0}} \qquad 5.37$$

The NPV, expressed in €, is calculated according to equation 5.38.

$$NPV = -N_{STES,tot}E_{STES,unit}SCC_{STES} + \sum_{i=1}^{lt_{STES}} \frac{\left(\boldsymbol{R}_{CM} + \sum_{t=1}^{t_{sim}}(\boldsymbol{R}_t - \boldsymbol{C}_t)\right)}{(1+IR)^i} \qquad 5.38$$

Here, t_{sim} represents the overall number of timesteps in the temporal domain, the first term on the right-hand side accounts for the STES CAPEX (capital expenditure) and the second term on the right-hand side represents the yearly cashflow stream. In this term, the double summation represents the yearly cashflow streams accounted for every year of the assumed STES lifetime. For each scenario, the NPV is normalized with respect to the NPV of the solution without the STES (equation 5.39).

$$NNPV = \frac{NPV}{NPV_{N_{STES,tot}=0}} \tag{5.39}$$

The levelized cost of storage is defined according to equation 5.40 and expressed in €/MWh.

$$LCOS = \frac{N_{STES,tot} E_{STES,unit} SCC_{STES} + \sum_{i=1}^{lt_{STES}} \left(\frac{\sum_{t=1}^{t_{sim}} (\boldsymbol{C}_t)}{(1+IR)^i} \right)}{\sum_{i=1}^{lt_{STES}} \left(\frac{\sum_{t=1}^{t_{sim}} (\boldsymbol{P}_{STES-s,t} \eta_{STES-s} \Delta t)}{(1+IR)^i} \right)} \tag{5.40}$$

Here, the first and second term of the numerator represent the initial investment for the STES and the yearly STES OPEX (operating expense), respectively. The denominator represents the yearly energy delivered from the STES to the DHN. It has to be remarked that in the NPV and $LCOS$ definition, further revenue and cost streams can be present, such as fixed and variable yearly maintenance costs, decommissioning costs, taxes and subsidies. Within this analysis, the abovementioned cashflow streams are not included.

5.5.1 Results overview

For each scenario highlight (Figure 5.9), the relative profit increase compared to the alternative of not having a storage for the investigated number storage units $N_{STES,tot}$ is displayed. The storage units are also expressed in terms of storage volume, estimated by only considering the sorption material volume.

From Figure 5.9, it is shown that for S1 the optimal solution does not include the storage. The reason is that the storage integration, even with the smallest investigated size, would have resulted in STES CAPEX and OPEX higher than the additional revenues stream generated by the ORC thanks to the STES presence. In S2, the optimal solution includes the storage, 10^3 units (~48 m^3), but the relative profit increase of ~0.03 % is so small compared to the solution without the storage that it is irrelevant.

In scenario S3, in which the CM service is active, the inclusion of the storage up to a size of 10^4 units (~481 m^3) increases the relative profit up to 3.2 %. Finally, S4 is the scenario with the highest amount of relative profit increase (41.3 %) in the optimal solution with $2 \cdot 10^4$ units (~962 m^3). For all scenarios, a relative profit decrease by increasing the amount of storage units means that the additional investment and operational STES costs would be higher than the revenues increase from the ORC.

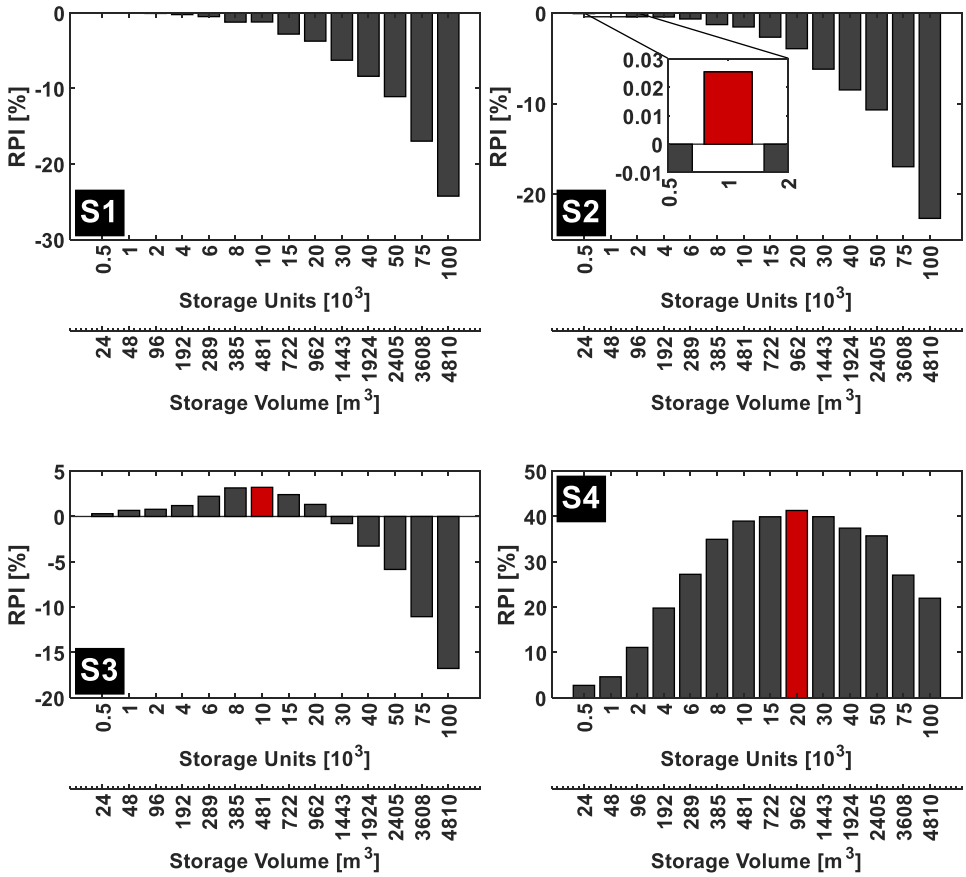

Figure 5.9: Relative profit increase (*RPI*) for the investigated scenarios by varying the STES size. Top left: Scenario S1 (Belgium, DAM). Top right: Scenario S2 (UK, DAM). Bottom left: Scenario S3 (UK, DAM+CM). Bottom right: Scenario S4 (UK, DAM+CM+STOR). STES size expressed in thousands of units and m^3 of sorption material.

Concerning the share of thermal energy from the heating grid (Figure 5.10), for S1 the fractions to the ORC and DHN are approximately 69.9 % and 29.8 %. For S2, the fractions were 69.8 %, 29.4 % and 0.4 % for the STES. On the other hand, the scenarios in UK, in which the balancing services were active, had an increase in overall profits by the STES integration into the energy system. For S3, the overall mass flow fractions directed to the three consumers during the system yearly operation are 69.1 % for the ORC, 24.7 % for the DHN, and 5.9 % for the storage. Finally, for S4, 8.7 % of the main grid energy is delivered to the STES, 68.7 % to the ORC, and 22.4 % to the DHN. It is remarkable to notice that, for roughly the same amount of main heating grid mass flow delivered to the ORC, compared to other scenarios, the STOR balancing service coupled to the STES dramatically increases the system profits (Figure 5.9 right).

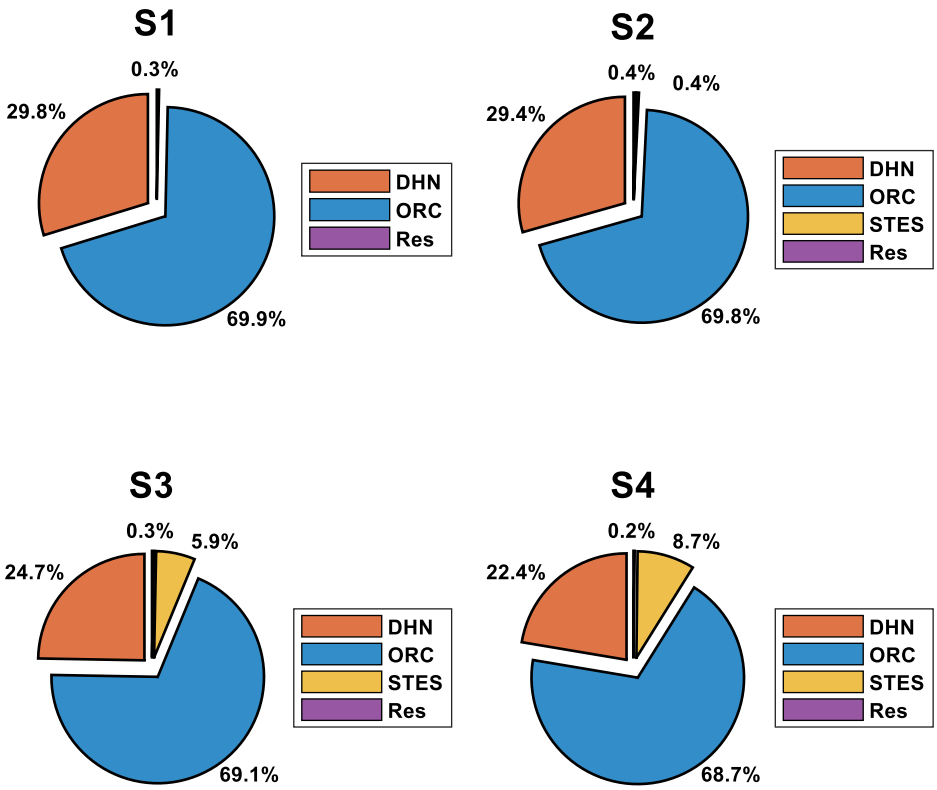

Figure 5.10: Thermal energy share from the main heating grid for the solution with the optimal STES size. Top left: Scenario S1. Top right: Scenario S2. Bottom left: Scenario S3. Bottom right: Scenario S4.

This is done by maximizing the energy produced by the ORC when the STOR market is active and providing the thermal energy to the DHN by discharging the STES as much as possible.

Finally, the normalized net present value ($NNPV$), levelized cost of storage ($LCOS$), and STES equivalent cycles for the scenarios in which the optimal solution included the STES (S2, S3, and S4) are shown in Figure 5.11. As expected also from Figure 5.9, the $NNPV$ for scenario S2 is almost equal to zero, meaning that investing in the STES would not contribute positively to the overall system profits. For scenarios S3 and S4 the $NNPV$ of the optimal solution is 3.21 % and 39.32 % meaning that the investment is profitable. This economic indicator is similar to the relative profit increase from Figure 5.9. However, the difference between the two indicators arises from the discounted cashflows over the STES lifetime

(lt_{STES}) that are present in the $NNPV$ calculation while for the relative profit increase only one year of operation is considered and part of the investment (equation 5.22) is compounded into it through the annuity factor (AF).

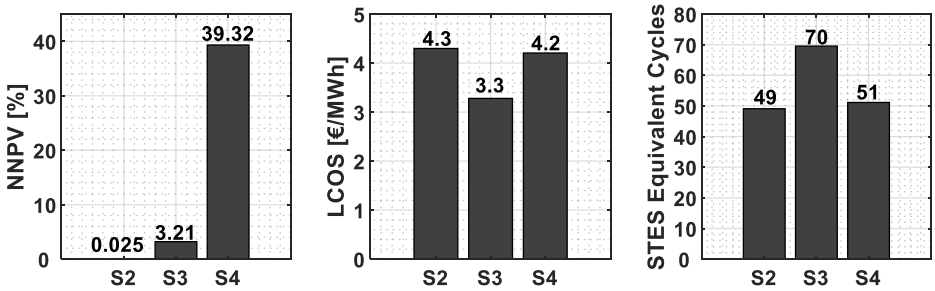

Figure 5.11: $NNPV$ (left), levelized cost of storage (middle), and STES equivalent cycles (right) for scenarios S2, S3, and S4 with the optimal STES size.

Concerning the $LCOS$, scenarios S2 and S4 have similar values, 4.3 and 4.2 €/MWh, respectively, while scenario S3 had an $LCOS$ of 3.3 €/MWh. This trend suggests that, for scenario S3, the yearly amount of energy delivered from the STES to the DHN relative to the storage installed capacity is higher compared to S2 or S4. This can be verified with Figure 5.11 right, in which the equivalent STES cycles are calculated by making the ratio between the yearly amount of thermal energy delivered to the DHN and the STES installed capacity. The difference in equivalent cycles can be due to the fact that, in scenario S3, the STES size is optimized for the CM-event, which has a duration of 4 hours. For the rest of the year, in S3, a STES size considerably larger than for scenario S2 is operating in the same DAM. The resulting STES operational behavior therefore can be different and it can have a larger impact on the final objective compared to a smaller STES.

5.5.2 Scenario S1 – Belgian DAM

Scenario S1 investigates the energy system within the Belgian market, in which no balancing services are considered. In Figure 5.12, the 2 hours averaged DAM prices for 2013 [205] are displayed, and a cyclic behavior of the electricity prices through the week can be noticed . In particular, the business days have a different pattern than the weekends. Moreover, it is also possible to see that in June, negative prices have been recorded with a minimum of 200 €/MWh. The reason was a combination of factors, namely a low local energy demand combined with a high renewable energy sources penetration, must-run conditions of conventional power plants, and constrained network export capabilities [206].
In Figure 5.13 left, the amount of yearly energy sold on the DAM market above and below the yearly average price $p_{DAM,mean}$ is displayed as a function of the number of storage units. By increasing the amount of storage units, the increase of energy sold at prices above $\bar{p}_{DAM}$

is only slightly increasing. Without the storage, 53.6 % of the total energy is sold above $\bar{p}_{DAM}$. This is because the ORC operation is strictly bounded to the DHN demand, with no possibility to decouple the two i.e. the main heating grid mass flow allocated for the ORC energy production can only be the fraction not used, at the same moment, for the DHN demand. The maximum percentage is achieved with $75 \cdot 10^3$ units (56.2 %) but the STES cost leads to a lower profit (-17 %) compared to not having the storage at all (Figure 5.9 top left) since price differences on the DAM are rather limited.

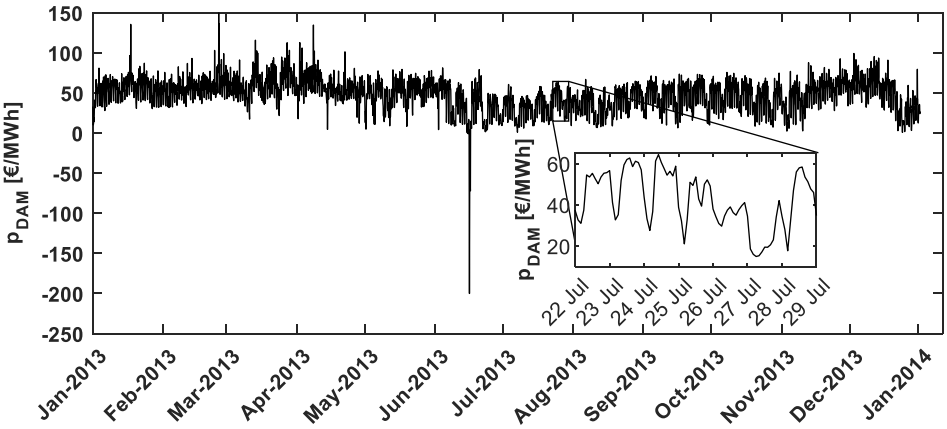

Figure 5.12: Electricity price expressed in €/MWh for DAM. Zoomed graph between 22nd of July and 27th of July.

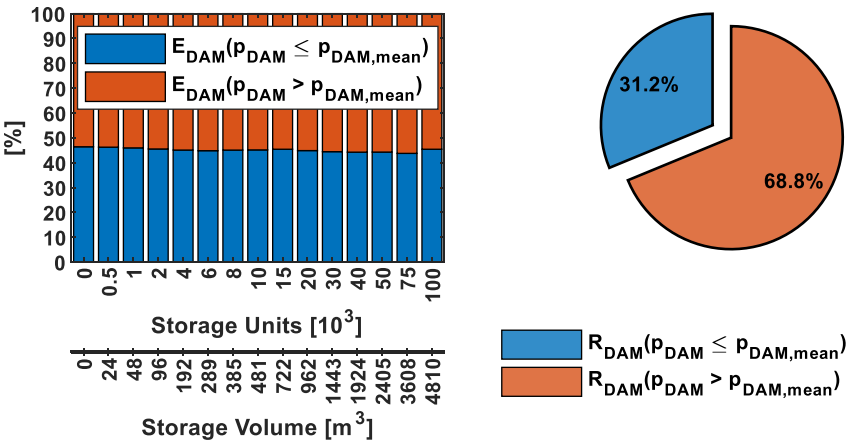

Figure 5.13: Left: Yearly energy sold on the DAM at a price above (red) and below (blue) the yearly average market price $p_{DAM,mean}$ for S1. Right: Revenues of the optimal solution (0 STES units) for scenario S1. Red: revenues from DAM sales above $p_{DAM,mean}$. Blue: revenues from DAM sales below $p_{DAM,mean}$.

Finally, in Figure 5.13 right, the yearly revenues of the optimal solution for S1, divided by the total yearly revenue, is shown. In this scenario, in which only the DAM is active, 54 % of energy sold above $p_{DAM,mean}$ (first bar of Figure 5.13 left) contributes for a 68.8 % to the total revenues while the rest contributes for 31.2 %.

5.5.3 Scenario S2 – UK DAM

Scenario S2 assumes that the investigated energy system is located in UK and that the only service available for the ORC for selling electrical energy is the day ahead market. In Figure 5.14, the 2 hours averaged price signal of the UK DAM is shown, for 2017. The highest price spike happened on May 17th. On that day, wind and solar dropped by two-thirds from the previous day, and several coal units had to be started up to fill the production gap [207]. Negative prices were also present (e.g. June 7th) for similar reasons described in section 5.5.2.

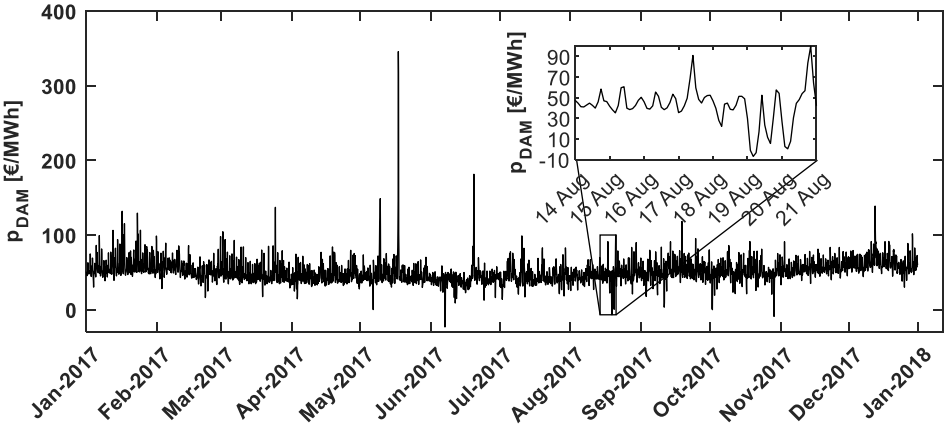

Figure 5.14: Electricity price expressed in €/MWh for DAM. Zoomed graph between 14th of August and 21st of August.

The optimal amount of STES units for the investigated energy system is 10^3. However, this led to a profit increase of only 0.03 % (Figure 5.9) compared to not having the storage installed at all. Nevertheless, it is interesting to look at the techno-economic behavior of the energy system. In Figure 5.15, the results are displayed over a representative time span of three days (2/04 – 5/04) are displayed. The ORC power produced (top right) in this period is fluctuating between 1 MW and 2 MW, approximately, and the revenues (bottom right) are varying from 50 € to 300 € every 2 hours. In order to maximize f_{ORC} (top left) during the electricity price spikes (e.g. 2/04 at 18:00), the STES is discharged (middle left) in order to partially provide the DHN demand (bottom left).

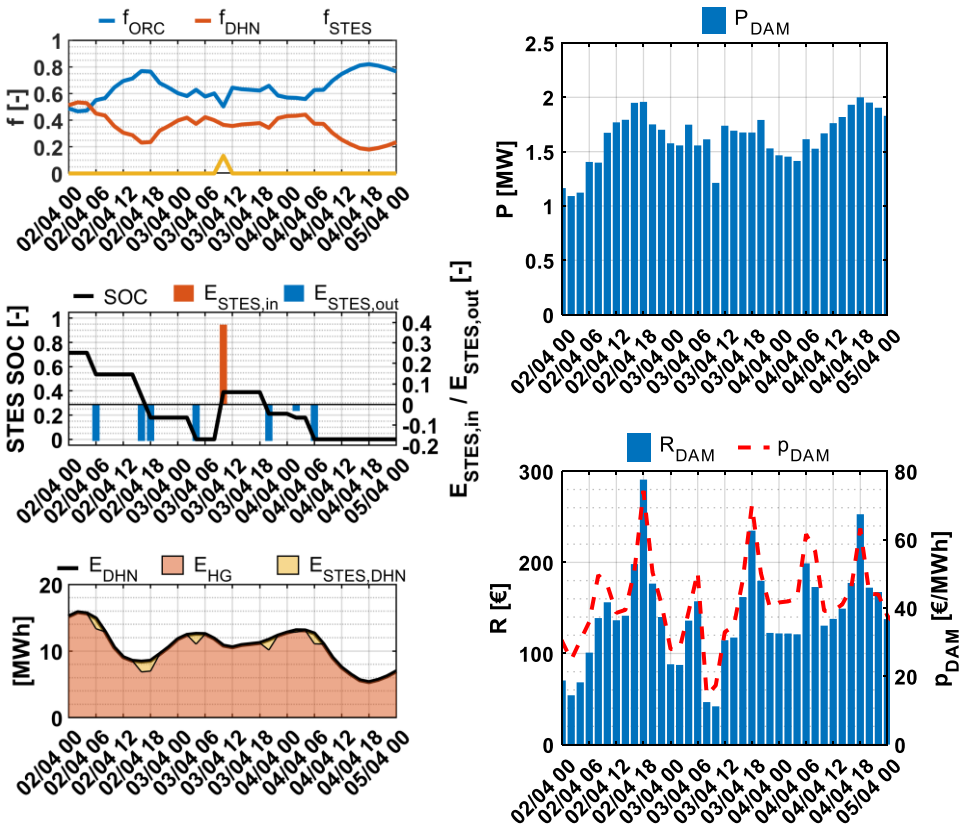

Figure 5.15: Operational behavior of S2 over 3 days for the optimal solution (10^3 STES units). Top left: mass flow fractions from the main heating grid to the district heating network (f_{DHN}), the ORC (f_{ORC}), and the STES (f_{STES}). Middle left: STES state of charge (SOC_{STES}) and normalized STES input ($E_{STES,in}$) and output energy ($E_{STES,out}$). Bottom left: District heating demand (E_{DHN}) provided by the main heating grid (E_{HG}) and by the STES ($E_{STES,DHN}$). Top right: Electrical power produced from the ORC for the day ahead market (P_{DAM}). Bottom right: Revenues from the day ahead market (R_{DAM}) and day ahead market electricity price (p_{DAM}).

In Figure 5.16 left, it is shown that, as opposite of S1 (Figure 5.13 left), most of the energy produced from the ORC is sold at a price below the yearly average DAM price. Without having a storage, 39.06 % of the energy is sold above $p_{DAM,mean}$. With the optimal number of storage units, it would be 39.5 % while the maximum achieved (41.6 %) coincides with the maximum amount of storage units investigated ($100 \cdot 10^3$). However, having $100 \cdot 10^3$ storage units would cause a profit decrease of -23 % (Figure 5.9 top right) compared to not having the storage at all.

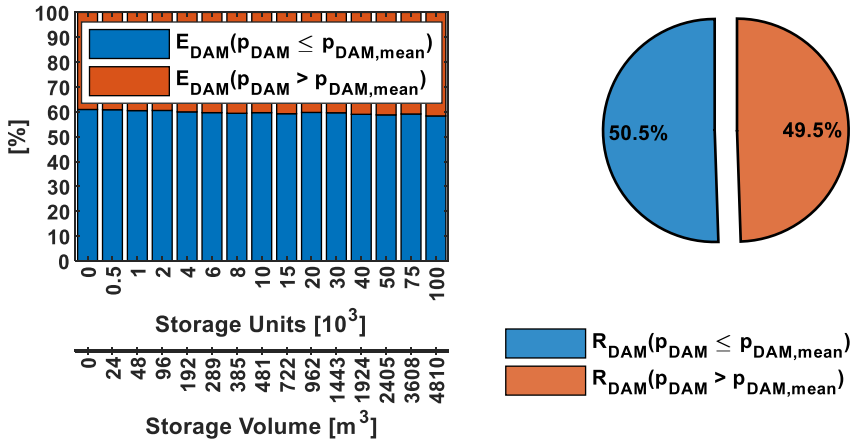

Figure 5.16: Left: Yearly energy sold on the DAM at a price above (red) and below (blue) the yearly average market price $p_{DAM,mean}$ for S2. Right: Revenues of the optimal solution (10^3 STES units) for scenario S2. Red: revenues from DAM sales above $p_{DAM,mean}$. Blue: revenues from DAM sales below $p_{DAM,mean}$.

The yearly revenues generated by selling the ORC energy to the DAM market at a price above or below $p_{DAM,mean}$, for the optimal amount of storage units, are almost equally contributing to the overall amount of revenues.

5.5.4 Scenario S3 – UK DAM-CM

Scenario S3 involves an additional market service in which the ORC can operate: the capacity market (CM). S3 assumes the same price signals as scenario S2 for the DAM market. The additional revenues from the CM are proportional to the amount of energy that the ORC can provide to the network during a stressful event (CM-event). In Figure 5.17, the techno-economic behavior of the system is shown for a period involving the CM-event, on January 5th between 12 pm and 4 pm. It is possible to see that during the event, although the DAM price is not at a relatively high peak (bottom right), all the mass flow from the main heating grid is directed towards the ORC (top left) and the DHN demand (bottom left) is provided entirely by the STES discharge (middle left).

In Figure 5.18 left, the committed amount of ORC power during the CM-event, relative to the maximum ORC power during those environmental conditions, is shown. It is possible to see that a large increase is present especially for 10^3 to 10^4 storage units. Within this interval, the ORC committed power during the CM-event increases from 51.1 % to 98.1 %.

A higher amount of storage units leads to a moderate improvement. For this reason, the optimal solution for S3 includes 10^4 storage units, and further increasing the number of units is not beneficial and indeed it leads to a relative profit decrease (Figure 5.9 bottom left).

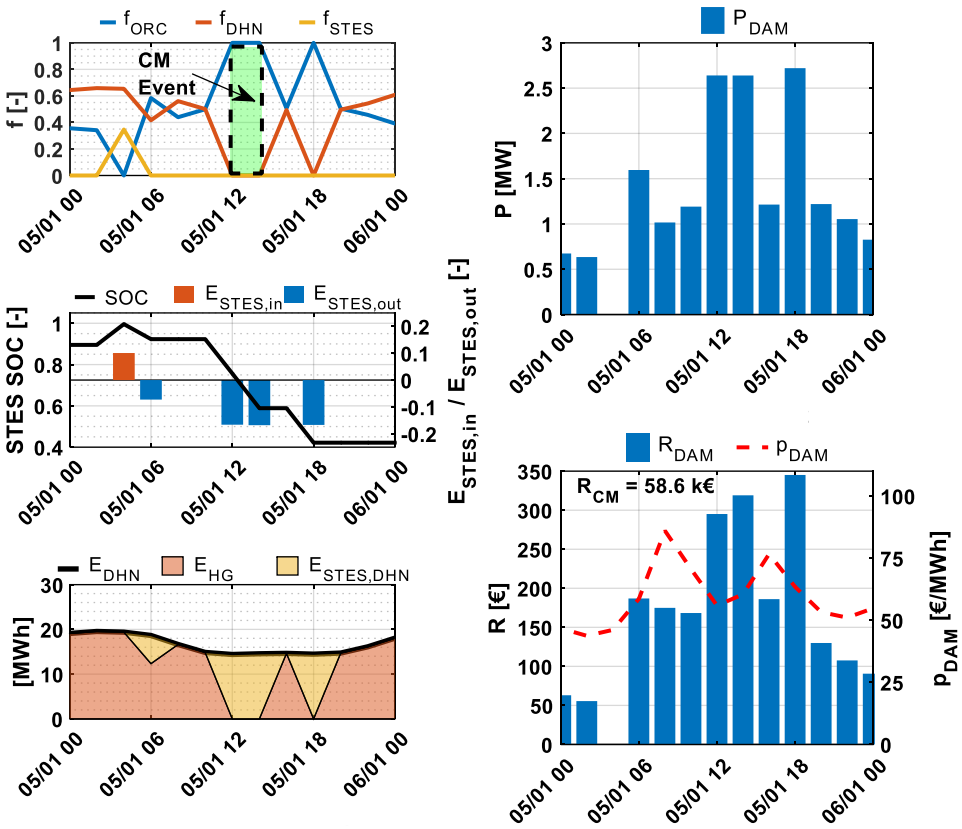

Figure 5.17: Operational behavior of S3 for the CM event day for the optimal solution (10^4 STES units). Top left: mass flow fractions from the main heating grid to the district heating network (f_{DHN}), the ORC (f_{ORC}), and the STES (f_{STES}). Middle left: STES state of charge (SOC_{STES}) and normalized STES input ($E_{STES,in}$) and output energy ($E_{STES,out}$). Bottom left: District heating demand (E_{DHN}) provided by the main heating grid (E_{HG}) and by the STES ($E_{STES,DHN}$). Top right: Electrical power produced from the ORC for the day ahead market (P_{DAM}). Bottom right: Revenues from the day ahead market (R_{DAM}), CM market (R_{CM}) and day ahead market electricity price (p_{DAM}).

In Figure 5.18 right, a sensitivity analysis on the STES capacity cost is shown. The storage capacity cost is varied from 2.5 €/kWh$_{cap}$ to 12.5 €/kWh$_{cap}$. The amount of STES units for each optimal solution is shown between round brackets next to the markers, and it is expressed in thousands of units. The amount of storage units in the optimal solution tends to decrease with the increase in storage capacity costs. The reason is that the profit gain due to the storage operation is not counterbalancing the increased fixed cost of the storage. Therefore, a solution with a smaller storage size becomes optimal. A storage capacity cost increase from 2.5 €/kWh$_{cap}$ to 5 €/kWh$_{cap}$ is more than halving the relative profit increase

from 3.2 % to 1.3 %. Further increase in the capacity cost above 7.5 €/kWh$_{cap}$ leads the STES to be economically unfeasible.

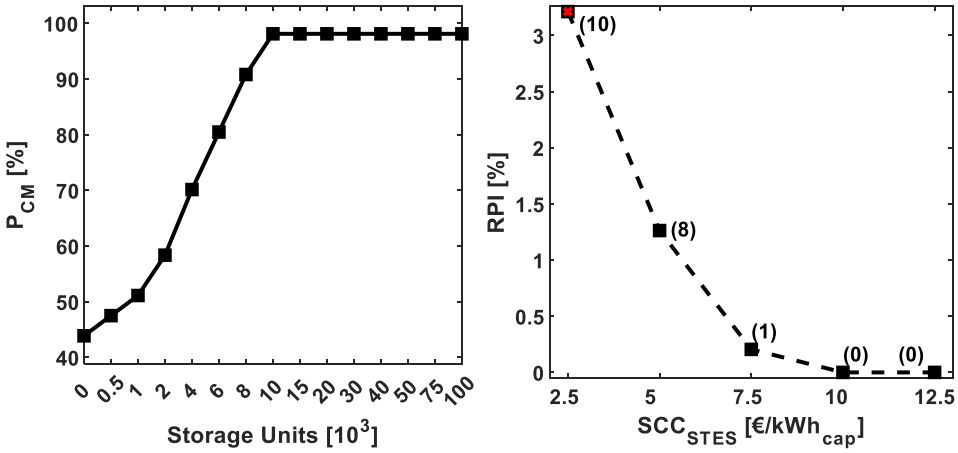

Figure 5.18: Left: ORC power production during the CM-event (P_{CM}) compared to the maximum producible ORC power during the CM-event. Right: Relative profit increase compared to the alternative of not having a storage for the optimal solutions in function of the fixed STES cost for S3. The amount of storage units in every optimal solution is expressed, between round brackets, in thousands of units. Red marker: Initial reference value.

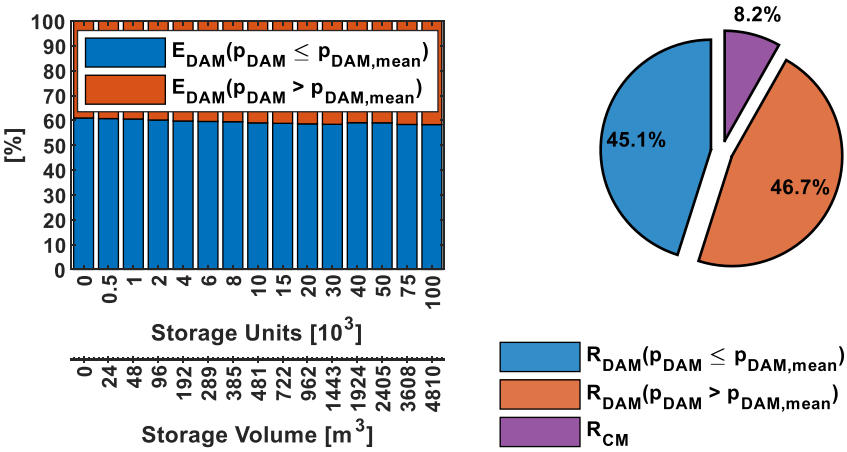

Figure 5.19: Left: Yearly energy sold on the DAM at a price above (red) and below (blue) the yearly average market price $p_{DAM,mean}$ for S3. Right: Revenues of the optimal solution (10^4 STES units) for scenario S3. Red: revenues from DAM sales above $p_{DAM,mean}$. Blue: revenues from DAM sales below $p_{DAM,mean}$. Purple: revenues from the capacity market.

The amount of energy sold in the DAM market above and below the yearly average price (Figure 5.19 left) is very similar to scenario S2. The reason is that the DAM market prices

are the same as in S2, and the difference relies on a market event (CM-event) of approximately 4 hours, which is only slightly influencing the yearly operational behavior of the system. For S3, the optimal solution with $8 \cdot 10^3$ storage units, leads to an energy share sold above $p_{DAM,mean}$ of 46.7 %. Concerning the yearly revenues, by maximizing the ORC power produced during the CM-event led to additional revenues (Figure 5.19 right) accounting for 8.2 % of the total revenues flow. The remainder is almost equally spread between the energy sales in the DAM above and below $p_{DAM,mean}$.

5.5.5 Scenario S4 – UK DAM-CM-STOR

In scenario S4, the STOR market is added as possible source of revenues in selling the ORC energy. The same price signals for the DAM and capacity market conditions of scenario S3 are assumed. In this scenario, the power delivered to the ORC during the STOR availability windows is maximized since the STOR utilization price is greater than the average DAM price. Therefore, operating as much as possible in this market is convenient for the energy system. In Figure 5.20 left, the operational behavior of the system is shown. On the top left it is shown how, during the STOR windows, the mass flow from the main heating grid is mostly directed towards the ORC and the DHN demand is supplied partially or totally by the STES (bottom left). Outside the STOR availability windows and when $\bar{p}_{DAM}$ is relatively low, the system charges the STES (e.g. 31/03 at 00:00). In Figure 5.20 top right, the ORC power sold to the STOR market (red) or to the DAM (blue) is shown. It is shown that the power sold to the STOR is constant through the same STOR season. In particular, in Figure 5.20 bottom right, it is possible to see that the STOR season changes from season 6 to season 1 on 1/04 at 00 am, and the ORC changed the committed STOR power from 2.2 MW to 1.76 MW. This has an impact on both the revenues from the plant availability received when the unit is not called to produce and on the revenues from the plant utilization.

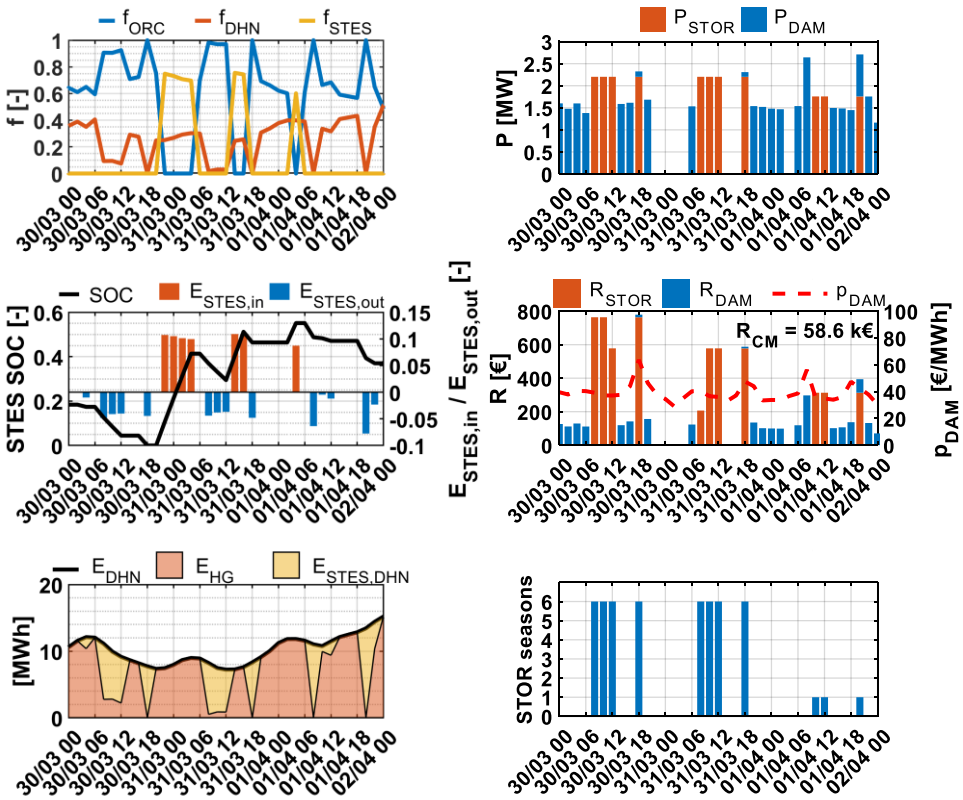

Figure 5.20: Operational behavior of S4 over 3 days for the optimal solution (2·10^4 STES units). Top left: mass flow fractions from the main heating grid to the district heating network (f_{DHN}), the ORC (f_{ORC}), and the STES (f_{STES}). Middle left: STES state of charge (SOC_{STES}) and normalized STES input ($E_{STES,in}$) and output energy ($E_{STES,out}$). Bottom left: District heating demand (E_{DHN}) provided by the main heating grid (E_{HG}) and by the STES ($E_{STES,DHN}$). Top right: Electrical power produced from the ORC for the day ahead market (P_{DAM}) and for the STOR market (P_{STOR}). Middle right: Revenues from the day ahead market (R_{DAM}), the STOR market (R_{STOR}), the CM market (R_{CM}), and the day ahead market electricity price (p_{DAM}). Bottom right: STOR seasons. In the graph, the STOR season changes on 01/04 at 00:00 am from season 6 to season 1.

In Figure 5.21 left, the relative profit in function of the STES capacity cost is displayed. For the same reasons of scenario S3 (Figure 5.18 right), the relative profit compared to the solution of not having a storage decreases by increasing the STES capacity cost. Moreover, also the optimal number of units decreases as for scenario S3. However, while for scenario S3 the STES had a positive impact on the profit up to costs of 7.5 €/kWh$_{cap}$, the presence of the STOR market in this scenario allows the storage to be profitable up to a cost of approximately 70 €/kWh$_{cap}$. In Figure 5.21 right, the STOR utilization price, which is having the major impact on the STOR revenues, has been varied over a range of 50 % - 150 %. The

trend shows that even with a utilization price halved, a profit approximately 13.3 % higher compared to not having a STES is still present. The amount of STES units in each optimal solution is decreasing for lower STOR utilization prices, as expected.

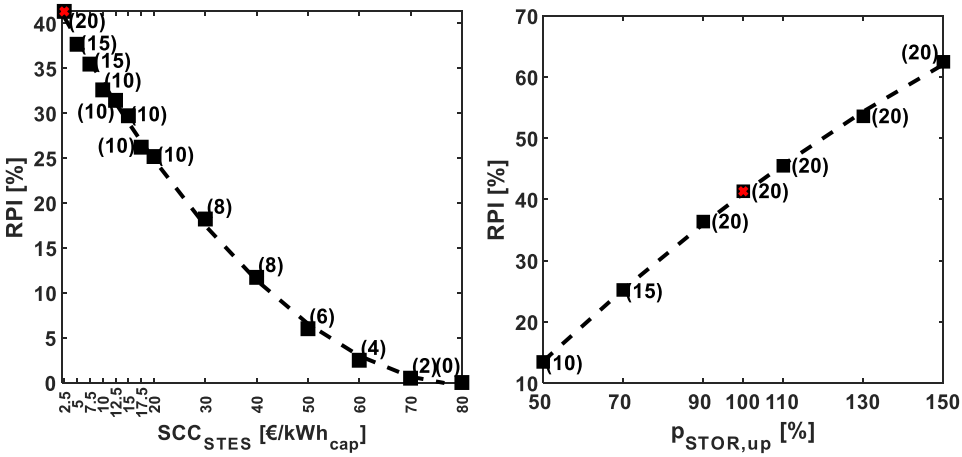

Figure 5.21: Left: Relative profit increase compared to the alternative of not having a storage for the optimal solutions in function of the fixed STES cost for S4. Right: Relative profit increase compared to the alternative of not having a storage for the optimal solutions in function of the STOR utilization price for S4. The amount of storage units in every optimal solution is expressed, between round brackets, in thousands of units. Red marker: Initial reference value. Red markers: Initial reference values.

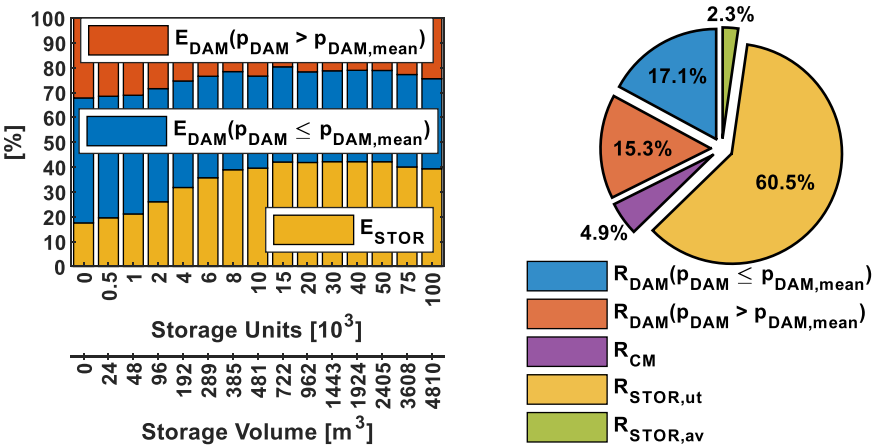

Figure 5.22: Left: Yearly energy sold on the STOR market (yellow), and on the DAM at a price above (red) and below (blue) the yearly average market price $p_{DAM,mean}$ for scenario S4. Right: Revenues of the optimal solution ($2 \cdot 10^4$ STES units) for scenario S4. Red: revenues from DAM sales above $p_{DAM,mean}$. Blue: revenues from DAM sales below $p_{DAM,mean}$. Purple: revenues from the capacity market. Green: Revenues from committing the ORC plant to the STOR market. Yellow: Revenues from selling the energy to the STOR market.

In Figure 5.22 left, it is shown that the energy sold to the STOR market is increasing from approximately 17 % (without STES) to 42 % (with $40 \cdot 10^3$ units). After that STES size, the amount of energy sold to the STOR market slightly decreases in favor of the energy sold on the DAM above $p_{DAM,mean}$. The optimal solution ($2 \cdot 10^4$ units) allows 41.9 % of energy to be sold to the STOR market, and 36.5 % and 21.6 % to be sold on the DAM market above and below $p_{DAM,mean}$, respectively. In Figure 5.22 right, the yearly revenues flow for scenario S4 are shown. The STOR market has the highest revenues share with approximately 60.5 % from the plant utilization and 2.3 % from the plant commitment. The capacity market brings revenues of approximately 4.9 % of the total revenues flow, and the DAM market contributes for 15.3 % and 17.1 % for the energy sold above and below $p_{DAM,mean}$, respectively.

5.6 Discussion and conclusions

5.6.1 Discussion on main assumptions and parameters choice

The techno-economic analysis performed in this work has intrinsic limitations due to the assumptions and parameter choices that have been made. From the STES perspective, the sorption material considered in this work is potassium carbonate. The choice of a different sorption material can lead to different outcomes especially if the resulting STES energy density and fixed capacity costs are far from those of potassium carbonate. Moreover, the STES fan and the heat recovery unit efficiencies have been selected based on typical nominal values and are assumed constant. However, these quantities are not normally fixed and vary according to the system operating conditions. From the economic perspective, this analysis has been done by considering the electricity markets for two specific years from two specific countries. Moreover, the time resolution of the optimization model is 2 hours. Finer resolutions (i.e. hourly or every 15 minutes) can give more accurate insights on the overall system profits since now local price spikes are averaged over the time intervals. However, the computational costs of the model would increase exponentially. Regarding the capacity market, the capacity market event has been arbitrarily placed in a specific period of the year, in winter, in which the district heating network demand is relatively high. The capacity market event location will have an impact on the RPI for a specific STES size. If, for example, a capacity market event would happen in summer, it is probable that a smaller STES could maximize the system profits because the district heating network demand would be lower, and the ORC could already use most of the main heating grid mass flow. However, by placing the capacity market event in winter, a worst-case scenario for the STES size is considered. Therefore, the yearly committed ORC capacity to the capacity market could be guaranteed through the whole year with this approach. Finally, the STOR profile has been produced based on a probability-based approach. Further investigations involving multiple

STOR profiles produced with the same approach should be performed to investigate the sensitivity of the STOR profile on the system profits.

5.6.2 Conclusions

The integration of a sorption thermal energy storage (STES) in an energy system operating in different energy markets has been investigated for current (2013 – 2017) market pricing. The energy system consists of a main heating grid supplying thermal energy to a low temperature district heating network (DHN) and an organic Rankine cycle. The impact of integrating a STES in different scenarios, with the aim of maximizing the overall energy system profits, has been investigated.

It has been found that the STES integration is not profitable for scenarios operating only in traditional markets such as the day ahead market, for the investigated day ahead market profiles (i.e. 2013 for Belgium and 2017 for UK). For the Belgian case (S1), the optimal solution did not include the STES, meaning that the STES CAPEX and OPEX were higher than the additional revenue stream generated by the ORC due to a higher flexibility provided by the STES. For the scenario in UK (S2), the STES was included in the optimal solution but it did not bring substantial additional profits, i.e. the CAPEX and OPEX were barely counterbalanced by the additional revenue stream.

When balancing services were also considered into the reference energy system, the STES integration becomes a profitable alternative. The STES presence allows for roughly 3.2 % higher $NNPV$ when the capacity market was included as market mechanism (S3). In particular, the STES allows the ORC to commit 98 % of its producible power during a CM-event compared to 43.9 % without STES. In turn, this led to a more than doubled revenue stream from this market mechanism.

Finally, by adding also the STOR market as a balancing service (S4), the STES integration allowed for approximately 40 % higher $NNPV$, which resulted from the maximization of the ORC energy produced for the STOR market. A sensitivity analysis on the STES capacity cost showed that, especially for S4, the storage integration was profitable up to a STES capacity cost of 70 €/kWh$_{cap}$. Finally, an additional sensitivity analysis on the STOR utilization price, causing the major part of the revenue streams, has been performed. The results showed that even by halving the STOR utilization price, the STES integration would have led to approximately 13.3 % higher profits in scenario S4.

To conclude, it is clear that the presence of balancing market mechanisms could greatly increase the commercial viability of a thermal storage technology such as sorption thermal energy storage for the reference energy system investigated in this work.

In this analysis, sorption thermal energy storage showed the potential to be already profitable under current market conditions, for the investigated scenarios. By considering that the share of fluctuating and distributed energy producers in the future energy system will increase, and

that the energy grid will have to increase its flexibility, the potential for this storage technology could increase further.

Future research should investigate and compare other possible storage technologies and their impact on similar energy systems, considering the economic framework in which these systems are operating. Thus, valuable insights on the economic viability of these technologies, also still in an early development stage, can be obtained. Then, policies and guidelines can be developed to foster their integration in the future energy networks.

CHAPTER 6

ENERGY SYSTEM OPTIMIZATION II

THE POTENTIAL OF A DECENTRALIZED STES OPERATING IN A DOMESTIC ENVIRONMENT

In this chapter, the impact of integrating a decentralized STES, within a techno-economic optimization framework, is investigated. In particular, the aim of the optimization is to minimize the yearly costs of a single-family house for space heating and domestic hot water needs. This chapter is divided into four main sections, beside the introduction (6.1). In section 6.2 a general description of the reference energy system is present (6.2.1). Then, every system component is described in detail (sections 6.2.2 - 6.2.6) and the economic variables and indicators are introduced (6.2.7). Section 6.3 shows the optimization variables (6.3.1) and the optimization model formulation (6.3.2). Section 6.4 presents the results of the parametric analysis carried out, and in section 6.5 the main conclusions of this work are presented.

6.1 Introduction

The aim of this chapter is to investigate, within the same optimization framework of Chapter 5, the economic benefits of integrating an open solid sorption thermal energy storage in a domestic environment, focusing on existing houses under present economic pricing conditions. Thus, differently from the energy system from Chapter 5, the reference energy system in this chapter consists of a single-family house, which has fixed electricity and gas tariffs throughout the year. It is also assumed that the dwelling has solar thermal collectors installed, together with a water tank and a conventional gas boiler. The aim of the optimization is to minimize the yearly costs for the provision of space heating and domestic hot water.

Differently from Chapter 5, the charging (desorption) STES temperature can vary according to the amount of solar energy available at a specific moment in time. Therefore, the STES charging power is variable. This results in a different formulation of the STES. In particular, in Chapter 5 it is assumed that the STES units can be charged and discharged in parallel with the same constant charging and discharging powers. In this chapter, it is assumed that the STES units are charged one by one, and that during desorption the charging power can vary. During sorption, it is assumed that the STES units are discharged one by one, with a constant power resulting from the maximum airflow deliverable by the installed fan. This STES formulation can be more logical for this reference scenario because, being a domestic system, the amount of STES units would be lower than the centralized system in Chapter 5. Thus, a series operation mode can be more realistic for a relatively small system.

This chapter has two main contributions. The first contribution is an alternative formulation of the STES in the MILP optimization framework [164], for an operational mode that charges and discharges the single STES units one by one and not in parallel (as in Chapter 5 section 5.3.4). The second contribution is a parametric analysis in which different reference system parameters (e.g. STES capacity cost, water tank volume, etc.) are varied, and the impact on the yearly system costs and solar fraction is estimated. Beside the chapter outline, a conceptual representation of the chapter structure is shown in Figure 6.1.

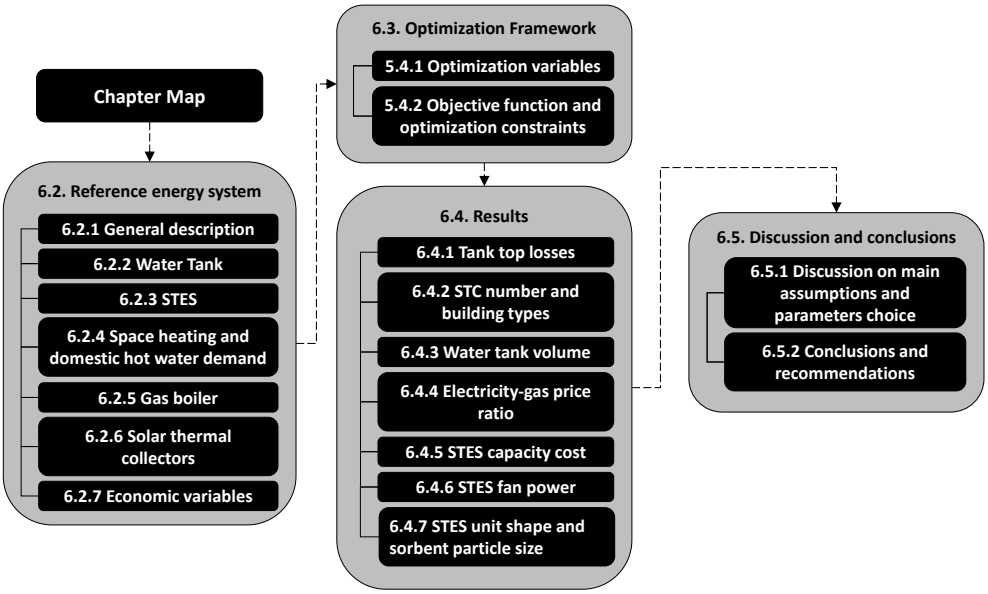

Figure 6.1: Conceptual map of the chapter structure.

6.2 Reference energy system

In this section, the reference energy system is presented (6.2.1) and the single system components are described in more detail in sections 6.2.2 - 6.2.6. Finally, in section 6.2.7, the main economic variables and indicators are introduced.

6.2.1 General description

The reference energy system (Figure 6.2) consists of a single-family household with a space heating and a domestic hot water demand. The dwelling can satisfy its thermal energy demand with a gas boiler and solar thermal collectors (STCs) that are considered to be already installed. Both gas boiler and STCs are connected to a water tank, which is used as short-term storage that copes with the daily demand fluctuations. A STES is integrated into the reference energy system, and it can be charged by the STCs when enough solar radiation is available to achieve an STC thermal fluid temperature sufficient for the STES charging process. Moreover, the STES is connected to the water tank, and it can be used to heat up the water. It is assumed that the building uses a low temperature space heating system (e.g. floor heating) with predefined supply temperature ($T_{SH,sp}$) and return temperature ($T_{SH,rt}$). Moreover, the DHW energy is also supplied by the tank at fixed supply (T_{DHW}) and return temperatures (T_{MAIN}). In this analysis, it is assumed that the heat exchangers between the STC thermal fluid, the STES airflow, and the water tank circuits are able to transfer the

energy between the two fluids until a minimum temperature difference $\Delta T_{HX,min}$ of 1 °C is reached.

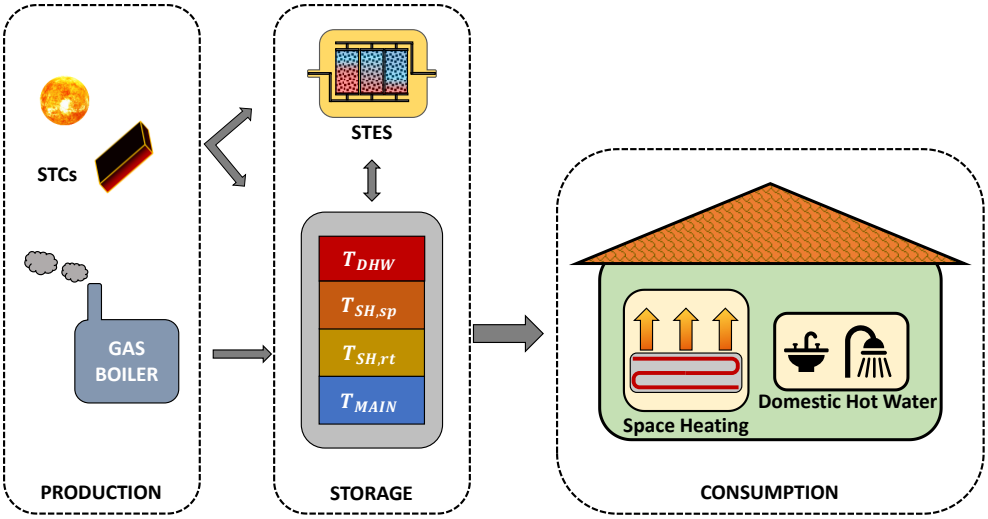

Figure 6.2: Reference energy system. STCs = solar thermal collectors. STES = sorption thermal energy storage.

6.2.2 Water tank

In previous works involving a water tank formulated within the MILP framework, for example [175,208], the water tank has been assumed as a mass of water divided into two perfectly mixed segments at T_{hot} and T_{cold}, respectively. The layer between the two segments is considered a perfect thermocline i.e. no heat transfer over the boundaries. Therefore, the state of charge of the storage tank depends on one single variable: the position of the thermocline along the water tank height. The thermal losses consist of a fixed term corresponding to the losses at the top and bottom of the tank (assumed always at T_{hot} and T_{cold}, respectively), and a variable term depending on the SOC. In this work, a similar approach is used. However, the water tank is divided into four segments ($N_{seg} = 4$) corresponding to the amount of water at the four different temperature levels (T_{DHW}, $T_{SH,sp}$, $T_{SH,rt}$, T_{MAIN}) considered in the reference energy system (Figure 6.3). The main assumptions are:

- There is no mixing between the segments, thus the tank is perfectly stratified.
- Thermal losses do not influence the temperature in each segment, but they change the amount of water in it. A constant heat transfer coefficient (U) of 0.5 W/(m^{2}K) from the water tank to the external environment is assumed.

- Water in a segment at T_n can be heated up to every temperature level $T_{m>n}$ by the gas boiler, the STCs, and the STES with a charging power $P_{n\rightarrow m,t}$.
- Water in a segment at T_n can be cooled down to the temperature level T_{n-1} due to thermal losses.
- Water in a segment at T_n can be cooled down to the temperature level $T_{m<n}$ with a mass flow $\dot{M}_{n\rightarrow m}$ due to the thermal energy demand for SH and DHW.
- The thermal losses at the bottom of the tank and at the coldest tank temperature, are neglected.

The derivation of the tank model is based on the mass balance for a single segment n (equation 6.1).

$$\frac{d(M_{n,t})}{dt} = \sum_{m=1}^{N_{seg}} \dot{M}_{m\rightarrow n,t} - \sum_{m=1}^{N_{seg}} \dot{M}_{n\rightarrow m,t} - \dot{M}_{loss,n,t} \qquad 6.1$$

$$\dot{M}_{loss,n,t} = \dot{M}_{loss-side,n,t} + \dot{M}_{loss-top,n,t} \qquad 6.2$$

Here $M_{n,t}$ is the mass of water of segment n at time t and temperature T_n; $\dot{M}_{m\rightarrow n,t}$ is the mass flow of water entering in segment n after that it has been heated up from a lower segment or cooled down from an upper segment as a result of a thermal energy supply or demand, respectively; $\dot{M}_{n\rightarrow m,t}$ is the mass flow of water leaving segment n to be either transferred to an upper segment due to an energy supply (i.e. from gas boiler, STCs, or STES) or to a lower segment due to an energy withdraw (i.e. due to SH and DHW demand). $\dot{M}_{loss,n,t}$ is the amount of water that, due to thermal losses with the environment, is cooled down to the lower temperature T_{n-1}, and it is calculated according to equation 6.2. The thermal losses consist of two contributions if the segment n is the top segment. The first contribution models the thermal losses from the water tank side ($\dot{M}_{loss-side,n,t}$) and the second term models the thermal losses from the top of the tank ($\dot{M}_{loss-top,n,t}$). If segment n is not the top segment at time t or the whole tank is at the lowest temperature level ($n_{top,t}$ = 1), then only the first contribution is present. The losses through the top of the tank are assumed constant for a specific segment n if the segment is the top segment $n_{top,t}$ and it is not equal to the segment at the lowest temperature, according to equation 6.3.

$$\begin{cases} \dot{M}_{loss-top,n,t} = \dfrac{UA_{top}(T_n - T_{amb,t})}{c_{p,w}(T_n - T_{n-1})} & n = n_{top,t} \wedge n \neq 1 \\ \dot{M}_{loss-top,n,t} = 0 & n \neq n_{top,t} \vee n_{top,t} = 1 \end{cases} \qquad 6.3$$

Here U is the heat transfer coefficient, A_{top} is the surface area of the top of the tank, $T_{amb,t}$ is the ambient temperature, and $c_{p,w}$ is the water specific heat capacity.
The thermal losses through the side of the tank ($\dot{M}_{loss-side,n,t}$) are calculated (equation 6.4) based on the amount of lateral area (A_{side}) covered by segment n ($A_{side,n,t}$) through the ratio between the water mass in segment n at time t ($M_{n,t}$) and the overall water mass in the tank (M_{tank}).

$$\dot{M}_{loss-side,n,t} = \frac{UA_{side,n,t}\left(T_n - T_{amb,t}\right)}{c_{p,w}(T_n - T_{n-1})} = \frac{U\frac{M_{n,t}}{M_{tank}}A_{side}\left(T_n - T_{amb,t}\right)}{c_{p,w}(T_n - T_{n-1})} \qquad 6.4$$

By considering $\dot{M}_{loss-top,n,t}$ independent from $M_{n,t}$ and constant during a single timestep, inserting 6.2 in 6.1, and grouping all the constant terms ($\dot{M}_{loss-top,n,t}$, $\sum_{m=1}^{N}\dot{M}_{m\to n,t}$ and $\sum_{m=1}^{N}\dot{M}_{n\to m,t}$) into $\dot{M}_{const,n,t}$,the water tank mass balance can be written as in equation 6.5.

$$\begin{cases} \dfrac{d\left(M_{n,t}\right)}{dt} + \dfrac{UA_{side}\left(T_n - T_{amb,t}\right)}{M_{tank}c_{p,w}(T_n - T_{n-1})}M_{n,t} = \dot{M}_{const,n,t} \\ \dot{M}_{const,n,t} = \displaystyle\sum_{m=1}^{N_{seg}}\dot{M}_{m\to n,t} - \sum_{m=1}^{N_{seg}}\dot{M}_{n\to m,t} - \dot{M}_{loss-top,n,t} \end{cases} \qquad 6.5$$

Equation 6.5 is a first order linear differential equation, which can be solved assuming the initial value of the state variable $M_n(t=0) = M_{n,0}$. By defining the time constant $\tau_{n,t}$ as in equation 6.6 and by considering a discrete timestep Δt, equation 6.5 can be rewritten into equation 6.7, which describes the evolution of $M_{n,t}$. The exponential terms in the equation account for the behavior of the thermal losses on a timescale smaller than a single timestep.

$$\tau_{n,t} = \frac{M_{tank}c_{p,w}(T_n - T_{n-1})}{UA_{side}\left(T_n - T_{amb,t}\right)} \qquad 6.6$$

$$M_{n,t} = M_{n,0}e^{-\frac{\Delta t}{\tau_{n,t}}} + \dot{M}_{const,n,t}\tau_{n,t}\left(1 - e^{-\frac{\Delta t}{\tau_{n,t}}}\right) \qquad 6.7$$

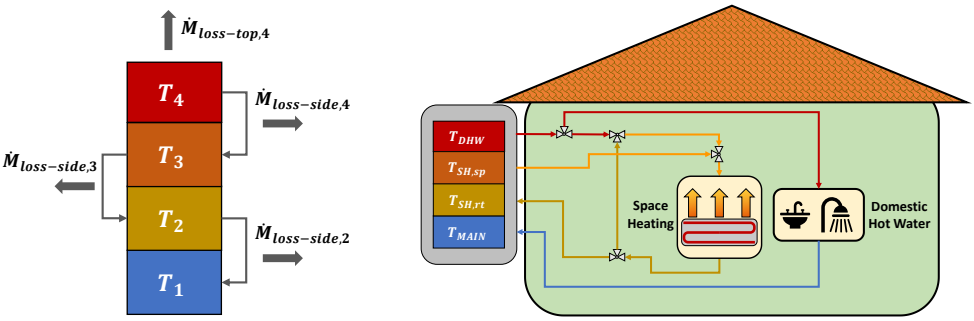

Figure 6.3: Left: Water tank model concept with four segments, in which segment n = 4 is the top segment. Right: Space heating and domestic hot water consumption. The top segment at T_{DHW} can be used to satisfy both DHW and SH demand. The latter, is achieved by premixing the incoming water with the return temperature of the SH system.

From the water tank energy content perspective, the water tank state of charge can be defined by considering the tank fully discharged if all the water is at the bottom segment temperature and fully charged if it is all at the top segment temperature (equation 6.8).

$$SOC_{TANK,t} = \sum_{n=1}^{N_{seg}} \frac{M_{n,t} c_{p,w} (T_n - T_1)}{M_{tank} c_{p,w} (T_{N_{seg}} - T_1)} \qquad 6.8$$

Regarding the water tank state of charge, the following two remarks are made.

- Due to the different thermal energy needs that can be satisfied from the different segments, having $SOC_{tank,t} > 0$ does not necessarily imply that all the thermal energy demand types can be satisfied. For example, having the whole water amount at T_2 results in a $SOC_{tank} > 0$ but the thermal energy demand can be only satisfied using water at T_3 (SH) or T_4 (DHW).
- Assuming that all the water in the tank is at T_2 ($SOC_{tank} > 0$), it would not be possible to satisfy any thermal energy need. However, the boiler gas consumption to provide water at e.g. T_4 will be lower than if all the water mass was initially at T_1 (i.e. $SOC_{tank,t} = 0$).

6.2.3 Sorption thermal energy storage

The STES is considered as a segmented packed bed in which one segment at the time can be operated in charging or discharging mode as illustrated in Figure 6.4. Each segment is considered as a cylindrical porous packed bed with a predefined diameter d_{STES} and axial length L_{STES}.

The overall STES energy content ($E_{STES,max}$) can be estimated according to equation 6.9.

$$E_{STES,max} = \frac{N_{STES}(1-\varepsilon_b)\rho_{sm}V_{STES,unit}\nu\Delta H_{reac}}{M_{mol,sm}} \qquad 6.9$$

Here N_{STES} is the number of STES segments, ε_b is the packed bed porosity, ρ_{sm} and $M_{mol,sm}$ are the sorption material density and molar mass, respectively; ΔH_{reac} is the reversible reaction enthalpy in J/mol$_w$, and ν is the reaction stoichiometric coefficient in mol$_w$/mol$_{sm}$.

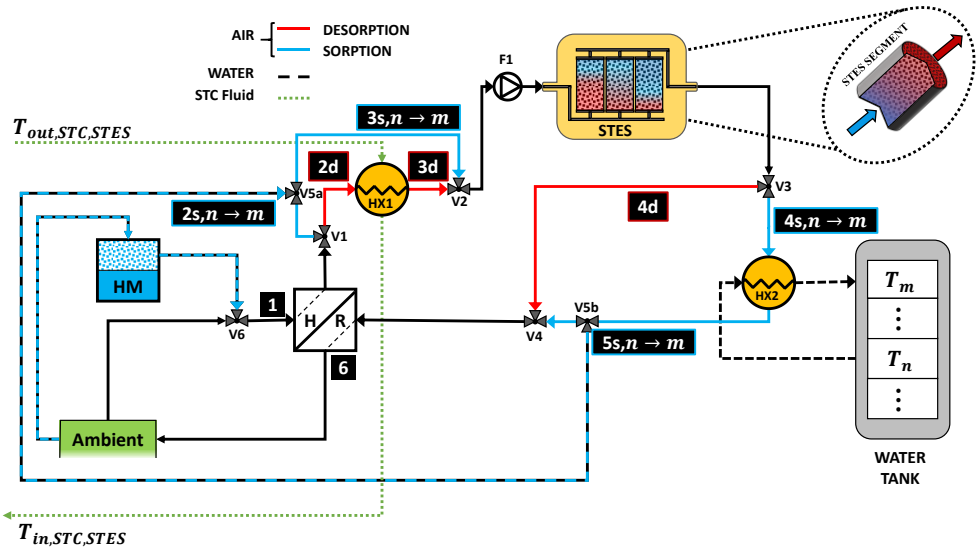

Figure 6.4: Sorption thermal energy storage system. HR=heat recovery unit. HX1 = STES charge heat exchanger. HX2 = STES discharge heat exchanger. F1: Fan.

From the system integration perspective, the STES is charged through a heat exchanger HX1, which transfers the thermal energy from the STC thermal fluid to the airflow. During the discharge phase, a second air/water heat exchanger (HX2) transfers the thermal energy to the water tank. A heat recovery unit (HR) with a heat recovery efficiency (ε_{HR}) of 90 % is assumed [107], which is used to recover the residual heat in the exhaust STES airflow to preheat the incoming ambient air during both charge and discharge phases. During the charge phase (desorption), valves V1 and V2 direct the heat towards HX1, and V3 and V4 bypass HX2. Vice versa, during the discharge phase (sorption), V1 and V2 bypass HX1 while V3 and V4 direct the airflow towards HX2 to deliver energy to the water tank. As for the system in Chapter 5 (Figure 5.8), during sorption the ambient airflow can be mixed with saturated air through valve V6 or mixed with the exhaust dry air through valves V5a and V5b (blue-black dashed lines). This is done, in order to prevent the sorption material deliquescence and to guarantee, where possible, a minimum temperature lift in the sorption reactor.

STES charge (desorption)

By knowing the thermal power ($P_{STC,STES,t}$) that can be transferred from the STCs to the STES at time t (see section 6.2.6), it is possible to calculate the respective STES air mass flow rates on the secondary side of the thermal fluid/air heat exchanger according to equation 6.10, following the process in Figure 6.5, and assuming that $\dot{m}_{STES,d,t}$ should have values within the range $[\dot{m}_{STES,min}, \dot{m}_{STES,max}]$.

$$\dot{m}_{STES,d,t} = \frac{P_{STC,STES,t}}{c_{p,a}(T_{3d,t} - T_{2d,t})} \qquad 6.10$$

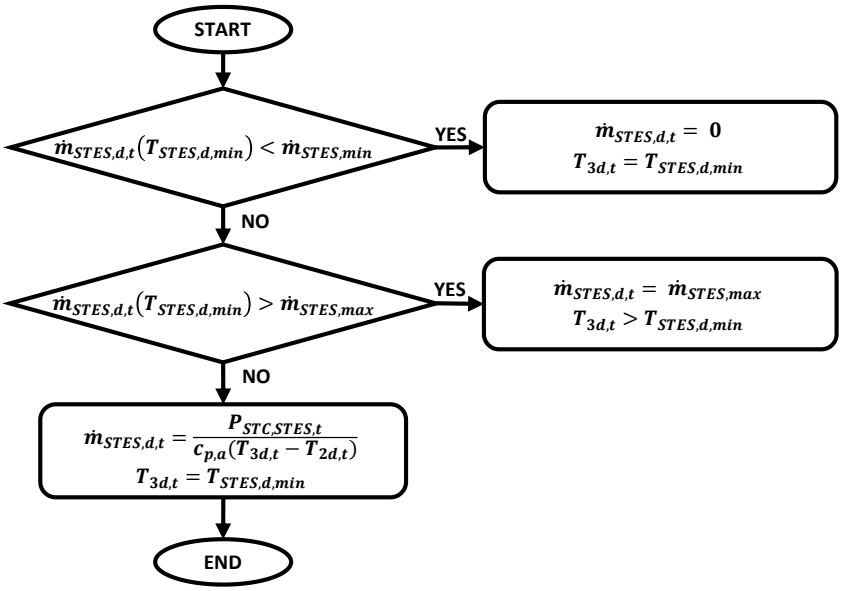

Figure 6.5: Flow diagram for the STES desorption temperature and mass flow determination.

In Figure 6.5, $\dot{m}_{STES,d,t}$ is the STES air mass flow rate that flows through the storage segment, $c_{p,a}$ is the air specific heat capacity, $T_{3d,t}$ is the STES inlet temperature. The mass flow rate is first estimated with equation 6.10 by imposing $T_{3d,t} = T_{STES,d,min}$. In order to charge the STES, the minimum desorption temperature has to be higher than the reaction equilibrium temperature ($T_{eq,STES,d,t}$), which oscillates approximately in the range of 55 °C – 65 °C according to the ambient conditions. In order to guarantee always a minimum driving force (Chapter 4, Figure 4.2 right) for the desorption reaction, a minimum desorption temperature ($T_{STES,d,min}$) of 80 °C has been selected.

If the resulting mass flow rate is smaller than $\dot{m}_{STES,min}$, then at that timestep it is not possible to charge the STES (i.e. $\dot{m}_{STES,d,t} = 0$). Counter wise, if the maximum mass flow rate is exceeded, then $T_{3d,t}$ is increased from the minimum value $T_{STES,d,min}$.

Not all the thermal power transferred from the STCs to the STES ($P_{STC,STES,t}$) is useful to charge it. It is assumed that only the thermal power released above the STES charging equilibrium temperature ($T_{eq,STES,d,t}$) of the reversible reaction can be used to separate the sorbent from the sorbate (equation 6.11). Then, part of the residual thermal energy is recovered through the heat recovery unit that preheats the incoming air from ambient temperature to $T_{2d,t}$ with the exhaust air out of the STES during charge (equation 6.12).

$$P_{STES,d,t} = \dot{m}_{STES,d,t} c_{p,a} \left(T_{3d,t} - T_{eq,STES,d,t} \right) \qquad 6.11$$

$$T_{2d,t} = T_{amb,t} + \varepsilon_{HR} (T_{eq,STES,d,t} - T_{amb,t}) \qquad 6.12$$

Here ε_{HR} is the heat recovery unit efficiency. The equilibrium temperature is calculated according to equation 6.13. ΔH_{reac} and ΔS_{reac} are the reaction enthalpy and entropy expressed in J/mol$_w$ and J/(mol$_w$·K), respectively; R_g is the universal gas constant, and $p_{v,t}$ is the water vapor (sorbate) pressure in the air flow expressed in bar. The water vapor pressure can be estimated by knowing its temperature and water vapor molar concentration at the reactor inlet. The water vapor molar concentration is equal to the one present in the ambient air ($c_{amb,t}$), while the minimum desorption temperature ($T_{STES,d,min}$) is used as inlet reactor temperature during desorption.

$$T_{eq,STES,d,t} = \frac{-\Delta H_{reac}}{-\Delta S_{reac} - R_g ln \left(\frac{1}{p_{v,t}\left(T_{STES,d,min}, c_{amb,t} \right)} \right)} \qquad 6.13$$

It has to be remarked that, in a real system, not all the power $P_{STES,d,t}$ contributes to the endothermic reaction. Part of it is lost due to thermal losses or used to heat up the STES.

STES discharge (sorption)

As for the STCs, it is assumed that the STES can heat up any segment n at T_n of the water tank to a higher segment $m > n$ at T_m. However, this is possible only if the STES discharge temperature ($T_{4s,n\rightarrow m,t}$) is above $T_m + \Delta T_{HX,min}$. During discharge, the air mass flow through the packed bed is assumed to be constant and equal to $\dot{m}_{STES,max}$. The STES outlet temperature is calculated assuming that it cannot exceed the equilibrium temperature of the reaction, and that all the energy from the exothermic reaction is transferred to the air (equation 6.14), ignoring sensible heating of the STES.

$$T_{4s,n\rightarrow m,t} = \min\left(T_{3s,n\rightarrow m,t} + \Delta T_{lift,STES,n\rightarrow m,t}\ , T_{eq,STES,s,n\rightarrow m,t}\ \right) \qquad 6.14$$

Here $T_{eq,STES,s,n\rightarrow m,t}$ is the equilibrium temperature calculated as in equation 6.13, assuming that the water vapor pressure is calculated as function of the STES inlet air temperature $T_{3s,n\rightarrow m,t}$ and water vapor concentration $c_{3s,n\rightarrow m,t}$.
The maximum temperature lift obtainable within the STES packed bed is calculated according to equation 6.15.

$$\Delta T_{lift,STES,n\rightarrow m,t} = \frac{c_{3s,n\rightarrow m,t}\Delta H_{reac}}{\rho_a c_{p,a}} \qquad 6.15$$

For the estimation of $c_{3s,n\rightarrow m,t}$ and $T_{1,t}$, the same assumptions as for the STES system in Chapter 5 (section 5.3.4) are made in order to prevent the sorption material deliquescence and to achieve a minimum temperature lift inside the reactor. The first assumption is that, if the sorbate concentration ($c_{3s,n\rightarrow m,t}$) exceeds 95 % of the deliquescence concentration $c_{del,n\rightarrow m}$ (Chapter 5, Figure 5.6), the ambient air is mixed with part of the reactor exhaust dry air (with a mixing ratio $X_{mix,dry,n\rightarrow m,t}$) at $T_{5s,n\rightarrow m}$ and indicated in Figure 6.4, in order to decrease its water vapor concentration. This is done to prevent the sorption material to go into deliquescence and inevitably compromise the porous material structure.
The second assumption is that saturated air at T_{hum} = 10 °C is always available, and if the deliquescence conditions are not violated at the STES inlet, the ambient air can be mixed with this saturated airflow with a mixing ratio $X_{mix,hum,n\rightarrow m,t}$ before the preheating in the heat recovery unit. This is done to guarantee a minimum temperature lift in the packed bed and still avoiding the material deliquescence. The additional air humidification system could be, for example, a borehole or additional solar thermal collectors that can keep a water reservoir at 10 °C also in winter. Within this work, no further investigation is done regarding this matter, nor is the humidification source taken into account in the techno-economic analysis.
Therefore, the concentration at every timestep t of the year can be defined according to equation 6.16, which is similar to equation 5.8 in Chapter 5, except for the fact that there are three different deliquescence concentrations. This is because the STES inlet air temperature, and as a consequence the deliquescence concentration, is different according to which water tank segment is heated up.

$$c_{3s,n\rightarrow m,t} = \min\left(\max\left(c_{sat,10°C}, c_{amb,t}\right), 0.95c_{del,n\rightarrow m,t}\ \right) \qquad 6.16$$

If air humidification is possible, then the incoming temperature in the system is calculated according to equation 6.17. Otherwise, if the incoming air needs to be mixed with dry air to

prevent the material deliquescence, the resulting airflow temperature entering in the STES is calculated according to equation 6.18.

$$T_{1,t} = T_{hum} X_{mix,hum,n\rightarrow m,t} + \left(1 - X_{mix,hum,n\rightarrow m,t}\right) T_{amb,t} \qquad 6.17$$

$$T_{3s,n\rightarrow m,t} = X_{mix,dry,n\rightarrow m,t} T_{5s,n\rightarrow m} + \left(1 - X_{mix,dry,n\rightarrow m,t}\right) T_{2s,n\rightarrow m,t} \qquad 6.18$$

Here, $T_{2s,n\rightarrow m,t}$ is the ambient air preheated in the heat recovery unit from the STES exhaust airflow (at $T_{5s,n\rightarrow m} = T_n + \Delta T_{HX,min}$) after the thermal load, calculated according to equation 6.19.

$$T_{2s,n\rightarrow m,t} = T_{1,t} + \varepsilon_{HR}\left(T_{5s,n\rightarrow m} - T_{1,t}\right) \qquad 6.19$$

With the abovementioned assumptions, the possible STES discharge power $P_{STES,s,n\rightarrow m,t}$ for upgrading a mass of water from segment n to m in the water tank can be calculated (equation 6.20).

$$P_{STES,s,n\rightarrow m,t} = \dot{m}_{STES,max} c_{p,a}\left(T_{4s,n\rightarrow m,t} - T_{5s,n\rightarrow m}\right) \qquad 6.20$$

If the outlet STES temperature $T_{4s,n\rightarrow m,t}$ is not higher than the minimum temperature necessary to bring the water from temperature T_n to temperature T_m ($T_{4s,n\rightarrow m,t} < T_m + \Delta T_{HX,min}$), then it is not possible to discharge the STES for this purpose, at time t (i.e. $P_{STES,s,n\rightarrow m,t} = 0$).

STES fan consumption

In order to drive the airflow through the STES packed bed during the charge and discharge modes, a fan is required. It is assumed to be a radial fan with a constant efficiency (η_{fan}) of 70 % [196]. The fan power ($P_{fan,t}$) can be estimated at every time step using equation 6.21. During discharge mode, the fan power corresponds always to the maximum deliverable fan power.

$$P_{fan,d,t} = \frac{\dot{m}_{STES,d,t} \Delta p_{STES,d,t}}{\eta_{fan} \rho_a}$$
$$P_{fan,s,t} = P_{fan,max} = \frac{\dot{m}_{STES,max} \Delta p_{STES,s}}{\eta_{fan} \rho_a} \qquad 6.21$$

Here η_{fan} is the fan efficiency, and $\Delta p_{STES,d,t}$ the estimated pressure loss expressed in Pa through the Ergun equation (equation 6.22), assuming that the STES segment is a porous cylindrical bed with porosity ε_b, an axial length $L_{STES,unit}$ and uniform spherical particles with a diameter d_p.

$$\frac{\Delta p_{STES,d,t}}{L_{STES,unit}} = \frac{\alpha_{erg}\rho_a(1-\varepsilon_b)}{d_p\varepsilon_b^3}\left|u_{a,t}\right|^2 + \frac{\beta_{erg}\mu_a(1-\varepsilon_b)^2}{d_p^2\varepsilon_b^3}\left|u_{a,t}\right| \qquad 6.22$$

In equation 6.22, α_{erg} and β_{erg} are determined according to Cheng et al. [197], $u_{a,t}$ is the superficial air velocity in the packed bed at time t and μ_a is the air viscosity. The pressure drop during the discharge mode ($\Delta p_{STES,s}$) is calculated according to the same equation imposing a fixed $u_{a,t}$ obtained with the maximum airflow $\dot{m}_{STES,max}$, which is depending on the maximum fan power $P_{fan,max}$ and the geometrical characteristics of the STES segment. Most of the main parameters needed for the STES operational behavior estimation are similar to those in Chapter 5 (Table 5.2), and are listed in Table 6.1. The packed bed axial length ($L_{STES,unit}$) and diameter ($d_{STES,unit}$) are the same as in Chapter 5 (5.3.4), and they result in a STES unit geometrical aspect ratio (d_{STES}/L_{STES}) of 0.7. However, differently from Chapter 5, the STES unit flow rate can vary, and a too high flow rate can lead to high pressure drop over the packed bed and a too high fan energy consumption. Therefore, this STES unit geometrical shape is not optimized for the operating conditions of this specific reference scenario.

Table 6.1: Parameters used for the STES system in the current chapter.

Parameter	Value	Parameter	Value
ρ_{sm} [kg/m^3]	2400	$\dot{m}_{STES,min}$ [kg/min]	0.01
$M_{mol,sm}$ [g/mol]	165.2	$T_{STES,d,min}$ [° C]	80
ν [-]	1.5	ε_{HR} [-]	0.9
ε_b [-]	0.5	ΔS_{reac} [J/(mol$_w$·K)]	155
ΔH_{reac} [kJ/mol$_w$]	63.6	η_{fan} [-]	0.7
$d_{STES,unit}$ [m]	0.35	d_p [mm]	2
$L_{STES,unit}$ [m]	0.5	lt_{STES} [years]	20
$V_{STES,unit}$ [m^3]	0.048	IR [%]	3

6.2.4 Space heating and domestic hot water demand

Three different single-family house dwellings types (terraced, semi-detached and detached), in the same location (Genk, BE), are investigated within this work. In order to have realistic energy demand profiles, a tool based on the work of Remmen et al. [188] and De Jaeger et al. [189] has been used to estimate the thermal energy demand of the three existing buildings

built after 2000, and using the same meteorological data as in Chapter 5 (section 5.3.2). The tool includes building models taking into account the building type and the year of construction, together with a stochastic occupancy model [190]. Among the main parameters, the models consider the building geometry, the surface orientations, the heated floor and roof area (A_{floor} and A_{roof}, respectively), the number of floors, the window area, the inner and outer wall areas, the infiltration rates, and the building thermal transmittances towards the external environment. Concerning the space heating demand, as in Chapter 5, a variable set point temperature, within a range between 15 °C and 20 °C, has been used in the model. The main building parameters are shown in (Table 6.2). Concerning the DHW demand, typical values for European households vary from 30 to 70 liters per occupant per day [209], considering a temperature rise of 45 °C, as in this work. Here, the estimated DHW demand E_{DHW} (Table 6.2) results approximately in 157 l/day, 80 l/day, and 34 l/day for buildings B1, B2, and B3, respectively. Therefore, these values can be realistic assuming from one (B3) to three (B1) occupants, in the investigated buildings.

Table 6.2: Main parameters, SH and DHW yearly demand of the single-family houses investigated.

ID	Type	A_{floor} [m^2]	A_{roof} [m^2]	E_{SH} [MWh]	E_{DHW} [MWh]
B1	Terrraced	120	82	15.70	2.99
B2	Semi-Detached	148	84	17.42	1.52
B3	Detached	149	166	23.50	0.70

The household space heating and DHW demands are supplied from the water tank as shown in Figure 6.3 right. In particular, DHW is provided only by the hottest segment ($n = 4$), which is at temperature T_{DHW}. The water is then sent back to the water tank in the coldest segment ($n = 1$) at T_{MAIN}. Space heating is provided in two ways. First, water can be extracted from segment 3 at $T_{SH,sp}$ and reinjected in the tank at $T_{SH,rt}$ in the lower segment ($n = 2$). Alternatively, a mass flow of water $\dot{M}_{DHW\rightarrow SH,t}$ can be extracted from segment 4 (at T_{DHW}) and mixed with part of the return water at $T_{SH,rt}$ from the space heating system (Figure 6.3 right) in order to have an amount of water $\dot{M}_{SH,sp,t}$ at $T_{SH,sp}$ (equation 6.23). The conversion factor $\Psi_{DHW\rightarrow SH}$ can be calculated according to the mixing law of fluids in equation 6.24.

$$\dot{M}_{SH,sp,t} = \Psi_{DHW\rightarrow SH}\dot{M}_{DHW\rightarrow SH,t} \qquad 6.23$$

$$\Psi_{DHW\rightarrow SH} = \frac{T_{DHW} - T_{SH,rt}}{T_{SH,sp} - T_{SH,rt}} \qquad 6.24$$

The space heating and domestic hot water supply and return temperatures are assumed according to Table 6.3.

Table 6.3: Assumed supply and return temperatures for space heating ($T_{SH,sp}$, $T_{SH,rt}$) and domestic hot water (T_{DHW}, T_{MAIN}).

	[°C]	N_{seg}
T_{DHW}	55	4
$T_{SH,sp}$	40	3
$T_{SH,rt}$	28	2
T_{MAIN}	10	1

6.2.5 Gas boiler

The gas boiler is assumed to convert the energy content of gas into thermal energy with a fixed rated efficiency η_{boiler}, based on the high heating value of gas, of 94 % [210] (equation 6.25).

$$E_{boiler,t} = \eta_{boiler} E_{gas,t} \qquad 6.25$$

6.2.6 Solar thermal collectors

The solar thermal collectors (STCs) are assumed to be evacuated tube collectors and oriented towards the south. It is assumed that multiple STC units can be combined together, and the STC units number is a model parameter. The main STC unit parameters are taken from an existing evacuated tube collector (ECOTHERM® ESC V18 [211]). The collector efficiency is estimated according to equation 6.26, which includes the collector optical efficiency $\eta_{0,STC}$ and the first ($\alpha_{1,STC}$) and second ($\alpha_{2,STC}$) order parameters accounting for the temperature influence. The thermal properties of the solar thermal fluid are assumed to be those of Tyfocor® LS® [212], except for the boiling point, which is assumed to be sufficiently high for the system operating conditions.

$$\eta_{STC,t} = \eta_{0,STC} - \frac{\alpha_{1,STC}\left(T_{mean,STC,t} - T_{amb,t}\right)}{I_t} - \frac{\alpha_{2,STC}\left(T_{mean,STC,t} - T_{amb,t}\right)^2}{I_t} \qquad 6.26$$

In equation 6.26, I_t is the incident solar radiation on the collectors at time t. The collector mean temperature ($T_{mean,STC,t}$) is calculated according to equation 6.27, in which $T_{in,STC,t}$ and $T_{out,STC,t}$ are the inlet and outlet temperatures of the STC thermal fluid, $P_{STC,t}$ is the solar power transferred to the STC thermal fluid and $\dot{m}_{STC,t}$ and $c_{p,STC}$ are the solar thermal fluid mass flow and specific heat capacity, respectively.

$$T_{mean,STC,t} = \frac{T_{out,STC,t} + T_{in,STC,t}}{2} = T_{in,STC,t} + \frac{P_{STC_t}}{2\dot{m}_{STC,t}c_{p,STC}} \quad 6.27$$

The STC thermal power (P_{STC_t}) can be estimated by inserting equations 6.26 and 6.27 into equation 6.28, in which A_{STC} is the collector aperture area. The resulting thermal fluid outlet temperature ($T_{STC,out,t}$) follows from equation 6.29.

$$P_{STC,t} = \eta_{STC} I_t A_{STC,t} \quad 6.28$$

$$T_{out,STC,t} = T_{in,STC,t} + \frac{P_{STC,t}}{\dot{m}_{STC,t}c_{p,STC}} \quad 6.29$$

The main STC parameters used in this work are listed in Table 6.4.

Table 6.4: Solar thermal collector parameters. Efficiency parameters and aperture area from the evacuated tube collector ECOTHERM® ESC V18 [211].

Parameter	Value	Parameter	Value
$\eta_{0,STC}$ [-]	0.642	$A_{STC,unit}$ [m^2]	3
$\alpha_{1,STC}$ [W/(m^{2}K)]	0.89	$\dot{m}_{STC,min}$ [l/min]	0.01
$\alpha_{2,STC}$ [W/(m^{2}K^2)]	0.001	$\dot{m}_{STC,max}$ [l/min]	5

Operational behavior of the solar thermal collectors

In this work, the STCs can deliver the energy to heat up the water from a water tank segment n to a segment m with the heat exchanger HX3, or to charge the STES with the heat exchanger HX1 (Figure 6.6).

It is assumed that the STCs can vary the thermal fluid mass flow rate according to where (water tank segment or STES) the thermal energy is transferred (equation 6.30).

$$P_{STC,t} = \begin{cases} P_{STC,n\to m,t} = \dot{m}_{STC,n\to m,t}c_{p,STC}\left(T_{out,STC,n\to m,t} - T_{in,STC,n\to m}\right) \\ P_{STC,STES,t} = \dot{m}_{STC,STES,t}c_{p,STC}\left(T_{out,STC,STES,t} - T_{in,STC,STES,t}\right) \end{cases} \quad 6.30$$

Here $T_{out,STC,n\to m,t}$ and $T_{in,STC,n\to m}$ are the STC thermal fluid outlet and inlet temperatures, respectively. $T_{out,STC,n\to m,t}$ depends on the STC fluid mass flow ($\dot{m}_{STC,n\to m,t}$) and $T_{in,STC,n\to m} = T_n + \Delta T_{HX,min}$ is fixed. $T_{out,STC,STES,t}$ and $T_{in,STC,STES,t}$ are the STC outlet and inlet thermal fluid temperatures when the STES is being charged. The latter is imposed equal to $T_{in,STC,STES,t} = T_{2d,t} + \Delta T_{HX,min}$, in which $T_{2d,t}$ is the preheated air temperature at the outlet of the heat recovery unit HR during the charging mode (Figure 6.4).

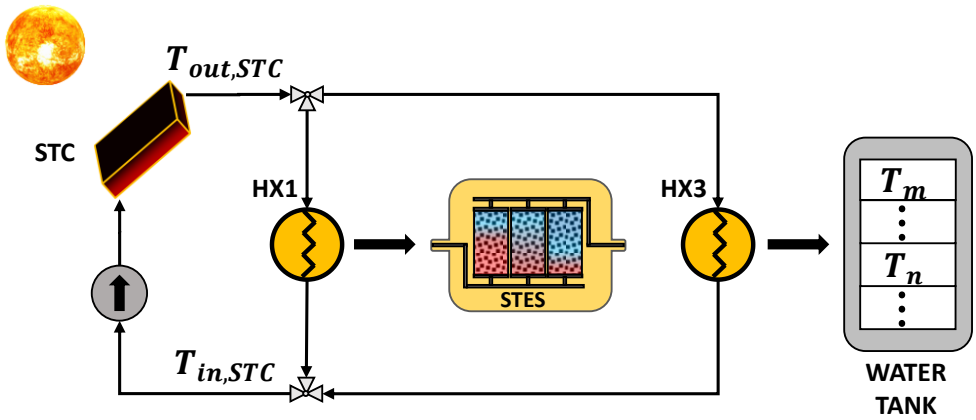

Figure 6.6: Solar thermal collectors conceptual scheme. At every time step, the solar energy can be used to charge the STES or the water tank segments provided that the minimum heat transfer fluid temperature required fora specific operational mode is achieved.

For every combination of n and $m > n$, the STC mass flow rates ($\dot{m}_{STC,n\to m,t}$) are calculated through equation 6.30 ($P_{STC,n\to m,t}$) following the process in Figure 6.7.

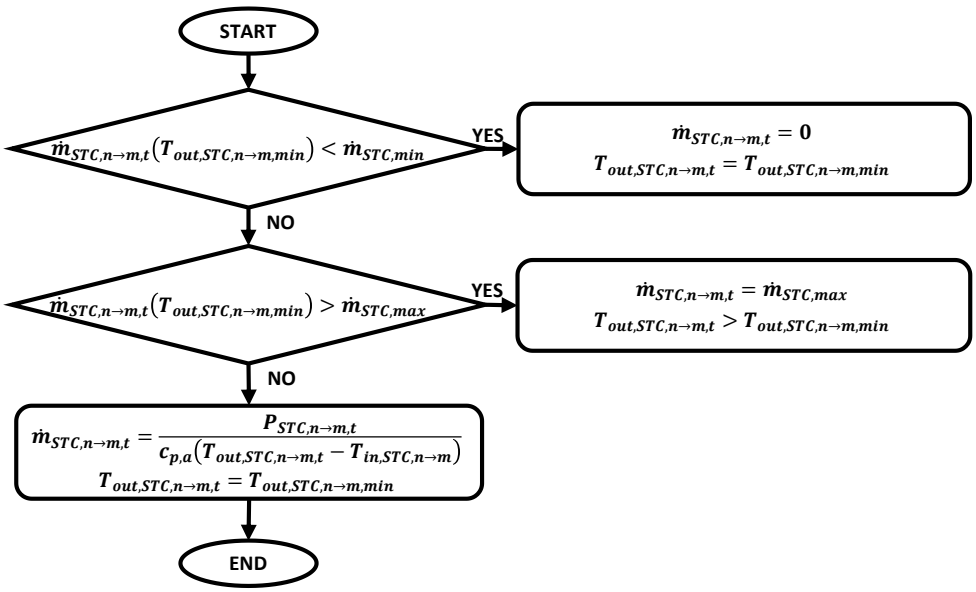

Figure 6.7: Flow diagram for the STC thermal fluid outlet temperature and mass flow determination, during the water tank heating mode.

Here $T_{out,STC,n\to m,min} = T_m + \Delta T_{HX,min}$ is the minimum STC thermal fluid temperature needed to heat the water in the tank from segment n to segment m. If the STC mass flow rate

$\dot{m}_{STC,n\rightarrow m,t}$ calculated with $T_{out,STC,n\rightarrow m,t} = T_{out,STC,n\rightarrow m,min}$ is lower than the minimum mass flow rate allowed in the STC circuit ($\dot{m}_{STC,min}$), then it is set equal to zero and in that specific time step t and the STCs cannot operate in this specific mode. On the other hand, if $\dot{m}_{STC,n\rightarrow m,t}(T_{out,STC,n\rightarrow m,min}) > \dot{m}_{STC,max}$, then the mass flow rate is set equal to $\dot{m}_{STC,max}$ and the STC outlet temperature is calculated as a consequence ($T_{out,STC,n\rightarrow m,t} > T_{out,STC,n\rightarrow m,min}$). Finally, if none of the two cases above happens, the STC mass flow rate is calculated within the range $[\dot{m}_{STC,min}, \dot{m}_{STC,max}]$ imposing $T_{out,STC,n\rightarrow m,t} = T_{out,STC,n\rightarrow m,min}$. A similar strategy is adopted for the STES charging process, in which $T_{out,STC,STES,min} = T_{STES,d,min} + \Delta T_{HX,min}$, and the STC mass flow ($\dot{m}_{STC,STES,t}$) and outlet temperature ($T_{out,STC,STES,t}$) are estimated with equation 6.30 ($P_{STC,STES,t}$) and following the process described in Figure 6.8.

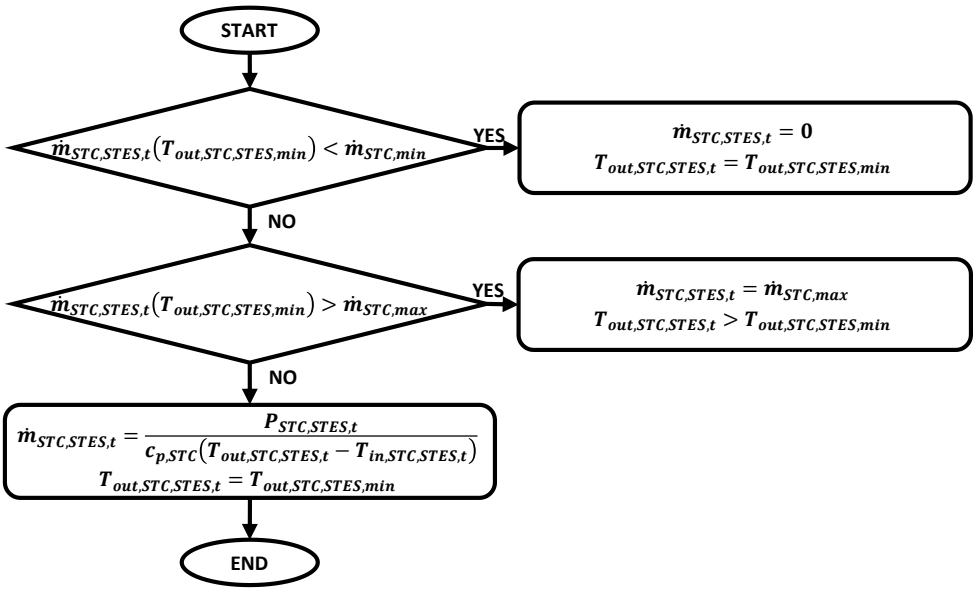

Figure 6.8: Flow diagram for the STC thermal fluid outlet temperature and mass flow determination, during the STES desorption mode.

6.2.7 Economic variables

Concerning the economics related to the energy system, in this analysis three main cost components are included: the STES CAPEX and the STES and boiler OPEX. It is assumed that the other system components are already present in the system, and only the impact of adding the STES in the scenario is assessed.

The STES yearly fixed cost ($C_{STES,fix}$) can be estimated by knowing the overall STES energy content (E_{STES}), the estimated storage capacity cost (SCC_{STES}) and applying an annuity factor

calculated as in equation 5.23 that takes into account the estimated STES lifetime (lt_{STES}) and an yearly interest rate IR (equation 6.31).

$$C_{STES,fix} = E_{STES} SCC_{STES} AF \quad 6.31$$

Here SCC_{STES} is expressed in function of the installed capacity (€/kW$_{cap}$).
The STES operational costs considered are those depending on the fan consumption to drive the airflow through the porous packed bed during charge ($C_{fan,d,t}$) and discharge ($C_{fan,s,t}$) in equations 6.32 and 6.33, respectively.

$$C_{fan,d,t} = E_{fan,d,t} p_{el} \quad 6.32$$

$$C_{fan,s,t} = E_{fan,s,t} p_{el} \quad 6.33$$

Here $C_{fan,d/s,t}$ is expressed in €. The required fan energy at timestep t ($E_{fan,d/s,t}$) depends on the fan powers required at that time step for charging or discharging the STES ($P_{fan,d,t}$ and $P_{fan,s,t}$) and on the timestep fraction in which the STES is used in charge or discharge mode in that particular timestep.
Finally, the gas boiler operational costs account for the gas consumption, as in equation 6.34.

$$C_{boiler,t} = E_{gas,t} p_{gas} \quad 6.34$$

The electricity (p_{el}) and gas prices (p_{gas}) are expressed in €/MWh.

6.3 Optimization framework

In this section, the optimization model is formulated considering the physical description and operational behavior of the components as described in section 6.2. The optimization structure consists of an objective function to be minimized respecting the optimization constraints. The latter consist of the boundary conditions of each optimization variable, and a set of equalities and inequalities that translate the physical behavior of each component in a formulation suitable for the optimization modeling technique. The optimization variables are shown in **bold** while constants and parameters are displayed in plain text. The temporal domain of the model is one year (t_{sim} = 1 year) with an hourly resolution (Δt = 1 h). Moreover, the temporal domain periodicity is imposed at the domain boundaries i.e. $\{t_1 \dots, t_{end}, t_1, \dots t_{end}, t_1\}$. Thus, a cyclic behavior is imposed on optimization variables

depending on their own values at the previous timestep such as the STES state of charge ($\boldsymbol{SOC}_{STES}$). The model is solved with MATLAB© as modeling environment, Gurobi [202] as solver, and YALMIP [203] as interface between the solver and the modeling environment.

6.3.1 Optimization variables

The optimization variables solved in this optimization model are displayed in Table 6.5. The variables $\boldsymbol{E}$ represent the energy, expressed in MWh. This type of optimization variable can take any value in the positive domain. Variables $\boldsymbol{M}$ represent a mass of water, expressed in kg, and can take any value between zero and the maximum amount of water in the water tank (M_{tank}). Variables $\dot{\boldsymbol{M}}$ represent a mass flow of water and can take any positive value between 0 and M_{TANK}. Variables $\boldsymbol{\mathcal{X}}$ are continuous variables that can take any value in the domain [0,1] and are used to represent a timestep fraction for which a certain component is in operation. For example, if a component A requiring a power P_A operates 30 minutes, during the one-hour timestep Δt, the energy required, expressed in Wh, is calculated as $E_A = \boldsymbol{\mathcal{X}}_A P_A$ with $\boldsymbol{\mathcal{X}}_A = 0.5$. The variables representing the state of charge ($\boldsymbol{SOC}$) are also continuous variables bounded in the domain [0,1]. Finally, the binary variables $\boldsymbol{Y}$ are used to formulate the optimization problem by considering also the water tank losses through the top part of the water tank ($\dot{M}_{loss-top,n,t}$) expressed as in equations 6.3. A binary decision variable representing an "on/off behavior" is required in order to describe the behavior of $\dot{M}_{loss-top,n,t}$. In fact, $\dot{M}_{loss-top,n,t} = 0$ if $n \neq n_{top,t}$ or $n = 1$, or it is defined as $\dot{M}_{loss-top,n,t} = UA_{top}(T_n - T_{amb,t})/c_{p,w}(T_n - T_{n-1})$ if $n = n_{top,t}$ and $n \neq 1$.

Table 6.5: Optimization variables and their units, boundaries and validity domains. C = continuous. B = Binary.

Optimization variable	Type	Boundaries	Units
$\boldsymbol{E}$	C	$[0, +\infty)$	MWh
$\boldsymbol{M}$	C	$[0, M_{TANK}]$	kg
$\dot{\boldsymbol{M}}$	C	$[0, M_{TANK}]$	kg/h
$\boldsymbol{\mathcal{X}}$	C	[0,1]	-
$\boldsymbol{SOC}$	C	[0,1]	-
$\boldsymbol{Y}$	B	{0,1}	-

6.3.2 Objective function and optimization constraints

The objective function aims to minimize the reference energy system costs during one year of operation, under present day economic conditions. The costs considered are the operational costs of the boiler and the STES fan, and the fixed costs of the STES system. All the other components are assumed to be already present in the reference energy system.

$$min\,\mathbf{z} = \sum_{t=1}^{t_{sim}=1\,year} \left(\frac{\boldsymbol{E}_{boiler,t}}{\eta_{boiler}} p_{gas} + \boldsymbol{E}_{fan,t} p_{el}\right) + C_{STES,fix} \qquad 6.35$$

In equation 6.35, $\boldsymbol{E}_{boiler,t}$ is the boiler thermal energy produced during timestep t, p_{gas} is the gas price, $\boldsymbol{E}_{fan,t}$ is the electrical energy required by the fan for its operation and p_{el} is the electricity price. Electricity and gas prices are considered constant throughout the whole year assuming a residential consumer with a typical fixed price contract of the two energy carriers. $C_{STES,fix}$ is the annual fixed STES cost.

The reference energy system has to satisfy the space heating and domestic hot water demand at every moment in time, expressed according to the mass balances in equations 6.36 and 6.37, respectively.

$$\dot{\boldsymbol{M}}_{4\to1,t} = \dot{M}_{DHW,t} \qquad \forall t \quad 6.36$$

$$\dot{\boldsymbol{M}}_{3\to2,t} + \Psi_{DHW\to SH}\dot{\boldsymbol{M}}_{4\to2,t} = \dot{M}_{SH,t} \qquad \forall t \quad 6.37$$

Here $\dot{\boldsymbol{M}}_{4\to1,t}$ is the water extracted from segment 4 and reinjected to segment 1 to satisfy the DHW demand $\dot{M}_{DHW,t}$. $\dot{\boldsymbol{M}}_{4\to2,t}$ is the water extracted from segment 4 and reinjected into segment 2 for providing space heating demand ($\dot{M}_{SH,t}$) through mixing with part of the space heating return water (Figure 6.3 right). Finally, $\dot{\boldsymbol{M}}_{3\to2,t}$ is the water from segment 3 to segment 2 which is directly used for space heating.

The amount of water heated up from the solar thermal collectors from segment n to segment m at a specific timestep t ($\dot{\boldsymbol{M}}_{STC,n\to m,t}$) can be estimated according to equations 6.38 -6.39.

$$\dot{\boldsymbol{M}}_{STC,n\to m,t} = \boldsymbol{\mathcal{X}}_{STC,n\to m,t}\frac{P_{STC,n\to m,t}}{c_{p,w}(T_m - T_n)}\Delta t \qquad \forall t \quad 6.38$$

$$\boldsymbol{\mathcal{X}}_{STES,d,t} + \sum_{n=1}^{N_{seg}-1}\sum_{m=n+1}^{N_{seg}} \boldsymbol{\mathcal{X}}_{STC,n\to m,t} \leq 1 \qquad \forall t \quad 6.39$$

Here $\boldsymbol{\mathcal{X}}_{STES,d,t}$ and $\boldsymbol{\mathcal{X}}_{STC,n\to m,t}$ are optimization variables representing the time step fraction in which the STCs have been used for charging the STES or heating water from T_n to T_m, at timestep t, respectively.

The amount of water heated up by the boiler from T_n to T_m at every timestep ($\dot{\boldsymbol{M}}_{boiler,n\to m,t}$) is linked to the thermal energy delivered by the boiler according to equation 6.40.

$$\boldsymbol{E}_{boiler,t} = \sum_{n=1}^{n=N_{seg}-1} \sum_{m=n+1}^{N_{seg}} \dot{\boldsymbol{M}}_{boiler,n\to m,t} c_{p,w}(T_m - T_n) \qquad \forall t \quad 6.40$$

The STES state of charge ($\boldsymbol{SOC}_{STES,t}$) is estimated according to equation 6.41, and it is expressed in relation to the maximum energy content of the STES. Moreover, as for the STCs, the STES operational behavior is described through the optimization variables, $\boldsymbol{\mathcal{X}}_{STES,d,t}$ and $\boldsymbol{\mathcal{X}}_{STES,s,n\to m,t}$, accounting for the time fraction spent in every operational mode during timestep t. Equation 6.42 ensures that the overall timestep fraction in which the STES is operating in a timestep t does not exceed 1.

$$\begin{aligned}&\boldsymbol{SOC}_{STES,t}\\&= \boldsymbol{SOC}_{STES,t-1}\\&+ \frac{\left(\boldsymbol{\mathcal{X}}_{STES,d,t} P_{STES,d,t} - \sum_{n=1}^{N_{seg}-1} \sum_{m=n+1}^{N_{seg}} \left(\boldsymbol{\mathcal{X}}_{STES,s,n\to m,t} P_{STES,s,n\to m,t}\right)\right) \Delta t}{E_{STES,max}}\end{aligned} \qquad \forall t \quad 6.41$$

$$\boldsymbol{\mathcal{X}}_{STES,d,t} + \sum_{n=1}^{N_{seg}-1} \sum_{m=n+1}^{N_{seg}} \boldsymbol{\mathcal{X}}_{STES,s,n\to m,t} \leq 1 \qquad \forall t \quad 6.42$$

The fan energy required for the STES charge and discharge, can be estimated by considering the timestep fraction in which the STES is operating in charging mode ($\boldsymbol{\mathcal{X}}_{STES,d,t}$) or discharging mode to heat up water from a segment $n < m$ to segment m (equation 6.43).

$$\boldsymbol{E}_{fan,t} = \left(\boldsymbol{\mathcal{X}}_{STES,d,t} P_{fan,d,t} + \left(\sum_{n=1}^{N_{seg}-1} \sum_{m=n+1}^{N_{seg}} \boldsymbol{\mathcal{X}}_{STES,s,n\to m,t}\right) P_{fan,max}\right) \Delta t \qquad \forall t \quad 6.43$$

The mass balance of every water tank segment (equation 6.7), in the optimization framework, can be derived along the lines of equation 6.44.

$$\begin{aligned}\boldsymbol{M}_{n,t} = \boldsymbol{M}_{n,t-1} e^{-\frac{\Delta t}{\tau_{n,t}}}&\\ + \Bigg(\sum_{m=1}^{m=n-1} &\left(\dot{\boldsymbol{M}}_{boiler,m\to n,t} + \dot{\boldsymbol{M}}_{STC,m\to n,t} + \dot{\boldsymbol{M}}_{STES,m\to n,t}\right)\\ &- \dot{\boldsymbol{M}}_{loss-top,n,t} - \sum_{m=1}^{m=n-1} \left(\dot{\boldsymbol{M}}_{n\to m,t}\right)\Bigg) \tau_{n,t} \left(1 - e^{-\frac{\Delta t}{\tau_{n,t}}}\right)\end{aligned} \qquad \forall t \quad 6.44$$

In equation 6.44, the first term on the right-hand side models the tank side losses (equations 6.6 - 6.7). It has to be remarked that not all the terms $\dot{\boldsymbol{M}}_{n\rightarrow m,t}$ are existing for every segment n. In fact, only specific terms exist for every segment according to Table 6.6, and equations 6.36 and 6.37.

Table 6.6: Optimization variables representing the water mass flows from a water tank segment n to a segment m due to the thermal losses, and the thermal energy demand of SH and DHW.

	m=1	m=2	m=3	m=4
n=1				$-\dot{\boldsymbol{M}}_{4\rightarrow 1,t}$
n=2	$\dot{\boldsymbol{M}}_{2\rightarrow 1,t}$		$-\dot{\boldsymbol{M}}_{3\rightarrow 2,t}$	$-\dot{\boldsymbol{M}}_{4\rightarrow 2,t}$
n=3		$\dot{\boldsymbol{M}}_{3\rightarrow 2,t}$		
n=4	$\dot{\boldsymbol{M}}_{4\rightarrow 1,t}$	$\dot{\boldsymbol{M}}_{4\rightarrow 2,t}$	$\dot{\boldsymbol{M}}_{4\rightarrow 3,t}$	

In Table 6.6, the elements highlighted in orange include also the thermal losses causing the water mass from a segment n to be transferred to the lower segment $n-1$. The amount of water heated by the STES from segment n to m can be calculated according to equation 6.45.

$$\dot{\boldsymbol{M}}_{STES,n\rightarrow m,t} = \boldsymbol{X}_{STES,s,n\rightarrow m,t}\frac{P_{STES,s,n\rightarrow m}}{c_{p,w}(T_m - T_n)}\Delta t \qquad \forall t \qquad 6.45$$

The thermal losses through the water tank top in segment n, in the optimization framework, can be expressed (equations 6.46 - 6.47) along the lines of equation 6.3.

$$\dot{\boldsymbol{M}}_{loss-top,n,t} = \boldsymbol{Y}_{loss-top,n,t}\frac{UA_{top}(T_n - T_{amb,t})}{c_{p,w}(T_n - T_{n-1})}\Delta t \qquad \forall t, \forall n > 1 \qquad 6.46$$

$$\sum_{n=1}^{N_{seg}} \boldsymbol{Y}_{loss-top,n,t} = 1 \qquad \forall t \qquad 6.47$$

Here $\boldsymbol{Y}_{loss-top,n,t}$ is a binary optimization variable that has a value of 1 if and only if segment n is corresponding to the top segment $n_{top,t}$ and it is not the bottom segment ($n = 1$). The formulation of $\boldsymbol{Y}_{loss-top,n,t}$ is shown in Appendix F. By also considering equation 6.47, this ensures that there is always one and only one value of n that is selected as $n_{top,t}$. Finally, the overall water tank mass balance can be written in form of equation 6.48.

$$\sum_{n=1}^{N_{seg}} \boldsymbol{M}_{n,t} = M_{TANK} \qquad \forall t \qquad 6.48$$

6.4 Results

The impact of including a domestic STES system in the reference energy system described in 6.2 and formulated as an optimization problem in 6.3 is investigated. First, the impact of formulating the optimization problem without considering the water tank top losses, at the advantage of the computational cost, is analyzed in section 6.4.1. Then, eight main problem parameters are varied: the building type, the solar thermal collectors number, the water tank volume (V_{tank}), the electricity-to-gas price ratio ($p_{el/gas}$), the STES capacity cost (SCC_{STES}), the STES maximum fan power ($P_{fan,max}$), the STES unit aspect ratio (d_{STES}/L_{STES}), and the sorbent particle size (d_p). The reference values of the parameters are shown in Table 6.7. The reference scenario considers the building with the largest rooftop area (Table 6.2, building B3) and a collector area that covers approximately 50 % of the rooftop area. A 0.5 m^3 water tank volume is selected. This size is considered acceptable in terms of house space usage for a single-family house, and within a reasonable size range for solar water tanks for systems producing space heating and DHW. The water tank is assumed to have an aspect ratio of 1.5, resulting in a side area of 2.66 m^2, and top and bottom areas of 0.44 m^2 each. The impact on the energy system of the ratio between the electricity and gas prices ($p_{el/gas}$) is also investigated. In 2018, this ratio varied across Europe from a minimum of 1.4 (Sweden) up to 4.3 (Belgium) with a European average of 2.5 (Figure 6.9).

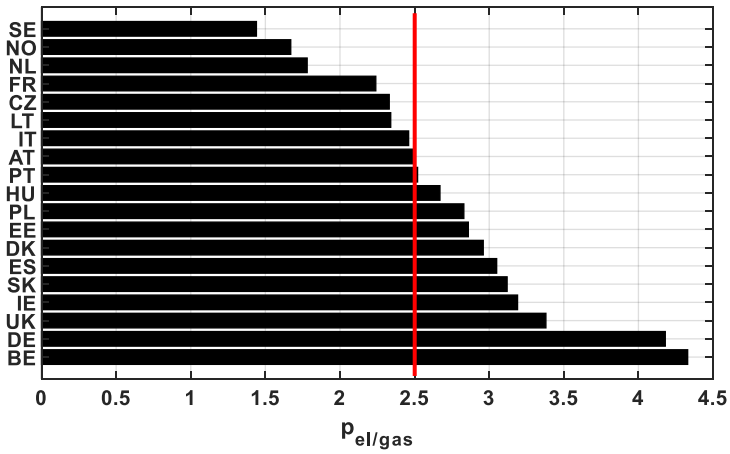

Figure 6.9: Ratio between the electricity price and the gas price (based on the high heating value) for various European countries in 2018 [213]**. Red line: European average.**

Both gas and electricity prices are the result of the different cost components (i.e. commodity price, network costs, taxes and levies, VAT) applied at country level [214]. The impact of this price ratio affects the energy system analyzed in this chapter because the STES fan utilization depends on the electricity price while the boiler utilization depends on the gas

price. A reference value of 2.5 is selected according to the European average [213]. Concerning the electricity price (p_{el}), a fixed value of 0.27 €/kWh, corresponding to the average price for Belgian households in the first semester of 2018 [215], has been used. The STES unit shape and sorbent particle size can have an effect on the STES operational costs because they directly influence the fan consumption. A reference aspect ratio of 0.7 has been considered based on similar existing lab prototype [121], and a sorbent particle size of 2 mm has been selected.

As in Chapter 5 (section 5.3.4), a STES capacity cost (SCC_{STES}) of 2.5 €/kWh$_{cap}$ corresponding roughly to 0.4 €/kg of active material is assumed. As already mentioned in Chapter 5, this value would consider only the sorbent cost, and it assumed a relatively inexpensive material. Concerning the STES fan, it is assumed that a fan power with a maximum power of 1 kW is installed. Finally, it is assumed that a STES unit consists of a cylindrical segment with an aspect ratio (d_{STES}/L_{STES}) of 0.7 and a volume ($V_{STES,unit}$) of approximately 48 liters (Table 6.1), and that the sorbent material has a particle size diameter of 2 mm. The abovementioned parameters are then varied in a sensitivity analysis to understand their influence on the energy system performance.

Table 6.7: Reference value for the investigated parameters.

Parameter	Reference Value	Units
Building Type	B3	-
STCs number	25	-
V_{tank}	0.5	m^3
$p_{el/gas}$	2.5	-
SCC_{STES}	2.5	€/kWh$_{cap}$
$P_{fan,max}$	1	kW
d_{STES}/L_{STES}	0.7	-
d_p	2	mm

The impact of the variation of the abovementioned parameters is estimated in terms of the relative cost decrease (RCD) and the solar fraction (SF). In this analysis, the relative cost decrease (RCD) is defined in equation 6.49 similarly to the relative profit increase (RPI) in Chapter 5 (equation 5.37).

$$RCD = \frac{\left(\boldsymbol{z}_{N_{STES,tot}=0} - \boldsymbol{z}\right)}{\boldsymbol{z}_{N_{STES,tot}=0}} \qquad 6.49$$

Here, $\boldsymbol{z}$ is the objective function value (equation 6.35) for the optimization problem with a specific number of STES units, and $\boldsymbol{z}_{N_{STES,tot}=0}$ is the value of the objective function without the STES integrated into the energy system. A positive RCD value implies that the solution

with the STES is less expensive than the solution without the STES integrated into the system.

The solar fraction (SF) is defined as the ratio between the yearly solar gains (E_{Solar}) minus the thermal losses ($E_{tank,loss}$), and the amount of energy provided by the system for space heating (E_{SH}) and domestic hot water demand (E_{DHW}). This assumption is based on the fact that, without the solar thermal collectors in the system, there would not be the need of having a water tank in the system at all because the gas boiler would be able to provide instantaneously the thermal energy required for both space heating and domestic hot water. The solar gains can be defined according to equation 6.50.

$$E_{Solar} = \sum_{t=1}^{t_{sim}} \sum_{n=1}^{N-1} \sum_{m=n+1}^{N_{seg}} \left(\boldsymbol{\mathcal{X}}_{STES,s,n\to m,t} P_{STES,s,n\to m,t} + \boldsymbol{\mathcal{X}}_{STC,n\to m,t} P_{STC,n\to m,t} \right) \Delta t \qquad 6.50$$

Here, the first term of the summations on the right-hand side represent the yearly energy provided to each segment of the water tank from the STES, and the second term represents the yearly energy provided to each segment of the water tank directly from the solar thermal collectors. The water tank thermal losses are defined as in equations 6.51 - 6.53.

$$E_{tank,loss} = E_{tank,loss,side} + E_{tank,loss,top} \qquad 6.51$$

$$E_{tank,loss,side} = \sum_{t=1}^{t_{sim}} \sum_{n=2}^{N_{seg}} \boldsymbol{M}_{n,t-1} \left(1 - e^{-\frac{\Delta t}{\tau_{n,t}}} \right) c_{p,w} (T_n - T_{n-1}) \qquad 6.52$$

$$E_{tank,loss,top} = \sum_{t=1}^{t_{sim}} \sum_{n=2}^{N_{seg}} \dot{\boldsymbol{M}}_{loss-top,n,t} \tau_{n,t} \left(1 - e^{-\frac{\Delta t}{\tau_{n,t}}} \right) c_{p,w} (T_n - T_{n-1}) \qquad 6.53$$

Here, equation 6.52 represents the thermal losses from the side of the water tank, and equation 6.53 represents the thermal losses from the top of the tank. Finally, the solar fraction can be defined according to equation 6.54.

$$SF = \frac{E_{Solar} - E_{tank,loss}}{E_{SH} + E_{DHW}} \qquad 6.54$$

6.4.1 Tank top losses

The inclusion of the water tank thermal losses through the top ($\dot{\boldsymbol{M}}_{loss-top,n,t}$) makes the optimization problem a mixed integer linear problem due to the presence of the binary variables $\boldsymbol{Y}_{loss-top,n,t}$. The resulting optimization problem is much more computationally expensive compared to the optimization problem that does not consider the tank top losses. By neglecting these losses, the problem can be formulated as a linear program and solved considerably faster. From the computational perspective, this means including constraints 6.46, 6.47, and F.3 (Appendix F) or excluding them and setting $\dot{\boldsymbol{M}}_{loss-top,n,t}$ always equal to zero for every segment n and timestep t. In this section, the impact of neglecting the tank top thermal losses in a scenario with different water tank sizes is investigated.
The investigated scenario has the parameters value according to Table 6.7. In Figure 6.10 top left, the relative difference between the objective function value including ($\boldsymbol{z}_{N_{STES}=0,Loss}$) or excluding ($\boldsymbol{z}_{N_{STES}=0,Noloss}$) the water tank top losses is shown for the solution without the STES integrated. The value is expressed in percentage relative to the solution that does not consider the tank losses (equation 6.55).

$$\Delta \boldsymbol{z}_{N_{STES}=0} = \frac{\boldsymbol{z}_{N_{STES}=0,loss} - \boldsymbol{z}_{N_{STES}=0,Noloss}}{\boldsymbol{z}_{N_{STES}=0,Noloss}} \qquad 6.55$$

A positive value of $\Delta \boldsymbol{z}_{N_{STES}=0}$ would indicate that the solution including the top losses has a higher value of the objective function, hence higher yearly costs. A $\Delta \boldsymbol{z}_{N_{STES}=0}$ value approaching zero would imply that the solutions with and without the water tank top losses included have similar system costs. Therefore, a small $\Delta \boldsymbol{z}_{N_{STES}=0}$ would support the assumption of not considering the tank top losses.
Following the same logic, the relative difference between the solar fraction ($\Delta SF_{N_{STES}=0}$) values in the same conditions are estimated (Figure 6.10 bottom left). A negative value of $\Delta SF_{N_{STES}=0}$ would imply that the solution that considers the tank top losses has a lower SF than the solution including the losses, which is the expected system behavior.
As it is possible to see from Figure 6.10 top left, by not considering the top losses, the objective function differences in the four simulations varying the water tank size are relatively small. As expected, the difference has positive values implying that the solutions considering the water tank losses have higher yearly operational costs. The minimum difference occurred for a water tank size of 0.25 m^3 (0.04 %) and it increases by increasing the water tank volume up to the maximum occurring for a tank volume of 2 m^3 (0.61 %).
Concerning the solar fraction (Figure 6.10 bottom left), which has the same trend, the minimum difference between the two models occurred for 0.25 m^3 (0.65 %) and increased with the tank volume up to the maximum for a tank volume of 2 m^3 (1.79 %).

In Figure 6.10 top right, the water tank thermal losses are displayed for the solutions with or without considering the tank top losses. In the solutions considering the tank top losses, as expected, the overall thermal losses are higher compared to the solution without considering the tank top losses.

Finally, in Figure 6.10 bottom right, the boiler and solar energy fractions supplied to the water tank for different water tank volumes are displayed. As expected, the amount of solar energy delivered to the tank increases by increasing the water tank size for both solutions with (black edge bars) and without (red edge bars) considering the tank top losses. The energy delivered by the boiler is slightly higher for all the cases with tank top losses, which in turns causes higher values of $\Delta z_{N_{STES}=0}$. In particular, the thermal energy supplied by the boiler in the solutions considering the tank top losses is 0.01 MWh (V_{tank}= 0.25 m^3), 0.02 MWh (V_{tank}= 0.5 m^3), 0.04 MWh (V_{tank}= 1 m^3), and 0.06 MWh (V_{tank}= 2 m^3) more than the solutions without tank top losses.

The average simulation time of the linear problem (LP) excluding the top losses was 11 minutes, while for the MILP problem including the top losses was 109 minutes. Therefore, given the relatively small loss of accuracy and the gain in computational time, the simulations in this work are solved without considering the top losses from the water tank.

An alternative choice could have been to consider the tank top losses always present, with an average temperature. However, this would give an equal importance to the water tank segments, and the optimization process would not penalize the presence of segments at high temperature being at the top of the tank. Thus, an average temperature value could still lead to an underestimation of the thermal losses. Another alternative choice would have been to impose the presence of the thermal losses at the top of the tank only for the segment at the highest temperature ($n = 4$). The issue with this last approach is that the optimization process would penalize only the presence of water of the hottest segment. This might lead to an entirely different optimal solution and water tank operational behavior, which is mainly focused on avoiding having water at T_4.

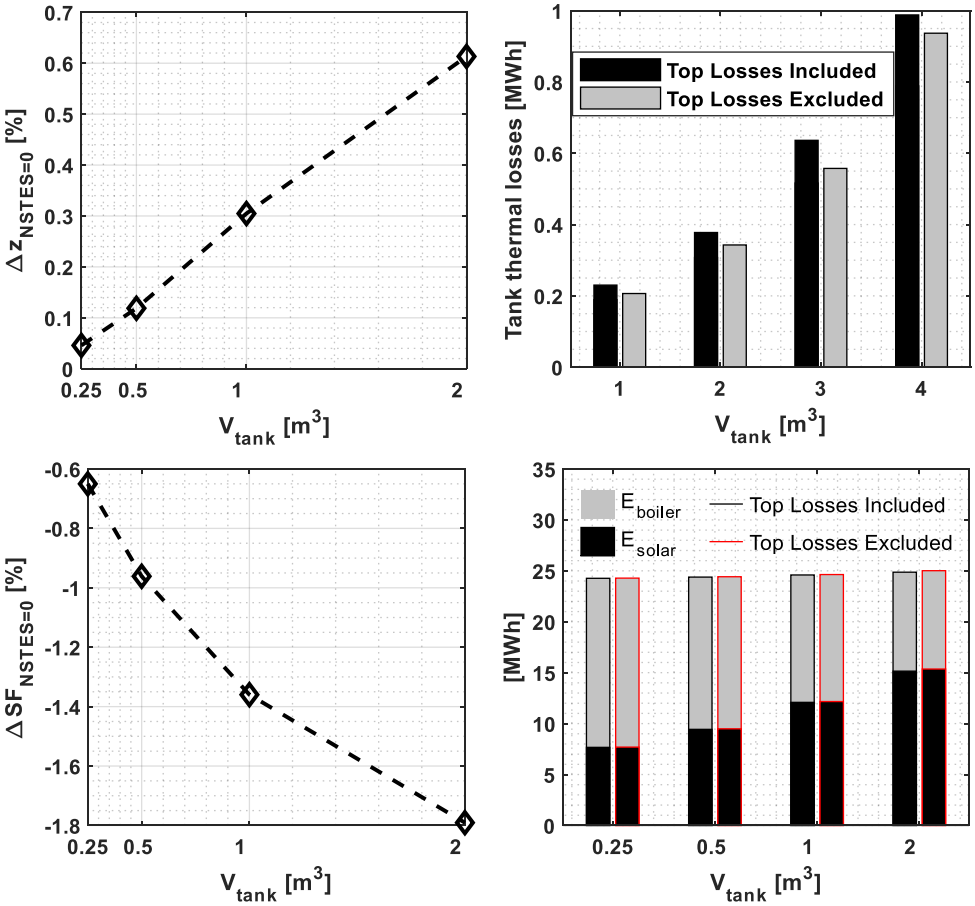

Figure 6.10: Top left: Relative difference between the optimal solutions with and without considering the water tank top losses, without STES integrated ($\Delta z_{N_{STES}=0}$). Top right: Thermal losses for the solutions with (black) and without (grey) top losses included in the solutions. Bottom left: Relative solar fraction difference for different water tank sizes with and without considering the water tank top losses, without STES integrated ($\Delta SF_{N_{STES}=0}$). Bottom right: Boiler (grey) and solar (black) energy supplied to the water tank for the solutions with (black edge) and without (red edge) tank top losses. Water tanks aspect ratio = 1.5. House type = B3, STCs = 25, $p_{el/gas}$=2.5, SCC_{STES}=2.5 €/kWh$_{cap}$, $P_{fan,max}$=1 kW, d_{STES}/L_{STES} = 0.7, d_p = 2 mm, $V_{STES,unit}$ = 0.048 m^3, $A_{STC,unit}$ = 3 m^2.

6.4.2 Solar thermal collectors number and building types

The number of solar thermal collectors, is varied in multiples of 5 units until approximately half of the roof area of each building, and their orientation is assumed towards the south. In Figure 6.11 left, the RCD by carrying the STC number for the three investigated buildings is shown. Next to the markers, the number of STES units in the optimal solution, for each STC number, is presented. For each building, the amount of STES units increases by increasing

the STC number, and the RCD has a significant increase especially if more than 10 STCs are present for each building. The STES integration leads to a cost decrease of approximately 0.15 – 0.33 % if only 5 STCs are present. If 15 STCs are installed, the RCD increases for each scenario up to 1.9 – 2.6 %. For building B3, which has a larger roof area, the STCs are increased up to 25 units, and a RCD of 6.9 % can be achieved with 10 STES units ($V_{STES} \cong$ 0.48 m^3).

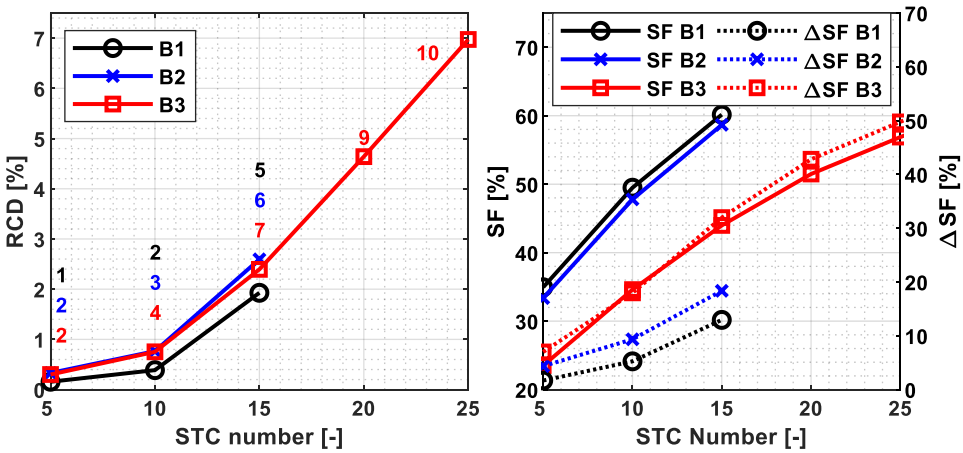

Figure 6.11: RCD and optimal amount of STES segments (left) and solar fraction (right) for the different house types investigated (B1, B2, B3) and different amount of STCs. V_{tank}= 0.5 m^3, $p_{el/gas}$=2.5, SCC_{STES}=2.5 €/kWh$_{cap}$, $P_{fan,max}$=1 kW, d_{STES}/L_{STES} = 0.7, d_p = 2 mm, $V_{STES,unit}$ = 0.048 m^3, $A_{STC,unit}$ = 3 m^2.

In Figure 6.11 right, the solar fraction SF for buildings B1 and B2 increases from approximately 34 % to 60 % for the investigated STC numbers, with the optimal STES units. The STES integration has a relatively small contribution for the solutions with 5 STCs since the solar fraction increase (ΔSF) due to the STES integration is approximately 1.7 % and 4.3 % for buildings 1 and 2, respectively. However, for larger numbers of STCs, the STES contribution increases the solar fraction up to 13 % and 18 % for buildings B1 and B2, respectively. Building B3, achieves a solar fraction of 57 % with the optimal amount of STES units (10), with an approximately 50 % increase of solar fraction compared to the solution without STES integrated. In general, for the same number of STCs, building B3 has a lower solar fraction due to its higher yearly energy demand (Table 6.2).

6.4.3 Water tank volume

The water tank volume is varied from 250 liters to 2000 liters to understand its influence towards the optimization objective. A larger water tank can store more energy but thermal losses towards the environment can also be larger.

In Figure 6.12 top left, the RCD by increasing the water tank size decreases from 7.5 % (V_{tank} = 0.25 m^3) to 2.8 % (V_{tank} = 2 m^3). This decrease implies that the STES added value on the overall energy system costs is diminishing by increasing the water tank size. The reason for this decrease is due to the fact that the water tank is already assumed to be present in the energy system.

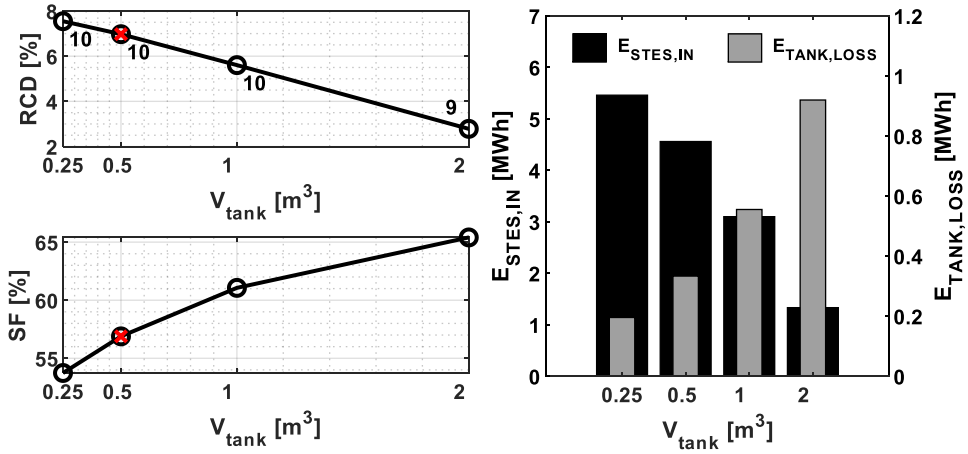

Figure 6.12. Left: RCD and optimal amount of STES segments (top) and solar fraction (bottom) for different water tank volumes. Red marker: Reference value from the parameters of Table 6.7. Right: Yearly energy stored into the STES and yearly energy lost due to the water tank thermal losses. House type = B3, STCs = 25, $p_{el/gas}$=2.5, SCC_{STES}=2.5 €/kWh$_{cap}$, $P_{fan,max}$=1 kW, d_{STES}/L_{STES} = 0.7, d_p = 2 mm, $V_{STES,unit}$ = 0.048 m^3, $A_{STC,unit}$ = 3 m^2.

By not including the water tank investment and operational costs, the optimal solution stores more solar energy in the water tank, which is considered almost as a free storage. The only penalty in the optimization model for storing energy in the water tank are the thermal losses. Therefore, as shown in Figure 6.12 right, the STES is used less often having a total yearly injected energy of 5.5 MWh for a tank volume of 0.25 m^3 and a decrease up to 1.3 MWh for a tank volume of 2 m^3, respectively. On the contrary, the thermal losses in the water tank are increasing by increasing the tank size from 0.19 MWh (V_{tank} = 0.25 m^3) up to 0.92 MWh (V_{tank} = 2 m^3). The solar fraction (Figure 6.12 bottom left) increases from 54 % (V_{tank} = 0.25 m^3) up to 65 % (V_{tank} = 2 m^3) due to the possibility to store more thermal energy at the only cost of the tank thermal losses.

In Figure 6.13, it is shown that the larger the water tank, the more it is used as a seasonal heat storage. In Figure 6.13 left, the amount of water at the four different temperature levels is shown. The amount of water at high temperature increases by increasing the tank size and it is more present during the summer months. The water tank state of charge (Figure 6.13 middle) shows that for small water tank sizes, the state of charge has frequent charge and discharge cycles during the whole year. For large sizes (i.e. 1 m^3 or 2 m^3), the water tank

SOC is always above 0.5 during summer, and the charge and discharge cycles are more present during the months of February – March and October – November. Finally, in Figure 6.13 right, the STES SOC is displayed, and it is evident that the STES usage is reduced with the increase of the water tank volume.

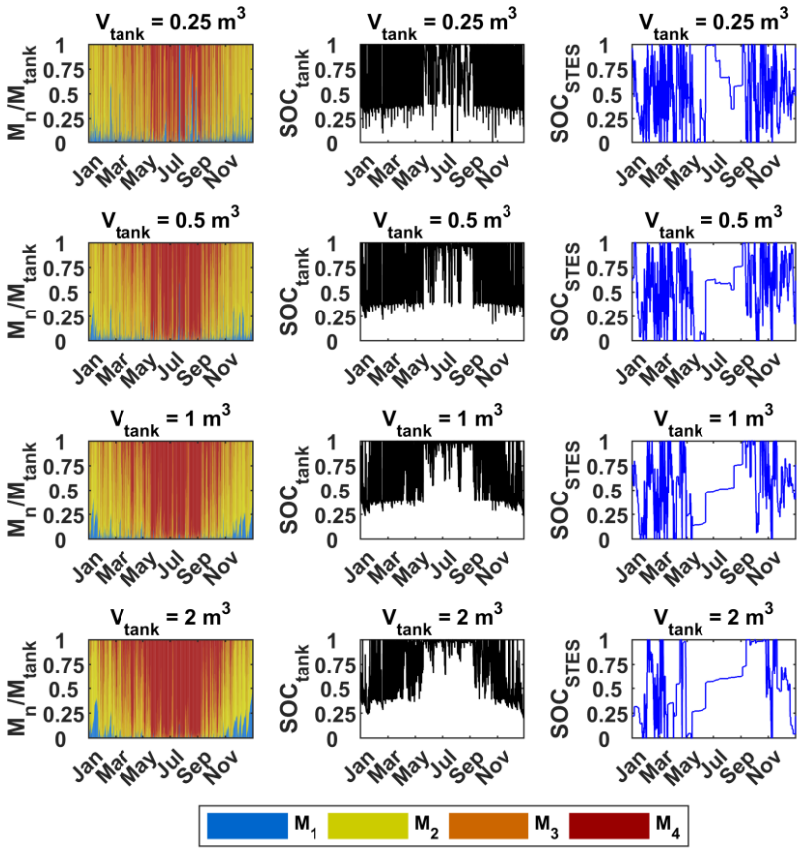

Figure 6.13: Left: Water fractions in different segments through the year. M_4 at T_{DHW}, M_3 at $T_{SH,sp}$, M_2 at $T_{SH,rt}$, M_1 at T_{MAIN}. Middle: Water tank yearly state of charge evolution. Right: STES yearly state of charge evolution. House type = B3, STCs = 25, $p_{el/gas}$=2.5, SCC_{STES}=2.5 €/kWh$_{cap}$, $P_{fan,max}$=1 kW, d_{STES}/L_{STES} = 0.7, d_p = 2 mm, $V_{STES,unit}$ = 0.048 m^3, $A_{STC,unit}$ = 3 m^2.

6.4.4 Electricity-gas price ratio

The electricity-gas price ratio is varied from 1 to 5 to understand its impact on the energy system investigated. In particular, the STES fan and the boiler operation are directly affected by this parameter. In Figure 6.14 right, it is shown that for lower $p_{el/gas}$ the STES integration becomes more favorable. For the average European $p_{el/gas}$ value ($p_{el/gas}$ = 2.5) the optimal

amount of STES units (N_{STES} = 10) leads to an RCD of 6.9 % and a solar fraction of 57 %. For higher $p_{el/gas}$ values the STES integration becomes less favorable and, for $p_{el/gas}$ values of 4 and above, the STES is not integrated anymore in the energy system resulting in the solar fraction that would be achieved without the STES (SF = 38 %). On the other hand, it is remarkable to notice that if $p_{el/gas}$ would have a value of 1, a very high number of STES units would be integrated in the optimal solution (N_{STES} = 700), resulting in a RCD of 28.1 % and a solar fraction of 85 %. The same effect of a $p_{el/gas}$ decrease could be equally obtained by an improvement of the STES seasonal performance factor (SPF). In fact, halving $p_{el/gas}$ would produce the same effect of having a STES with a doubled SPF. The STES SPF is investigated more in detail in section 6.4.7 in relation to the STES unit shape and sorbent particle size.

The number of STES units in the optimal solution for each $p_{el/gas}$ value drastically influences the STES behavior over the year. Figure 6.15 left shows the SOC_{STES} for $p_{el/gas}$ = 2.5, which included 10 STES units. The STES operates with frequent charge/discharge cycles as a short- or medium-term storage. Only between the months of June – August, the STES mainly stores energy to be used in the first discharge cycles approximately at the beginning of September. For the solution with $p_{el/gas}$ = 1 and 700 STES units, the STES behaves as a seasonal heat storage, mostly charging during the summer months and discharging during the winter months.

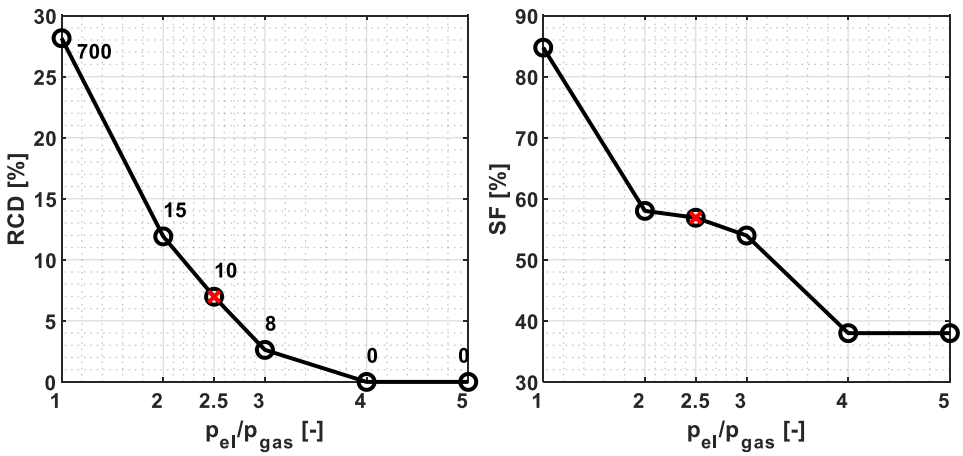

Figure 6.14: RCD and optimal amount of STES segments (left) and solar fraction (right) for different electricity-gas price ratio. Red marker: Reference value from the parameters of Table 6.7. House type = B3, STCs = 25, V_{tank}=0.5 m^3, SCC_{STES}=2.5 €/kWh$_{cap}$, $P_{fan,max}$=1 kW, d_{STES}/L_{STES} = 0.7, d_p = 2 mm, $V_{STES,unit}$ = 0.048 m^3, $A_{STC,unit}$ = 3 m^2.

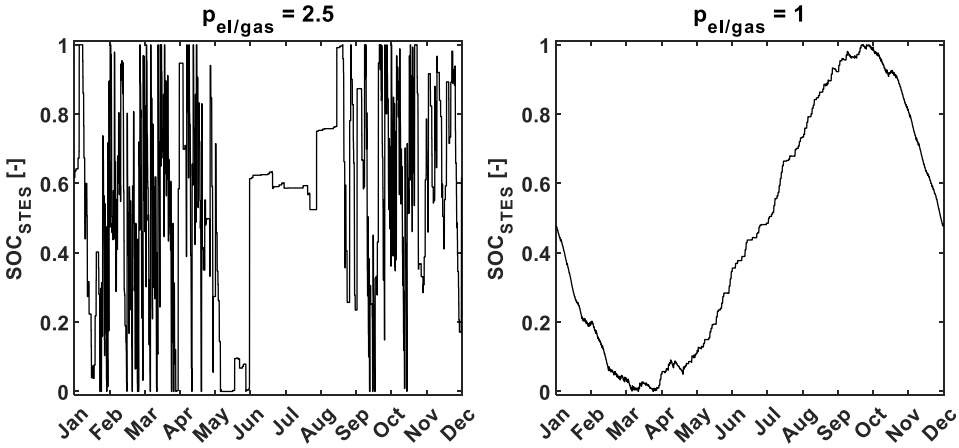

Figure 6.15: STES state of charge for the optimal solution with $p_{el/gas}$ = 2.5 and N_{STES} = 10 (left) and for the optimal solution with $p_{el/gas}$ = 1 and N_{STES} = 700 (right).

6.4.5 STES capacity cost

A realistic value for the STES capacity costs (SCC_{STES}) is uncertain due to the fact that the technology is still at a relatively early technology readiness level. A minimum SCC_{STES} has been assumed equal to 2.5 €/kWh$_{cap}$, and it has been increased up to 80 €/kWh$_{cap}$ in order to study its influence on the overall system costs and optimization objective.

In Figure 6.16 left, the RCD decrease with the SCC_{STES} increase is shown. A decrease from 6.9 % to 0.20 % is present if SCC_{STES} is increased from 2.5 €/kWh$_{cap}$ to 60 €/kWh$_{cap}$, respectively.

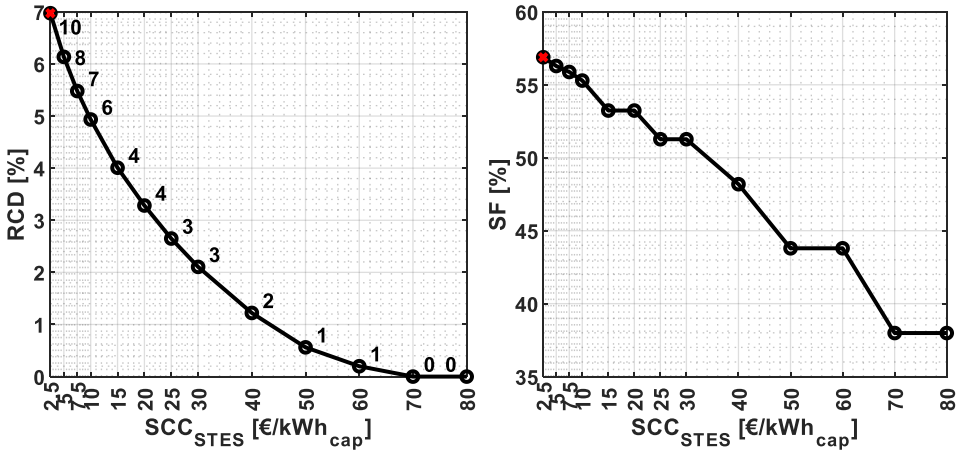

Figure 6.16: Left: RCD and optimal amount of STES segments for different SCC_{STES}. Right: Solar fraction for different STES capacity costs. Red marker: Reference value from the parameters of Table 6.7. House type = B3, STCs = 25, V_{tank} = 0.5 m^3, $p_{el/gas}$= 2.5, $P_{fan,max}$=1 kW, d_{STES}/L_{STES} = 0.7, d_p = 2 mm, $V_{STES,unit}$ = 0.048 m^3, $A_{STC,unit}$ = 3 m^2.

For SCC_{STES} higher than 60 €/kWh$_{cap}$, the economically optimal solution does not include the STES anymore. As expected, also the STES units in the optimal solution are decreasing from 10 (SCC_{STES} = 2.5 €/kWh$_{cap}$) up to 1 (SCC_{STES} = 60 €/kWh$_{cap}$). By increasing the STES capacity cost, the economically optimized system has a lower amount of STES modules, resulting in a solar fraction decrease from 57 % to 44 % for capacity costs of 2.5 €/kWh$_{cap}$ and 60 €/kWh$_{cap}$, respectively (Figure 6.16 right). It is possible to notice how the solar fraction depends on the amount of STES units present in the optimal solutions. For example, the solutions with SCC_{STES} of 25 €/kWh$_{cap}$ and 30 €/kWh$_{cap}$ achieve the same solar fraction since they both have the same number of STES units (N_{STES} = 3) and the same yearly operational behavior. However, the former has a higher RCD than the latter (2.6 % and 2.1 %, respectively) due to the lower STES CAPEX.

In Figure 6.17, it is possible to assess impact of the different cost components for the investigated energy system (Figure 6.17 left), and their relative impact compared to the overall costs (Figure 6.17 right). The yearly STES CAPEX in the optimal solutions, even by increasing the capacity costs, accounts for a small fraction compared to the operating costs of the gas boiler and the STES.

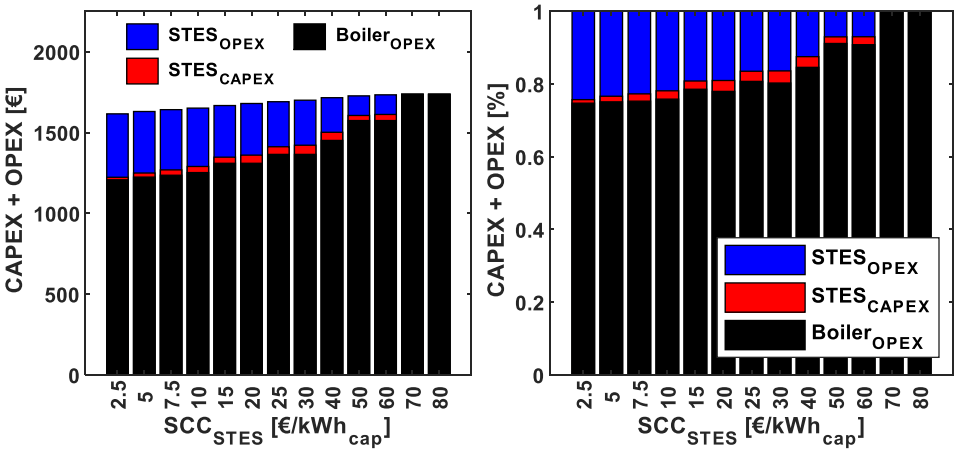

Figure 6.17: CAPEX and OPEX considered in this analysis for different SCC_{STES} (left) and their relative percentage compared to the overall system costs considered in this analysis (right). House type = B3, STCs = 25, V_{tank}=0.5 m^3, $p_{el/gas}$=2.5, $P_{fan,max}$=1 kW, d_{STES}/L_{STES} = 0.7, d_p = 2 mm, $V_{STES,unit}$ = 0.048 m^3, $A_{STC,unit}$ = 3 m^2.

In particular, for STES capacity costs of 2.5 €/kWh$_{cap}$, the gas consumption costs account for 74.7 % (1207 €), the STES CAPEX for 1.0 % (16 €), and the STES operational costs for 24.3 % (392 €). For a STES capacity cost of 60 €/kWh$_{cap}$, gas consumption accounts for 90.8 % (1574 €), the STES CAPEX for 2.2 % (38 €) and the STES OPEX for 7.0 % (121 €). The relatively low STES CAPEX is due to the relatively low amount of STES units present in the optimal solution and the estimated STES lifetime (lt_{STES}) of 20 years. For example, for the

optimal solution with SCC_{STES} = 60 €/kWh$_{cap}$, only 1 STES unit is present. A single STES unit corresponds to approximately 9.3 kWh$_{cap}$ (equation 6.9). Thus, according to equation 6.31, this would result in a yearly CAPEX of approximately 38 €. Finally, it is remarkable to notice the low impact of the STES CAPEX compared to the STES OPEX. Thus, improving the STES performance would allow for larger STES sizes.

6.4.6 STES fan power

The maximum fan power ($P_{fan,max}$) has been varied from a minimum value of 250 W up to 10 kW to see how the optimal STES charge and discharge behavior is affected. During the STES discharge the fan has a constant power corresponding to its maximum power while during the STES charge the fan has a variable power according to the amount of available solar energy for the STES charge, at every timestep (section 6.2.3).

In Figure 6.18 left, the RCD is shown for different $P_{fan,max}$ values ranging from 0.25 kW to 10 kW. For an electricity-gas price ratio of 2.5, the RCD has a maximum for a $P_{fan,max}$ of 0.25 kW (13.9 %) and it decreases up to a $P_{fan,max}$ value of 1.5 kW (1.6 %), after which OPEX costs for the fan become too large to include the STES in the economically optimized configuration. For an electricity-gas price ratio of 1, the maximum RCD (29.7 %) is achieved for a $P_{fan,max}$ value of 0.5 kW, and 600 STES units in the optimal solution. For increasing values of $P_{fan,max}$, the pressure loss becomes significant, and the RCD decreases until a $P_{fan,max}$ value of 10 kW is reached, a RCD of 0.03 % is achieved, and only 1 STES unit ($V_{STES,unit}$ = 0.048 m^3) is present in the optimal solution. The RCD behavior for $p_{el/gas}$=1 shows that for too low values of $P_{fan,max}$, the fan power limits the amount of energy that can be stored or extracted from the STES. If the fan power is increased, a larger number of STES units in the optimal solution is present, and a higher RCD value can be achieved. Then, by further increasing $P_{fan,max}$, the pressure loss impact becomes dominant and the RCD decreases.

In Figure 6.18 right, the solar fraction achieved for every optimal solution by varying $P_{fan,max}$ is shown. The SF value is directly related to the amount of STES units in the optimal solution. In particular, the higher N_{STES} is, the higher is SF. For solutions with an equal number of N_{STES}, the higher the $P_{fan,max}$ is, the higher is the SF. However, as shown in Figure 6.18 left, for the same number of STES units (i.e. N_{STES} = 10, $p_{el/gas}$ = 2.5), a higher fan power would lower the RCD. For an electricity-gas price ratio of 1, the maximum SF value (89 %) is achieved for a $P_{fan,max}$ of 1.5 kW and a N_{STES} of 750. For an electricity to gas price ratio of 2.5, the maximum SF value (57 %) is achieved for a $P_{fan,max}$ of 1 kW, the highest $P_{fan,max}$ in which N_{STES} remains equal to 10. For larger $P_{fan,max}$ values, the N_{STES} decreases and SF decreases up to the minimum base value of 38 %, which is the value of the optimal solution without STES integrated.

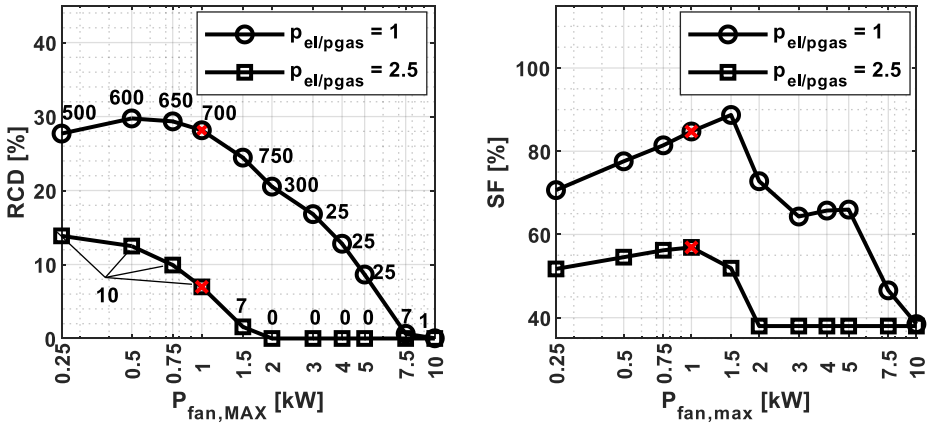

Figure 6.18: RCD and optimal amount of STES segments (left) and solar fraction (right) for different $P_{fan,max}$ values and for two $p_{el/gas}$ values (1 and 2.5). Red marker: Reference value from the parameters of Table 6.7. House type = B3, STCs = 25, V_{tank}=0.5 m^3, SCC_{STES}= 2.5 €/kWh$_{cap}$, d_{STES}/L_{STES} = 0.7, d_p = 2 mm, $V_{STES,unit}$ = 0.048 m^3, $A_{STC,unit}$ = 3 m^2.

In Figure 6.19, the STES CAPEX and the STES and boiler OPEX are displayed for an electricity to gas ratio of 1 (left) and 2.5 (right), respectively. From Figure 6.19 left, the solution with the minimum RCD ($P_{fan,max}$ = 0.5 kW, N_{STES} = 600) has the CAPEX impacting for roughly 30.9 %, the STES OPEX for 17.8 % and the boiler OPEX for 51.3 %. For an electricity to gas price ratio of 2.5 (Figure 6.19 right), the optimal RCD is achieved for a $P_{fan,max}$ of 0.25 kW (N_{STES} = 10). In this optimal solution, the STES CAPEX impact for 1.1 %, the STES OPEX for 8.5 %, and the boiler OPEX for 90.4 %, respectively.

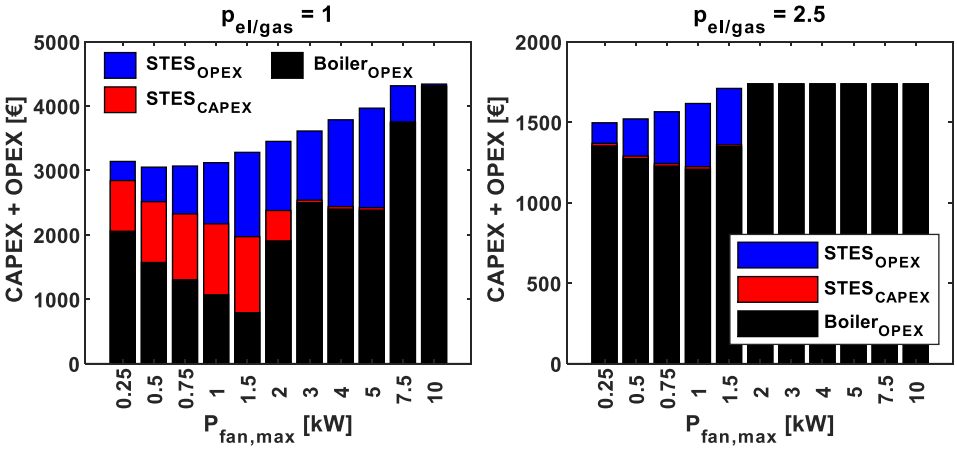

Figure 6.19: CAPEX and OPEX considered in this analysis varying $P_{fan,max}$ for two $p_{el/gas}$ values (1 and 2.5). House type = B3, STCs = 25, V_{tank}=0.5 m^3, SCC_{STES}= 2.5 €/kWh$_{cap}$, d_{STES}/L_{STES} = 0.7, d_p = 2 mm, $V_{STES,unit}$ = 0.048 m^3, $A_{STC,unit}$ = 3 m^2.

6.4.7 STES unit shape and sorbent particle size

The single STES unit shape and certain material characteristics have an influence on the overall STES performance. In particular, the aspect ratio of a single STES unit (d_{STES}/L_{STES}) and the sorbent particle diameter (d_p) influence the pressure loss (equation 6.22), and therefore the fan consumption and, consequently, the yearly STES operational costs.
In Figure 6.20 left, it is shown that the RCD increases by increasing the aspect ratio and the particle diameter. For the reference case, increasing the particle diameter from 2 mm to 4 mm would increase the RCD from 6.9 % to 17.4 % due to the lower fan consumption. The same effect is present when the STES unit aspect ratio is increased, by making the cylindrical segment with a shorter axial length and a larger diameter. By increasing the aspect ratio from the reference value of 0.7 to 1 and 1.3, the RCD increases from 6.9 % to 12.5 %, and 16.6 %, respectively. The same trends are followed by the solar fraction, which increases from 57 % to 63 % by increasing the particle diameter from 2 mm to 4 mm in the reference case (d_{STES}/L_{STES} = 0.7). By increasing the aspect ratio, the solar fraction increases from 57 % (d_{STES}/L_{STES} = 0.7) to approximately 62 % (d_{STES}/L_{STES} = 1.3).

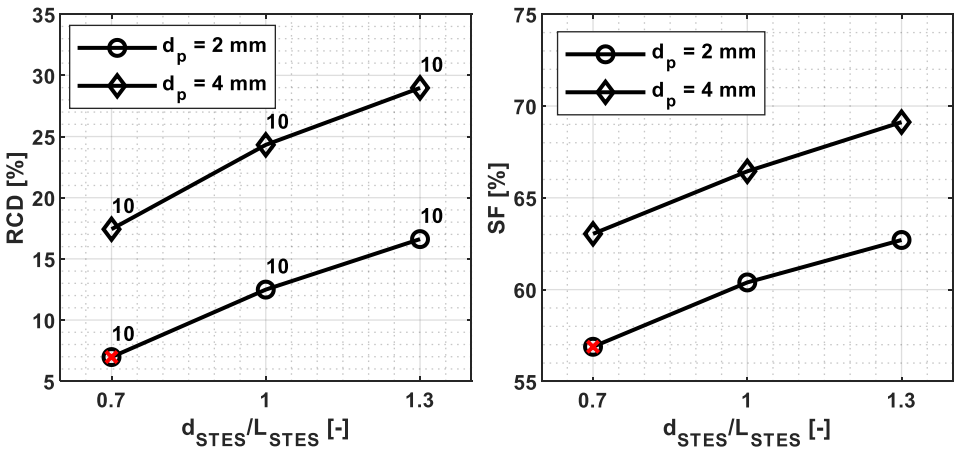

Figure 6.20: RCD and optimal amount of STES segments (left) and solar fraction (right) for different particle diameters d_p. Red marker: Reference value from the parameters of Table 6.7. House type = B3, STCs = 25, V_{tank}=0.5 m³, SCC_{STES}= 2.5 €/kWh$_{cap}$, , $p_{el/gas}$=2.5, $P_{fan,max}$= 1 kW, $V_{STES,unit}$ = 0.048 m³, $A_{STC,unit}$ = 3 m².

Two additional performance indicators are used to assess the STES performance by varying the STES unit shape and particle diameters. The first indicator is the coefficient of performance (COP_t), calculated as in equation 6.56, and defined as the ratio between the charging or discharging STES energy in a single timestep ($\boldsymbol{E}_{STES,s/d,t}$) and the fan energy consumption ($\boldsymbol{E}_{fan,t}$) during that timestep.

$$COP_t = \frac{\boldsymbol{E}_{STES,s/d,t}}{\boldsymbol{E}_{fan,t}} \qquad 6.56$$

The second indicator is the seasonal performance factor (SPF) [216], calculated as in equation 6.57, and defined as the yearly discharged STES energy and the yearly fan energy consumption.

$$SPF = \frac{\sum_{t=1}^{t_{sim}} \boldsymbol{E}_{STES,s,t}}{\sum_{t=1}^{t_{sim}} \boldsymbol{E}_{fan,t}} \qquad 6.57$$

In Figure 6.21 left, the STES charging and discharging energy, the fan energy, and the COP are shown for the reference case and for a specific period in the year (11/09 – 12/09). During the STES discharge ($\boldsymbol{E}_{STES,s,t}$), the STES provides the energy ($\boldsymbol{E}_{STES,s,2\rightarrow3,t}$) to heat up the water from segment 2 to segment 3 (Figure 6.21 right), with a COP_t of 4.37. No other STES discharge modes are present in this time period. Therefore, the total discharged energy during a single timestep ($\boldsymbol{E}_{STES,s,t}$) is equal to the discharged energy to heat up water from segment 2 to segment 3. During the STES charge ($\boldsymbol{E}_{STES,d,t}$), the COP_t is approximately equal to 22.1. This higher value compared to the discharge phase is due to the higher temperature difference between the inlet and outlet air temperature of the STES unit, for approximately the same fan power.

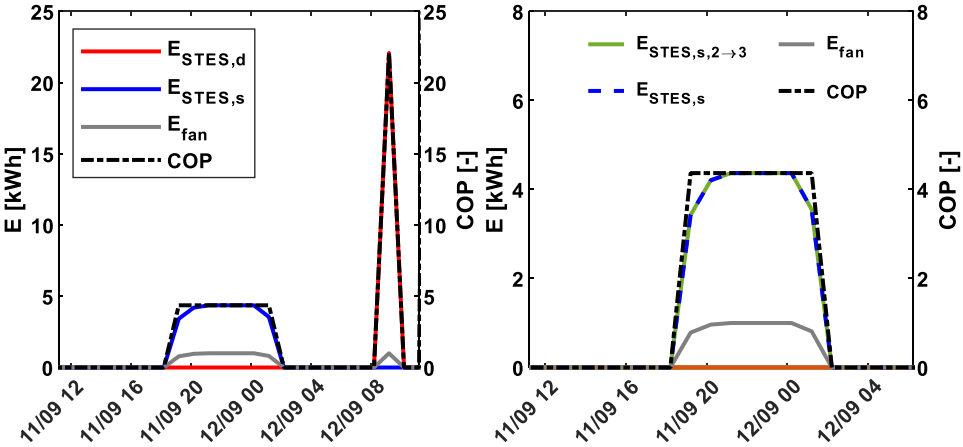

Figure 6.21: Left: STES charging (red), discharging (blue), fan energy (gray), and COP (back) between 11/09 and 12/09. Right: Zoom-in on the STES discharging energy for every operational mode. Green: from segment 2 to segment 3. Blue: Overall STES discharging energy. Gray: STES fan energy. Black: COP. House type = B3, STCs = 25, V_{tank}=0.5 m^3, $p_{el/gas}$=2.5, SCC_{STES}= 2.5 €/kWh$_{cap}$, $P_{fan,max}$= 1 kW, d_{STES}/L_{STES} = 0.7, d_p = 2 mm, $V_{STES,unit}$ = 0.048 m^3, $A_{STC,unit}$ = 3 m^2.

The STES COP in the reference case is relatively low, given the fact that the average COP values for air source heat pumps and ground source heat pumps are in the range of 3.2 – 4.5 and 4.2 – 5.2, respectively [217], with testing conditions according to EN 14511.
For the case in which the maximum fan power ($P_{fan,max}$) is imposed equal to 0.25 kW (Figure 6.22), the COP is more than doubled. In particular, during the same time period, for the discharging phase the COP is 10.0, and for the charging phase it has values between 50.4 and 44.3. In Figure 6.22 right, a slightly lower COP value (9.7) is shown during the discharge phase, immediately before 11/09 at 16:00. The reason for that decrease is because, only during that timestep, the STES is discharged also to provide energy for heating up the water from the water tank segment 3 to segment 4. The energy produced in this operating mode ($\boldsymbol{E}_{STES,s,3\rightarrow4,t}$) has a lower COP (~8) compared to $\boldsymbol{E}_{STES,s,2\rightarrow3,t}$. Thus, the resulting COP is the weighted average between the COP of the two operating modes, and the weights are the timestep fractions during which each operating mode has been active ($\boldsymbol{\mathcal{X}}_{STES,s,2\rightarrow3,t}$ and $\boldsymbol{\mathcal{X}}_{STES,s,3\rightarrow4,t}$) in that timestep.

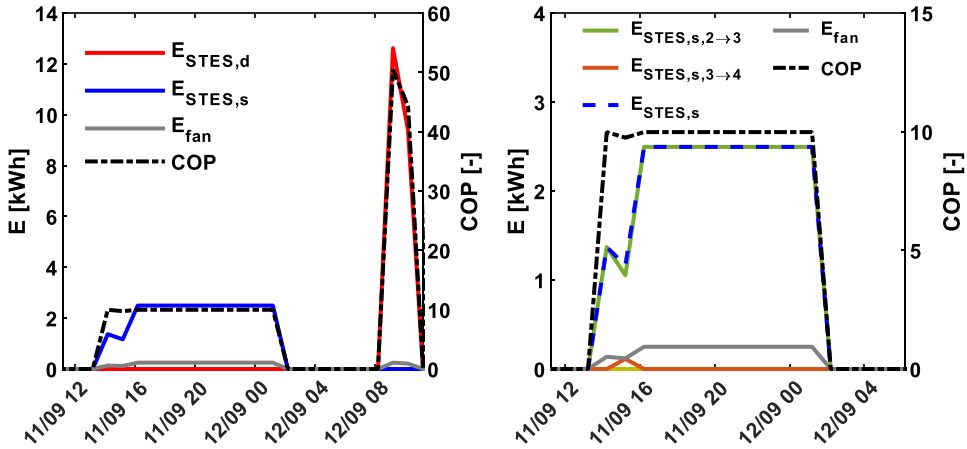

Figure 6.22: Left: STES charging (red), discharging (blue), fan energy (gray), and COP (back) between 11/09 and 12/09. Right: Zoom-in on the STES discharging energy for every water tank segment. Green: from segment 2 to segment 3, Red: from segment 3 to segment 4. Blue: Overall STES discharging energy. Gray: STES fan energy. Black: COP. House type = B3, STCs = 25, V_{tank}=0.5 m^3, $p_{el/gas}$=2.5, SCC_{STES}= 2.5 €/kWh$_{cap}$ $P_{fan,max}$ = 0.25 kW , d_{STES}/L_{STES} = 0.7, d_p = 2 mm, $V_{STES,unit}$ = 0.048 m^3, $A_{STC,unit}$ = 3 m^2.

Finally, in Figure 6.23 left, the SPF value is shown for different maximum fan powers, aspect ratios, and for a sorbent particle size diameter of 2 mm. For the reference case, the SPF is equal to 3.2, and it increases up to 4.4 if the aspect ratio is increased from 0.7 up to 1.3. By decreasing the maximum fan power, the SPF increases accordingly. If a maximum fan power of 0.25 kW is present, an SPF of 7.1 is achieved (d_{STES}/L_{STES} = 0.7), and it increases up to 9.5 if an aspect ratio of 1.3 is used. In Figure 6.23 left, the same trends are shown for a sorbent particle diameter of 4 mm. For a maximum fan power of 1 kW, the SPF increases from 4.5

to 6.5 by increasing the aspect ratio from 0.7 to 1.3. Similarly, for a maximum fan power of 0.25 kW, the *SPF* increases from 10.6 to 15.2.

From this analysis it is shown that, for a real system design, the STES unit geometry and the particles diameter in the packed bed play a crucial role in the STES performance, and an optimization of these parameters based on the real system operating conditions is an essential step in order to make this technology competitive in the market.

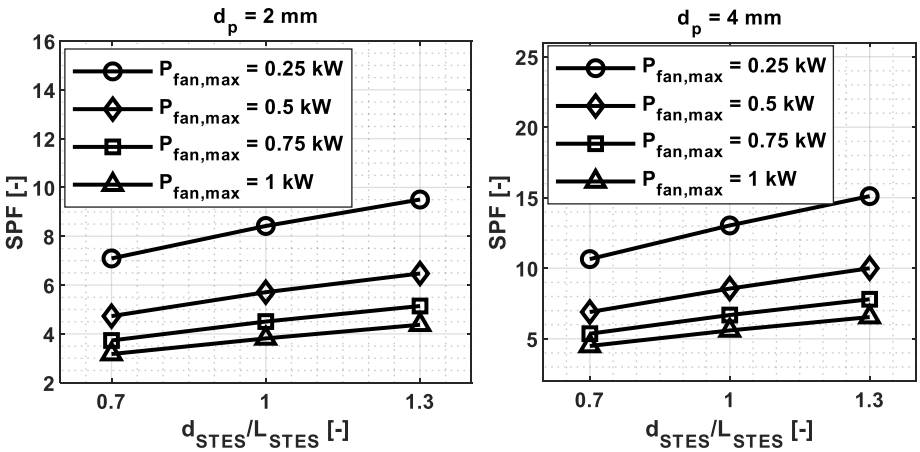

Figure 6.23: SPF for different aspect ratios (d_{STES}/L_{STES}) of the STES segments and different maximum STES fan powers. Left: Assuming a sorption material particles diameter of 2 mm. Right: Assuming a sorption material particles diameter of 4 mm. Circles: $P_{fan,max}$= 0.25 kW, Rhomboids: $P_{fan,max}$= 0.5 kW, Squares: $P_{fan,max}$= 0.75 kW, Triangles: $P_{fan,max}$= 1 kW. House type = B3, STCs = 25, V_{tank}=0.5 m^3, $p_{el/gas}$=2.5, SCC_{STES}= 2.5 €/kWh$_{cap}$, $V_{STES,unit}$ = 0.048 m^3, $A_{STC,unit}$ = 3 m^2.

6.5 Discussion and conclusions

6.5.1 Discussion on the main assumptions and parameters choice

As for the techno-economic analysis of Chapter 5, the analysis performed in this chapter has limitations due to the effects of the parameter choices and the assumptions that have been made.

Concerning the STES parameters selection, similar choices to Chapter 5 have been made. In particular, the properties of potassium carbonate have been used. A different sorption material could have led to a different energy density in a STES unit, affecting the number of STES units in a specific optimal solution. As a comparison, the crystal energy density values in Table 2.2 of Chapter 2 for other salt hydrates or the energy density of zeolite 13X in Table 2.3 can give an idea of the possible changes in the STES unit energy density by changing the sorption material. For example, strontium bromide and zeolite 13X have roughly 1.5 times and 0.5 times the energy density of potassium carbonate, respectively.

A STES lifetime of 20 years has been assumed. However, this will effectively depend on, among other factors, the material stability and degradation over time. A shorter system lifetime would increase the yearly STES investment cost (equation 6.31).
Additionally, the same STES unit geometrical aspect ratio as in Chapter 5 (5.3.4) has been assumed, and its design has not been optimized for its operation in the current energy system. In fact, the last part of the sensitivity analysis (section 6.4.7) shows that a larger aspect ratio can remarkably increase the energy system performance by reducing the pressure drop in the reactor. During the design phase of a real system, the STES unit design should be optimized to minimize the fan energy consumption at the expected system operating conditions and, consequently, improve the STES COP and SPF.
Concerning the building type selection, the focus of this analysis was on single-family houses, and three existing building geometries have been considered. As for Chapter 5, the space heating and DHW demand have been estimated using a typical meteorological year [191] from a weather station of Uccle (BE). However, it has to be remarked that this is the result of using historical data to produce typical conditions for 12 representative months, and it does not represent well e.g. extreme conditions or conditions from which a design procedure should be performed.
A stochastic occupancy model has been used to estimate the space heating and domestic hot water demand of the selected buildings. However, the real demand can vary from the values presented in Table 6.2, and it strongly depends on building type and insulation level, as well as user behavior. In particular, the user behavior heavily affects the DHW consumption, which strongly depends on the behavior and number of occupants in each building. Moreover, the space heating demand has been calculated assuming a variable set point temperature between 15 °C and 20 °C according to the building occupancy and time of the day. A constant set point temperature could have led to different results due to the lower peaks of the space heating power demand. The investigated buildings had a space heating demand in the range of 125 - 158 kWh/(m^2·year). The demand is therefore much higher than, for example, the consumption for a passive house (15 kWh/(m^2·year)) [218,219]. However, most of the existing buildings have a higher energy consumption than a passive house, and it is important to investigate possible solutions to improve their performance because these buildings will continue to exist in the coming decades. Therefore, any strategy aimed to increase the energy efficiency in the built environment sector should extensively involve existing buildings. For example, an existing detached house in the Netherlands, built between 1992 and 2005, is estimated to have a gas consumption of approximately 1882 m^3/year [220]. By considering Figure 1.1 of Chapter 1, assuming that 100 % of the gas is used for space heating, domestic hot water consumption and cooking, and assuming an average boiler efficiency of 94 % for space heating and 70 % for DHW production, a consumption of approximately 95 kWh/(m^2·year) can be estimated. In this work, the building consumption profiles available for this analysis (section 6.2.4) had a higher yearly energy demand compared to the average one estimated for Dutch houses built between 1992 and 2005.

However, these consumption profiles could also be representative for older buildings, which will also need to be involved in a strategy for the energy efficiency improvement in the built environment.
Regarding the STES integration in these buildings with a large heating demand, it can be more beneficial to improve the building envelope first, whenever possible. With a reduced yearly energy demand, it would be possible to reduce the thermal storage size, especially in case a seasonal storage has to be installed. Moreover, if the building is renovated and a low-temperature space heating system such as floor heating is installed, it would be possible to reduce the space heating power peaks, which are present when e.g. heating systems operating with different set points during the day are used.
Concerning the solar thermal collectors, their performance is estimated assuming a specific STC type (evacuated tube collector). However, the STC type and configuration has a direct impact on the achievable temperatures and solar energy extracted for the STES and water tank charging process.
Besides the parameters choice, further modeling assumptions have been made in this study. Regarding the model time resolution, one-hour timesteps have been used in this analysis. Finer resolutions could vary the optimization results. This is because eventual peaks in the energy demand, with a duration lower than one hour, are smoothed. Therefore, the energy consumption peaks might be higher if a finer temporal resolution is used, and this can have an impact on the overall system performance. The water tank model is a relatively simplified model, which is suitable for the integration in the MILP optimization framework. It is assumed that there is no mixing between the different water segments at different temperatures, and perfect stratification. In reality, various mixing effects due to, for example, natural convection and fluid entrainment during charge or discharge, are present. Finally, the STES fan and heat recovery unit efficiencies have been assumed constant, while in reality they can vary according to the system operating conditions.

6.5.2 Conclusions and recommendations

In this chapter, a techno-economic optimization has been carried out to estimate the impact of adding a decentralized STES in a reference energy system consisting of an existing single-family house. The house can produce thermal energy for space heating and DHW with solar thermal evacuated tube collectors or a conventional gas boiler. The STES can be charged by the solar thermal collectors, assumed already present in the system, and can be discharged to a water tank. The water tank can be charged by the STES or directly by the gas boiler or the STCs.
First, the optimization model formulation is investigated by considering the effect of the thermal losses from the top of the water tank for the case without STES. It has been found that, for different water tank sizes, the effect of the top loss on the economic performance between the two models ($\Delta z_{N_{STES}=0}$) was less than 1 % (Figure 6.10). As expected, the effect

is larger for larger water tank sizes since the tank top thermal loss is also higher. Simultaneously, the effect on the solar fraction increases in absolute value (from -0.65 % to -1.8 %), and it is larger for large water tank sizes. Due to the significantly lower computational time of the model without considering the water tank top losses, roughly ten times faster, it has been decided to use the model without tank top losses for the techno-economic optimization.

A reference case scenario has been investigated. The reference building consists of a large single-family house (building B3, Table 6.2) with 25 STCs (A_{STC} = 75 m^2) occupying approximately 50% of the roof area, and operating in an energy system with an electricity-gas price ratio of 2.5. Building B3 has been selected as reference scenario due to its large rooftop area, which allowed to investigate an energy system with 25 STCs, and a higher potential of having a positive impact from the STES integration in terms of RCD and SF increase, compared to the other scenarios. Moreover, a STES capacity cost of 2.5 €/kWh$_{cap}$ has been used, by considering only the sorbent material cost, and assuming an inexpensive material. It has been found that, using the reference values in Table 6.7 for the investigated parameters, the reference scenario achieves a relative cost decrease compared to the case without STES (RCD) of 6.9 % and a solar fraction of 57 % with 10 STES units (V_{STES} = 0.48 m^3) present in the optimal solution. However, it has been found that the yearly STES operational costs were dominant (24 %) compared to the yearly STES investment cost (1 %). This is the result of an unoptimized STES unit aspect ratio (d_{STES}/L_{STES} = 0.7) not optimized for the investigated reference scenario that directly impacts, together with the sorbent particle size diameter (2 mm), the pressure drop and consequently the fan consumption. For the reference case configuration, a seasonal performance factor (SPF) of 3.2 has been calculated, which is rather low and comparable to existing heat pump systems. Therefore, it should be improved by reducing the pressure drop in the STES.

Afterwards, a sensitivity analysis on eight parameters has been performed: the building type, the STC number, the water tank volume, the electricity-gas price ratio, the STES capacity cost, the STES maximum fan power, the STES unit aspect ratio, and the sorption material particles diameter.

Three different building types have been investigated, and the STC number has been varied up to roughly 50 % of rooftop area for each building. The relative cost decrease (RCD) and STES unit number is proportional to the number of STCs in each building. In particular, the higher the number of STCs is, the higher the RCD can be, due to a higher amount of solar energy used by the system (i.e. higher solar fractions) if STES is added and also a higher amount of STES units is needed to store the energy.

Among the main results, it has been found that the electricity-gas price ratio ($p_{el/gas}$) is a crucial parameter for the economic viability of the STES integration. In particular, for a $p_{el/gas}$ of 2.5, the European average, the optimal STES solution has only 10 STES units (V_{STES} = 0.48 m^3), resulting in an RCD of 6.9 % and a SF of 57 % (Figure 6.14). If $p_{el/gas}$ is

set equal to 1, the optimal solution would include a much larger number of STES units (N_{STES} = 700), and the STES would operate as a seasonal heat storage (Figure 6.15 right), resulting in a RCD of 28.1 % and a SF of 84.7 %, respectively. Moreover, this same effect as the decreasing the electricity-gas price ratio can be obtained by improving the STES performance (COP and SPF) i.e. by reducing the STES units pressure drop and fan consumption through the optimization of the STES unit shape. Also in this case, a lower STES unit operating cost due to the improved COP would allow for more STES units to be present in an optimal solution.

Sorption heat storage is a technology still under research with large cost uncertainties. Therefore, a sensitivity analysis on the STES capacity cost has been carried out, and it showed the potential of this technology by varying its cost in terms of €/kWh$_{cap}$. The STES capacity cost has been increased from 2.5 €/kWh$_{cap}$, representing only the active material cost of an inexpensive sorbent, up to a maximum value of 80 €/kWh$_{cap}$. For the reference configuration of the energy system (Table 6.7) the RCD and SF decrease from 6.9 % (RCD) and 57 % (SF) for a STES capacity cost of 2.5 €/kWh$_{cap}$ (N_{STES} = 10) until 0.2 % (RCD) and 43.7 % (SF) for a STES capacity cost of 60 €/kWh$_{cap}$ (N_{STES} = 1). A higher STES cost would cause the STES to not be integrated in the optimal solution.

The STES maximum fan power ($P_{fan,max}$) has been varied from 0.25 kW to 10 kW. It has been found that for an electricity-gas price ratio of 1, the maximum RCD (29.7 %) can be achieved with a fan power of 0.5 kW (N_{STES} = 600). A lower fan power would cause a limitation in the energy that can be stored in the STES while a higher fan power would decrease the RCD due to the higher STES operating costs. For an electricity-gas price ratio of 2.5, the maximum RCD is achieved with 0.25 kW (13.9 %), and higher fan powers cause an RCD decrease due to the higher STES operational costs. For optimal solutions with the same number of STES units, it has been found that SF increases by increasing $P_{fan,max}$. However, the effect of $P_{fan,max}$ on SF will probably be lower if a passive house with a constant set point temperature and, as a consequence, lower peaks in the heating power, is considered as a consumer.

Concerning the aspect ratio (d_{STES}/L_{STES}) and sorbent particle diameter (d_p) variation, it has been found that an increase from an aspect ratio of 0.7 to 1.3 would increase the RCD from 6.9 % to 16.4 %, the SF from 57 % to 62 % and the SPF from 3.2 to 4.4, respectively. Likewise, d_p increase from 2 mm to 4 mm would increase the RCD from 6.9 % to 17.4 %, the SF from 57 % to 63 % and the SPF from 3.2 to 4.5, respectively. Moreover, it is found that, for the reference aspect ratio and particle size, by reducing the maximum fan power from 1 kW to 0.25 kW the SPF increases from 3.2 to 7.1 due to the lower operational STES fan costs. Finally, a much higher SPF value of 15.1 can be achieved with a maximum fan power of 0.25 kW, a particle size diameter of 4 mm and an aspect ratio of 1.3. This last result highlights the importance of optimizing the STES unit design in order to maximize the STES COP and, consequently, the SPF.

As a possible follow up of the analyses performed in this chapter, a proper comparison with a sensible water storage tank should be performed, considering also the water storage operating costs and investment costs. The aim should be to investigate what is the additional water storage size to obtain the same RCD and SF of an energy system with a STES integrated. For small-scale seasonal heat storage purposes, the thermal losses from a water tank would be too large, while a STES would be able to store the energy more efficiently from the summer to the winter months.

It has to be remarked that the optimization model focuses solely on the yearly costs minimization, considering the STES CAPEX, and the boiler and STES OPEX. In real case scenarios, more selection criteria would be applied. For example, the STES volume would be limited due to the volume availability of the building. An optimal solution including e.g. 10 STES units implies roughly 0.48 m^3 of volume for the STES units, according to the axial length and diameter of a single STES unit (Table 6.1). However, this estimation does not take into account the volume occupied by the auxiliary components of the system such as the fan, the heat recovery unit and the eventual humidification system. An optimal solution that included 700 STES units, such as the optimal solution with $p_{el/gas}$ =1, would imply a storage volume of approximately 33 m^3. For a domestic decentralized system, this volume is probably prohibitively high, and additional system design criteria have to be applied.

Another possible optimization objective could be the maximization of the energy system solar fraction and, consequently, the minimization of the yearly CO_2 emissions. However, this design criterion alone might lead to an oversized system aimed solely at the solar fraction maximization without considering the costs. Finally, a further option could be to define an optimization objective aimed at identifying the most cost-effective solution to reach a specific energy performance indicator for a building.

The sensitivity analysis shows that the economic framework in which the domestic system is operating is drastically affecting the viability of integrating the thermal storage investigated in this work. In future market conditions, it is possible that the electricity-gas price ratio will decrease due to a gas price increase e.g. due to geopolitical facts or due to a heavier taxation on gas in order to promote renewable energy sources. Moreover, in future buildings the gas connection could be absent. In 2016, the Dutch government [221,222] announced that new residential buildings will not be connected to the gas grid, and existing buildings will be gradually disconnected in favor of more sustainable energy sources. Therefore, the future competitiveness of energy storage systems will possibly improve. Future research should compare different storage technologies through similar analyses, to determine the best solution for a specific energy system. Concerning the STES technology, the capacity cost that will be achieved in real systems, which will have to include the sorbent material, the reactors cost, and all the system auxiliary components, will determine its economic feasibility.

In the case of a decentralized STES, a possible interesting entry market could be new large residential or commercial buildings, in which a relatively large amount of solar energy is

harvested with e.g. solar thermal collectors or waste heat sources are available. In light of a seasonal or medium-term storage (e.g. few weeks), a STES coupled with a short-term water storage would possibly require less space than a conventional sensible heat storage. In case of commercial buildings with multiple intended uses, large peak power variations might be absent due to the aggregated demand of the different users, making the STES integration a feasible option to provide a relatively constant energy demand. Finally, passive houses could be another potential entry market, especially if located in remote areas or far from centralized thermal energy systems such as district heating networks, where a centralized energy storage might be a better solution.

CHAPTER 7

CONCLUSIONS

The work presented in this thesis addresses several aspects at system-scale related to sorption thermal energy storage. Sorption thermal energy storage is still under research, and scientific challenges at multiple scales need to be solved before deployment of this technology in the energy grid can be carried out.

Chapter 2 presents the recent advancements, at material- and prototype-scale, on sorption thermal energy storage for long-term low-temperature applications. Main bottlenecks are still present at material-scale. In particular, research is still focusing on finding suitable sorption materials with sufficient stability, cyclability, and high energy density for commercial applications. To this extent, research is mostly focusing on composite materials, in which the sorbent (e.g. a salt hydrate) is combined with another material to enhance certain properties such as mechanical stability or thermal conductivity. The drawback is mostly an energy density reduction at material-scale because an inert material, not participating into the sorption reaction, is combined with the sorbent. Moreover, it is possible that the process required to make the composite material is severely increasing the material cost, making it less attractive from a commercial point of view. This is particularly relevant because the STES capacity cost is a crucial aspect, as shown in chapters 3, 5 and 6 of this dissertation.
Research at reactor-scale showed that modular reactors, especially in open systems, are essential to limit the pressure drop and in turn the fan energy consumption used to drive the sorbate flow. The development of separate reactors with a sorbent transport system could improve the overall system performance and avoid storing the sorption material in the same location. This can be an essential feature if a STES is used as a seasonal storage and space availability is an issue (see e.g. Chapter 6), or if the sorption material is hydrated and dehydrated at different locations.

In this thesis, the first approach to the system-scale is an estimation of the STES potential for space heating applications. In Chapter 3, a simple comparison in terms of energy density and storage capacity costs of different ideal STES systems is carried out. This analysis showed that, for the assumed reactor layouts, solid open systems have lower storage capacity costs than closed systems when considering also the reactor material costs. This is due to the larger amount of reactor material required in the closed system layout compared to the open system layout investigated in this work. Moreover, open systems have a higher energy density due to the fact that the sorbate storage volume is not considered in the system volume estimation. Concerning the sorption materials, the most affordable options were also those who suffer from instability such as $MgCl_2$ or safety issues such as Na_2S. An open system using an ideal composite with 50 %vol based on $CaCl_2$ is a good compromise between energy density (0.43 GJ/m^3) and storage capacity costs (0.53 €/kWh_{cap}), resulting in a system affordable for buildings users. However, the ideal composite should be able to prevent the deliquescence of $CaCl_2$ at normal system operating conditions, in particular during hydration. The analysis performed in Chapter 3 showed that the cost of some of the investigated STES systems are

higher than the range of acceptable storage capacity costs [118] for the investigated applications, especially considering that only the active material costs were taken into account in the analysis. The reactor material costs and the cost of the auxiliary system components would further increase the overall system costs. However, the range of acceptable storage capacity costs used in this work [118], can vary according to the market conditions, and the energy prices in each country. Therefore, the systems investigated in this analysis might become more competitive under future energy market conditions and policy mechanisms.

With the aim of performing dynamic system simulations of energy systems with a STES integrated, two compact sorption reactor models have been investigated in Chapter 4: a physics-based model and a data-driven model. Both models estimate the STES state of charge (SOC) and outlet temperature (T_{out}), from the inlet temperature and sorbate concentration used as model inputs, together with the STES SOC at the previous timestep The physics-based model is based on a spectral method for the spatial discretization and a semi-implicit method for the time discretization, respectively. The data-driven model is based on two neural networks, a nonlinear autoregressive neural network with exogenous inputs (NARX) and a feed forward neural network (FFNN), to estimate SOC and T_{out}, respectively. The performance of both models has been compared with a high-fidelity model in terms of mean squared error (MSE). The results showed that the physics-based model had a lower MSE in the performed tests, and hence a higher accuracy, than the neural networks. The main reason was that the neural networks model was not able to reproduce the thermal inertia effect of the STES, causing an error in the outputs when large input gradients are present. To partially overcome this issue, a more complex architecture has been investigated and applied for the SOC estimation, and it partially reduced the MSE of the data-driven model for both SOC and T_{out} estimations. Ultimately, the STES configuration, the nature of the inputs, and their gradients during real system operating conditions determine the impact of the observed thermal inertia effect and whether a more complex architecture for the SOC would be necessary or not.

The simulation time of the physics-based model for the performed tests was between 500 s and 2500 s, while the data-driven model was much faster, between 0.12 s and 0.16 s. However, the time required for the training process of the data-driven model was in the order of two weeks. Thus, if simulation speed during the dynamic energy system simulation is a strict requirement, for example for control applications, a data-driven model can be a suitable solution providing that a sufficient accuracy is achieved.

Furthermore, in case of an existing STES prototype, it could be possible to develop a relatively light and efficient model based solely on the experimental measurements of its relevant inputs and outputs, without the need to simulate a possibly complex geometry and physical interaction among various parts of the STES. Being a data driven model, the quality and amount of experimental data used for the training and validation process are crucial.

Further investigation on different neural networks architectures, such as recurrent neural networks, should be carried out to increase the model accuracy especially for the STES outlet temperature estimation. Moreover, additional inputs could be used in order to increase the generalization capabilities of the STES model. For example, the air mass flow can be added among the variable inputs to simulate the STES with different inlet airflows.

In chapters 5 and 6, the focus was on assessing the impact of integrating a STES in different energy systems. In particular, two techno-economic optimization models have been developed based on mixed integer linear programming, in which a STES model has been formulated in two different operation modes: a centralized STES with several units operating in parallel (Chapter 5), and a decentralized STES with several units operating one at a time (Chapter 6).
In Chapter 5, the integration of a centralized STES in an energy system consisting of a geothermal doublet, a low temperature district heating network, and an organic Rankine cycle, is investigated. Different scenarios have been analyzed, in which the system operates under different market conditions. For the scenarios operating in Belgium (2013 data) and the UK (2017 markets data) without market balancing services, it is found that the STES integration is not profitable. However, when the system could also operate with balancing market services such as the capacity market (CM) and the short term operating reserve (STOR) market, it has been found that a net present value increase up to approximately 40 % could be achieved compared to the solutions without the STES integrated. With STES being a technology still under research, a main source of uncertainty was the STES capacity cost, initially assumed to be 2.5 €/kWh$_{cap}$. The results showed that the STES integration was profitable up to STES capacity costs of 70 €/kWh$_{cap}$. Moreover, when also the STOR market was included as balancing service, with the average utilization price of 2017 (168 €/MWh), an additional sensitivity analysis on the STOR utilization price has been made. The results showed that, even with a utilization price reduced by 50 %, the system could achieve approximately 13 % higher profits compared to the solution without the STES integrated.

On a different system-scale, Chapter 6 investigates the potential of integrating a decentralized STES in a single-family house with a yearly fixed electricity and gas tariff. It is assumed that a conventional solar system, consisting of solar thermal collectors (STCs) with a water tank and an auxiliary gas boiler are used for the production of thermal energy for space heating and domestic hot water. The contribution of adding a STES, which can be charged with the solar thermal collectors and discharged to heat the water tank, is analyzed. A reference scenario is considered; consisting of a detached building with 150 m^2 of floor area, a 0.5 m^3 water tank and 25 STCs corresponding to an aperture area of 75 m^2. A sensitivity analysis on different relevant parameters has been carried out to understand how they impact on the system performance in terms of solar fraction (SF) and relative cost decrease due to the addition of STES (RCD) compared to the alternative of not having the STES integrated. It is

found that the electricity/gas price ratio ($p_{el/gas}$) heavily influences the economic viability of the STES. In particular, for the European average $p_{el/gas}$ of 2.5, the system with the STES integrated would achieve a 6.9 % RCD and a solar fraction of 57 %. By decreasing $p_{el/gas}$, the benefit of adding a STES increases due to the fact that the STES operational costs considered in this analysis, the fan costs, are decreasing as well. If the electricity and gas prices would be equal, a theoretical RCD of 28.1 % and a solar fraction of 85 % would be achieved, and the STES would operate as a seasonal storage due to its large capacity for this optimal solution. However, the STES volume requested for this optimal solution, due to the relatively large energy consumption of the investigated building compared to e.g. a passive house, would be probably excessive, and additional design criteria need to be applied. As in Chapter 5, the STES capacity cost has been initially assumed equal to 2.5 €/kWh$_{cap}$ and increased up to 80 €/kWh$_{cap}$. It has been found that the STES integration for the reference scenario would be profitable up to STES capacity costs of 60 €/kWh$_{cap}$. Finally, the reference STES unit aspect ratio was not optimal for the investigated reference scenario. By increasing the aspect ratio from the reference value of 0.7 up to 1.3, the RCD and the solar fraction increased from 6.9 % to 16.4 % and from 57 % to 62 %, respectively. Thus, a proper STES reactor design optimization process is crucial in real case scenarios in order to maximize the STES performance and, in turn, minimize the STES operational costs.

Ultimately, the analyses carried out in chapters 5 and 6 should be compared with similar studies, in which different storage technologies are integrated in these energy systems. Afterwards, the most suitable storage technologies for a specific energy system, sized according to the optimization models, should be further investigated with dynamic system simulations. The aim would be to estimate the discrepancy between the operational behavior of the optimization model and the more detailed dynamic simulation and, eventually, iterate between the two models to achieve an optimal design and operational behavior. In the dynamic simulation model, the individual system components could be based on physics-based models or alternatively on black-box models such as the ones described in Chapter 4.

To conclude, the potential of sorption heat storage, especially for low-temperature applications such as space heating and domestic hot water production, is still hindered by several challenges at material- reactor- and system-scale. This thesis, mainly focused on the system-scale, investigated the possible benefits of this thermal storage technology in different scenarios. In certain scenarios, STES proved to have the potential for reducing the costs (for a decentralized STES operating in a domestic environment) or increasing the profits (for a centralized STES operating with balancing market mechanisms) of the investigated energy systems. However, several challenges at smaller scales need to be overcome to have a technically and economically viable product that can compete in the market. The future market conditions, influenced by environmental policies, geopolitical changes, and

technological innovations, will establish the market competitiveness of this and other energy storage technologies.

APPENDICES

Appendix A: Active materials data and equilibrium curves

Table A.1: Properties of Na2S (Na2S↔Na2S·2H2O, Na2S·2H2O↔Na2S·5H2O, Na2S·5H2O↔Na2S·9H2O), SrBr2 (SrBr2·H2O↔SrBr2·6H2O). and zeolite 13X. Reaction enthalpy data from [26].

Na_2S			$SrBr_2$		Zeolite 13X	
$\rho_{Na_2S\cdot 9H_2O}$ [kg/m^3]	1430		$\rho_{SrBr_2\cdot 6H_2O}$ [kg/m^3]	2386	$\rho_{Zeolite\ 13X}$ [kg/m^3]	1040
$\rho_{Na_2S\cdot 5H_2O}$ [kg/m^3]	1580		$M_{mol,SrBr_2\cdot 6H_2O}$ [g/mol]	355.53	ΔH_{reac}[kJ/mol$_w$]	63
$M_{mol,Na_2S\cdot 9H_2O}$ [g/mol]	240.18		Moles of water in solid phase	1↔6	mol$_w$/kg$_{Zeolite\ 13X}$	11
$M_{mol,Na_2S\cdot 5H_2O}$ [g/mol]	168.12		mol$_w$	5	$E_{vol,tot}$[GJ/m$^3_{Zeolite\ 13X}$]	0.72
Moles of water in solid phase	0.5↔2	2↔5	ΔH_{reac} [kJ/mol$_w$]	58.16	$E_{vol,bed}$[GJ/ m$^3_{Zeolite\ 13X}$]	0.36
mol$_w$	1.5	3	mol$_w$/kg$_{SrBr2\cdot 6H2O}$	14.06	$C_{wt,sm}$ [€/t] [34]	2500
ΔH_{reac} [kJ/ mol$_w$]	72	62.85	T_{eq} [°C]	50.45		
mol$_w$/kg$_{Na2S\cdot 5H2O}$	8.92	17.84	$E_{vol,tot}$[GJ/m$^3_{SrBr2\cdot 6H2O}$]	1.95		
T_{eq} [°C]	73.84	67.19	$E_{vol,bed}$ [GJ/ m$^3_{SrBr2\cdot 6H2O}$]	0.98		
E_{vol} [GJ/m$^3_{Na2S\cdot 5H2O}$]	1.01	1.77	$C_{wt,sm}$ [€/t] [34]	2400		
$E_{vol,tot}$ [GJ/m$^3_{Na2S\cdot 5H2O}$]	2.79					
$E_{vol,bed}$ [GJ/m$^3_{Na2S\cdot 5H2O}$]	1.39					
$C_{wt,sm}$[€/t] [34]	348					

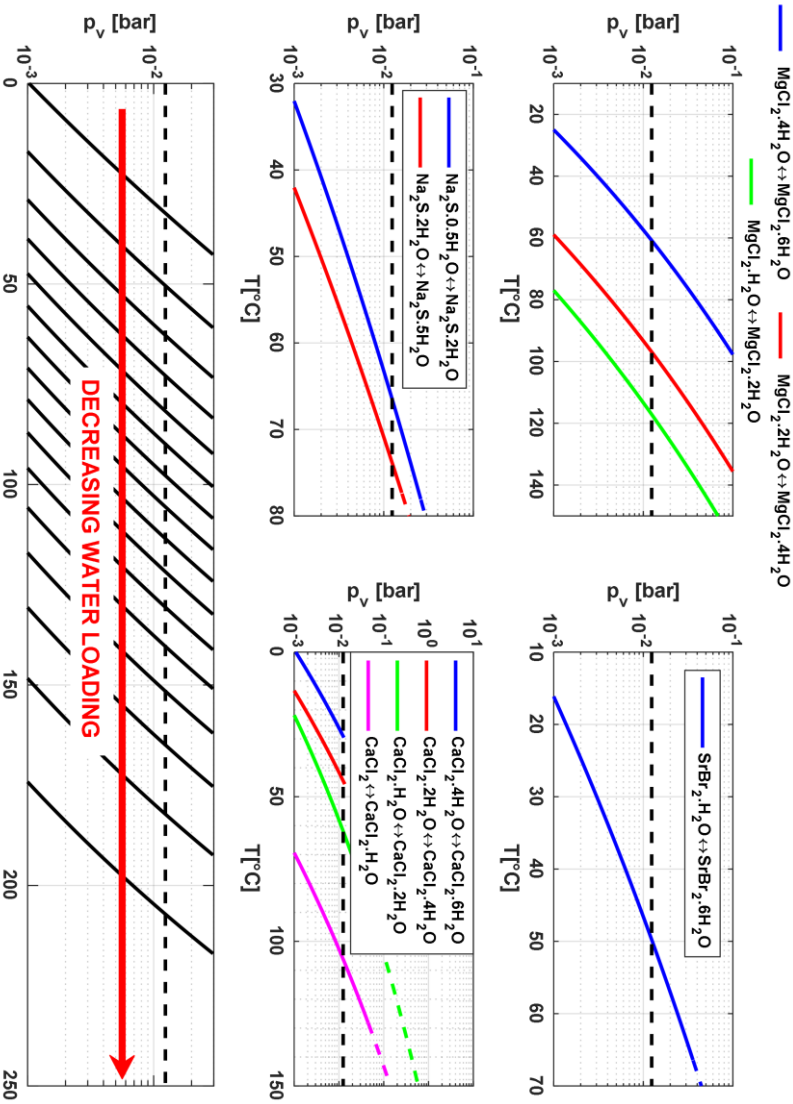

Figure A.1: Equilibrium curves for $MgCl_2$ (top left), $SrBr_2$ (top right), Na_2S (bottom left), $CaCl_2$ (bottom right) and adsorption iso-concentration lines (black lines) for zeolite 13X (bottom). Dashed line: p_v =12.4 mbar

Appendix B: Additional parameters for the systems design

Table B.1: Additional assumptions for the systems design estimation

Symbol	Value
d_p [mm]	1
ε_b [-]	0.5
ε_{HR} [%]	90
ρ_{SS} [kg/m^3] [223]	7740
C_{SS} [€/t] [224]	2500
ρ_a[kg/m^3]	1.2
μ_a [mPa·s]	$1.85 \cdot 10^{-5}$
$c_{p,a}$ [J/(kg·K)]	1004
$M_{mol,w}$ [g/mol]	18
$c_{p,w}$ [J/(kg·K)]	4186

Appendix C: Estimation of the ideal liquid sorption system

In this analysis, four states of the solution are defined. State 1 represents the storage conditions before the beginning of the sorption process. State 2 represent the beginning of the sorption process, when the solution starts to release heat at the highest sorbent concentration. State 3 represents the solution at the end of the useful heat release. State 3' represents the solution at the outlet of the absorber, after the further dilution to avoid solidification at $T_{storage}$. Finally, state E represents the evaporator state. By looking at the phase diagram of NaOH-H_2O [225] (Figure C.1), it is possible to see that at $T_{storage}$, the solution can be stored at a maximum concentration of approximately 48 $wt\%_{NaOH}$ (1). This has to be the maximum concentration in the storage system in order to avoid crystallization. At higher concentrations of NaOH at $T_{storage}$, the solidification curve would be crossed. According to Figure C.2 and the assumptions in this analysis, the minimum concentration of NaOH in order to produce heat above 35 °C is 40 $wt\%_{NaOH}$ (3). However, to avoid crystallization at $T_{storage}$, the solution has to be diluted further in order to reach a concentration lower than 32 $wt\%_{NaOH}$ (3'). The useful concentration difference in the absorber is 8 $wt\%_{NaOH}$, while the total concentration difference is 16 $wt\%_{NaOH}$. During discharge, the concentrated solution at 48 $wt\%_{NaOH}$ goes into the absorber from the storage tank (1→2). The solution concentration decreases up to the minimum concentration (40 wt%) in order to produce heat above 35 °C (2→3). Then, the solution is further diluted up to 32 wt% (3→3') to avoid crystallization at storage conditions (see Figure C.1). The required desorption temperature for this system, assuming a condenser temperature of 30 °C (p_v=4.2 kPa) as Liu et al. [111], would be approximately 75 °C.

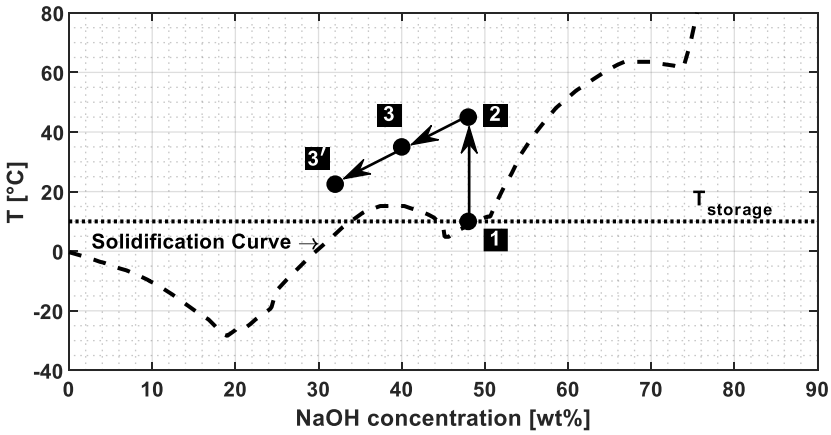

Figure C.1: Boiling and solidifying temperatures of aqueous caustic soda solutions. Partially adapted from [225]**. The system states during the evaporation process are 1: strong solution in the storage tank, 2: solution at the beginning of the absorption process, 3: solution at the end of the absorption process that produces useful heat above 35 °C, 3': solution diluted up to the minimum concentration in the system to prevent crystallization during storage.**

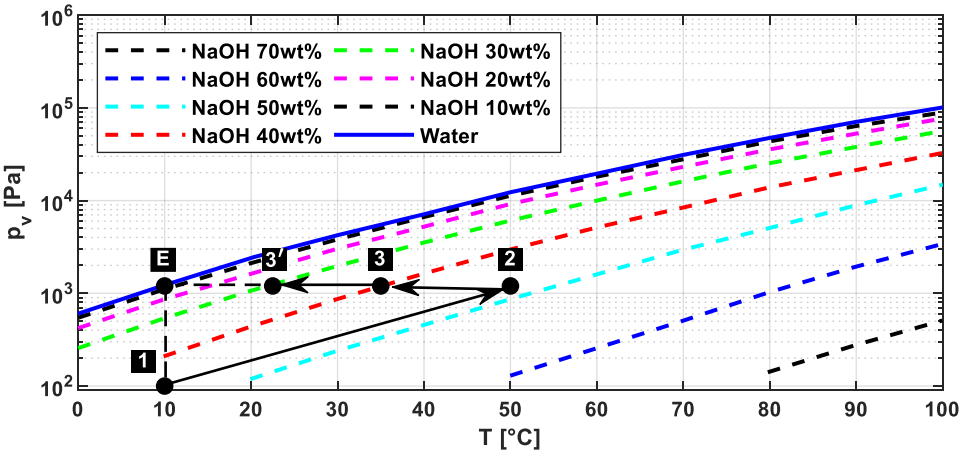

Figure C.2: Vapor pressure vs temperature curves for NaOH-H_2O absorption couple. Partially adapted from [226]**. The system states during the evaporation process are 1: strong solution in the storage tank, 2: solution at the beginning of the absorption process, 3: solution at the end of the absorption process that produces useful heat above 35 °C, 3': solution diluted up to the minimum concentration in the system to prevent crystallization during storage, E: the evaporator state.**

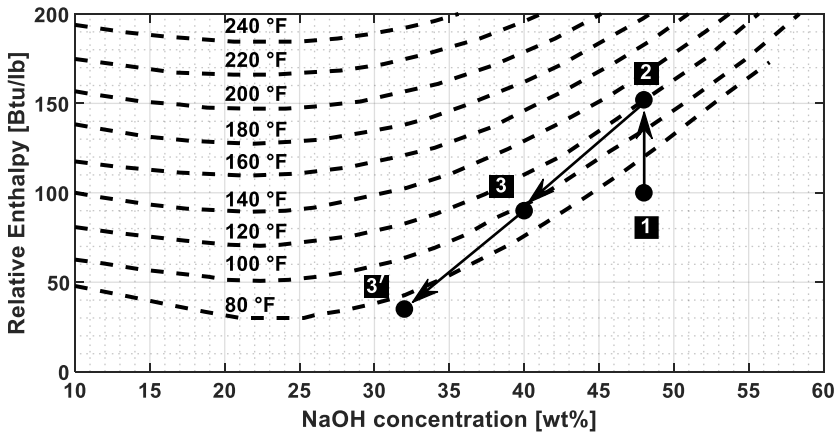

Figure C.3: Relative enthalpy of NaOH solutions. Partially adapted from [225]**. The system states during the evaporation process are 1: strong solution in the storage tank, 2: solution at the beginning of the absorption process, 3: solution at the end of the absorption process that produces useful heat above 35 °C, 3': solution diluted up to the minimum concentration in the system to prevent crystallization during storage**

Table C.1: Enthalpies of the solution at state 1 and 3; and saturated water vapor enthalpy at system conditions.

h_1 [kJ/kg$_{sol}$]	232.6
h_3 [kJ/kg$_{sol}$]	204.69
h_v [kJ/kg]	2519

The useful energy produced in the absorber is considered to be only the one extracted from 2→3. The energy released during the further dilution 3→3' is not considered. The energy balance can be done by considering the state of the solution during the storage immediately before the discharge phase at state 1, and state 3 (equation C.1).

$$\begin{aligned} e_{1\to3,T>35\,°C} &= m_{f,1}h_1 + (m_{f,3} - m_{f,1})h_v - m_{f,3}h_3 \\ &= \left(\frac{1}{0.48}\right)\cdot 232.6 + \left(\frac{1}{0.4} - \frac{1}{0.48}\right)\cdot 2519 - \frac{1}{0.4}\cdot 204.69 \\ &= 1022.535\ kJ/kg_{sm} \end{aligned} \qquad \text{C.1}$$

Here, $m_f = 1/x_{c,sm}$ the relative masses in [kg_{sol}/kg_{sm}], x_c the mass concentration of absorbent into the solution, h the solution specific sensible enthalpy and h_v the water vapor enthalpy at the evaporator state (saturated conditions at T =10 °C). The useful energy balance of the absorber can be solved considering the enthalpies calculated from Figure C.3 and presented in Table C.1, together with the water vapor enthalpy at system conditions. During the hydration of NaOH, the energy produced per cubic meter of absorbent above 35 °C is calculated according to equation C.2.

$$E_{vol,sm} = e_{1\to3}\rho_{sm} = 1022535 \cdot 2130 \cdot \frac{1}{10^9} = 2.18\ GJ/m^3_{sm} \qquad \text{C.2}$$

In order to satisfy the space heating energy demand of one year in the reference scenario, the amount of NaOH required is calculated as in equation C.3.

$$V_{sm} = \frac{E_{SH}}{E_{vol,sm}} = \frac{10}{2.18} = 4.587\ m^3_{sm} \qquad \text{C.3}$$

To calculate the energy density of the solution, the amount of water present at the most diluted concentration in the system is estimated as in equation C.4.

$$V_{w,weak} = \frac{x_{c,w}}{x_{c,sm}}\frac{\rho_{sm}}{\rho_w} = \frac{(1 - x_{c,sm})}{x_{c,sm}}\frac{\rho_{sm}}{\rho_w} = \frac{(1 - 0.32)}{0.32}\cdot\frac{2130}{1000} = 4.526\ \frac{m^3_w}{m^3_{sm}} \qquad \text{C.4}$$

At the abovementioned conditions, the solution energy density is calculated in equation C.5.

$$E_{vol,sol,weak} = \frac{E_{vol,sm}}{V_{sm} + V_w} = \frac{2.18}{1 + 4.526} = 0.39\ GJ/m^3_{sol} \qquad \text{C.5}$$

Similarly to equation C.4, the volume of water in the strong solution ($x_{c,sm} = 48\ wt\%$) can be found equal to $V_{w,strong} = 2.307$ m^3_w/m^3_{sm}. The amount of sorbate that has to be stored

separated from the solution is equal to $V_{w,pure} = 2.219$ m^3_w/m^3_{sm}. The total amount of water in the strong solution tank can be found according to equation C.6.

$$V_{w,HCT} = V_{sm} V_{w,strong} = 10.58\ m_w^3 \qquad \text{C.6}$$

The volumes of the low concentration tank and of the pure sorbate tank can be found similarly and are displayed in Table C.2.

Table C.2: Tanks parameters of the ideal liquid sorption system. An aspect ratio between the tanks diameter and height equal to 1 has been assumed.

	High Concentration Tank (HCT)	Low Concentration Tank (LCT)	Sorbate Tank (ST)
V_{tank} [m^3]	15.2	25.3	10.2
d_{tank} [m]	2.68	3.18	2.35
C_{tank} [€]	28.4	34.6	24.5

The energy density of the weak solution does not give a fair estimation of the system energy density. In particular, the system has to make use of at least three storage tanks. One tank has to store the strong solution (high concentration tank HCT), a second tank has to store the pure sorbate (sorbate tank ST), and a third tank has to store the weak solution (low concentration tank LCT). By adding the three volumes that the tanks have to store, a more realistic value ($E_{vol,sol,system}$) of the system energy density can be found according to equation C.7.

$$E_{vol,sol,system} = \frac{E_{SH}}{2V_{sm} + V_{w,HCT} + V_{w,ST} + V_{w,LCT}} = \frac{E_{SH}}{V_{HCT} + V_{LCT} + V_{ST}} = \frac{10}{15.2 + 25.3 + 10.2} = 0.20\ GJ/m_{sol}^3 \qquad \text{C.7}$$

The active material cost in the reference scenario (3.2.1) is calculated considering only the NaOH cost (Table 3.8) :

$$C_{sm} = \frac{E_{SH}}{E_{vol,NaOH}} \rho_{NaOH} C_{wt,NaOH} = \frac{10 \cdot 10^9}{2.18 \cdot 10^9} \cdot 2130 \cdot 0.4 = 3.91\ k€ \qquad \text{C.8}$$

The storage capacity cost by taking only into account the active material is found (equation C.9) by dividing the absorbent cost with the energy delivered for the space heating system E_{SH}, assuming that only one cycle is performed every year.

$$SCC_{sm} = \frac{C_{sm}}{E_{SH}} = 1.41\ €/\text{kWh}_{cap} \qquad \text{C.9}$$

The reactor material costs are estimated assuming that the system consists mainly of three stainless steel 316 storage tanks with a thickness of 3 mm, an aspect ratio diameter/height of approximately 1, and the cylinder ends consisting of domes with a 0.05 m height. The tanks cost are estimated by assuming the same cost and density of stainless steel 316 as in 3.3.1 (ρ_{SS} = 7740 kg/m^3, $C_{wt,SS}$ = 2.5 €/kg).The storage capacity cost including the material cost for the storage can be calculated according to equation C.10.

$$SCC_{sm+tanks} = \frac{C_{sm} + C_{tank,HCT} + C_{tank,LCT} + C_{tank,ST}}{E_{SH}} = 1.44\ €/\mathrm{kWh}_{cap} \qquad \text{C.10}$$

The absorber, which is assumed to be small compared to the storage tanks, is not taken into account in this cost estimation.

Appendix D: High-fidelity physics-based model parameters

Table D.1: Additional model parameters used in the high-fidelity model in Chapter 4.

Symbol	Value
$c_{p,sm,dehyd}$ [J/(kg·K)]	852
$c_{p,sm,hyd}$ [J/(kg·K)]	2486
$c_{p,wl}$ [J/(kg·K)]	500
ΔH_{reac} [kJ/mol$_w$]	63.6
ΔS_{reac} [J/(mol·K)]	155
$\lambda_{sm,dehyd}$ [W/(m·K)]	1.91
$\lambda_{sm,hyd}$ [W/(m·K)]	4.14
$\lambda_{ins,in}$ [W/(m·K)]	0.25
$\lambda_{ins,out}$ [W/(m·K)]	0.035
λ_{wl} [W/(m·K)]	16.3
u_a [m/s]	0.26
L [m]	0.5
d_i [m]	0.35
$M_{mol,sm,hyd}$ [g/mol]	165.2
$M_{mol,sm,dehyd}$ [g/mol]	138.2
$\rho_{sm,hyd}$ [kg/m^3]	2180
$\rho_{sm,dehyd}$ [kg/m^3]	2330
ρ_{wl} [kg/m^3]	8000
T_{amb} [°C]	10
$s_{ins,in}$ [m]	$5 \cdot 10^{-3}$
$s_{ins,out}$ [m]	0.03
s_{wl} [m]	0.01
$\varepsilon_{b,h}$ [-]	0.50
ν [mol$_w$/mol$_{sm}$]	1.5
k_{LDF} [1/s]	$5 \cdot 10^{-4}$
d_p [mm]	2

Appendix E: Additional simulation results for the spectral model

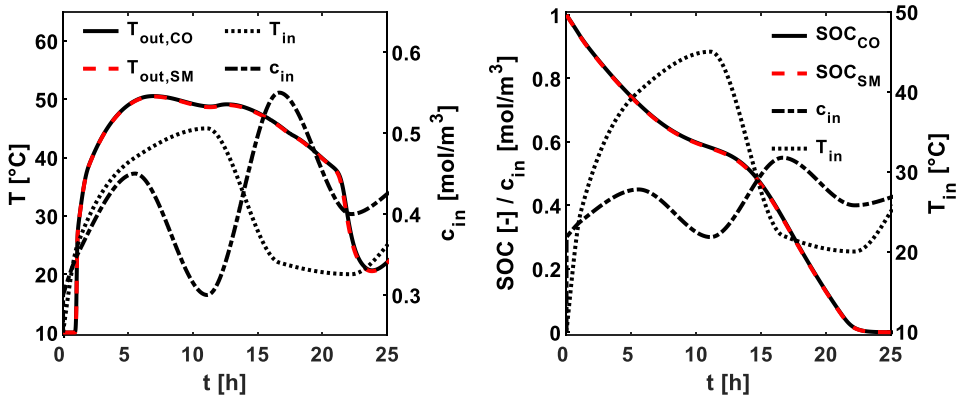

Figure E.1: Test H3 for the spectral model. CO = COMSOL model. SM = Spectral model. Left: Reactor outlet temperatures. Right: SOC. Black solid line: COMSOL model. Red dashed line: spectral model. Black dotted line: inlet temperature. Black dash-dotted line: inlet water vapor concentration. MSE_{SOC} = 3.1·10^{-6}. MSE_{Tout} = 3.6·10^{-2} °C^2.

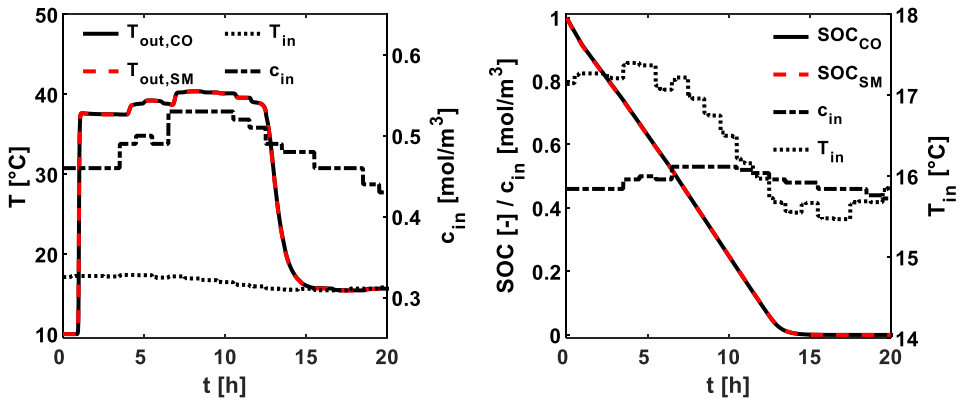

Figure E.2: Test H4 for the spectral model. CO = COMSOL model. SM = Spectral model. Left: Reactor outlet temperatures. Right: SOC. Black solid line: COMSOL model. Red dashed line: spectral model. Black dotted line: inlet temperature. Black dash-dotted line: inlet water vapor concentration. MSE_{SOC} = 10^{-6}. MSE_{Tout} = 1.6·10^{-2} °C^2.

Appendix F: The "big-M" method for conditional statements

A conditional statement in the form of equations F.1 can be formulated in the optimization software, which uses the "big-M" method to formulate the required optimization constraints. The optimization variable $\boldsymbol{y}$, which can have any value in the interval $[A, B]$ with A and B being defined boundaries, takes a value in function of a binary variable $\boldsymbol{x}$ and a constant α. If the value of $\boldsymbol{x}$ is equal to 1, then also the linear constraint $\boldsymbol{H} \geq \beta$ must be satisfied. It has to be noted that, in equation F.1, there is no condition on $\boldsymbol{H}$ when the variable $\boldsymbol{x}$ takes a value of zero.

$$\begin{gathered} \boldsymbol{y} = \boldsymbol{x}\alpha \\ (\boldsymbol{x} = 1) \rightarrow (\boldsymbol{H} \geq \beta) \\ \boldsymbol{x} \in \{0,1\} \\ \boldsymbol{H}, \boldsymbol{y} \in [A, B] \end{gathered} \qquad \text{F.1}$$

The problem in equation F.1 can be formulated with the constraint in equation F.2. Here M is an arbitrary number that has to be larger than any possible value that $(\beta - \boldsymbol{H})$ could take. Therefore, the boundaries of $\boldsymbol{H}$ must be defined within a specified range of values, i.e. $\boldsymbol{H} \in (-\infty, \infty)$ is not a valid interval.

$$-M\boldsymbol{x} \leq (\beta - \boldsymbol{H}) \leq M(1 - \boldsymbol{x}) \qquad \text{F.2}$$

With a similar approach, the value of the binary optimization variables $\boldsymbol{Y}_{loss-top,n,t}$ (equations 6.46 - 6.47) can be imposed, and it is possible to formulate the set of constraints in equation F.3. If the set of constraints defined on the right-hand side of the implication term are satisfied, then the binary variable is equal to 1. It has to be noted that the implication → does not influence the value of $\boldsymbol{Y}_{loss-top,n,t}$ if the set of constraints on the right-hand side is not satisfied. However, by also considering equation 6.47, this ensures that there is always one and only one value of n that is selected as $n_{top,t}$.

$$\boldsymbol{Y}_{loss-top,n,t} = 1 \rightarrow \left\{ \boldsymbol{M}_{n,t} \geq \frac{UA_{top}(T_n - T_{amb,t})}{c_{p,w}(T_n - T_{n-1})} \tau_{n,t} \left(1 - e^{-\frac{\Delta t}{\tau_{n,t}}}\right) \cap \right.$$
$$\left. \left\{ \boldsymbol{M}_{g,t} \leq \frac{UA_{top}(T_g - T_{amb,t})}{c_{p,w}(T_g - T_{g-1})} \tau_{g,t} \left(1 - e^{-\frac{\Delta t}{\tau_{g,t}}}\right) \forall\, g \in \{n+1 \dots N_{seg}\} \right\} \right\} \quad \begin{matrix} \forall t \\ \forall n > 1 \end{matrix} \quad \text{F.3}$$

Equation F.3 implies that the losses through the tank top from segment $n_{top,t}$ are present if and only if there is a minimum quantity of water at T_n corresponding to the one that would be lost due to these thermal losses, and if the top segment does not correspond to the segment at the lowest temperature (n = 1). The fact that the set of constraints on the right-hand side of equation F.3 is composed by non-strict inequalities could allow for more than one $\boldsymbol{Y}_{loss-top,n=\{1\dots N_{seg}\},t}$ at time t to be equal to one. However, from the numerical optimization perspective and considering that each number is in double-precision floating format, this is unlikely to occur, and its occurrence can be verified in the optimization results.

For example, assuming $T_{amb,\{t,t+\Delta t\}}$ = 10 °C, U = 0.5 W/(m^{2}K), a 500 liters water tank with aspect ratio 1.5 (A_{top} = 0.4436 m^2), $\tau_{n,t}\left(1 - \exp\left(-\frac{\Delta t}{\tau_{n,t}}\right)\right) \cong \Delta t$, and the segments temperatures as in Table 6.3, it would be possible that $\boldsymbol{M}_{3,t} = \left(UA_{top}(T_3 - T_{amb,t})\Delta t\right)/(c_{p,w}(T_3 - T_2))$ but also $\boldsymbol{M}_{4,t} = \left(UA_{top}(T_4 - T_{amb,t})\Delta t\right)/(c_{p,w}(T_4 - T_3))$. This implies that two binary variables could be equal to 1: $\boldsymbol{Y}_{loss-top,3,t}$ and $\boldsymbol{Y}_{loss-top,4,t}$. However, due to equation 6.47, only one can take a value equal to 1. The optimization algorithm will erroneously select $\boldsymbol{Y}_{loss-top,3,t}$ because it would imply a lower thermal loss to the environment, hence a lower penalty on the objective function compared to $\boldsymbol{Y}_{loss-top,4,t}$. This would transfer $\boldsymbol{M}_{3,t} = (0.5 \cdot 0.4436 \cdot (40 - 10) \cdot 3600)/(4186 \cdot (40 - 28)) = 0.48$ kg from segment 3 to segment 2 instead of $\boldsymbol{M}_{4,t} = (0.5 \cdot 0.4436 \cdot (55 - 10) \cdot 3600)/(4186 \cdot (55 - 40)) = 0.57$ kg from segment 4 to segment 3. This causes a relatively small error that is corrected at the following timestep when the right amount $\boldsymbol{M}_{4,t+\Delta t}$ would be removed from segment 4 because $\boldsymbol{M}_{3,t+\Delta t} < \left(UA_{top}(T_3 - T_{amb,t+\Delta t}) \cdot \Delta t\right)/(c_{p,w}(T_3 - T_2))$.

BIBLIOGRAPHY

[1] Cook J, Nuccitelli D, Green SA, Richardson M, Winkler B, Painting R, et al. Quantifying the consensus on anthropogenic global warming in the scientific literature. Environ Res Lett 2013:7. doi:10.1016/j.enpol.2014.06.003.

[2] Rafiq S, Salim R, Nielsen I. Urbanization, openness, emissions and energy intensity: A study of increasingly urbanized emerging economies. Energy Econ 2016; 56:20–8. doi:10.1016/j.eneco.2016.02.007.

[3] Cambridge Econometrics. Employment Effects of selected scenarios from the Energy roadmap 2050 - Final report for the European Commission (DG Energy). Cambridge: 2013.

[4] European Commission. 2050 low-carbon economy n.d. https://ec.europa.eu/clima/policies/strategies/2050_en (accessed June 5, 2018).

[5] Blarke MB, Lund H. The effectiveness of storage and relocation options in renewable energy systems. Renew Energy 2008; 33:1499–507. doi:10.1016/j.renene.2007.09.001.

[6] Blarke MB, Jenkins BM. SuperGrid or SmartGrid: Competing strategies for large-scale integration of intermittent renewables? Energy Policy 2013; 58:381–90. doi:10.1016/j.enpol.2013.03.039.

[7] Zhou K, Fu C, Yang S. Big data driven smart energy management: From big data to big insights. Renew Sustain Energy Rev 2016; 56:215–25. doi:10.1016/j.rser.2015.11.050.

[8] European Commission - Directorate General for Energy. Smart Grid Mandate - Standardization Mandate to European Standardisation Organisations (ESOs) to support European Smart Grid deployment. Brussels (BE): 2011.

[9] Smart Grids Task Force. European Task Force For The Implementation Of Smart Grids Into The European Internal Market 2009:1–15. https://ec.europa.eu/energy/sites/ener/files/documents/mission_and_workprogramme.pdf (accessed June 5, 2019).

[10] Lund PD, Lindgren J, Mikkola J, Salpakari J. Review of energy system flexibility measures to enable high levels of variable renewable electricity. Renew Sustain Energy Rev 2015; 45:785–807. doi:10.1016/j.rser.2015.01.057.

[11] Kalaiselvam S, Parameshwaran R. Energy Storage. Therm. energy storage Technol. Sustain. - Syst. Des. Assess. Appl., Elsevier Inc.; 2014, p. 21–56. doi:10.1016/B978-0-12-417291-3.00002-5.

[12] ODYSSEE-MURE. Household energy consumption in the EU 2019. http://www.odyssee-mure.eu/publications/efficiency-by-sector/households/declining-share-space-heating-eu.html (accessed May 31, 2019).

[13] Kalaiselvam S, Parameshwaran R. Seasonal Thermal Energy Storage. Therm. energy storage Technol. Sustain. - Syst. Des. Assess. Appl., Elsevier Inc.; 2014, p. 145–62. doi:10.1016/B978-0-12-417291-3.00007-4.

[14] Gao L, Zhao J, Tang Z. A Review on Borehole Seasonal Solar Thermal Energy Storage. Energy Procedia, vol. 70, Elsevier B.V.; 2015, p. 209–18. doi:10.1016/j.egypro.2015.02.117.

[15] Pinel P, Cruickshank C a., Beausoleil-Morrison I, Wills A. A review of available methods for seasonal storage of solar thermal energy in residential applications. Renew Sustain Energy Rev 2011; 15:3341–59. doi:10.1016/j.rser.2011.04.013.

[16] Pielichowska K, Pielichowski K. Phase change materials for thermal energy storage. Prog Mater Sci 2014; 65:67–123. doi:http://dx.doi.org/10.1016/j.pmatsci.2014.03.005.

[17] Nkwetta DN, Haghighat F. Thermal energy storage with phase change material - A state-of-the art review. Sustain Cities Soc 2014; 10:87–100. doi:10.1016/j.scs.2013.05.007.

[18] Sharif MKA, Al-abidi a a, Mat S, Sopian K, Ruslan MH. Review of the application of phase change material for heating and domestic hot water systems. Renew Sustain Energy Rev 2015; 42:557–68. doi:10.1016/j.rser.2014.09.034.

[19] Scapino L, Zondag HA, Van Bael J, Diriken J, Rindt CCM. Sorption heat storage for long-term low-temperature applications: A review on the advancements at material and prototype scale. Appl Energy 2017; 190:920–48. doi:10.1016/j.apenergy.2016.12.148.

[20] Solé A, Martorell I, Cabeza LF. State of the art on gas–solid thermochemical energy storage systems and reactors for building applications. Renew Sustain Energy Rev 2015; 47:386–98. doi:10.1016/j.rser.2015.03.077.

[21] Yu N, Wang RZ, Wang LW. Sorption thermal storage for solar energy. Prog Energy Combust Sci 2013; 39:489–514. doi:10.1016/j.pecs.2013.05.004 Review.

[22] Krönauer A, Lävemann E, Hauer A. Mobile Sorption Heat Storage in Industrial Waste Heat Recovery. 9th Int. Renew. Energy Storage Conf. IRES 2015, vol. 73, Elsevier B.V.; 2015, p. 1–8. doi:10.1016/j.egypro.2015.07.688.

[23] Nic M, Jirat J, Kosata B. IUPAC Compendium of Chemical Terminology. Oxford: 2006. doi:10.1351/goldbook.

[24] Srivastava NC, Eames IW. A review of adsorbents and adsorbates in solid–vapour adsorption heat pump systems. Appl Therm Eng 1998; 18:707–14. doi:10.1016/S1359-4311(97)00106-3.

[25] Fumey B, Weber R, Gantenbein P, Daguenet-Frick X, Hughes I, Dorer V. Limitations Imposed on Energy Density of Sorption Materials in Seasonal Thermal Storage Systems. Energy Procedia, vol. 70, Elsevier B.V.; 2015, p. 203–8. doi:10.1016/j.egypro.2015.02.116.

[26] Deng S. Sorbent technology. Encycl Chem Process 2006:2825–45. doi:10.1081/E-ECHP-120007963.

[27] van Essen VM, Zondag HA, Cot-Gores J, Bleijendaal LPJ, Bakker M, Schuitema R, et al. Characterization of MgSO4 Hydrate for Thermochemical Seasonal Heat Storage. J Sol Energy Eng 2009; 131:041014. doi:10.1115/1.4000275.

[28] van Essen VM, Cot-Gores J, Bleijendaal LPJ, Zondag HA, Schuitema R, Bakker M, et al. Characterization of Salt Hydrates for Compact Seasonal Thermochemical Storage. ASME 2009 3rd Int. Conf. Energy Sustain., 2009, p. 825–30. doi:10.1115/ES2009-90289.

[29] Ferchaud CJ, Zondag HA, de Boer R, Rindt CCM. Characterization of the sorption process in thermochemical materials for seasonal solar heat storage application. Innostock 2012 Proc. 12th Int. Conf. Energy Storage, 2012, p. 1–10.

[30] Ferchaud CJ, Scherpenborg RAA, Zondag HA, de Boer R. Thermochemical Seasonal Solar Heat Storage in Salt Hydrates for Residential Applications – Influence of the Water Vapor Pressure on the Desorption Kinetics of MgSO4.7H2O. Energy Procedia, vol. 57, Elsevier B.V.; 2014, p. 2436–40. doi:10.1016/j.egypro.2014.10.252.

[31] Bertsch F, Mette B, Asenbeck S, Kerskes H, Müller-Steinhagen H. Low temperature

chemical heat storage–an investigation of hydration reactions. Effstock Conf. Stock., 2009, p. 1–8.

[32] Linnow K, Niermann M, Bonatz D, Posern K, Steiger M. Experimental Studies of the Mechanism and Kinetics of Hydration Reactions. Energy Procedia, vol. 48, Elsevier B.V.; 2014, p. 394–404. doi:10.1016/j.egypro.2014.02.046.

[33] de Boer R, Haije WG, Veldhuis JBJ. Determination of structural , thermodynamic and phase properties in the Na 2 S – H 2 O system for application in a chemical heat pump. Thermochim Acta 2003; 395:3–19.

[34] Trausel F, de Jong A-J, Cuypers R. A review on the properties of salt hydrates for thermochemical storage. SHC 2013, Int. Conf. Sol. Heat. Cool. Build. Ind., vol. 48, Elsevier B.V.; 2014, p. 447–52. doi:10.1016/j.egypro.2014.02.053.

[35] Ferchaud CJ, Zondag HA, Rubino A. Seasonal Sorption Heat Storage – Research On Thermochemical Materials And Storage Performance. Proc. Heat Power Cycle 2012, Alkmaar, the Netherlands: 2012, p. 1–7.

[36] Huang Q, Lu G, Wang J, Yu J. Thermal decomposition mechanisms of MgCl2.6H2O and MgCl2.H2O. J Anal Appl Pyrolysis 2011; 91:159–64. doi:10.1016/j.jaap.2011.02.005.

[37] Zondag HA, van Essen VM, Bleijendaal LPJ, Kikkert B, Bakker M. Application of MgCl2· 6H2O for thermochemical seasonal solar heat storage. 5th Int. Renew. Energy Storage Conf. IRES 2010, Berlin, Germany: 2010.

[38] Rammelberg HU, Schmidt T, Ruck WKL. Hydration and dehydration of salt hydrates and hydroxides for thermal energy storage - Kinetics and energy release. Energy Procedia, vol. 30, Elsevier B.V.; 2012, p. 362–9. doi:10.1016/j.egypro.2012.11.043.

[39] Barreneche C, Fernández AI, Cabeza LF, Cuypers R. Thermophysical characterization and thermal cycling stability of two TCM: CaCl2 and zeolite. Appl Energy 2014; 137:726–30. doi:10.1016/j.apenergy.2014.09.025.

[40] Mauran S, Lahmidi H, Goetz V. Solar heating and cooling by a thermochemical process. First experiments of a prototype storing 60 kW h by a solid/gas reaction. Sol Energy 2008; 82:623–36. doi:10.1016/j.solener.2008.01.002.

[41] Lahmidi H, Mauran S, Goetz V. Definition, test and simulation of a thermochemical storage process adapted to solar thermal systems. Sol Energy 2006; 80:883–93. doi:10.1016/j.solener.2005.01.014.

[42] Michel B, Mazet N, Mauran S, Stitou D, Xu J. Thermochemical process for seasonal storage of solar energy: Characterization and modeling of a high density reactive bed. Energy 2012; 47:553–63. doi:10.1016/j.energy.2012.09.029.

[43] Donkers PAJ, Sögütoglu LC, Huinink HP, Fischer HR, Adan OCG. A review of salt hydrates for seasonal heat storage in domestic applications. Appl Energy 2017; 199:45–68. doi:10.1016/j.apenergy.2017.04.080.

[44] Sögütoglu LC, Donkers PAJ, Fischer HR, Huinink HP, Adan OCG. In-depth investigation of thermochemical performance in a heat battery: Cyclic analysis of K2CO3, MgCl2 and Na2S. Appl Energy 2018; 215:159–73. doi:10.1016/j.apenergy.2018.01.083.

[45] Gaeini M, Shaik SA, Rindt CCM. Characterization of potassium carbonate salt hydrate for thermochemical energy storage in buildings. Energy Build 2019; 196:178–93. doi:10.1016/j.enbuild.2019.05.029.

[46] Sigma-Aldrich. Copper(II) sulfate n.d. http://www.sigmaaldrich.com/catalog/search?term=copperiisulfate1596177589871 1&interface=Substance&N=0&mode=partialmax&lang=en&region=NL&focus=pr

oduct (accessed August 14, 2015).
[47] Zeeshan N, Jie Z, Fei W. Drastic enhancement of propene yield from 1-hexene catalytic cracking using a shape intensified Meso-SAPO-34 catalyst. J Eng Sci Technol 2009; 4:409–18.
[48] Yu N, Wang RZ, Lu ZS, Wang LW. Study on consolidated composite sorbents impregnated with LiCl for thermal energy storage. Int J Heat Mass Transf 2015; 84:660–70. doi:10.1016/j.ijheatmasstransfer.2015.01.065.
[49] Druske M-M, Fopah-Lele A, Korhammer K, Rammelberg HU, Wegscheider N, Ruck WKL, et al. Developed Materials for Thermal Energy Storage: Synthesis and Characterization. Energy Procedia, vol. 61, Elsevier B.V.; 2014, p. 96–9. doi:10.1016/j.egypro.2014.11.915.
[50] Fopah-Lele A, Korhammer K, Wegscheider N, Rammelberg HU, Schmidt T, Ruck WKL. Thermal Conductivity Measurement of Salt Hydrates As Porous Material Using Calorimetric (Dsc) Method. 8th World Conf. Exp. Heat Transf. Fluid Mech. Thermodyn., 2013, p. 2–6.
[51] Simonova IA, Aristov YI. Sorption properties of calcium nitrate dispersed in silica gel : The effect of pore size. Russ J Phys Chem n.d.; 79:1307–11.
[52] Aristov YI. Novel materials for adsorptive heat pumping and storage: Screening and nanotailoring of sorption properties. J Chem Eng Japan 2007; 40:1242–51. doi:10.1252/jcej.07WE228.
[53] Aristov YI, Glaznev IS, Freni A, Restuccia G. Kinetics of water sorption on SWS-1L (calcium chloride confined to mesoporous silica gel): Influence of grain size and temperature. Chem Eng Sci 2006; 61:1453–8. doi:10.1016/j.ces.2005.08.033.
[54] Casey SP, Elvins J, Riffat S, Robinson A. Salt impregnated desiccant matrices for ‘open’ thermochemical energy storage—Selection, synthesis and characterisation of candidate materials. Energy Build 2014; 84:412–25. doi:10.1016/j.enbuild.2014.08.028.
[55] Liu H, Nagano K, Togawa J. A composite material made of mesoporous siliceous shale impregnated with lithium chloride for an open sorption thermal energy storage system. Sol Energy 2015; 111:186–200. doi:10.1016/j.solener.2014.10.044.
[56] Opel O, Rammelberg HU, Gerard M, Ruck WKL. Thermochemical Storage Materials Research - Tga / Dsc-Hydration Studies 2006.
[57] Tanashev YY, Krainov A V., Aristov YI. Thermal conductivity of composite sorbents “salt in porous matrix” for heat storage and transformation. Appl Therm Eng 2013; 61:401–7. doi:10.1016/j.applthermaleng.2013.08.022.
[58] Ponomarenko IV, Glaznev IS, Gubar AV, Aristov YI, Kirik SD. Synthesis and water sorption properties of a new composite “CaCl2 confined into SBA-15 pores.” Microporous Mesoporous Mater 2010; 129:243–50. doi:10.1016/j.micromeso.2009.09.023.
[59] Hongois S, Kuznik F, Stevens P, Roux JJ. Development and characterisation of a new MgSO4-zeolite composite for long-term thermal energy storage. Sol Energy Mater Sol Cells 2011; 95:1831–7. doi:10.1016/j.solmat.2011.01.050.
[60] Jänchen J, Ackermann D, Stach H, Brösicke W. Studies of the water adsorption on Zeolites and modified mesoporous materials for seasonal storage of solar heat. Sol Energy 2004; 76:339–44. doi:10.1016/j.solener.2003.07.036.
[61] Jänchen J, Ackermann D, Weiler E, Stach H, Brösicke W. Calorimetric investigation on zeolites, AlPO4’s and CaCl 2 impregnated attapulgite for thermochemical storage of heat. Thermochim Acta 2005; 434:37–41. doi:10.1016/j.tca.2005.01.009.

[62] Posern K, Kaps C. Calorimetric studies of thermochemical heat storage materials based on mixtures of MgSO4 and MgCl2. Thermochim Acta 2010; 502:73–6. doi:10.1016/j.tca.2010.02.009.

[63] Ristić A, Maučec D, Henninger SK, Kaučič V. New two-component water sorbent CaCl2-FeKIL2 for solar thermal energy storage. Microporous Mesoporous Mater 2012; 164:266–72. doi:10.1016/j.micromeso.2012.06.054.

[64] Korhammer K, Druske M-M, Fopah-Lele A, Rammelberg HU, Wegscheider N, Opel O, et al. Sorption and thermal characterization of composite materials based on chlorides for thermal energy storage. Appl Energy 2016; 162:1462–1472. doi:10.1016/j.apenergy.2015.08.037.

[65] N'Tsoukpoe KE, Restuccia G, Schmidt T, Py X. The size of sorbents in low pressure sorption or thermochemical energy storage processes. Energy 2014; 77:983–98. doi:10.1016/j.energy.2014.10.013.

[66] de Jong A-J, Trausel F, Finck C, Van Vliet L, Cuypers R. Thermochemical heat storage - System design issues. Energy Procedia, vol. 48, Elsevier B.V.; 2014, p. 309–19. doi:10.1016/j.egypro.2014.02.036.

[67] Abedin AH, Rosen MA. Closed and open thermochemical energy storage: Energy- and exergy-based comparisons. Energy 2012; 41:83–92. doi:10.1016/j.energy.2011.06.034.

[68] Mette B, Kerskes H. Process and Reactor Design for Thermo-Chemical Energy Stores. ISES Sol. World Congr., Kassel, Germany: 2011, p. 1–12.

[69] Hauer A, Gschwander S, Kato Y, Martin V, Schossig P, Setterwall F. Transportation of Energy by Utilization of Thermal Energy Storage Technology - Final Report. 2010.

[70] Mette B, Kerskes H, Drück H, Müller-Steinhagen H. New highly efficient regeneration process for thermochemical energy storage. Appl Energy 2013; 109:352–9. doi:10.1016/j.apenergy.2013.01.087.

[71] Zondag H a., van Essen VM, Schuitema R, Bleijendaal LPJ, Kalbasenka A, van Helden WGJ, et al. Engineering Assessment of Reactor Designs for Thermochemical Storage of Solar Heat. Effstock, Stockholm, Sweden: 2009, p. 1–8.

[72] de Boer R, Haije WG, Veldhuis JBJ, Smeding S. Solid-Sorption Cooling With Integrated Thermal Storage: The SWEAT Prototype. Int. Conf. Heat Powerd Cycles, Larnaca, Cyprus: 2004.

[73] Bales C, Gantenbein P, Jaenig D, Kerskes H, Summer K, van Essen VM, et al. Laboratory Tests of Chemical Reactions and Prototype Sorption Storage Units. Borlange: 2008.

[74] Solé A, Miró L, Barreneche C, Martorell I, Cabeza LF. Corrosion Test of Salt Hydrates and Vessel Metals for Thermochemical Energy Storage. Energy Procedia 2014; 48:431–5. doi:10.1016/j.egypro.2014.02.050.

[75] EARTO. The TRL Scale as a Research & Innovation Policy Tool, EARTO Recommendations. 2014.

[76] Hauer A. Adsorption Systems for Tes—Design and Demonstration Projects. Therm. Energy Storage Sustain. Energy Consum., IOS Press; Springer; NATO; 2007, p. 409–27. doi:10.1016/0378-7788(89)90020-0.

[77] Hauer A. Thermal Energy Storage with Zeolite for Heating and Cooling Applications. 2nd Int. Heat Powered Cycles Conf. - Cool. Heat. power Gener. Syst., Paris: 2001, p. 343–8.

[78] Nunez T, Henning HM, Mittelbach W. High energy density heat storage system -

achievements and future work. ISES 2003, Sol. World Congr. Sol. energy a Sustain. Futur., Göteborg: 2003.

[79] Gartler G, Jähnig D, Purkarthofer G, Wagner W. Development of a High Energy Density Sorption Storage System - Basic Principles of an Adsorption Heat Storage System. Eurosun, 2003.

[80] N'Tsoukpoe KE, Liu H, Le Pierrès N, Luo L. A review on long-term sorption solar energy storage. Renew Sustain Energy Rev 2009; 13:2385–96. doi:10.1016/j.rser.2009.05.008.

[81] Iammak K, Wongsuwan W, Kiatsiriroj T. Investigation of modular chemical energy storage performance. Proc. Jt. Int. Conf. Energy Environ., Hua Hin, Thailand; 2004.

[82] Jähnig D, Hausner R, Wagner W, Isaksson C. Thermo-chemical storage for solar space heating in a single-family house. Ecostock Conf. New Jersey; 31 May - 02 June, 2006, p. 1–7.

[83] Kerskes H, Mette B, Bertsch F, Asenbeck S, Drück H. Development of a thermo-chemical energy storage for solar thermal applications. ISES, Sol. World Congr., Kassel, Germany: 2011.

[84] Lass-Seyoum A, Blicker M, Borozdenko D, Friedrich T, Langhof T. Transfer of laboratory results on closed sorption thermo-chemical energy storage to a large-scale technical system. SHC 2012, vol. 30, The Authors; 2012, p. 310–20. doi:10.1016/j.egypro.2012.11.037.

[85] Cuypers R, Maraz N, Eversdijk J, Finck C, Henquet E, Oversloot H, et al. Development of a seasonal thermochemical storage system. Energy Procedia, vol. 30, 2012, p. 207–14. doi:10.1016/j.egypro.2012.11.025.

[86] Zondag HA, Kikkert B, Smeding S, de Boer R, Bakker M. Prototype thermochemical heat storage with open reactor system. Appl Energy 2013; 109:360–5. doi:10.1016/j.apenergy.2013.01.082.

[87] de Boer R, Vanhoudt D, Claessens B, De Ridder F, Reynders G, Cuypers R, et al. Energy-Hub for residential and commercial districts and transport - D3.2 Report on a combination of thermal storage techniques and components. 2014.

[88] Finck C, Henquet E, Van Soest C, Oversloot H, de Jong A-J, Cuypers R, et al. Experimental results of a 3 kWh thermochemical heat storage module for space heating application. Energy Procedia, vol. 48, Elsevier B.V.; 2014, p. 320–6. doi:10.1016/j.egypro.2014.02.037.

[89] de Boer R, Smeding S, Zondag HA, Krol G. Development of a prototype system for seasonal solar heat storage using an open sorption process. Eurotherm Semin. #99 - Adv. Therm. Energy Storage, 2014, p. 1–9.

[90] Zettl B, Englmair G, Somitsch W. An Open Sorption Heat Storage Concept and Materials for Building Heat Supply. Energy Procedia, vol. 73, Elsevier B.V.; 2015, p. 297–304. doi:10.1016/j.egypro.2015.07.692.

[91] Zettl B, Englmair G, Steinmaurer G. Development of a revolving drum reactor for open-sorption heat storage processes. Appl Therm Eng 2014; 70:42–9. doi:10.1016/j.applthermaleng.2014.04.069.

[92] Michel B, Mazet N, Neveu P. Experimental investigation of an innovative thermochemical process operating with a hydrate salt and moist air for thermal storage of solar energy: Global performance. Appl Energy 2014; 129:177–86. doi:10.1016/j.apenergy.2014.04.073.

[93] Johannes K, Kuznik F, Hubert JL, Durier F, Obrecht C. Design and characterisation of a high powered energy dense zeolite thermal energy storage system for buildings.

Appl Energy 2015; 159:80–6. doi:10.1016/j.apenergy.2015.08.109.
[94] van Alebeek R, Scapino L, Beving MAJM, Gaeini M, Rindt CCM, Zondag HA. Investigation of a household-scale open sorption energy storage system based on the zeolite 13X/water reacting pair. Appl Therm Eng 2018; 139. doi:10.1016/j.applthermaleng.2018.04.092.
[95] Gaeini M, van Alebeek R, Scapino L, Zondag HA, Rindt CCM. Hot tap water production by a 4 kW sorption segmented reactor in household scale for seasonal heat storage. J Energy Storage 2018; 17. doi:10.1016/j.est.2018.02.014.
[96] Zhengzhou Gold Mountain Science and Technique Co. Ltd. Molecular Sieve Zeolite 13X n.d. http://www.adsorbentcn.com/13x.htm (accessed August 17, 2015).
[97] Ovchinnikov P, Borodiņecs A, Strelets K. Utilization potential of low temperature hydronic space heating systems: A comparative review. Build Environ 2016; 112:88–98. doi:10.1016/j.buildenv.2016.11.029.
[98] Wagemann DD, Evans WH, Parker VB, Schumm RH, Halow I, Baily SM, et al. The NBS tables of chemical thermodynamic properties: selected values for inorganic and C1 and C2 organic substances in SI units. vol. 11. 1982.
[99] Gaeini M, Zondag H a. Non-Isothermal Kinetics of Zeolite Water Vapor Adsorption Into a Packed Bed Lab Scale Thermochemical 2014:1–11.
[100] Expanded Vermiculite Price and Density n.d. http://www.alibaba.com (accessed April 8, 2016).
[101] N'Tsoukpoe KE, Rammelberg HU, Lele AF, Korhammer K, Watts BA, Schmidt T, et al. A review on the use of calcium chloride in applied thermal engineering. Appl Therm Eng 2015; 75:513–31. doi:10.1016/j.applthermaleng.2014.09.047.
[102] Tokarev M, Gordeeva L, Romannikov V, Glaznev I, Aristov Y. New composite sorbent CaCl2 in mesopores for sorption cooling/heating. Int J Therm Sci 2002; 41:470–747. doi:10.1016/S1290-0729(02)01339-X.
[103] Chan K, Chao CYH, Bahrami M. Heat and Mass Transfer Characteristics of a Zeolite 13X/CaCl2 Composite Adsorbent in Adsorption Cooling Systems. Proc ASME 2012 6th Int Conf Energy Sustain 10th Fuel Cell Sci Eng Technol Conf 2012:1–10.
[104] Gordeeva L, Grekova A, Krieger T, Aristov Y. Composites "binary salts in porous matrix" for adsorption heat transformation. Appl Therm Eng 2013; 50:1633–8. doi:10.1016/j.applthermaleng.2011.07.040.
[105] Donkers PAJ. Experimental study on thermochemical heat storage materials. Eindhoven University of Technology, 2015.
[106] Stainless steel 316 sheet n.d. www.alibaba.com.
[107] Merzkirch A, Maas S, Scholzen F, Waldmann D. Field tests of centralized and decentralized ventilation units in residential buildings - Specific fan power, heat recovery efficiency, shortcuts and volume flow unbalances. Energy Build 2016; 116:373–83. doi:10.1016/j.enbuild.2015.12.008.
[108] Donkers PAJ, Pel L, Adan OCG. Experimental studies for the cyclability of salt hydrates for thermochemical heat storage. J Energy Storage 2016; 5:25–32. doi:10.1016/j.est.2015.11.005.
[109] Eurostat. Electricity and gas prices, second half of year, 2013–15 (EUR per kWh) 2016. http://ec.europa.eu/eurostat/statistics-explained/index.php/File:Electricity_and_gas_prices,_second_half_of_year,_2013–15_(EUR_per_kWh)_YB16.png (accessed November 25, 2016).
[110] Liu H, Le Pierrès N, Luo L. Seasonal storage of solar energy for house heating by different absorption couples. 11th Int. Conf. Energy Storage, Effstock, Stockholm,

Sweden: n.d., p. 1–8.
[111] Liu H, N'Tsoukpoe KE, Nolwenn LP, Luo L. Evaluation of a seasonal storage system of solar energy for house heating using different absorption couples. Energy Convers Manag 2011; 52:2427–36. doi:10.1016/j.enconman.2010.12.049.
[112] Srikhirin P, Aphornratana S, Chungpaibulpatana S. A review of absorption refrigeration technologies. Renew Sustain Energy Rev 2001; 5:343–72. doi:10.1016/S1364-0321(01)00003-X.
[113] Siddiqui MU, Said S a. M. A review of solar powered absorption systems. Renew Sustain Energy Rev 2015; 42:93–115. doi:10.1016/j.rser.2014.10.014.
[114] Wu W, Wang B, Shi W, Li X. An overview of ammonia-based absorption chillers and heat pumps. Renew Sustain Energy Rev 2014; 31:681–707. doi:10.1016/j.rser.2013.12.021.
[115] Liquid sorption materials prices n.d. www.alibaba.com (accessed February 15, 2016).
[116] Fujioka K, Suzuki H. Thermophysical properties and reaction rate of composite reactant of calcium chloride and expanded graphite. Appl Therm Eng 2013; 50:1627–32. doi:10.1016/j.applthermaleng.2011.08.024.
[117] Rathgeber C, Hiebler S, Lävemann E, Dolado P, Lazaro A, Gasia J, et al. IEA SHC Task 42 / ECES Annex 29 – A simple tool for the economic evaluation of thermal energy storages. SHC 2015 , Int. Conf. Sol. Heat. Cool. Build. Ind., 2015.
[118] Rathgeber C, Lävemann E, Hauer A. Economic top–down evaluation of the costs of energy storages—A simple economic truth in two equations. J Energy Storage 2015; 2:43–6. doi:10.1016/j.est.2015.06.001.
[119] Eurostat. Natural gas price statistics 2019. https://ec.europa.eu/eurostat/statistics-explained/index.php/Natural_gas_price_statistics#Natural_gas_prices_for_non-household_consumers (accessed July 2, 2019).
[120] Werner S. European District Heating Price Series. 2016.
[121] Gaeini M, Zondag HA, Rindt CCM. Effect of kinetics on the thermal performance of a sorption heat storage reactor. Appl Therm Eng 2016; 102:520–31. doi:10.1016/j.applthermaleng.2016.03.055.
[122] Gaeini M, Wind R, Donkers PAJ, Zondag HA, Rindt CCM. Development of a validated 2D model for flow, moisture and heat transport in a packed bed reactor using MRI experiment and a lab-scale reactor setup. Int J Heat Mass Transf 2017; 113:1116–29. doi:10.1016/j.ijheatmasstransfer.2017.06.034.
[123] Fopah Lele A. A Thermochemical Heat Storage System for Households - Combined Investigations of Thermal Transfers Coupled to Chemical Reactions. Leuphana Universität Lüneburg, Germany, 2016. doi:10.1007/978-3-319-41228-3.
[124] Michel B, Neveu P, Mazet N. Comparison of closed and open thermochemical processes, for long-term thermal energy storage applications. Energy 2014; 72:702–16. doi:10.1016/j.energy.2014.05.097.
[125] Scapino L, Zondag HA, Van Bael J, Diriken J, Rindt CCM. Energy density and storage capacity cost comparison of conceptual solid and liquid sorption seasonal heat storage systems for low-temperature space heating. Renew Sustain Energy Rev 2017. doi:10.1016/j.rser.2017.03.101.
[126] Scapino L, Zondag HA, Diriken J, Rindt CCM, Van Bael J, Sciacovelli A. Modeling the performance of a sorption thermal energy storage reactor using artificial neural networks. Appl Energy 2019; 253:113525. doi:10.1016/j.apenergy.2019.113525.
[127] COMSOL Inc. COMSOL Multiphysics Reference Manual, version 5.3 2017.

[128] Gaeini M. Thermochemical seasonal heat storage for the built environment. Eindhoven University of Technology, 2017.
[129] Ahn H, Kim M, Lee C. Effects of Heat-Transfer Coefficients on Thermal Dynamics in a Near-Adiabatic Fixed Bed. Sep Sci Technol 2004; 39:2627–54. doi:10.1081/SS-200026757.
[130] Kandula M. On the Effective Thermal Conductivity of Porous Packed Beds with Uniform Spherical Particles. J Porous Media 2011; 14:919–26. doi:10.1615/JPorMedia.v14.i10.70.
[131] Delgado JMPQ. A critical review of dispersion in packed beds. Heat Mass Transf Und Stoffuebertragung 2006; 42:279–310. doi:10.1007/s00231-005-0019-0.
[132] Crawley DB, Lawrie LK, Winkelmann FC, Buhl WF, Huang YJ, Pedersen CO, et al. EnergyPlus: creating a new-generation building energy simulation program. Energy Build 2001; 33:319–31. doi:10.1016/S0378-7788(00)00114-6.
[133] Canuto C, Hussaini MY, Quarteroni A, Zang TA. Spectral Methods in Fluid Dynamics. 1988. doi:10.1007/978-3-642-84108-8.
[134] The MathWorks Inc. MATLAB 2018.
[135] Canuto C, Hussaini MY, Quarteroni A, Zang TA. Spectral Methods. Springer 2007:616. doi:10.1007/978-3-540-30728-0.
[136] Kim P. MATLAB Deep Learning. 2017. doi:10.1007/978-1-4842-2845-6.
[137] Hagan MT, Demuth HB, Beale MH. Neural Network Design. Bost Massachusetts PWS 1995; 2:734. doi:10.1007/1-84628-303-5.
[138] Henrique HM, Lima EL, Seborg DE. Model structure determination in neural network models. Chem Eng Sci 2000; 55:5457–69. doi:10.1016/S0009-2509(00)00170-6.
[139] Kenesei T, Feil B, Abonyi J. Visualization and Complexity Reduction of Neural Networks. Appl. Soft Comput., vol. 52, Berlin, Heidelberg: Springer Berlin Heidelberg; 2009, p. 43–52. doi:10.1007/978-3-540-88079-0_5.
[140] Nelles O. Nonlinear System Identification. vol. 13. Berlin, Heidelberg: Springer Berlin Heidelberg; 2001. doi:10.1007/978-3-662-04323-3.
[141] Mohanraj M, Jayaraj S, Muraleedharan C. Applications of artificial neural networks for thermal analysis of heat exchangers - A review. Int J Therm Sci 2015; 90:150–72. doi:10.1016/j.ijthermalsci.2014.11.030.
[142] Ghritlahre HK, Prasad RK. Prediction of Thermal Performance of Unidirectional Flow Porous Bed Solar Air Heater with Optimal Training Function Using Artificial Neural Network. Energy Procedia 2017; 109:369–76. doi:10.1016/j.egypro.2017.03.033.
[143] Buratti C, Orestano FC, Palladino D. Comparison of the Energy Performance of Existing Buildings by Means of Dynamic Simulations and Artificial Neural Networks. Energy Procedia 2016; 101:176–83. doi:10.1016/j.egypro.2016.11.023.
[144] Ermis K, Erek A, Dincer I. Heat transfer analysis of phase change process in a finned-tube thermal energy storage system using artificial neural network. Int J Heat Mass Transf 2007; 50:3163–75. doi:10.1016/j.ijheatmasstransfer.2006.12.017.
[145] Lecoeuche S, Lalot S, Desmet B. Modelling a non-stationary single tube heat exchanger using multiple coupled local neural networks. Int Commun Heat Mass Transf 2005; 32:913–22. doi:10.1016/j.icheatmasstransfer.2004.08.029.
[146] Richardson RR, Osborne MA, Howey DA. Gaussian process regression for forecasting battery state of health. J Power Sources 2017; 357:209–19. doi:10.1016/j.jpowsour.2017.05.004.

[147] Géczy-Víg P, Farkas I. Neural network modelling of thermal stratification in a solar DHW storage. Sol Energy 2010; 84:801–6. doi:10.1016/j.solener.2010.02.003.
[148] Ghani F, Waser R, O'Donovan TS, Schuetz P, Zaglio M, Wortischek J. Non-linear system identification of a latent heat thermal energy storage system. Appl Therm Eng 2018; 134:585–93. doi:10.1016/j.applthermaleng.2018.02.035.
[149] Jani DB, Mishra M, Sahoo PK. Application of artificial neural network for predicting performance of solid desiccant cooling systems – A review. Renew Sustain Energy Rev 2017; 80:352–66. doi:10.1016/j.rser.2017.05.169.
[150] Fopah Lele A, Kuznik F, Rammelberg HU, Schmidt T, Ruck WKL. Thermal decomposition kinetic of salt hydrates for heat storage systems. Appl Energy 2015; 154:447–58. doi:10.1016/j.apenergy.2015.02.011.
[151] Fopah-lele A, Kuznik F, Osterland T, Ruck WKL. Thermal synthesis of a thermochemical heat storage with heat exchanger optimization. Appl Therm Eng 2016; 101:669–77. doi:10.1016/j.applthermaleng.2015.12.103.
[152] Mette B, Kerskes H, Drück H, Müller-Steinhagen H. Experimental and numerical investigations on the water vapor adsorption isotherms and kinetics of binderless zeolite 13X. Int J Heat Mass Transf 2014; 71:555–61. doi:10.1016/j.ijheatmasstransfer.2013.12.061.
[153] Marquardt DW. An Algorithm for Least-Squares Estimation of Nonlinear Parameters. J Soc Ind Appl Math 1963; 11:431–41. doi:10.1137/0111030.
[154] Hagan MT, Menhaj MB. Training Feedforward Networks with the Marquardt Algorithm. IEEE Trans Neural Networks 1994; 5:989–93. doi:10.1109/72.329697.
[155] Rumelhart DE, Hinton GE, Williams RJ. Learning representations by back-propagating errors. Nature 1986; 323:533–6. doi:10.1038/323533a0.
[156] Dan Foresee F, Hagan MT. Gauss-Newton approximation to bayesian learning. IEEE Int Conf Neural Networks - Conf Proc 1997; 3:1930–5. doi:10.1109/ICNN.1997.614194.
[157] MacKay DJC. Bayesian Interpolation. Neural Comput 1992; 4:415–47. doi:10.1162/neco.1992.4.3.415.
[158] Beale MH, Hagan MT, Demuth HB. Neural Network Toolbox - User's Guide. MathWorks 2018:1–558.
[159] Scapino L, Zondag HA, Diriken J, Rindt CCM, Sciacovelli A. Modeling of a sorption heat storage reactor using nonlinear autoregressive neural networks. Eurotherm Semin. #112 - Adv. Therm. Energy Storage, Lleida: 2019, p. 1–10.
[160] Maas AL, Hannun AY, Ng AY. Rectifier Nonlinearities Improve Neural Network Acoustic Models Andrew 2013.
[161] Scardapane S, Van Vaerenbergh S, Totaro S, Uncini A. Kafnets: kernel-based non-parametric activation functions for neural networks. Neural Networks 2017; 110:19–32. doi:10.1016/j.neunet.2018.11.002.
[162] He K, Zhang X, Ren S, Sun J. Delving deep into rectifiers: Surpassing human-level performance on imagenet classification. Proc IEEE Int Conf Comput Vis 2015; 2015 Inter:1026–34. doi:10.1109/ICCV.2015.123.
[163] Sum JPF, Kan WK, Young GH. A note on the equivalence of NARX and RNN. Neural Comput Appl 1999; 8:33–9. doi:10.1007/s005210050005.
[164] Nemhauser G, Wolsey L. Integer and Combinatorial Optimization. Hoboken, NJ, USA: John Wiley & Sons, Inc.; 1988. doi:10.1002/9781118627372.
[165] Blarke MB. Towards an intermittency-friendly energy system: Comparing electric boilers and heat pumps in distributed cogeneration. Appl Energy 2012; 91:349–65.

doi:10.1016/j.apenergy.2011.09.038.
[166] Blarke MB, Dotzauer E. Intermittency-friendly and high-efficiency cogeneration: Operational optimisation of cogeneration with compression heat pump, flue gas heat recovery, and intermediate cold storage. Energy 2011; 36:6867–78. doi:10.1016/j.energy.2011.10.008.
[167] Amrollahi MH, Bathaee SMT. Techno-economic optimization of hybrid photovoltaic/wind generation together with energy storage system in a stand-alone micro-grid subjected to demand response. Appl Energy 2017; 202:66–77. doi:10.1016/j.apenergy.2017.05.116.
[168] Li Z, Xu Y. Optimal coordinated energy dispatch of a multi-energy microgrid in grid-connected and islanded modes. Appl Energy 2018; 210:974–86. doi:10.1016/j.apenergy.2017.08.197.
[169] Martínez Ceseña EA, Good N, Syrri ALA, Mancarella P. Techno-economic and business case assessment of multi-energy microgrids with co-optimization of energy, reserve and reliability services. Appl Energy 2018; 210:896–913. doi:10.1016/j.apenergy.2017.08.131.
[170] Terlouw T, AlSkaif T, Bauer C, van Sark W. Multi-objective optimization of energy arbitrage in community energy storage systems using different battery technologies. Appl Energy 2019; 239:356–72. doi:10.1016/j.apenergy.2019.01.227.
[171] Frate GF, Carro PP, Ferrari L, Desideri U. Techno-economic sizing of a battery energy storage coupled to a wind farm: An Italian case study. Energy Procedia 2018; 148:447–54. doi:10.1016/j.egypro.2018.08.119.
[172] Blarke MB, Yazawa K, Shakouri A, Carmo C. Thermal battery with CO 2 compression heat pump: Techno-economic optimization of a high-efficiency Smart Grid option for buildings. Energy Build 2012; 50:128–38. doi:10.1016/j.enbuild.2012.03.029.
[173] McKenna R, Fehrenbach D, Merkel E. The role of seasonal thermal energy storage in increasing renewable heating shares: a techno-economic analysis for a typical residential district. Energy Build 2019. doi:10.1016/j.enbuild.2019.01.044.
[174] Timmerman J, Hennen M, Bardow A, Lodewijks P, Vandevelde L, Van Eetvelde G. Towards low carbon business park energy systems: A holistic techno-economic optimisation model. Energy 2017; 125:747–70. doi:10.1016/j.energy.2017.02.081.
[175] van der Heijde B, Scapino L, Vandermeulen A, Patteeuw D, Salenbien R, Helsen L. Using representative time slices for optimization of thermal energy storage systems in low- temperature district heating systems. 31st Int. Conf. Effic. Cost, Optim. Simul. Environ. Impact Energy Syst., 2018, p. 1–13.
[176] Poncelet K, Hoschle H, Delarue E, Virag A, Drhaeseleer W. Selecting representative days for capturing the implications of integrating intermittent renewables in generation expansion planning problems. IEEE Trans Power Syst 2017; 32:1936–48. doi:10.1109/TPWRS.2016.2596803.
[177] Marquant JF, Evins R, Carmeliet J. Reducing computation time with a rolling horizon approach applied to a MILP formulation of multiple urban energy hub system. Procedia Comput Sci 2015; 51:2137–46. doi:10.1016/j.procs.2015.05.486.
[178] Marquant JF, Mavromatidis G, Evins R, Carmeliet J. Comparing different temporal dimension representations in distributed energy system design models. Energy Procedia 2017; 122:907–12. doi:10.1016/j.egypro.2017.07.403.
[179] Heijde B Van Der, Vandermeulen A, Salenbien R. Representative days selection for district energy system optimisation : a solar district heating system with seasonal

storage. Appl Energy 2019; 248:79–94. doi:10.1016/j.apenergy.2019.04.030.
[180] Kuznik F, Johannes K. A Review on Chemisorption Heat Storage in Low-energy Buildings. Energy Procedia 2014; 57:2333–41. doi:10.1016/j.egypro.2014.10.241.
[181] National Grid UK. Capacity (EMR and CMN) 2018. https://www.nationalgrid.com/uk/electricity/capacity-emr-and-cmn (accessed June 10, 2018).
[182] National Grid. GB Electricity Capacity Market Notices 2018. https://gbcmn.nationalgrid.co.uk/ (accessed October 25, 2018).
[183] Ofgem. Annual Report on the Operation of the Capacity Market in 2016/17. 2017.
[184] National Grid UK. Short term operating reserve (STOR) 2018. https://www.nationalgrid.com/uk/electricity/balancing-services/reserve-services/short-term-operating-reserve-stor (accessed June 10, 2018).
[185] National Grid UK. STOR Annual Market Report 2016/17. 2017.
[186] VITO NV. Balmatt Energy Plant 2019. https://vito.be/en/deep-geothermal/balmatt-energy-plant (accessed February 6, 2019).
[187] Lund H, Werner S, Wiltshire R, Svendsen S, Thorsen JE, Hvelplund F, et al. 4th Generation District Heating (4GDH). Integrating smart thermal grids into future sustainable energy systems. Energy 2014; 68:1–11. doi:10.1016/j.energy.2014.02.089.
[188] Remmen P, Lauster M, Mans M, Fuchs M, Osterhage T, Müller D. TEASER: an open tool for urban energy modelling of building stocks. J Build Perform Simul 2018; 11:84–98. doi:10.1080/19401493.2017.1283539.
[189] De Jaeger I, Reynders G, Ma Y, Saelens D. Impact of building geometry description within district energy simulations. Energy 2018; 158:1060–9. doi:10.1016/j.energy.2018.06.098.
[190] Baetens R, Saelens D. Modelling uncertainty in district energy simulations by stochastic residential occupant behaviour. J Build Perform Simul 2016; 9:431–47. doi:10.1080/19401493.2015.1070203.
[191] Wilcox S, Marion W. Users Manual for TMY3 Data Sets. Golden, Colorado: 2008.
[192] Bell IH, Wronski J, Quoilin S, Lemort V. Pure and pseudo-pure fluid thermophysical property evaluation and the open-source thermophysical property library coolprop. Ind Eng Chem Res 2014; 53:2498–508. doi:10.1021/ie4033999.
[193] R. K. SINNOTT. Chemical Engineering Design. 6th ed. Elsevier; 2005.
[194] Glasser L. Thermodynamics of inorganic hydration and of humidity control, with an extensive database of salt hydrate pairs. J Chem Eng Data 2014; 59:526–30. doi:10.1021/je401077x.
[195] Greenspan L. Humidity fixed points of binary saturated aqueous solutions. J Res Natl Bur Stand Sect A Phys Chem 1977; 81A:89. doi:10.6028/jres.081A.011.
[196] AMCA. Fan Efficiency Standards for Commercial & Industrial Buildings. Arlington Heights, USA: 2014.
[197] Cheng NS. Wall effect on pressure drop in packed beds. Powder Technol 2011; 210:261–6. doi:10.1016/j.powtec.2011.03.026.
[198] Gaeini M, Alebeek R Van, Scapino L, Zondag HA, Rindt CCM. Hot tap water production by a 4kW sorption segmented reactor in household scale for seasonal heat storage. J Energy Storage 2018; 17:118–28. doi:10.1016/j.est.2018.02.014.
[199] Gaeini M, Javed MR, Ouwerkerk H, Zondag HA, Rindt CCM. Realization of a 4kW Thermochemical Segmented Reactor in household Scale for Seasonal Heat Storage. IRES 2017, 2017.

[200] Boreal Science. Potassium Carbonate 1.5-Hydrate 2019. https://boreal.com/store/product/8884553/potassium-carbonate-1-5-hydrate.
[201] Till J, Engell S, Panek S, Stursberg O. Empirical Complexity Analysis of a MILP-Approach for Optimization of Hybrid Systems. IFAC Proc Vol 2003; 36:129–34. doi:10.1016/S1474-6670(17)36419-4.
[202] Gurobi Optimization Inc. Gurobi Optimizer Reference Manual 2017:717.
[203] Löfberg J. YALMIP : A Toolbox for Modeling and Optimization in MATLAB. CACSD Conf., Taipei, Taiwan: 2004.
[204] Lin MH, Carlsson JG, Ge D, Shi J, Tsai JF. A review of piecewise linearization methods. Math Probl Eng 2013; 2013. doi:10.1155/2013/101376.
[205] EPEX SPOT Belgium - Day Ahead Market n.d. https://www.belpex.be/market-results/the-market-today/dashboard/ (accessed March 30, 2014).
[206] De Vos K. Factsheet on Negative Electricity Market Prices. 2014.
[207] Staffell I, Scurlock J. Drax Electric Insights Quarterly - Q2 2017. 2018.
[208] Vandewalle J, D'Haeseleer W. The impact of small scale cogeneration on the gas demand at distribution level. Energy Convers Manag 2014; 78:137–50. doi:10.1016/j.enconman.2013.10.005.
[209] Fuentes E, Arce L, Salom J. A review of domestic hot water consumption profiles for application in systems and buildings energy performance analysis. Renew Sustain Energy Rev 2018; 81:1530–47. doi:10.1016/j.rser.2017.05.229.
[210] Bălănescu DT, Homutescu VM. Experimental investigation on performance of a condensing boiler and economic evaluation in real operating conditions. Appl Therm Eng 2018; 143:48–58. doi:10.1016/j.applthermaleng.2018.07.082.
[211] ECOTHERM®. Product Specifications and Design Guide - ESC V18 2011:20.
[212] TYFOROP Chemie GmbH. TYFOCOR® LS® 2015.
[213] European Heat Pump Association. Energy prices: electricity vs. gas 2018. http://stats.ehpa.org/hp_sales/story_prices/ (accessed March 11, 2019).
[214] PricewaterhouseCoopers (PwC). A European comparison of electricity and natural gas prices for residential and small professional consumers. 2018.
[215] Eurostat. Electricity prices for household consumers 2019. https://ec.europa.eu/eurostat/statistics-explained/index.php?title=Electricity_price_statistics#Electricity_prices_for_household_consumers (accessed July 1, 2019).
[216] Sarbu I, Sebarchievici C. Solar-Assisted Heat Pumps. Sol. Heat. Cool. Syst., 2017, p. 347–410. doi:10.1016/B978-0-12-811662-3.00009-8.
[217] Fischer D, Madani H. On heat pumps in smart grids: A review. Renew Sustain Energy Rev 2017; 70:342–57. doi:10.1016/j.rser.2016.11.182.
[218] Schnieders J, Feist W, Rongen L. Passive Houses for different climate zones. Energy Build 2015; 105:71–87. doi:10.1016/j.enbuild.2015.07.032.
[219] Passive House Institute. Passive House requirements 2015. https://passiv.de/en/02_informations/02_passive-house-requirements/02_passive-house-requirements.htm.
[220] Agentschap NL - NL Energie en Klimaat Swentiboldstraat. Voorbeeldwoningen 2011 - Bestande bouw. Sittard (NL): 2011.
[221] Ministry of Economic Affairs and Climate Policy. Energieagenda. Den Haag (NL): 2016. doi:97015.
[222] energypost.eu. A revolution: The Netherlands kisses gas goodbye – but will it help the climate? 2017. https://energypost.eu/a-revolution-the-netherlands-kisses-gas-

goodbye-but-will-it-help-the-climate/ (accessed June 22, 2019).
[223] Stainless steel density n.d. www.engineeringtoolbox.com/metal-alloys-densities-d_50.html (accessed February 18, 2016).
[224] Stainless steel prices n.d. www.alibaba.com (accessed February 18, 2016).
[225] Oxychem. Caustic Soda Handbook. Dallas, Texas (US): Oxychem; 2013.
[226] Weber R, Dorer V. Long-term heat storage with NaOH. Vacuum 2008; 82:708–16. doi:10.1016/j.vacuum.2007.10.018.

NOMENCLATURE

List of symbols

Symbol	Description	Unit
A	Area	m^2
AF	Annuity factor	-
a_{NN}	Neural network output	-
$b_{0,LF}$	Langmuir-Freundlich isotherm parameter	$1/Pa^n$
b_{LF}	Langmuir-Freundlich isotherm parameter	$1/Pa^n$
b_{NN}	Neural network bias	-
C	Cost	€
$C_{\mathcal{D}_{ij}}$	Derivatives discretization coefficients	-
C_{wt}	Specific cost per unit of mass	€/kg
COP	Coefficient of performance	-
c	Sorbate concentration	mol/m^3
c_{GL}	Gauss-Lobatto coefficients	-
c_p	Specific heat capacity	J/(kg·K)
$\mathcal{D}_1$	First derivative discretization matrix	-
$\mathcal{D}_2$	Second derivative discretization matrix	-
D_x	Mass dispersion coefficient	m^2/s
d	Diameter	m
E	Energy	J
ΔE_{LF}	Activation energy of desorption	J/mol
e	Specific energy density	kJ/kg
f_{NN}	Neural network activation function	-
F	Source term	-
f	Mass flow fraction	-
ΔG	Gibbs free energy variation	$J/(mol_w)$
ΔH	Enthalpy variation	$J/(mol_w)$
h	Specific enthalpy	kJ/kg
I	Identity matrix	-
I	Solar irradiation	W/m^2
IR	Yearly interest rate	%
J	Jacobian matrix	-
k_{LDF}	Kinetic constant	1/s
L	Axial length	m

$LCOS$	Levelized cost of storage	€/MWh
lt	Lifetime	years
M	Mass	kg
$\dot{M}$	Water tank mass flow	kg/h
M_{mol}	Molar mass	kg/mol
$\dot{m}$	Mass flow	kg/s
m_f	Mass fraction	-
N_{cycles}	Number of STES cycles	1/year
N_M	Number of modes	-
N_{mesh}	Number of mesh elements	-
N_{seg}	Number of water tank segments	-
N_{STES}	Number of STES units	-
$NNPV$	Normalized net present value	-
NPV	Net present value	€
$n_{1,LF}$	Langmuir-Freundlich isotherm parameter	-
$n_{2,LF}$	Langmuir-Freundlich isotherm parameter	K
n_{LF}	Langmuir-Freundlich isotherm parameter	-
P	Power	W
p	Price	€/MWh
p_0	Reference pressure	Pa
p_{CM}	Capacity market price	€/(kW·y)
p_{eq}	Equilibrium pressure	Pa
p_{NN}	Neural network neuron input	-
$p_{STOR,AP}$	STOR market availability price	€/(MW·h)
p_v	Vapor pressure	Pa
Δp	Pressure drop	Pa
Q	Number of data points	-
q	Sorbate loading in solid	mol/kg
R	Revenues	€
R_{cryst}	Ratio of crystallization	-
R_g	Universal gas constant	J/(mol·K)
R_{th}	Thermal resistance	(m·K/W)
RCD	Relative cost decrease	-
RH	Relative humidity	%
RPI	Relative profit increase	-
S	General state variable	-
SCC	Storage capacity cost	€/kWh$_{cap}$
SF	Solar fraction	%

SOC	State of charge	-
SPF	Seasonal performance factor	-
ΔS	Entropy variation	J/(mol$_w$·K)
s	Thickness	m
T	Temperature	°C
ΔT	Temperature difference	°C
t	Time	s
t_{sim}	Total simulation timesteps	-
Δt	Timestep	s
U	Heat transfer coefficient	W/(m^2·K)
u	Velocity	m/s
V	Volume	m^3
$\dot{V}$	Volumetric flow	m^3/s
w_{NN}	Neural network weight	-
X	Conversion degree	-
X_{mix}	Mixing ratio	-
x_c	Mass concentration	-
x	Spatial coordinate	m
$\mathcal{X}$	Continuous optimization variable	-
Y	Binary optimization variable	-
Z	Pressure ratio	-
z	Objective function	€

List of Greek symbols

Symbol	Description	Unit
$\alpha_{1,STC}$	STC first order parameter	W/(m^{2}K)
$\alpha_{2,STC}$	STC second order parameter	W/(m^{2}K^2)
ε_b	Porosity	-
ε_{HR}	Heat recovery unit efficiency	-
ε_{HX}	Heat exchanger effectiveness	-
η	Efficiency	-
$\eta_{0,STC}$	STC optical efficiency	-
λ	Thermal conductivity	W/(m·K)
μ	Viscosity	Pa·s
ν	Stoichiometric coefficient	-
ξ	Computational domain coordinate	-
ρ	Density	kg/m^3
τ	Time constant	s
ϕ_k	kth order Chebyshev polynomial	-
$\Psi_{DHW\rightarrow SH}$	Domestic hot water to space heating conversion factor	-

List of subscripts and superscripts

Subscripts and superscripts	Description
0	Initial/reference
a	Air
acc	Acceptable
amb	Ambient
b	Packed bed
cap	Capacity
cmp	composite
CO	Comsol model
conv	Convection
cross	Cross sectional
d	Desorption/dehydration/discharge
del	Deliquescence
dry	Drying
eff	Effective
el	Electricity / Electrical
eq	Equilibrium
fix	Fixed
hum	Humidification
i	Inner
in	Inlet
ins	Insulation
loss	Thermal loss
M	material
max	Maximum
min	Minimum
mx	matrix
o	Outer
out	Outlet
p	particle
reac	Reaction
Res	Residual
rt	Return
s	Sorption/Hydration/charge
sat	Saturated

seg	Segment
sens	Sensible
sm	Sorption material
SM	Spectral model
sol	solution
sp	Supply
SS	Stainless steel
th	Thermal
UP	Utilization price
v	Vapor
vol	Volumetric
w	Water
wl	Wall

List of Abbreviations

Abbreviation	Description
AF	Annuity factor
ANN	Artificial neural network
CAPEX	Capital expenditure
CM	Capacity market
DAM	Day ahead market
DHN	District heating network
DHW	Domestic hot water
DSC	Differential scanning calorimetry
ENG	Expanded natural graphite
FFNN	Feedforward neural network
HCT	High concentration tank
HG	Main heating grid
HR	Heat recovery
HTS	Hyperbolic tangent sigmoid function
HX	Heat exchanger
LCT	Low concentration tank
LReLU	Leaky rectified linear unit
MILP	Mixed integer linear programming
MSE	Mean squared error
NARX	Nonlinear autoregressive network with exogenous inputs
OPEX	Operating expense
ORC	Organic Rankine cycle
REC	Reference energy cost
SH	Space heating
ST	Sorbate tank
STC	Solar thermal collector
STES	Sorption thermal energy storage
STOR	Short term operating reserve market
TGA	Thermogravimetric analysis
TRL	Technology readiness level
Z13X	Zeolite 13X

SUMMARY

Sorption thermal energy storage for smart grids: A system-scale analysis

The awareness of humankind's role into climate change and the increasing world energy demand are among the main drivers for a more sustainable and efficient use of energy. The future energy grids, or smart grids, will have to efficiently manage and control the behavior of different types of stakeholders, including an increasing amount of intermittent and distributed energy sources that can lead to a temporal mismatch between the energy demand and supply. Concerning this, energy storage can allow the energy system to gain more flexibility. This dissertation deals with the integration of thermal energy storage (TES) into the future smart grids. TES is an attractive storage category because it can be more economical than other storage technologies, it has storage periods ranging from minutes to months and, finally, because thermal energy dominates the final energy use in sectors such as the built environment. With regard to the type of TES, the focus is on sorption thermal energy storage (STES). This form of energy storage has the potential to store large amounts of thermal energy through a reversible reaction, resulting in higher energy densities and relatively low thermal losses compared to other thermal storage technologies, making this technology especially suitable for long-term storage. In this research, STES for low temperature applications is investigated from different perspectives and scales. The main focus is on thermal energy needs in the built environment such as space heating and domestic hot water production.

STES being a technology still under research with only few existing prototypes in quasi-commercial state, a review on the current state of the art has been carried out in Chapter 2. In the review, possible candidate materials for a future STES system are investigated. Afterwards, the review focuses on the existing sorption reactor prototypes at lab scale and quasi-commercial scale. The main performance indicators (KPIs) such as energy density, power density and temperature lift are discussed in relation to the prototype operating conditions. The review highlighted the need to continue the research at material-scale, including also economic considerations, to find suitable materials with sufficient energy density and hydrothermal stability. Research at reactor-scale, especially for open systems, should focus on modular designs to minimize the pressure drop or on separate reactors to minimize the overall reactor thermal mass. Finally, common practices and reference conditions to calculate the KPIs should be adopted by the scientific community to make different experimental studies comparable.

Then, in Chapter 3, a comparison of different types of conceptual sorption systems is presented in terms of energy density and storage capacity costs for seasonal heat storage applications in a common reference scenario. The aim of this investigation is to provide, with simple techno-economic estimations for conceptual designs, an idea of the potential of this

technology within the current energy market. First, the conceptual sorption systems are presented together with their main advantages and drawbacks. Then, the system size and cost are estimated for different sorption materials and operating conditions. Finally, their material energy density and storage capacity costs (SCC) are compared with previously defined acceptable storage capacity costs (SCC_{acc}) for different users such as industries and dwellings. The results show that, under present-day market conditions, the investigated conceptual systems are not affordable for industrial users (SCC_{acc} < 0.16 €/kWh$_{cap}$), while only certain types of systems based on pure but unstable sorption materials (i.e. $MgCl_2$ and Na_2S) or on ideal composite materials are acceptable for building applications (SCC_{acc}< 1.4 €/kWh$_{cap}$). More stable systems based on zeolite or systems with a higher energy density based on $SrBr_2$ appeared to be unaffordable (SCC> 10 €/kWh$_{cap}$) for all of the investigated user categories. Since the SCC_{acc} is largely affected by the energy prices, which are dependent on multiple factors determining the market conditions, systems like the ones investigated can become more competitive due to, for example, the increase of fossil fuel prices in the upcoming future or the implementation of new market policies.

Next, in Chapter 4, this work focuses on the simulation of a STES reactor using two different approaches: a data-driven model and a physics-based model. The aim was to develop computationally inexpensive models of the sorption reactor to be used in broader energy system models, in which other system components could be co-simulated in a common environment. The physics-based model is based on a global method for the spatial discretization and a semi-implicit method for the temporal discretization, while for the data-driven model, artificial neural networks have been investigated. The aim of the two models is to simulate the STES state of charge and outlet temperature, given as inputs the inlet temperature and reactant concentration. The model results are compared with a high-fidelity model based on computational fluid dynamics. The physics-based model showed good capabilities in predicting the STES dynamics, and it had a higher accuracy than the data-driven model in the performed tests. The data-driven model showed good agreement with the high-fidelity model as well, but it was not able to fully include the thermal inertia effects of the STES in case of, for example, steep inlet temperature gradients. However, the computational cost of the data-driven model resulted to be much lower, and suitable for dynamic system simulations in which computational efficiency is a main requirement (e.g. control applications), provided that a sufficient accuracy is achieved. Nevertheless, for the data-driven model, a relatively extensive training time should be also considered before the model integration into a broader system model.

Finally, the last part of this research studies the impact of STES on different energy systems and market scenarios by performing techno-economic optimizations. In Chapter 5, a system consisting of a district heating network, an organic Rankine cycle, and a centralized STES was investigated for different markets scenarios. Among the main results, the STES integration coupled with balancing market mechanisms increased the yearly system profits up to 41 % compared to the alternative of not integrating the STES, in one of the investigated

scenarios. Moreover, with a 50 % reduction of the energy price for the balancing market accounting for the largest system revenue flow, the system could still achieve approximately 13 % higher profits compared to the solution without the STES integrated.

In Chapter 6, following the same methods of Chapter 5, the integration of a decentralized STES in a domestic environment has been investigated. The system, consisting of solar thermal collectors, a conventional gas boiler, a water tank and a STES, provided the thermal energy for space heating and domestic hot water production of an existing single-family house. The benefits of integrating the STES in terms of system yearly relative cost decrease and solar fraction have been assessed in a reference scenario consisting of an existing large single-family house. The economically optimal solution, in the reference scenario, included a STES with a volume of 0.5 m^3, and it achieved approximately a solar fraction of 57 % and a relative cost decrease of 6.9 % compared to the solution without the STES integrated. Afterwards, the influence of various parameters, such as the electricity-gas price ratio and the STES storage capacity cost, have been investigated. It has been found that the geometrical aspect ratio of the STES units parameters and the particle size had an important influence on the system performance. Thus, the single STES unit optimization for the specific operating conditions of a system is a crucial step to maximize the STES yearly performance. Similarly, the impact of the electricity-gas price ratio, the water tank volume, the STES capacity cost, and the STES fan power on the yearly system costs and solar fraction have been investigated.

From this research project, it is concluded that STES has the potential to be an interesting technology for increasing the smart grids flexibility. However, main challenges at multiple scales still have to be solved. From the economic perspective, the storage capacity cost of a commercialized product will have to be competitive with other storage technologies, and favorable market mechanisms and tariffs proved to be key enabling factors to foster the integration of this storage technology.

LIST OF PUBLICATIONS

Journal publications

Scapino L, Zondag HA, Van Bael J, Diriken J, Rindt CCM. Sorption heat storage for long-term low-temperature applications: A review on the advancements at material and prototype scale. Appl Energy 2017;190:920–48. doi:10.1016/j.apenergy.2016.12.148.

Scapino L, Zondag HA, Van Bael J, Diriken J, Rindt CCM. Energy density and storage capacity cost comparison of conceptual solid and liquid sorption seasonal heat storage systems for low-temperature space heating. Renew Sustain Energy Rev 2017;76:1314–31. doi:10.1016/j.rser.2017.03.101.

Scapino L, Zondag HA, Diriken J, Rindt C, Bael J Van, Sciacovelli A. Modeling the performance of a sorption thermal energy storage reactor using artificial neural networks. Appl Energy 2019;253:113525. doi:10.1016/j.apenergy.2019.113525.

Scapino L, De Servi C, Zondag HA, Diriken J, Rindt C, Sciacovelli A. Techno-economic optimization of an energy system with sorption thermal energy storage in different energy markets. Submitted, 2019.

Gaeini M, van Alebeek R, Scapino L, Zondag HA, Rindt CCM. Hot tap water production by a 4 kW sorption segmented reactor in household scale for seasonal heat storage. J Energy Storage 2018;17. doi:10.1016/j.est.2018.02.014.

van Alebeek R, Scapino L, Beving MAJM, Gaeini M, Rindt CCM, Zondag HA. Investigation of a household-scale open sorption energy storage system based on the zeolite 13X/water reacting pair. Appl Therm Eng 2018;139. doi:10.1016/j.applthermaleng.2018.04.092.

Conference proceedings

Scapino L, Zondag HA, Diriken J, Rindt CCM, Sciacovelli A. Modeling of a sorption heat storage reactor using nonlinear autoregressive neural networks. Eurotherm Semin. #112 - Adv. Therm. Energy Storage, Lleida: 2019, p. 1–10.

van der Heijde B, Scapino L, Vandermeulen A, Patteeuw D, Salenbien R, Helsen L. Using representative time slices for optimization of thermal energy storage systems in low-temperature district heating systems. 31st Int. Conf. Effic. Cost, Optim. Simul. Environ. Impact Energy Syst., 2018, p. 1–13.

Scapino L, Zondag HA, Van Bael J, Diriken J, Rindt CCM. Thermochemical storage for long-term low-temperature applications: A review on current research at material and prototype scales. 10th International Renewable Energy Storage Conference (IRES 2016), Dusseldorf, Germany, March 2016.

Scapino L, De Servi C, Speetjens MFM, Zondag HA, Van Bael J, Diriken J, Rindt CCM. Sorption heat storage integration in future energy grids: reactor model development. 12th International Renewable Energy Storage Conference (IRES 2018), Dusseldorf, Germany, March 2018.

Ferchaud CJ, Scherpenborg R a a, Scapino L, Veldhuis JBJ, Zondag H a, Boer R De. Performance overview of different salt hydrates as thermochemical materials for seasonal solar heat storage in a residential environment. Eurotherm Semin. 99 - Adv. Therm. Energy Storage, 2014, p. 1–9.

ACKNOWLEDGEMENTS

This PhD dissertation is the result of a four years journey. A challenging journey along which I increased my knowledge on new topics, I made new experiences, and I went beyond what I thought were some of my personal limits. This journey made me also discover wonderful people, countries and cultures. Some parts of the journey had to be made alone, but thankfully I was often surrounded by great supervisors, colleagues, friends and family. Without them, the results of this dissertation would have not been possible.

First of all, I would like to thank my first promotor, **Herbert Zondag**, for his supervision during these four years. Herbert, you already supervised me long time ago, in 2013, during my internship at ECN. That internship was probably the very beginning of this PhD journey, being the first opportunity to explore the topic of sorption heat storage. Thanks to your careful supervision, I got very interested in the subject and, almost two years later, I decided to start this PhD project. Within these four years, you always provided valuable, in-depth and meticulous feedback that greatly increased the quality of my work. I always mention that my second paper originated from a small side-comment that you made on my first paper! Your passion for research and your mindset always prompted me to improve my work and look at it from multiple perspectives and with a critical mindset.

Then, I wish to thank my second promotor, **Camilo Rindt**, who supervised me as well since 2013, during my master thesis. Camilo, if the internship at ECN was the very beginning of this long journey, you are definitely the one who made it happen. You mentioned the opportunity of doing a PhD in a joint project with a research institute (VITO), and I realized that it was what I was looking for, in that period. Within these years, you supervised me with your helpful feedback and personal advices. I particularly appreciated your support and freedom that you gave me during this PhD. I think that, sometimes, you and Herbert believed in me more than myself.

I thank my supervisors at VITO, **Jan Diriken** and **Johan Van Bael**, for giving me the opportunity to prove that I was a good candidate for this project, and for your help in preparing the yearly VITO defenses. During this project, you always supported my work and you have given valuable ideas and discussion points.

I wish to thank **Adriano Sciacovelli** for his supervision during my research period at the University of Birmingham. Adriano, I really thank you for your valuable and insightful advices that you gave me at every meeting. When I arrived in Birmingham, I had vague ideas about what I wanted to achieve within those four months. You immediately helped me a lot in transforming those ideas into valuable scientific work, in a relatively short amount of time.

This work is now an important part of this dissertation. Also, I thank you for your inspiring presentations during the research group meetings that you were organizing once a month.

I sincerely thank the external committee members, prof. **Kuznik**, prof. **Hensen**, and prof. **Smeulders**, for their availability to read and evaluate this dissertation.

Part of this journey was possible thanks to the Innoenergy PhD School Programme and the European Institute of Technology (EIT). Within this European programme, I had the opportunity to meet likeminded PhD candidates, to travel in various countries and to follow various courses that enhanced my professional skills with knowledge on entrepreneurship and economics, and improved various soft skills. Moreover, it gave me the opportunity to spend four months to Birmingham for a research period abroad. Thanks to all the people and institutions who made this possible. Special thanks to **Fabien**, **Isabelle**, **Christine** and **Scarlett**, who made everything as smooth as possible and who organized all the events.

I sincerely thank the Energy Technology group for supporting me in these years and providing me the necessary knowledge for advancing in my research. A special thanks to **Michel Speetjens**, who helped me in the development of the spectral model. I really thank you for your help and your time. I really appreciated your enthusiasm for the research and your interest in my research challenge. Sincere thanks to **Claire**, for having supervised me in my internship at ECN, in 2013. Claire, you taught me how to work in a lab, how to write a scientific report, and you did that always with a smile. Together with Herbert and Camilo, you probably contributed most in my decision to start a PhD on this topic. I wish also to thank **Jaap**, **Jan** and **Hans** for their precious work in the lab and their help with every day challenges. **Max**, thank you for your amazing humor, and for always surprising us with the amount of sweets that you can eat. **Koen**, thank you for being our athlete in the group, basically increasing the average group fitness, and for hosting our fry-days. **Mauro**, thanks for your (Italian) humor and for always reminding me what are the good things that are waiting for me in Italy, especially food. A big thank goes to all my PhD present and past colleagues from the Energy Technology group, **Manoj**, **Shahin**, **Shravan**, **Ruud**, **Sergio**, **Sebastian**, **Mengting**, **Raluca**, **Mohammadreza**, **Pim**, **Remco**, **Taha**, **Hakan**, **Camila**, **Len**, **Karunesh**, **Ionut** and **Svetlana**, with whom I shared wonderful moments, discussions, coffee breaks, conferences and outings.

I would like to thank all my colleagues at VITO for providing always a nice work environment and for their support. I really appreciated the team outings, the VITO events, and the great Belgian beers that I could taste with you after work, in Mol. In particular, I would like to thank **Carlo** for helping me with the ORC model. A special thanks goes to **Bram**. We started this challenging journey almost together, and we finished it almost at the same time. Luckily, we also had the opportunity to briefly cross our scientific research paths

and collaborate on the same topic. I really enjoyed our scientific discussions and the results that we achieved. In Barcelona, we had wonderful time at the Business School, and I appreciated your humor, passion for music and books, knowledge of art and history. I think that everything mostly originated from an innate curiosity, an important quality for every scientist.

I wish to thank all the wonderful people that I met in Birmingham, who made me enjoy my stay there since the first day. Thanks to **Robin** for the scientific and non-scientific discussions we had! I wish you good luck with the final part of your PhD. A big thank to **Anabel**, **Serena**, **Sara**, **Helena**, **Alessio**, **Patricia**, **Gilmore**, **Emiliano**, **Ilaria**, **Shivangi**, **Aina**, **Gan**, **Zhong Buzhong**, **Camila**, **Marco**, **Barton** and **Aris** for all the moments we had together.

When I moved to the Netherlands for my master's degree, I thought it was only for two years. However, it turned out to be much more, and I learnt to appreciate many things from this wonderful country and from its people. However, food and weather will always be a daily subject of discussion and complaint for an Italian. In Eindhoven, I met a lot of wonderful people, wonderful friends, with whom I shared a lot of great moments. A special thanks to **Berkay** and **Bersan** for all the amazing experiences we had together in the past years! And a big thank to all my friends that I met in Eindhoven, among which **Valentina B.** and **Sergio**, **Valentina M.**, **Simona** and **Edu**, **Michele** and **Irene**, **Kostis**, **Jad**, **Luca** and **Noemi**, **Mauro**, **Borko**, **Basar**, **Maria Chiara**, **Michalis** and **Maria**, **Pietro**, **Andrea**, **Will** and **Gunnar**.

Aiman, as you would also say: a big thank to you for being awesome. In these years, you inspired me in searching always for the best side of the people and in helping others. Moreover, I also like a lot your movies!

Cristian, amico mio, la prima persona che ho incontrato appena arrivato in Eindhoven. Ed entrambi abbiamo pensato "ecco, subito un altro italiano!". Abbiamo condiviso momenti fantastici, mi hai insegnato molto (ma non la breakdance), ci siamo ritrovati sul tetto del campidoglio a Roma insieme a **Pietro** ed **Andrea** alla ricerca della mobilità sostenibile, hai fondato una realtà bellissima che è *wedowe*, hai creduto in te stesso e hai preso tante decisioni, anche non facili. È stato un onore aver condiviso con te molti di questi momenti.

Tutto questo non sarebbe stato possibile senza i miei amici in Italia. Voi siete stati e sarete sempre la mia famiglia allargata ed i miei compagni di viaggio. Mi darete sempre un motivo per tornare a casa ancora una volta. Spenderei intere pagine a ringraziarvi uno ad uno, e per ognuno di voi avrei aneddoti che raddoppierebbero le pagine di questa tesi. Ma purtroppo dovrò essere breve. Un enorme ringraziamento a **Posta Sauer**, nello specifico grazie a **Matte**, **Marche**, **Leo**, **Bruno**, **Mauro**, **Dade**, **Silve**, **Giudice**, **Cocco**, **Perroz**, **Point**, **Simo**, **Enri** e **Billy**. Uno speciale ringraziamento a **Matte** e **Marche** per aver passato parte della loro estate

a disegnarmi la copertina della tesi. Un grazie a **Luigi** e **Gian** che, anche se ormai siamo sparsi per il mondo, riusciamo ancora a ritrovarci e fare dei fantastici viaggi insieme, e recentemente ed affrontare bestie pericolose insieme a **Stefano**. Grazie anche a **Monica**, **Carola**, **Marta**, **Ila**, **Martina G.**, **Martina T.**, lo chef **Andrea**, **Myriam** e **Gigi**, **Dario** e **Maio**, **Fede**, **Irene**, **Anna**, **Giulia**, **Alessia** e **Boris** perché, anche se non ve ne renderete conto, avete contribuito un pochino a questa tesi.

Sara, la mia compagna di un viaggio molto più grande e molto più lungo del dottorato. Senza di te, tutto sarebbe stato più difficile. Mi hai supportato e sopportato in questo percorso ed hai reso ogni giorno migliore. Queste poche righe non ti renderebbero mai giustizia, ma spero tu sappia quanto ti sono grato per tutto l'amore, l'aiuto ed i momenti fantastici che abbiamo passato insieme. Non vedo l'ora di passarne molti altri.

Un grazie alla mia famiglia che ha sempre saputo sostenermi con amore incondizionato. Grazie a **Roby**, **Laura**, **Isa** e **Tiz**, **Paola** e **Mottola**. Un grazie a **Jolanda** e **Margherita**, a cui inevitabilmente strappo ancora una lacrimuccia ogni volta che le saluto prima di ripartire per l'Olanda. Grazie ai piccoli **Simone**, **Riccardo** e **Viola**. Questa tesi è dedicata anche a voi, il nostro futuro.

Un immenso grazie ai miei genitori, **Vanda** e **Dario**, che sin da quando ero piccolo mi hanno spinto ad essere curioso, a pormi delle domande ed a cercarne le risposte. Mamma, ricorderò per sempre un cartello che appendesti in cucina quando avevo 3 anni, diceva: "Potrai comprargli quello che vuoi ma senza cultura tuo figlio rimarrà sempre vuoto". Quel cartello rimase lì appeso per vent'anni. Ancora oggi, ventisette anni dopo, non hai mai smesso di insegnarmi, e rimani la maestra migliore che abbia mai avuto. Papà, sin da quando ero piccolo il tuo ottimismo mi ha accompagnato nei momenti più difficili. Mi hai insegnato che, alla fine, sono le piccole gioie quotidiane che ci danno la forza d'animo per affrontare le sfide più grandi. Farò di tutto per arrivare ad avere la tua felicità ed energia, tra trent'anni.

Grazie di tutto.

Luca Scapino, 25th October 2019

CURRICULUM VITAE

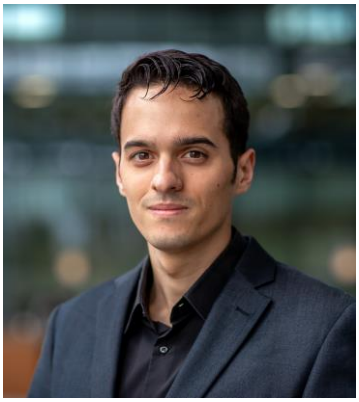

Luca Scapino was born on June 23rd 1989 in Turin, Italy. He received his Bachelor of Science in Energy Engineering in 2012 at Politecnico di Torino.
He then moved to the Netherlands to study the master program Sustainable Energy Technology in the Mechanical Engineering Department at the Eindhoven University of Technology. In 2014, Luca finished his master thesis in the Energy Technology group under the supervision of dr. ir. Camilo C.M. Rindt and dr. ir. Henk Ouwerkerk, and he received his Master of Science degree. From 2015, he started a joint PhD project between the Flemish Institute for Technological Research (VITO) and the Eindhoven University of Technology. During his PhD, Luca got admitted at the InnoEnergy PhD School, which gave him the opportunity to follow various courses in different European countries, among which an entrepreneurship summer school at the ESADE Business & Law School, in Barcelona (Spain). Within this European program, Luca had also the opportunity to do a research period at the Birmingham Centre for Energy Storage, at the University of Birmingham, where he collaborated with Dr. Adriano Sciacovelli. The Ph.D. project entitled “Sorption thermal energy storage for smart grids: a system-scale analysis” was supervised by prof. Herbert Zondag and dr. Camilo Rindt. The results of his research are presented in this dissertation.
Since 2019, he is employed at the Flemish Institute for Technological Research (VITO).